Solid-Phase On-Chip Nucleic Acid Hybridization Assays Using Spatial Profiles from Fluorescence Resonance Energy Transfer by Immobilized Quantum Dots

by

Anthony Tavares

A thesis submitted in conformity with the requirements
for the degree of Doctor of Philosophy

Department of Chemistry
University of Toronto

Solid-Phase On-Chip Nucleic Acid Hybridization Assays Using Spatial Profiles from Fluorescence Resonance Energy Transfer by Immobilized Quantum Dots

Anthony Tavares

Doctor of Philosophy

Department of Chemistry
University of Toronto

2014

Abstract

The research that is presented herein explores the development of a solid-phase DNA hybridization assay in an electrokinetically controlled biochip. Transduction of nucleic acid hybridization is accomplished by fluorescence resonance energy transfer (FRET) from a layer of immobilized quantum dots (QDs) in microfluidic channels. The chip assay platform was assembled as a composite of glass and polydimethylsiloxane (PDMS), where the glass surface was functionalized with immobilization chemistry to support the spontaneous assembly of QDs. Probe oligonucleotides were subsequently conjugated to the immobilized QDs and hybridization served as the selective interaction for target binding. Since the entire microchannel was derivatized with the transduction element, hybridization of dye labeled oligonucleotides along the channel length created well defined spatial profiles of FRET sensitized acceptor emission. The length of the FRET spatial profiles was related to the quantity of nucleic acid delivered and enabled quantitative transduction of tens of fmol amounts of target within minutes. This chip based assay offered multiplexed analysis where the concurrent detection of two targets was possible with a dynamic range spanning more than an order of magnitude. The robustness of the assay was demonstrated by transduction of nucleic acid targets in a variety of complex matrices

including sample solutions that contained an excess of genomic DNA and also serum proteins. Furthermore, the assay offered excellent selectivity toward determination of the presence of a single nucleotide polymorphism (SNP), with contrast ratios exceeding 100:1. A non-traditional approach to SNP transduction was explored, where the size of the QD was found to impact the stringency of interfacial hybridization. Detection of unlabeled target oligonucleotide using a sandwich assay approach enabled transduction of oligonucleotides up to 40 nucleotides in length. The research described herein advances the development of a selective interfacial transduction strategy for the detection of nucleic acid markers such as might be characteristic of disease or pathogens. The on-chip assay format is amenable to point-of-care analysis and can be combined with nucleic acid amplification technologies for highly sensitive on demand DNA analysis.

Acknowledgments

I would like to extend sincere gratitude to my supervisor Professor Ulrich J. Krull, whom I first became inspired by during my second year of undergraduate studies. Thank you for unparalleled guidance and support, not only toward my doctoral studies, but to all aspects of my professional development.

I am also grateful to my doctoral advisory committee members R. Scott Prosser and Aaron R. Wheeler, who have always offered outstanding advice and motivational discussion in committee meetings. I would also like to thank Paul A. E. Piunno for countless discussions and mentorship, and Warren C. W. Chan for useful discussion and guidance during my comprehensive examination. Great thanks are extended to W. Russ Algar for mentorship, guidance, and actively contributing to the work described herein.

Much of the work completed over the course of this thesis would not have been possible without the help from the many talented employees at the University of Toronto. Dr. Ilya Gourevich and Dr. Neil Coombs are thanked for assistance with SEM and Dr. Rana Sodhi is thanked for acquisition of XPS measurements. Peter Mitrakos is also thanked for assistance with NMR and MS. Extended thanks is also given to the Academic Workshop, UTM Stores, and Microelectronics. Sincere gratitude must also be extended to Carmen Bryson for outstanding administrative support to our research team.

I can’t express how fortunate I was to conduct my doctorate research in the chemical sensors group. The presence of innovative and supportive graduate and undergraduate students during my tenure at UTM has been an invaluable experience. Much of the work described herein could not have been realized without outstanding contributions from M. Omair Noor, Eleonora Petryayeva, and Uvaraj Uddayasankar both in research and discussion. These individuals along with many former and current colleagues have provided such an enjoyable team environment with special mention to: Lu Chen, Lori Chong, Rhys Crasto, Matthew DaCosta, Samer Doughan, Laura Fedoryshin, Yi Han, David Hrovat, Qiang Ju, Connie Le, Melissa Massey, Max Prigozhin, Philip Rolo, Anna Shahmuradyan, Ravi T. Shergill, Charles Vannoy, Misa Vujaklija, April Wong, and Feng Zhou.

To my mom and dad, I am so grateful for your support throughout my entire academic career. I would not be where I am today without your unparalleled guidance and motivation.

To my lovely wife, you bring out the best in me. Thank you for your unabated compassion, patience, and support throughout my doctoral program.

List of Abbreviations

A	Acceptor - FRET
A488	Alexa Fluor 488
A594	Alexa Fluor 594
A647	Alexa Fluor 647
At647	Atto 647
ATPMS	3-aminopropyl trimethoxysilane
Au NP	Gold Nanoparticle
Av	Avidin
BFHB	Bifurcated hydrogen bond
BHQ-2	Black-hole quencher-2
BRET	Bioluminescence resonance energy transfer
CAD	Computer aided design
CE	Capillary electrophoresis
CF	Cystic Fibrosis
CRET	Chemiluminescence resonance energy transfer
Cy3	Cyanine 3
Cy5	Cyanine 5
D	Donor - FRET
dA	Adenine
DABCYL	4-((4-(dimethylamino) phenyl)azo)benzoic acid
dC	Cytosine
dG	Guanine
DHLA	dihydrolipoic acid
DNA	Deoxyribonucleic acid
dNTPs	Deoxynucleotide triphosphates
dsDNA	Double stranded DNA
dT	Thymine
EB	Ethidium Bromide
EDL	Electrical double layer
EOF	electroosmotic flow
EPF	electrophoretic force
EWOD	Electrowetting-on-dielectric
EWOD	Electrowetting-on-dielectric
FC	Fully complementary
FCS	Fluorescence correlation spectroscopy
FISH	fluorescence in situ hybridization
FRET	Fluorescence resonance energy transfer
FWHM	full-width-at-half-maximum
GOPs	3-glycidoxypropyltrimethoxysilane
H-bond	Hydrogen bond
HDA	Hexadecylamine
HOMO	Highest occupied molecular orbital
IaB	Iowa Black FQ
IRF	Instrument response function
LOC	lab-on-a-chip
LOD	Limit of detection
LUMO	Lowest unoccupied molecular orbital
MAA	mercaptoacetic acid
MB	Molecular beacon
MiRNA	microRNA
n-BPM	N-base pair mismatch
NC	Noncomplementary
NIR	Near Infrared
NP	Nanoparticle
NR	Nanorod
NW	Nanowire
OHP	Outer Helmholtz plane
PC	Probe Conjugates
PCR	Polymerase chain reaction
PDMS	Polydimethyl siloxane
PEG	Polyethylene glycol
PL	Photoluminescence
POC	Point-of-care
QD	Quantum Dot
QD-PC	Quantum dot-probe conjugate
QDXYZ	QD with peak PL at XYZ

RAHB	Resonance-assisted hydrogen bonding
REP	Reporter oligonucleotide
RLUC	Renilla luciferase
RNA	Ribonucleic acid
Sav	Streptavidin
SEM	Scanning electron microscopy
SMA	Spinal muscular atrophy
SMN	Survival motor neuron
SNP	Single nucleotide polymorphism
ssDNA	Single stranded DNA
TEG	Triethylene glycol
TEM	Transmission electron microscopy
TGT	Target
Tm	Melt temperature of a DNA duplex
TMS-S	Hexamethyldisilathiane
TOP	trioctylphospine
TOPO	trioctylphosphine oxide
UNL-TGT	Unlabeled target
Xmer	An oligonucleotide that is "x" nucleobases in length

Table of Contents

List of Tables

List of Figures

saturation of recognition sites for a defined channel area should require less amount of target and ultimately this should increase the profile for a given target concentration. (ii) Control over flow injection parameters should enable an “on the fly” tunable dynamic response to ensure a given target concentration falls within the dynamic range of the assay. Furthermore, control over injection parameters could be coupled with channel dimensions as smaller microchannels can afford higher electric field strengths and still maintain low current and Joule heating effects. Optimization of such control could offer lower LODs and a collective dynamic range spanning more than two-three orders of magnitude based. (b) A schematic design of a LOC system for amplification of nucleic acid targets followed by on-chip spatial transduction. The inlet ports and central channel at the top of the chip illustrate the zone of amplification, were enzymes and dNTP precursors can be added for nucleic acid amplification. Controlled micro heating elements can be patterned into the chip design to afford isothermal conditions for amplification to proceed. Assay assembly is localized at the end of the chip, where a plug injection of amplified material can proceed using the additional inlet ports toward the detection platform. (c) Improved spatial assay sensitivity and LODs toward longer nucleic acid targets as a result of reduced hybridization efficiency with immobilized probe. Such a phenomenon would further highlight the advantage of spatial transduction and may overcome limitations discussed in much of the literature about analyses by hybridization of nucleic acid targets associated with real samples.136

List of Appendices

1 Introduction

1.1 Nucleic Acid Bioassays and Biosensors

The continued demand for rapid screening systems for biological markers characteristic of disease, pathogens, and or small molecule toxins to improve the well-being of a population has fueled the growth of the bioanalytical field known as bio-sensors. A biosensor is comprised of two main components: a selective biorecognition element and a transduction mechanism to translate the binding event into a measureable analytical signal. The former is usually an immobilized biomolecule that offers selective binding to a target analyte and can be for example a protein, peptide, or a derivative of nucleic acid. The latter is a transducer that can operate, optically, electrochemically, or piezoelectrically depending on the nature of the target and the response induced upon binding.

The choice of biomolecule to build the recognition element is primarily dependent on the specific analyte in question although for example a bacterium species such as *E.coli* may be transduced by interrogation of a characteristic enzyme or nucleic acid sequence. Proteins such as antibodies are highly selective with affinity constants ranging from 10^{9}-10^{12} M^{-1} and moreover the environment of the assay can be tuned to make them *specific*. However, an important aspect of a biosensor is that it should offer regeneration of the selective interface and enable analysis of a subsequent sample; this is the fundamental difference between a biosensor and a bioassay or bioprobe. DNA probes also offer a high degree of selectivity due to the inherent nature of nucleic acid hybridization where a single base-pair mismatch (1BPM) results in a significant change in the thermodynamics of duplex annealing to offer selectivity between targets. Moreover, chaotropic agents or increases in temperature can enable duplex melting, and probe regeneration with no consequence on the selectivity to subsequent samples. On the contrary, these conditions may degrade the integrity of the protein based recognition by causing denaturation of tertiary or quaternary structure. In addition to robustness, DNA detection enables application to a diverse set of analytes ranging from markers of pathogens to genetic disorders as nucleic acids serve as the fundamental coding material for life, where portions of the genetic code or *genes* are unique to organism identity.

Of the aforementioned transduction strategies, all find application in DNA detection and each can have significant advantages. Electrochemical methods are marked by high speed and sensitivity and can provide a dynamic range spanning several orders of magnitude. Piezoelectric methods on the other hand serve as mass recognition sensors and do not require labelling of target analyte. Optical methods of transduction are generally classified by high sensitivity and low detection limits. Fluorescence, plasmonic, and Raman techniques, provide single molecule detection.[1-3]

Optical methods have also benefited from the impact of nanotechnology where functional nanoparticles (NPs) such as gold NPs (AuNPs) and quantum dots (QDs) have been integrated into localized surface plasmon resonance (LSPR), surface-enhanced Raman spectroscopy (SERS) and fluorescence transduction mechanisms, respectively. In plasmonic based approaches, DNA detection can be transduced by wavelength shift measurements, angular resolved and imaging detection modalities,[4, 5] and through the proximal dependence of plasmonic coupling between adjacent NPs.[6] The unique optical properties of QDs such as high quantum yield and resistance to photobleaching have made them superior to organic fluorophores and effectively replaced them as labels for fluorescence based nucleic acid detection. Fluorimetric assays including microarrays and those based on molecular biology techniques such as polymerase chain reaction (PCR) and more recently isothermal amplification methods have proven reliable for nucleic acid detection. The former is used to process a large number of nucleic acid targets as to provide comprehensive genetic analysis, while the latter in theory, can offer detection of a single nucleic acid duplex after multiple cycles of amplification. While both techniques are robust, microarray methods suffer from long analysis times and amplification methods are highly sensitive to contamination and required the need for trained personnel. Fluorimetric DNA bioassays and biosensors can overcome these challenges and offer a cost-effective, rapid screening strategy for on demand analysis. QDs have been integrated as labels into fluorescence based sensors and have been incorporated into those based on fluorescence resonance energy transfer (FRET) where the latter transduction mechanism alleviates the need to wash after sample measurements as to avoid background fluorescence. A comprehensive literature review of QD-FRET bioassays and biosensors relevant to the research work described herein is provided in section 1.4.5. Prior to this discussion, a theoretical background is presented on the biochemistry of nucleic acids, the principles of fluorescence spectroscopy, the fundamentals of

QDs, and the concepts of microfluidics. The chapter concludes with a description of the contributions to the field made by the research work that is described in this thesis.

1.2 Molecular Structure and Energetics of Deoxyribonucleic Acid

1.2.1 Composition of Deoxyribonucleic Acid

The double helix structure of deoxyribonucleic acid (DNA) was first proposed in 1953 by Watson and Crick[7] who analyzed the collective data of base composition rules from Chargaff and the X-ray diffraction pattern acquired by Franklin.[8] The secondary helical structure is composed of two polymeric single strands made up by the four nucleotides shown in Fig. 2 that are ultimately the unit building blocks of DNA. The monomeric nucleotides contain a phosphate group, a sugar, and a pyrimidine or purine base. As the name implies, the pyrimidine bases cytosine and thymine are derivatives of the compound pyrimidine, guanine and adenine comprise the purine bases.[9] The pentose sugar in the nucleotide is deoxyribose, where the prefix deoxy refers to the absence of the 2′ hydroxyl. The absence of the 2′ hydroxyl in DNA greatly reduces the extent of hydrolysis and is responsible for the increased fidelity of molecule. On the contrary, the half-life of ribonucleic acid (RNA) in the cytoplasm is on the order of minutes to hours and varies dependent upon gene regulation.[10] Single stranded DNA (ssDNA) biopolymers are formed through a condensation reaction between the 5′ phosphate and the 3′ hydroxyl of the nucleobase molecules. These phosphodiester bonds are what link thousands to millions of nucleotides in a ssDNA sequence.[9] Interactions between bases of ssDNA molecules are what form the secondary double stranded DNA (dsDNA) structure. The Watson and Crick base pairing rules were derived from the X-ray diffraction data where only a purine base paired with a pyrimidine base gave rise to a helical radius consistent with the data. Furthermore, while this suggested four possible combinations of base pairing, the only two consistent with Chargaff's studies were deoxyguanine-deoxycytosine (dG-dC) and deoxyadenine-deoxythymine (dA-dT) pairing.[8] The A-T and G-C base pairs are held together by two and three hydrogen bonds, respectively (Fig. 2). The base pairing aligns the two ssDNA segments in an anti-parallel orientation relative to each other. The result is a right-handed helix that turns in a clockwise direction with alternating major and minor grooves (Fig. 2).[8]

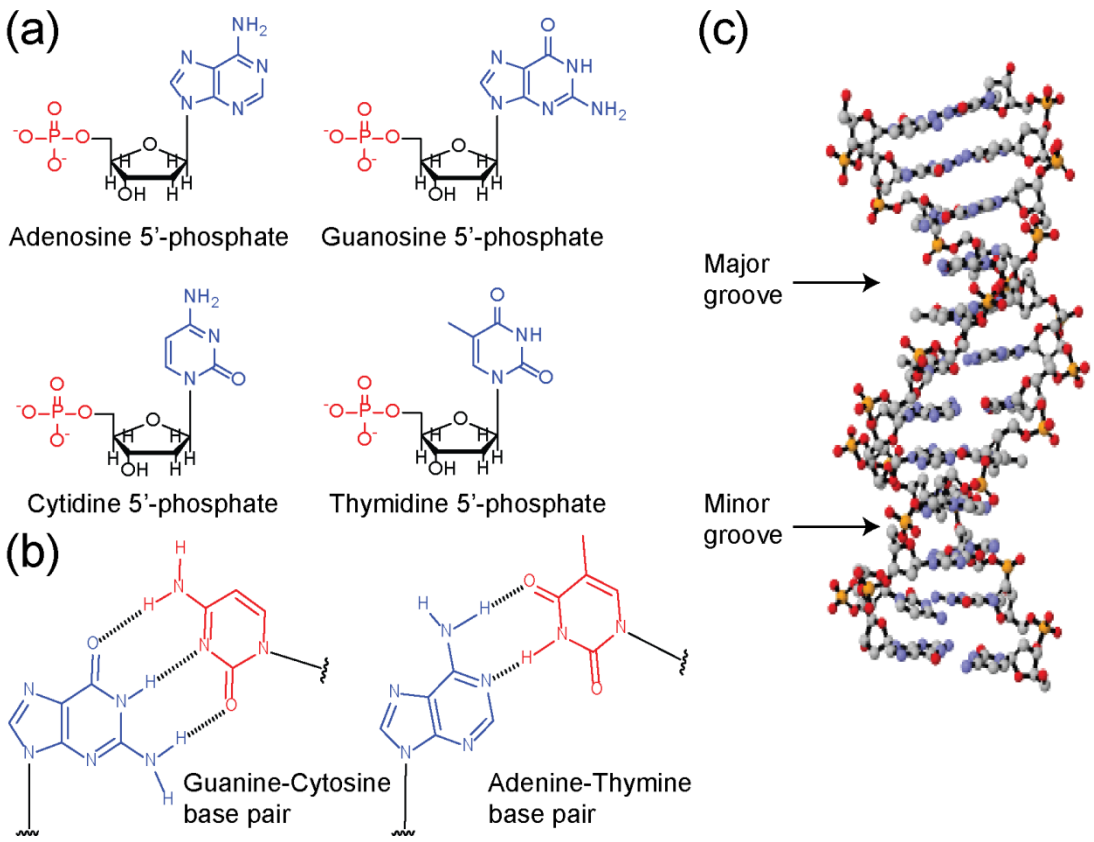

Figure 1. Molecular composition of DNA. The deoxyribonucleotides **(a)** are comprised of a 5' phosphate (red) deoxypentose sugar (black) and a nitrogenous purine or pyrimidine base (blue). The purine bases adenine and guanine base pair with the pyrimidine bases thymine and cytosine, respectively **(b)** where guanine-cytosine form three hydrogen bonds and two are formed between adenine-thymine. Hydrogen bonding between adjacent ssDNA strands generates the secondary double helix structure **(c)**. The right-handed helical structure has alternating major and minor grooves as a result of the anti-parallel orientation of the ssDNA sequences; one sequence is oriented from the 5′ phosphate to the 3′ hydroxyl of the sugar while the other is directly opposite. The polyanionic sugar-phosphate backbone renders DNA with a net overall negative charge allowing high solubility in aqueous media. The interior is hydrophobic and is primarily occupied by the planar aromatic nucleobases. In addition to hydrogen bonding between bases, π-π stacking interactions among bases also stabilize the dsDNA helix.

One sequence is oriented from the 5′ phosphate to the 3′ hydroxyl of the deoxyribose, while the complementary strand is oriented from the 3′ hydroxyl of the deoxyribose to the the 5′ phosphate. At each end of the duplex exists a free phosphate and sugar, and importantly a 3′ hydroxyl. Both of these functional groups can be further modified with nucleophilic or electrophilic groups to enable routine modification and or bioconjugation. The 5′-3′ orientation is often used in convention for the notation of a ssDNA or dsDNA sequence. The former is listed from 5′ to 3′ with single letter abbreviations for each nucleobase: 5′-AGCT-3′, the latter adopts a similar notation where the sequence with 5′ to 3′ orientation is listed first and the complementary strand is listed below from 3′ to 5′ to display basepairing.[9] The exterior of the duplex is hydrophilic as a result of the polyanionic phosphate backbone which creates a net negative

charge for the biomolecule. The interior of the duplex is hydrophobic as it is occupied by the planar aromatic nucleobases. While hydrogen bonding is the predominant force of attraction in formation of the helix, other intramolecular and intermolecular interactions assist in stabilizing the duplex. The delocalized electron density of the aromatic bases form π-π stacking interactions along the interior of the helix where the distance between two successive bases is 0.34 nm. Moreover, interaction with solvent water molecules also adds stability. For every 12 base pairs, there can be up to 72 water molecules associated with the duplex and are numerous in the minor groove and in the major groove. This is due to the extension of the keto and amino groups of the bases into the grooves which can form hydrogen bonds with the water molecules.[9] In one complete turn of the duplex there are 10 nucleobases that occupy a length of 3.4 nm and the width of the duplex is 2 nm. The structure of dsDNA is somewhat dynamic and experiences "breathing" like motion, particularly within a few bases of both the 5′ and 3′ ends.

Closer examination of the nucleobase structure and the hydrogen bonding between both G-C and A-T pairs, suggests that potential resonance structures among bases could contribute to the increased stability of the inter-base hydrogen bonds (H-bond). This phenomenon is known as resonance-assisted hydrogen bonding (RAHB) and was identified by Gilli et al.[11] in a study that investigated H-bonding in keto-enol tautomers of acetylacetone, *β*-diketones, and *β*-keto esters. Increases of 20 $kJ \cdot mol^{-1}$ in bond strength was reported for an intramolecular H-bond in malonaldehyde and the strength of the H-bond was found to be proportional to the degree of electron delocalization from conjugated double bonds. A qualitative illustration of RAHB in base pair coupling can be seen by the resonance structures in Figure 2(a). In this notation, the dashed bonds represent delocalization of the electron density of the aromatic bases, where the hydrogens are not formally assigned to either an amino or carbonyl group, and are located at a distance defined by the relative strength of the H-bond donor-acceptor as induced from resonance. Furthermore, while an H-bond is a special case of a dipole-dipole interaction, in RAHB the interaction exhibits more ion-dipole character due to the formal charges on atoms in the resonance structure. In addition to RAHB, bifurcated H-bonds (BFHB) have been reported in DNA hybrids and are characteristic of A-T base pairs. BFHB were found to induce a characteristic propeller twist in dsDNA structure in regions of A-T repeats.[12] The structure of a

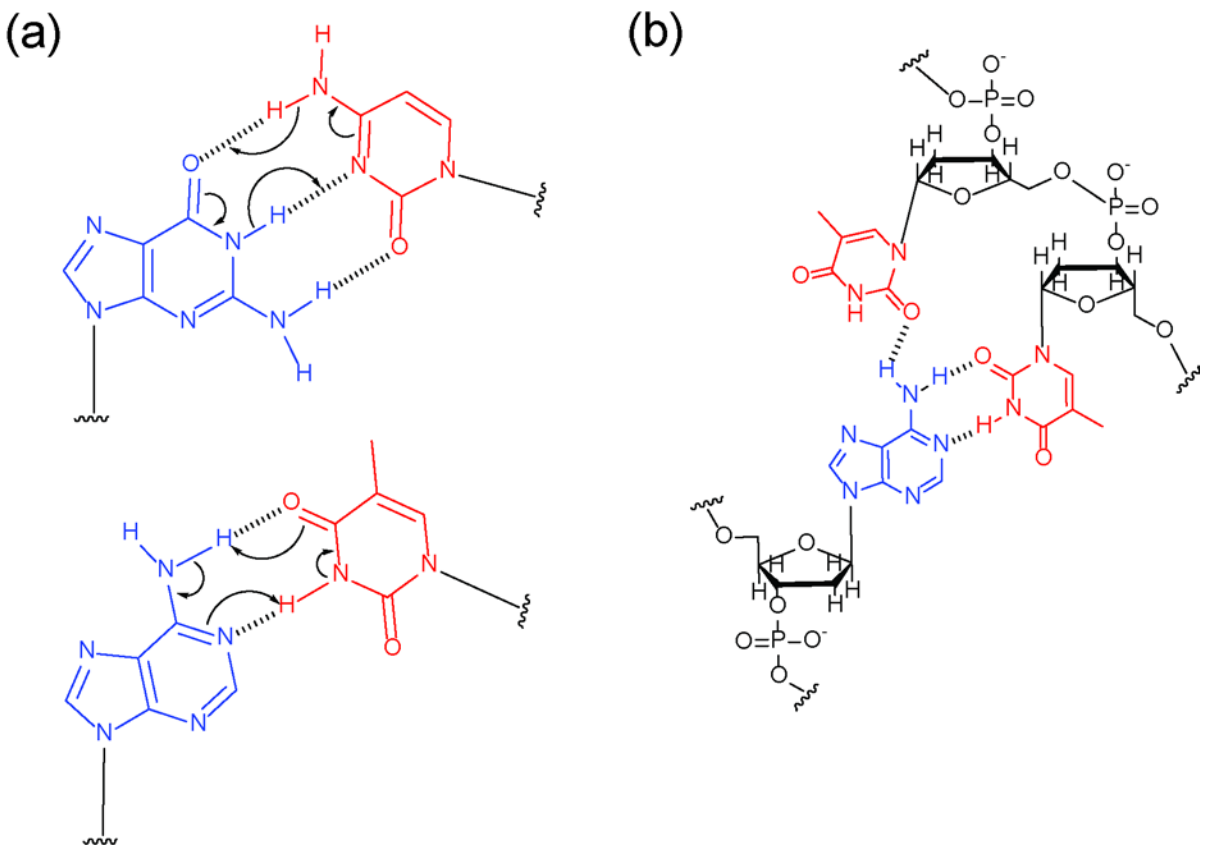

Figure 2. RAHB and BFHB in base pair interactions. RAHB **(a)** in G-C (top) and A-T (bottom) base pairs. In the G-C base pair, RAHB can also exist between the bottom and center H-bonds but has been omitted for clarity in the mechanism. **(b)** A BFHB between an adenine residue and two successive thymine residues in the opposite strand. The same carbonyl group of the base is involved in the BFHB and has been observed to create propeller like twists in the dsDNA.[12]

BFHB is shown in Figure 2(b) where the primary amino group of adenine which contains two H-bond donors can form a BFHB with two successive thymine residues in the duplex. These structures extend along the major groove of the dsDNA and effectively narrow the minor groove. Evidence for BFHB is also supported by the twisted right-handed duplex of polyA-polyT hybrids and the increased stability of this duplex compared to polyAT-polyAT hybrids.[12] While no covalent character is responsible for duplex annealing and the energetics of these intermolecular forces range from a few to tens of kJ·mol^{-1}, the collective strength of these interactions enables dsDNA duplexes longer than 5 nucleotides in length to exist at room temperature.

1.2.2 Energetics of DNA Hybridization

The stability of dsDNA is often discussed in terms of the melt temperature (T_m) of the duplex which describes the helix-coil transition for a particular sequence or segment. How T_m is

calculated varies for DNA-DNA, RNA-RNA, and DNA-RNA polynucleotide hybrids.[13] For polynucleotide sequences on the order of hundreds of base pairs, T_m (ºC) is described by Eqn. 1 which considers DNA-DNA polynucleotide hybrids.

$$T_m = 81.5 + 16.6\left\{\log_{10}\left(\frac{[\mathrm{Na^+}]}{1 + 0.7[\mathrm{Na^+}]}\right)\right\} + 0.7(\%\ \mathrm{G + C}) - \frac{500}{n} - P \qquad (1)$$

For a polynucleotide duplex, T_m is defined as the temperature at which 50% of the bases pairs have been separated and result in loops or separated ends in the duplex.[13] T_m is a function of the intrinsic makeup of the sequence as seen in Eqn. 1, where a higher percentage of guanine and cytosine residues (% G + C) and a longer duplex length in nucleotides (n) afford higher stability. Given that three H-bonds form between a single G-C base pair, it is apparent how a higher G + C content leads to an increased T_m. The percentage of mismatch in the duplex (P) refers to positions of energetically unfavorable base pairs, which can be one or more of all other permutations of base pairs other than determined by the aforementioned Watson and Crick rules. Details of the impact of mismatch percentage and location on duplex stability are discussed at the end of this section. In addition to the characteristics of the duplex, the effect of the local environment on hybridization is also prominent, where the local concentration of sodium ([Na]) influences duplex stability. The contribution from ionic strength can be understood by discussion of the proposed kinetic model of hybridization which proceeds first by nucleation of the two ssDNA sequences, followed by rapid zippering of the strands via base pairing to form the double helix.[13] At neutral pH and under most physiologically relevant buffers, the phosphate backbone of the oligonucleotide is completely ionized. This creates a barrier to hybridization as nucleation of two polyanionic structures is highly unfavorable at low ionic strength. Addition of cations such as sodium, potassium or magnesium suppressed the Debye length of each negatively charged phosphate and screens the overall effective charge. This improves hybridization efficiency and also affords a higher T_m to the resultant duplex.

While Eqn. 1 is sufficient for predicting the stability of polynucleotide duplexes it is not applicable in describing the hybridization of oligonucleotides. First and foremost, T_m for an oligonucleotide duplex is defined as the temperature at which 50% of the duplexes are separated into ssDNA coils and is dependent on the total strand concentration (C) since hybridization is intermolecular and reaches equilibrium.[13] In order to describe the T_m for an oligonucleotide a

nearest neighbor model[14] is considered which includes the collective standard free energy (ΔG^o) and enthalpy (ΔH^o) of all nucleotides in the duplex as shown by Eqn. 2.[13]

$$T_m = \frac{T°\Delta H°}{\left(\Delta H° - \Delta G° + RT°\ln(C/4)\right)} + 16.6\left\{\log_{10}\left(\frac{[\mathrm{Na^+}]}{1 + 0.7[\mathrm{Na^+}]}\right)\right\} - 269.3 \qquad (2)$$

It is important to note that in Eqn. 2 both ΔH^o and ΔG^o are temperature independent and for a self-complementary oligonucleotide duplex, the denominator of the first term is changed slightly to $C/2$. Using the first fraction in Eqn. 2, a semi-quantitative description of the spontaneity of oligonucleotide hybridization can be provided by considering the collective contributions to ΔG^o and ΔH^o from N nearest-neighbor (nn) interactions and dangling ends (e) as given by Eqn. 3 and Eqn. 4, respectively.[13]

$$\Delta G° = \sum\nolimits_{nn} (N_{nn} \cdot \Delta G°_{nn}) + \Delta G°_{i} + \Delta G°_{e} \qquad (3)$$

$$\Delta H° = \sum\nolimits_{nn} (N_{nn} \cdot \Delta H°_{nn}) + \Delta H°_{P} + \Delta H°_{e} \qquad (4)$$

Contributions from dangling ends are relevant for PCR, where primers may be designed to amplify an internal segment of a larger dsDNA sequence. In Eqn. 3 the standard free energy of initiation (ΔG^o_i) refers to the primary nucleation event resulting in formation of the first base-pair(s) and is +2.2 kcal·mol^{-1}.[13] A positive term for ΔG^o_i is expected because of the loss of translational entropy of each ssDNA segment in formation of a relatively more ordered rigid duplex.[15] Standard free energies of nearest neighbor interactions range from -0.9 to -3.4 kcal·mol^{-1}, which is expected for the rapid zippering of the remaining base pairs in the duplex.[15] The enthalpies of nearest neighbor and dangling ends are +8.0 kcal·mol^{-1} and -8.0 kcal·mol^{-1}, respectively where the free energy of a dangling end is -1 kcal·mol^{-1}.[13] The standard entropy change for a nearest neighbor interaction is -24.9 cal·mol^{-1}·k^{-1}.[15] A qualitative description of the process can be understood by weighing both enthalpic and entropic contributions. Considering two ssDNA coils solvated in solution, enthalpic interactions exist between solvent water and the sugar-phosphate backbone. H-bonding with amino and carbonyl groups of the nucleobases also exist, however solvation of the entire planar aromatic structure creates an ordered network of H-bonded water. Nucleation followed by rapid zippering of the base pairs creates new H-bonds after those with solvent have been broken and ultimately ΔH^o remains relatively unchanged.

Considering entropic contributions, while a loss in translation energy is expected for each ssDNA, displacement of ordered water around the nucleobases to bulk solution after hybridization is entropically favorable. For an oligonucleotide 20 residues long (20mer) and 50% G-C content, Eqn. 2 predicts a T_m of 70 ºC for 1.0 µM of ssDNA at a [Na^+] of 1.0 M.[13] The level of theory described by Eqn. 1 and Eqn. 2 has enabled creation of a web interface that allows routine computation of T_m for a desired duplex in a variety of environments.[16] Such an interface is not only extremely valuable to probe selection, but also to primer design for PCR. Experimental determination of T_m is also possible through UV-visible absorbance measurements as a function of increasing temperature where the resultant plot is commonly referred to as a melt curve. The nucleobases of ssDNA exhibit strong absorbance in the short UV region with an absorbance maximum at 260 nm.[9] In dsDNA, the delocalized electrons of the bases form π-π stacking interactions and as a result, coupling between neighboring transient dipoles also takes place. As a consequence, absorbance at 260 nm decreases and the resonant transition exhibits a hypochromic shift toward 200 nm. This allows one to monitor the increased absorptivity at 260 nm as the duplex-coil transition takes place, where increases between 20-30% are common[9]. While dsDNA exhibits hypochromism, the integrated area across the entire UV absorbance band remains unchanged.[15]

Earlier discussion on factors influencing T_m for an oligonucleotide duplex has shown that destabilization can be induced through intrinsic sequence characteristics and by control over the external environment, where ionic strength is a significant factor. The presence of base pair mismatches (BPM) also cause reductions in T_m as shown in Eqn. 1, where for polynucleotides ΔT_m is 1 ºC for a 1% sequence mismatch.[13] In the case of an oligonucleotide duplex, a 1BPM causes a greater degree of destabilization since the dsDNA is on the order of tens of base pairs in length and two nearest neighbor contributions are effectively lost. For a 20mer, a single BPM can cause a reduction in T_m of up to 5 ºC.[13] Theoretical and experimental investigations by Allawi and SantaLucia have made a significant contribution toward understanding the destabilization of duplexes by intrinsic mismatches.[17-21] Considering a 10mer oligonucleotide duplex, the experimentally determined standard free energies and melt temperatures are summarized in Table 1, along with resultant effects of a central 1BPM.[21]

Table 1. Standard free energies and melt temperatures for a 10mer duplex at 0.11M $[Na^+]$ with all possible permutations of a central 1BPM.[21]

Sequence	ΔG^o (37 ºC) kcal·mol^{-1}	T_m (ºC)
GGTT**A**TTGG CCAA**T**AACC	-6.39	40.4
GGTT**C**TTGG CCAA**G**AACC	-7.50	45.7
Mismatch		
A-A	-2.86	21.4
A-G	-4.63	31.0
A-C	-3.46	24.1
C-C	-1.76	17.1
C-T	-2.95	22.6
G-G	-4.38	29.7
G-T	-4.56	31.8
T-T	-3.39	25.2

Two duplexes are used as a reference for comparison, while the central base pair is different; this location is flanked by the exact same residues. For all the possible mismatches, the C-C mismatch is the most energetically unfavorable and results in lowering of T_m by *ca*. 28 ºC, where A-G, G-G, and G-T only resulted in *ca.* 10-15 ºC lower melt temperatures. It is important to note that while this observed trend should be applicable to other dsDNA sequences, the numerical impact on T_m may differ. Furthermore, when residues of the mismatch were reversed with respect to the ssDNA strands, differences between 1-3 ºC were observed for the same mismatch. When considering the effect of a 1BPM on T_m, the nearest neighbor model is in good agreement with what is observed experimentally.[21] Moreover, the location of the mismatch is also a factor in the degree of duplex destabilization. Mismatches located in the center of the duplex create a bulge in the helix and are more energetically unfavorable then those at the ends of the dsDNA. This is conceptualized by considering the dynamic "breathing" of the duplex where the probability of finding a dissociated base pair is 10^{-5} and a single base pair breathes 100 times per second.[9] Base pairs at each terminal end can only form π-π stacking interactions with nucleobases on one face and results in decreased rigidity at these regions of the duplex.

The significance of mismatches in dsDNA is that they are often associated with genetic disorders. After transcription and translation, a 1BPM can cause insertion of an amino acid

residue that can generate a misfolded and dysfunctional protein. While there are proofreading mechanisms in DNA replication, constant exposure to mutagens can still elicit base pair mutations.[8] Common causes are: insertion of an incorrect nucleotide during replication and deletion or insertion of extra nucleotide(s). In the case of the autosomal recessive disorder spinal muscular atrophy (SMA), deletions of base segments and resultant mismatches on the survival motor neuron (SMN) gene are responsible for the disease.[22] Mismatch variations or single nucleotide polymorphisms (SNPs) are responsible for expression of the diseased state. SMA is second only to cystic fibrosis for the cause of death in newborns.[22] The SMN1 and SMN2 genes encode similar proteins where only dysfunctional SMN1 protein leads to the diseased state. This is often a result of conversion of SMN1 exon 7 to SMN2 and the resultant protein encoded by SMN2 is inadequate to prevent disease progression.[23] The relative amounts of SMN1 and SMN2 are ultimately responsible for the diseased state. In cystic fibrosis (CF), a three base pair deletion and subsequent loss of phenylalanine at position 508 in the CF transmembrane protein receptor is responsible for at least 70% of patient cases.[24] Base mismatches offer a unique opportunity to build inherent selectivity into oligonucleotide probe sequences since the energetic differences relative to the perfectly matched sequence can enable resolution of healthy vs. diseased states.

Other external factors can also be controlled to destabilize dsDNA in addition to temperature and ionic strength. Solutions at both pH extremes and chaotropic additives such as formamide and urea can cause a lowering of T_m. These organic agents act by disrupting the intermolecular forces of attraction that stabilize the duplex both internally and externally. Formamide for example contains both H-bond donors and acceptors and can effectively interact with nucleobases in the hydrophobic interior and along the major and minor grooves displacing solvated water molecules. For every 1% v/v formamide, the T_m of an oligonucleotide is lowered by 0.6 ºC.[25]

The stability of DNA in various forms is remarkable, and the selectivity of hybridization is attractive to exploit for building selective chemistry for assay development. Given the many external factors that influence hybridization, one can further tune the stringency of the assay to specifically transduce a hybridization event for a desired nucleic acid target.

1.3 Fluorescence Spectroscopy

Luminescence is defined as the emission of a photon from a compound through transitions between electronically excited states.[26] Fluorescence and phosphorescence are two forms of

luminescence that are often classified as *photoluminescence* (PL) since they are caused by absorption of a photon.[27] Additional forms of luminescence include chemiluminescence and bioluminescence. The former involves emission of a photon due to a chemical reaction while the latter is similar but specific to an enzyme-substrate reaction. Fluorescence and phosphorescence are both luminescent forms of excited state relaxation but differ in that phosphorescence requires spin of the electron to flip prior to relaxation.[27] The following section is dedicated to discussion of fluorescence with a brief description of phosphorescence. Prior to discussion of luminescent processes, it is necessary to describe the fundamentals of the absorption of electromagnetic radiation. Both processes can be explained simultaneously by considering the pioneering work of Alexander Jablonski, where a Jablonski diagram is used to illustrate the processes of molecular absorbance and luminescence.

1.3.1 Jablonski Diagram

Professor Alexander Jablonski is regarded as a pioneer in fluorescence spectroscopy from his contributions in understanding anisotropic fluorescence measurements.[26] A Jablonski diagram as shown in Fig. 4 is often used to qualitatively describe molecular absorption and excited state processes such as luminescence. The diagram is a simplified representation of the wavefunctions or *orbitals* occupied by electrons in a molecule as denoted by S_0, S_1, S_2, and T_1 which refer to the singlet ground state, first excited state, second excited state, and triplet state, respectively.[27] The orbitals are positioned on a relative energy scale and as a function of the separation distance between neighboring atomic nuclei. Since the overall energy of a molecule is the collective sum of the contributions from electronic, vibrational, rotational, and translational energy, vibrational energy levels of each electronic state are also illustrated and denoted by v_0 - v_5. Rotational energy levels are in fact superimposed on each vibrational state but are omitted as the energy associated with transitions between these levels is relatively small.

1.3.1.1 Absorption of Electromagnetic Radiation

Absorption of a photon by an atom or molecule, proceeds by promotion of an electron in the highest occupied molecular orbital (HOMO) to the lowest unoccupied molecular orbital (LUMO) in the atom or molecule. Absorption occurs when the energy of the incoming photon matches the difference in energy between the HOMO and the LUMO; the energy of the photon (E_{photon}) is in *resonance* with the energy of the electronic transition.[28] Absorption is shown in

Figure 4 by the purple and blue transitions from S_0 to S_2 and S_1, respectively and can be represented mathematically by Eqn. 5.

$$E_{photon} = {}^{hC}/_{\lambda} = ES_n\nu_i - ES_0\nu_i \quad (5)$$

In Eqn. 5 h is Planck's constant and is 6.626×10^{-34} J·s, C is the speed of light and equal to 3.00×10^{8} m·s^{-1}, $ES_n\nu_i$ and $ES_0\nu_i$ refer to the *ith* vibrational level of the *nth* excited singlet state and singlet ground state, respectively. Figure 4 depicts that in each electronic state the electron can reside in any one of the vibrational levels and thus a range of photon energies can satisfy the

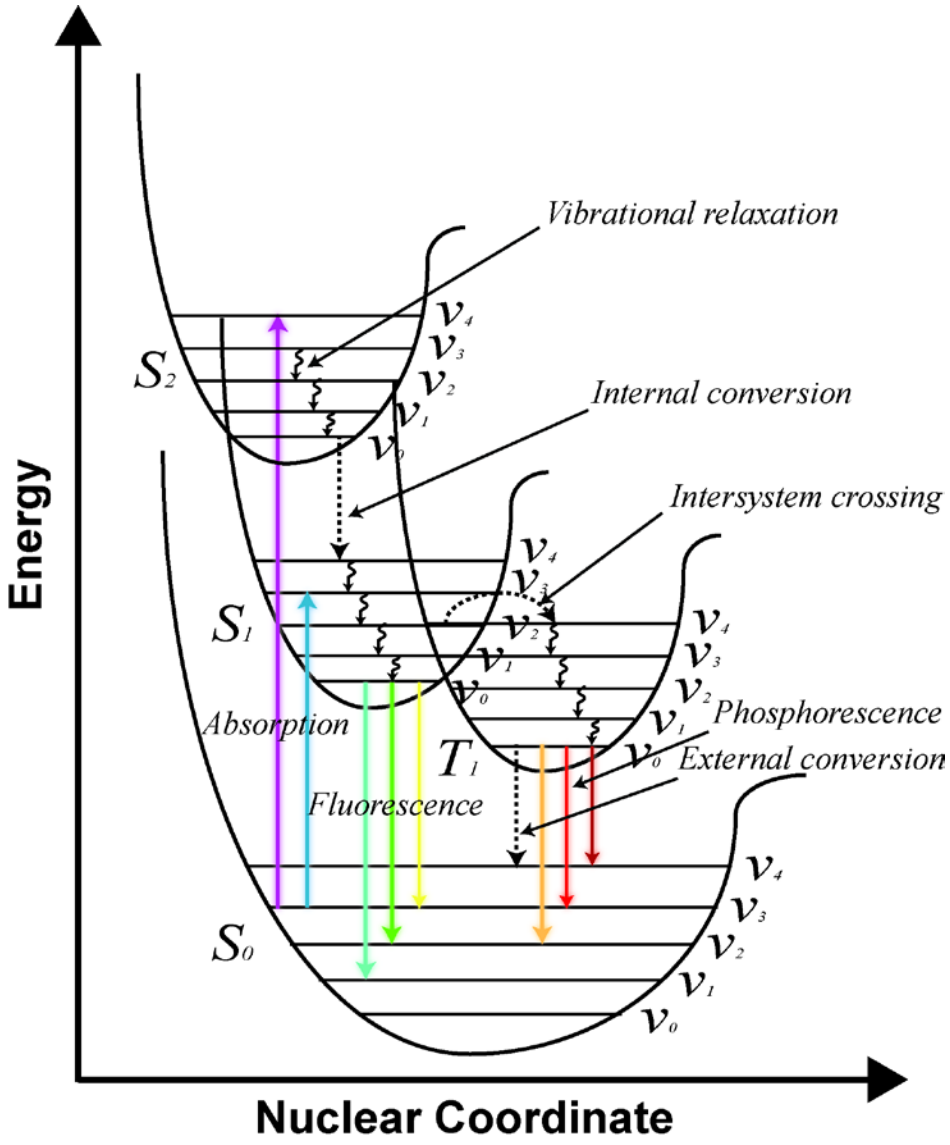

Figure 3. Jablonski diagram for absorption and luminescence.[27] The electronic singlet states are given by S_0, S_1, and S_2 which refer to the ground state, and first and second excited states, respectively. Vibrational energy levels are

superimposed in each electronic potential well as given by v_0 to v_5. The triplet state is given by T_1, where the spin of the electron must first flip to enter this state given that overlap exists between the singlet vibrational levels and those of the triplet state. Electronic excitation of an electron from the ground state to one of the excited states is facilitated by resonance absorption of a photon which occurs in 10^{-15}s. The electron can reside in any of the vibrational levels of either S_1 or S_2, where the electron rapidly (10^{-12}s) decays by vibrational relaxation due to collision with solvent to lowest vibrational level of the electronic state. In addition to vibrational relaxation, other forms of nonradiative relaxation include internal and external conversion. In the case of the former, the mechanism is thought to be a result of overlap between vibrational energy levels of the excited state and ground state. The latter is due to collisions with adjacent molecules of sufficient energy to cause deactivation of the excited state. Fluorescence is defined as the radiative relaxation of the electron from the lowest vibrational level of the S_1 to any of the vibrational levels of S_0. The timescale of fluorescence ranges from 10^{-7} to 10^{-9} s and thus this is why vibrational relaxation processes dominate prior to radiative decay. The presence of heavy atoms such as halides can cause spin-orbit coupling interactions with the excited electron causing intersystem crossing of the electron into the triplet state. The radiative relaxation from the triplet state back to the ground singlet state is known as phosphorescence and occurs at a relatively slower rate compared to fluorescence (10^{-5} to 10 s) since the spin of the electron must first flip prior to relaxation.

resonance condition in Eqn. 5. While the electrons will mostly reside in the lowest vibrational level of the ground state as described by the equilibrium bond length[29], the population of vibrational states is a function of the average available kinetic energy as described by Boltzmann statistics. Discussion of molecular partition functions is beyond the scope of this chapter and the average available kinetic energy to a molecule is often approximated by kT, where k is Boltzmann's constant and is equal to 1.38×10^{-23} J·k^{-1} and T is the temperature in Kelvin. Electronic transitions are governed by quantum mechanical selection rules, where transitions that result in a nonzero value of the transition dipole moment are allowed and the electric field of the photon must be aligned with the transient dipole of the molecule.[29] Electronic transitions also result in changes to the vibrational and rotational states of the molecule. The change in the vibrational state during a transition can be described using the Born-Oppenheimer approximation – which states that since the proton is heavier than the electron by a factor of *ca*. 2000, the charge of the electron moves quickly in response to slower nuclear harmonic motion. The significant difference in time scales enables one to describe the wave function as two components where one is dependent on the position of the electrons and the other on the position of the nuclei.[29] The wave function for the transition can then be expressed as a product of the both electronic and vibrational contributions. The result is that for a transient dipole in the molecule, an overlap exists between the vibrational wave functions of both the ground and excited states. The magnitude of the square of the wave function in this notion represents the probability vibrational-electronic transition. For this transient dipole, the magnitude of this square is known as the *Franck-Condon factor* which is a quantitative measure of the intensity for this transition as given by Eqn. 6.[29]

$$S^2 = \left| \int \left(\phi_f^{vibrational}\right) \phi_i^{vibrational} d\tau \right|^2 \quad (6)$$

The wave function for the vibrational level of the excited and ground states are given by ϕ_f and ϕ_i, respectively. Eqn. 6 describes the selection rule for vibrational transitions in electronic states and is the basis for the *Franck-Condon principle*, which states that electronic transitions are vertical lines on energy diagrams as a function of the relative distance between nuclei. As seen by the Jablonski diagram in Figure 3, absorption is represented as a vertical transition since the timescale of an electronic transition is much faster than nuclear motion where absorption takes place on the order of 10^{-15} s.

The appearance of absorption spectra of molecules differs substantially from those of individual component atoms as a result of vibrational fine structure in electronic transitions of molecules. In atoms, only a few photons can satisfy the resonance condition for electronic transition due to the absence of vibration where the energy of an atom of the summation of contributions from translational and rotational energies. This results in absorption spectra with discrete, narrow spectral line widths. For molecular absorption, spectra contain broad absorption bands from the collective contributions of rotational and vibrational states and appear as a continuum across a range of photon wavelengths. Since a molecule can contain many tens of atoms, a myriad of rotational and translation energies can exist and effectively overlap in energy, this leads to the continuous broad absorption profile with minimal vibrational fine structure.[29] Absorption bands of many polyatomic molecules typically exist in the UV-visible region of the electromagnetic spectrum. This characteristic absorption window arises from the nature of the bonding in the molecule where functional groups with delocalized electrons give rise to these transitions. Most organic compounds that consist of planar, aromatic or polycyclic conjugated systems of π electrons exhibit transitions in the UV-visible region. The functional groups of these organic compounds which can include, alkenes, carbonyls, and or cyano structures that have similar absorbance regions across different molecules are often termed *chromophores*.[29] Rather than referring to individual substituents, molecules that exhibit UV-Visible absorption are often abbreviated as chromophores. As previously mentioned, electronic transitions take place from the HOMO to the LUMO and for delocalized electrons in *p* or various *sp* hybridized orbitals, these are often π-π^* transitions from bonding to anti-bonding character. In anti-bonding orbitals,

electron density is shifted outside the equilibrium bond length and in some molecules radical excited states can result. Additional transitions include σ-σ* which are higher energy and often found in alkanes due to the lack of π-bonding.[29]

Absorption of incident photons by a chromophore can be related to its concentration in solution; this is known as the Beer-Lambert law.[28] The concentration dependence of absorption can be described by considering a cuvette containing an absorbing molecule at concentration *C*. As light with intensity P_0 passes through the chromophore solution absorption proceeds over the width or path length of the cuvette *b* where the intensity of the light is now reduced to *P*. Since the transmittance of the light can be described as a relative ratio of the measured power against the incident power on the cuvette, the transmittance can then be related to the absorbance *A* with a logarithmic dependence as given by Eqn. 7.[28]

$$A = \log {}^{P_0}/_{P} = \varepsilon b C \tag{7}$$

A proportionality constant denoted by ε, is referred to as the molar absorptivity coefficient and is a measure of the molecules ability to absorb at a given wavelength. Epsilon has units of $L \cdot mol^{-1} \cdot cm^{-1}$ and thus the absorbance is a unitless measurement, although it is sometimes referred to in units of optical density.[28] The molar absorptivity is a combination of the transition probability *P* and the cross-sectional area *A* in cm^2 as shown by Eqn. 8.[27]

$$\varepsilon = 8.7 \times 10^{19} PA \tag{8}$$

For many organic chromophores, ε ranges from 10^4-10^5 $L \cdot mol^{-1} \cdot cm^{-1}$ at the maximum wavelength of absorption. These range of wavelengths are characteristic of allowed electronic transitions where absorption coefficients less than two orders of magnitude lower are often characteristic of forbidden transitions.[27]

1.3.1.2 Radiative and Nonradiative Relaxation Mechanisms

If the molecule resides at an excited state energy, many pathways exist to return the electron back into a ground state orbital. The length of the excited state lifetime can range between 10^{-7}-10^{-9} s for singlet excited state transitions. In the singlet excited state, the electron spin does not change and rather remains paired with the additional electron in the ground state molecular

orbital. This is due to the *Pauli exclusion principle* which states that no two electrons may have the same four quantum numbers.[27] Figure 4 also shows that absorption can cause transitions into the second excited singlet state and relaxation directly back to the ground state is often sidelined by other efficient nonradiative relaxation processes. Vibrational relaxation is a form of nonradiative decay that involves thermal equilibration of the molecule with surrounding solvent and vibrational deactivation is a result of collision with these solvent molecules.[26] The time scale for vibrational relaxation is on the order of 10^{-12} s and occurs almost instantaneously in comparison to the lifetime of the excited singlet state. Since transitions result in the electron occupying any one of the vibrational states of the excited state, vibrational relaxation immediately shifts the electron to the lowest vibrational energy level of the excited state. Relaxation of the electron from this energy level to any one of the vibrational levels of the ground state and produces the simultaneous emission of a photon is known as *fluorescence*.[27] Fluorescence lifetimes are on the order of 10^{-8} s and are much longer lived than vibrational deactivation.[26] The resultant energy dissipated by vibrational relaxation causes longer wavelength fluorescence emission where this bathochromic shift is commonly referred to as the Stokes shift. Another form of nonradiative relaxation is the process of internal conversion which returns the molecule to the ground state without any subsequent photon emission. While the mechanisms are unclear, an intermolecular deactivation process is proposed.[27] Internal conversion is a probable pathway for relaxation when overlap exists between vibrational energy levels of different excited states. For internal conversion from the excited state to the ground state, the mechanism is still unknown but its existence is evident in chromophores that do not fluoresce.[27] External conversion as shown by the transition in Figure 4 from the excited triplet state to the ground state is due to collision of the excited state molecule with solvent and other adjacent molecules. Collisions are of sufficient energy to cause deactivation of the excited state, where evidence of external conversion is marked by the influence of solvent on fluorescence.[27] Also known as solvatochromism, depending on the nature of the solvent and the intermolecular forces involved in solvation, solvent molecules can rearrange to stabilize the transient dipole. Solvatochromic effects on fluorophores result in changes in the appearance of the emission spectrum since the energetics of the excited state are influenced. The interested reader is referred elsewhere for an in depth discussion on solvatochromic effects of fluorescence.[26] For fluorescent nanocrystals the effect is not as pronounced and mainly results in nonradiative relaxation of the exciton. As mentioned previously, radical mediated excited states can also exist and often lead to

the degradation of the molecule. The major culprit in solution is the presence of dissolved oxygen which has a diradical resonance structure that can further react with a radical excited state. This usually results in a change to the molecular structure that renders it nonfluorescent and is known as photobleaching. Alternatively, excitation to vibrational energy levels that exceed the energy of the bond can also cause bond rupture, degradation and influence luminescent properties.

While discussion of excited state processes has been limited to transitions from singlet states, transfer of the electron from an excited singlet state to an excited triplet state is known as intersystem crossing. Due to the presence of heavy atoms such as halides, the excited electron spin can flip where spin-orbital interactions generate a transition into the triplet state. As shown in Figure 4, strong overlap between excited singlet states and the triplet state increase the probability of intersystem crossing since transitions from the ground state to the triplet state are spin forbidden. Since the electron spin must flip prior to relaxation to the ground state, excited triplet state lifetimes are on the order of 10^{-5}-10 s and are long lived in comparison to excited singlet states. Similar to fluorescence, *phosphorescence* is emission of a photon due to relaxation from the excited triplet state to the singlet ground state. Furthermore, since both external and internal conversion can also lead to deactivation of the excited triplet state, these processes often outcompete phosphorescence and this phenomenon is generally observed in the solid-state or in highly viscous solvents.[27]

1.3.2 Quantitative Fluorescence Measurements

Measurements of fluorescence intensity can be acquired as a function of wavelength and also with respect to time. The former is referred to as steady-state measurements as the intensity of emission is recorded against wavelength where the resultant plot is known as an emission spectrum. The latter is known as time-resolved fluorescence and monitors the lifetime of the excited state, where the resultant plot is known as a fluorescence decay curve. Both steady-state and time-resolved measurements can be made using spectrofluorimeters, microplate readers, and fluorescence microscopes.

1.3.2.1 Steady-state Fluorescence Measurements

In acquisition of fluorescence spectra, a sample solution containing the fluorophore is excited at a wavelength or range of wavelengths of strong absorption. The fluorescence emission is scanned step wise on an increment of usually nm to provide the analyst with a fluorescence spectrum. The characteristic emission band in the spectrum often mirrors the absorption profile, since the same electronic states are involved in the transitions.[26] Moreover, since multiple excited states exist, excitation at multiple wavelengths is possible but does not influence the appearance of the emission band. This is known as Kasha's rule where nonradiative relaxation mechanisms occur faster relative to fluorescence until the electron resides in the lowest vibrational energy level of the first excited state.[26] The probability of fluorescence as a result of absorption of a photon is defined as the *quantum yield* of the fluorophore, Φ. The quantum yield of a fluorophore is the ratio of the radiative decay rate (k_f) over all rates of relaxation from the excited state; this is shown mathematically by Eqn. 9.

$$\Phi = \frac{k_f}{k_f + k_{ic} + k_{ec} + k_i + k_{pd} + k_d + k_{et}} \tag{9}$$

The processes associated with nonradiative decay are shown as individual rate constants in the denominator of Eqn. 9 and include internal conversion (k_{ic}), external conversion (k_{ec}), intersystem crossing (k_i), predissociation (k_{pd}), dissociation (k_d), and energy transfer (k_{et}).[27] The rates of predissociation and dissociation are a function of the structure of the fluorophore where both mechanisms cause bond rupture. The additional nonradiative rates are controlled by the environment[27], with the exception of k_{et} which is discussed in detail in section 1.4. From Eqn. 9 it is evident that the quantum yield is a measure of the brightness of a fluorophore and is an important parameter to consider in analyses concerning fluorescence. While the quantum yield is often thought of as an intrinsic property of the fluorophore, the presence of additional compounds in solution can substantially reduce the brightness through quenching mechanisms. Quenchers in solution act to enhance the rate constants of nonradiative relaxation processes. Two common types of quenching are collisional quenching and static quenching. As the name implies, collisional quenching results when an excited state fluorophore is deactivated through collision with another compound in solution and is governed by the Stern-Volmer relationship.

In static quenching, the fluorophore forms a nonfluorescent complex with a molecule that immediately deactivates the excited state.[26]

Fluorescence emission can also be related to the concentration of the fluorophore in a manner similar to absorption, and incorporates the Beer-Lambert law. The intensity of fluorescence (F) is proportional to the incident power (P_0) of excitation light as given by Eqn. 10.

$$F = K'(P_0 - P) \tag{10}$$

The resultant light transmitted after excitation is given by P where the fluorescence intensity emitted is determined by the quantum yield K'. Recalling that Beer's law for absorption can be written as a relative ratio of the intensity of incident and transmitted light through a known path length, substitution into Eqn. 10 gives Eqn. 11. Expanding the exponential term in Eqn. 11 as Maclaurin series gives rise to Eqn. 12.[27]

$$F = K'P_0(1 - 10^{\varepsilon bC}) \tag{11}$$

$$F = 2.3K'\varepsilon bCP_0 \tag{12}$$

In Eqn. 12, only the first term is considered after expansion of the Maclaurin series as the second and third terms correspond to higher order two-photon and three-photon excitation. In conventional fluorescence instruments, the probability of these excitation processes are low and often require high frequency pulsed laser sources. Furthermore, dropping the high order terms only introduces a relative error of 0.13%.[27]

1.3.2.2 Time-resolved Fluorescence Measurements

Measurements of fluorescence can also be done as a function of time after the initial excitation process. Through time-resolved measurements the average time the fluorophore spends in the excited state can be determined where this is known as the *fluorescence lifetime*.[26] The fluorescence lifetime (τ) is given by Eqn. 13, and is expressed as the inverse of the sum of the rates of radiative and nonradiative relaxation.

$$\tau = \frac{1}{k_f + \sum k_{nr}} \tag{13}$$

Since there are many processes of nonradiative relaxation, these are represented collectively as k_{nr} in Eqn. 13. After the initial excitation, a period of a few to tens of ns may pass prior to all fluorophores relaxing to the ground state. While the lifetime is described as an average time spent in the excited state, for a single exponential decay the fluorescence lifetime is defined as the time where *1/e* or 63% of the fluorophores have relaxed to the ground state.[26]

Measurement of the fluorescence lifetime can be done using time-domain or frequency-domain methods. Time-domain methods include time-correlated single photon counting or the stroboscopic technique developed by Photon Technologies International.[1] In time-domain methods, a laser pulse is used to excite the entire fluorophore population in a couple of ns which is often a fraction (*ca.* 1 ns) of the intrinsic fluorescence lifetime as to avoid missing any luminescent decay. The excited fluorophores decay as a function of time described by Eqn. 14:

$$\frac{dn(t)}{dt} = (k_f + \sum k_{nr})\, n(t) \tag{14}$$

where the number of excited state fluorophores at time *t* is given by *n*(*t*). Relating the number of excited state molecules to the intensity of fluorescence at a given time *I*(*t*), followed by integrating Eqn. 14 gives Eqn. 15, where a plot of the log of intensity vs. time has slope τ.[26]

$$I(t) = I_0 e^{-t/\tau} \tag{15}$$

The intensity of fluorescence at time 0 is given by (I_0), and decays exponentially with time. Data can be fit by deconvolution of the laser pulse or instrument response function (IRF), followed by single or multiple exponential fits of the data. The IRF must be acquired prior to sample measurements by using a standard scattering solution. In frequency-domain methods, phase modulation is used to determine the lifetime, where the intensity of the excitation source is modulated using a sinusoidal function. The fluorescence intensity of the sample will mirror the intensity of the source light where the delay or phase shift in the two frequencies can be used to determine the characteristic fluorescence lifetime. For detailed discussion of frequency-domain measurements the interested reader is referred elsewhere.[26]

---

[1] A brochure describing the principles of operation behind the stroboscopic technique can be found at the Photon Technologies International webpage at “http://www.pti-nj.com/brochures/LaserStrobe.pdf”.

1.3.3 Fluorescence Resonance Energy Transfer

The process of fluorescence resonance energy transfer (FRET) is defined as a non-radiative, through-space coupling of transition dipoles as no photon is emitted and reabsorbed in the transition.[26] The mechanism considers an excited state donor *D* and a ground state acceptor *A* in close proximity, where the difference in energy between the excited state and ground state of *D* match resonant transitions in the molecular orbitals of *A*. FRET is depicted qualitatively by Figure 4, where the colored fluorescence transitions of *D* match the energy required for absorption by *A*. The accepted FRET range for energy transfer is 1-10 nm[30]. The *D-A* separation distance (*r*) determines the degree of energy transfer, where the FRET efficiency is a function of the inverse sixth power of the distance between the *D-A* as governed by the Förster formalism. The rate of energy transfer (k_{ET}) is given in Eqn. 16:[26]

$$k_{ET} = \frac{9(ln10)\kappa^2 \Phi_D J}{128\pi^5 n^4 N \tau_D r^6} = \left(\frac{1}{\tau_D}\right)\left(\frac{R_0}{r}\right)^6 \tag{16}$$

where κ^2 is an orientation factor that describes the angle between the two transient dipoles. Other parameters include the refractive index (n) of the medium, the quantum yield (Φ_D) and fluorescence lifetime (τ_D) of the donor in absence of the acceptor, Avogadros number (N) and J, the spectral overlap between the donor emission band and the absorption spectrum of the acceptor.

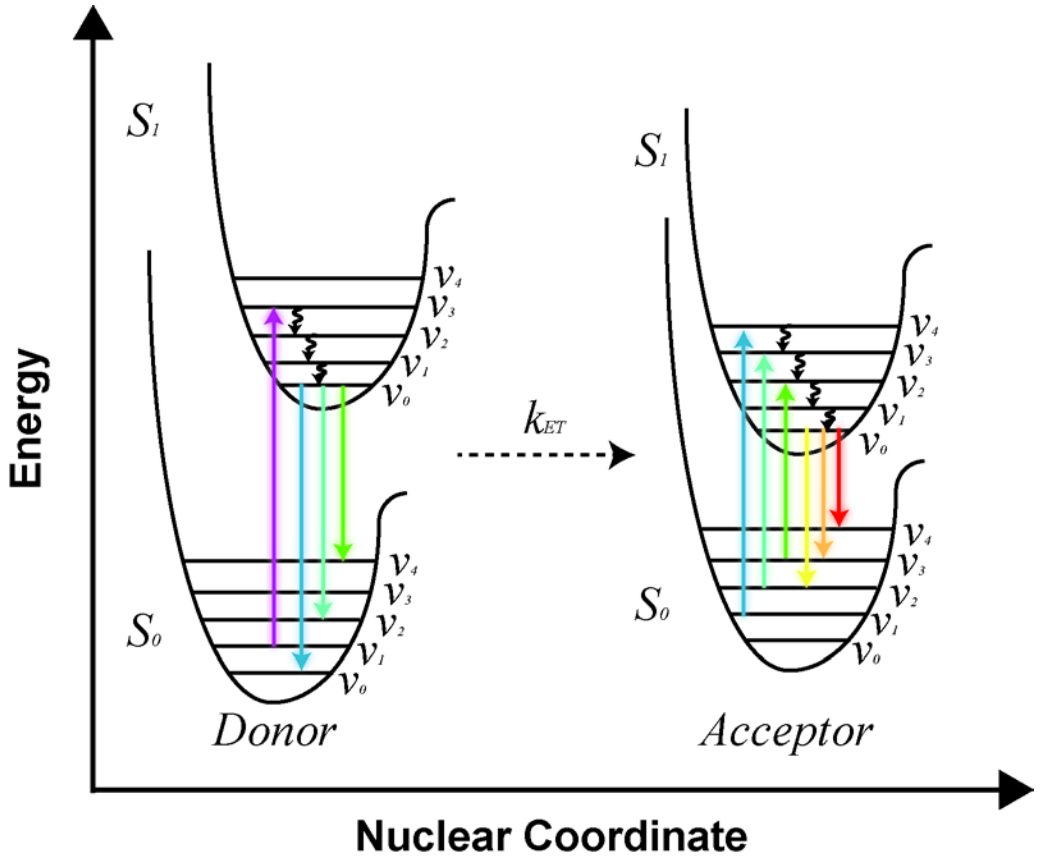

Figure 4. Modified Jablonski diagram depicting the process of energy transfer (k_{ET}) from a hypothetical donor molecule to a proximal acceptor. The coloured emission bands in donor relaxation are identical to those in acceptor excitation to qualitatively display the spectral overlap (J). The ground states and excited states are denoted by S_0 and S_1 respectively, where the vibrational states of each electronic state are given by (v_0- v_4). Vibrational relaxation (bolded arrows) is still faster than the rate of energy transfer from the donor, along with other forms of nonradiative decay; these however have been omitted for clarity.

Often the rate of energy transfer is expressed as a function of the characteristic Förster distance (R_0), which is defined as the distance between the *D*-*A* when the efficiency of energy transfer is 50%. The Förster distance can be determined experimentally as given in Eqn. 17 where the spectral overlap as a function of the wavelength is shown in Eqn. 18.[26]

$$R_0^6 = (8.79 \times 10^{-28}) n^{-4} \Phi_D \kappa^2 J(\lambda) \tag{17}$$

$$J(\lambda) = \frac{\int F_D(\lambda)\, \varepsilon_A(\lambda) \lambda^4 d\lambda}{\int F_D(\lambda)} \tag{18}$$

The fluorescence emission of the donor, $F_D(\lambda)$ and the acceptor absorption coefficient, $\varepsilon_A(\lambda)$ in units of $M^{-1}cm^{-1}$ are integrated across the resonant wavelength range of characteristic overlap.

Eqn. 17 is perhaps the most important relationship, as it identifies the parameters one must consider in designing an optimal FRET pair. In addition to the highly sensitive distance dependence of energy transfer, the quantum yield of the donor and the magnitude of the spectral overlap scale linearly with the Förster distance. Selection of a brighter donor and an acceptor with maximum spectral overlap will ultimately allow for an increased rate of energy transfer at larger *D-A* separation distance. The orientation factor is also influential in the calculation of the Förster distance, where κ^2 is given by Eqn. 19:

$$\kappa^2 = (\cos\theta_T - 3\cos\theta_D \cos\theta_A)^2 \tag{19}$$

where a vector representing the distance between the donor and acceptor dipoles is used a frame of reference to which θ_D and θ_A represent the angle of the donor and acceptor transient dipoles with this axis, respectively. θ_T is the angle between the donor and acceptor transient dipoles.[26] As seen in the absorption of electromagnetic radiation, the electric field vector of the incoming photon must match the alignment of the transition dipole of the molecule for absorption to take place. This similarity requirement must be met for coupling of the transient donor-acceptor dipoles. The value of κ^2 is between 0 and 4, where 0 represents perpendicular dipoles and 4 for dipole vectors oriented head-to-tail dipoles.[26] The true value for κ^2 can be determined experimentally through anisotropic fluorescence measurements, nonetheless κ^2 is often assumed to be 2/3 which corresponds to two freely rotating isotropic dipoles. For donor-acceptor systems that are more rigid and have less degrees of freedom, a value of 0.476 is assumed given that the dipoles will not change during the lifetime of radiative decay.[26] The rate of energy transfer is also proportional to the fluorescence lifetime of the donor, where donor molecules with longer lived decays offer improved rates of energy transfer.[26] Considering the ratio of the rate of energy transfer to the total radiative decay rate, the efficiency of energy transfer, E at a given *D-A* separation distance is given in Eqn. 20.[26] In the case for multivalent applications in FRET, Eqn. 20 takes on another form to account for the acceptor valency, a around a given donor since it is possible to have FRET systems beyond the traditional one donor – one acceptor arrangement.[31]

$$E = \left(\frac{R_0}{R_0 + r}\right)^6 = \left(\frac{aR_0}{aR_0 + r}\right)^6 \tag{20}$$

Eqn. 20 highlights the strong distance dependence of the efficiency of energy transfer as related to the Förster distance for the FRET pair as a plot of E vs. r/R_0 shows a sigmoidal dependence.

When $r < R_0$, efficiencies rapidly increase to unity where at $0.5R_0$, the FRET efficiency reaches 0.985. At $r > R_0$, energy transfer efficiencies rapidly decrease to 0, where at $2R_0$ the efficiency is 0.015.[26] As an increased number of acceptors are added around a single donor, more pathways exist for energy transfer. The sigmoidal dependence in Eqn. 20 shifts toward higher FRET efficiencies for larger ratios of r/R_0.

FRET efficiencies can be determined through both steady state and time-resolved fluorescence measurements. The former evaluates the change in magnitude of the donor emission spectrum, while the latter investigates the change in the luminescent lifetime of the donor. This is shown mathematically by Eqn. 21[26]:

$$E = 1 - \frac{F_{DA}}{F_D} = 1 - \frac{\tau_{DA}}{\tau_D} \tag{21}$$

where the integrated fluorescence spectrum of the donor in the presence and absence of the acceptor are given by F_{DA} and F_D, respectively. For time-resolved measurements the ratio of the donor lifetime in the presence (τ_{DA}) and absence (τ_D) of the acceptor is used. In steady state measurements, it may be necessary to first perform deconvolution on the FRET emission spectrum if the acceptor is luminescent so as to ensure that only the donor emission band is being integrated in Eqn. 21. For this reason, time-resolved fluorescence measurements offer a greater convenience since the lifetime of the emission can be monitored at a single wavelength that can be selected to minimize overlap or crosstalk from the acceptor luminescence band.

1.4 Semiconductor Quantum Dots

Quantum dots (QDs) are semiconductor colloidal nanocrystals composed of 10^3-10^4 atoms and are often referred to as artificial atoms. The discovery and emergence of QDs is highlighted in a perspective in *ACS Nano* written by A. P. Alivisatos[32], one of the major contributors toward the discovery. In brief, over three decades ago L. Brus and S. Ijima at Bell Laboratories initiated research that would shape the field of nanotechnology by introducing the carbon nanotube and the colloidal QD. Continued work by Brus focused on controlling the size and shape distribution of QDs and identifying suitable materials to provide for more stable nanocrystals. These goals were realized when A. P. Alivisatos, M. G. Bawendi and M. Steigerwald joined the team.[32]

Collectively, the contributions of these scientists would catalyze the increased widespread research about QDs that has scaled exponentially until the present day.

1.4.1 Quantum Dot Structure and Composition

As for most classifications of NPs, size, structure and shape are the fundamental parameters that create their unique properties. The interest in QDs resides mainly due to their unique optical properties[33], where the most exquisite feature is the size-tunable PL as a result of quantum confinement effects. Since QDs are semiconductors, they also warrant application in electrical[34] and electrochemical systems[35] in addition to optical applications. The photophysical properties of QDs are discussed in detail in section 1.4.2. Nonetheless, in order emphasize the importance of QD size and structure on the optical properties, quantum confinement can be described in short by considering the "particle-in-a-box" model where confining an electron to a box of known dimensions allows computation of the wavefunction and electronic energies. As the dimensions of the box are reduced, the position of the electron is better defined but the spacing between energy levels increases. Transitions between electronic energies are then characteristic of higher energy photons, and this is the fundamental principle behind the *size-tunable* PL.

QDs are generally composed of II-VI or III-V periodic elements where the former can be CdSe and the latter InAs for example.[36] Of the II-VI systems, CdSe remains the most studied[37] but S and Te are alternate chalcogens that can be used to produce QDs that have PL emission in the purple-blue and red to near-infrared (NIR) region of the spectrum, respectively.[38] CdSe QDs have PL emissions that span across most of the visible spectrum except below the blue region, as shown in Figure 5(a).[32] For all QDs, the composition material determines the range of PL emission.[33] The physical structure of the QD is specific to the inorganic elemental composition. For CdSe, the material adopts a wurtzite configuration as shown in Figure 5(b) and (c) ii. CdS QDs conform to a tetrahedral, zinc blende structure as shown by the unit cell in Figure 5(b) and the cluster of atoms in Figure 5(c) i. The first two images in Figure 5(c) display tens of unit cells to illustrate the foundations for the resultant geometries of the QDs. The final QD structures are shown by the high-resolution transmission electron microscope (TEM) images in Figure 5(c) iii and iv. In these TEM images, the individual lattice indices of CdS and CdSe are visible. An interesting feature of QD structure depicted in Figure 5 is that the Cd atoms in both the zinc

blende and wurtzite unit cells are bound to the chalcogens in a tetrahedral arrangement, however the resultant nanostructures are tetrahedral and hexagonal, respectively.

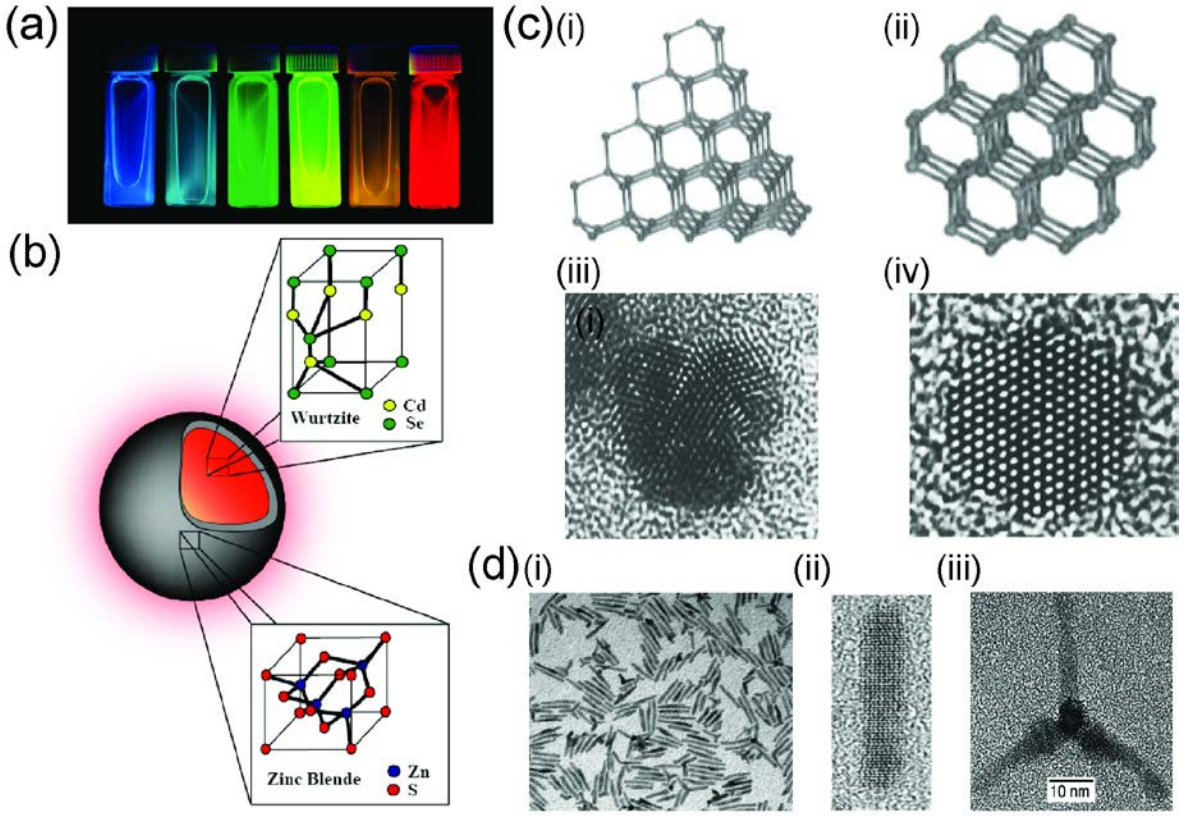

Figure 5. QD composition and resultant nanostructures. (a) The size-tunable photoluminescence of CdSe QDs as a result of illumination with a UV light. The blue vial on the left is characteristic of QDs *ca.* 2 nm in diameter where the red sample on the far right is *ca.* 6 nm. (b) Structure of a core-shell QD where the core is composed of CdSe and the shell of ZnS. The structure of CdSe in the core adopts a wurtzite configuration, while the ZnS shell conforms to a zinc blende unit cell. (c) Higher order zinc blende (i) and wurtzite (ii) structures displaying tens of unit cells to illustrate the resultant shape of the CdS (iii) and CdSe (iv) QDs in the TEM images. (d) (i) TEM image of alternate CdSe nanostructures: NRs and tetrapods, enhanced TEM images of an individual NR (ii) and tetrapod (iii). Panel (a) reprinted with permission from ref. [32]. Copyright 2008 American Chemical Society. Panel (c) adapted with permission from ref. [39]. Copyright 1996 American Chemical Society. Panel (d) adapted with permission from ref. [40]. Copyright 2000 American Chemical Society.

The ionic nature of the crystal leads to Coulombic attractive forces amongst rings 180º apart favouring the wurtzite structure and hexagonal QDs.[39] QDs are only one subset of other NP structures from the same semiconductor material and refer to a zero dimensional system, where nanowires (NWs) and nanorods (NRs) are classified as one dimensional (1-D) and two dimensional systems, respectively. The description three dimensional material is used in reference to the bulk material.[39] Advanced synthetic methods have afforded control over nanostructure shape by tweaking conditions to enable selective epitaxial growth on certain

crystal facets to produce NPs with high aspect ratios. The preferential binding of ligands to specific facets has enabled differential growth kinetics to afford the synthesis of CdSe NWs, NRs, and tetrapods as shown by Figure 5(d).[40, 41] Discussion of QDs up to this point has only introduced the idea of the QD being comprised of a single inorganic crystallite although the QD structure shown in Figure 5(b) is a core-shell composite of CdSe and ZnS. While the chemistry and size of the core nanocrystal is responsible for the unique optical properties of the QD, encapsulation of the core with a shell of a similar material can act to passivate the core QDs from oxidation and degradation. Furthermore, a shell material of higher bandgap energy acts to confine the electronic wavefunction of the core and enhances the quantum yield of the nanocrystal, where improvements of 5-fold in quantum yield have been reported.[42] Criteria for shell selection include minimizing mismatches in lattice parameters since the capping material is forced to grow on facets of a crystal structure foreign to the bulk structure. For ZnS, the lattice mismatch with CdSe is 12%, while that of ZnSe is 7%.[37] CdS shells[43] have also offered passivation of the core, but for toxicity considerations the presence of Cd atoms at the QD interface are of concern. Alternate QD compositions include ternary alloy QDs such as CdTeSe which differ from binary nanocrystals in that luminescence is no longer controlled by size and rather the ratio of Te to Se in the alloy. The composition based tuning of PL emission arises from the principle that the effective exciton mass in the alloy is less than in the binary materials.[44] Group VI materials such as C and Si have also been used in the synthesis of QDs.[45, 46] While these materials are likely less toxic due to composition, Si is an indirect bandgap semiconductor with weak optical transitions in the bulk material since optical transitions are momentum forbidden.[47] Although quantum size effects improve the probability of transitions and enhance luminescence, the fundamental nature of the semiconductor is still evident in the nanocrystal structure.[48]

1.4.1.1 Synthesis of Quantum Dots

The protocol described herein is for the synthesis of CdSe core and CdSe/ZnS core-shell nanocrystals, although experimental design is similar for all types of nanocrystals. The reaction proceeds as a precipitation of the inorganic precursors at high temperature in coordinating solvent. In the earliest reports of the synthesis of high quality QDs, dimethylcadmium and selenium shot initiated the nucleation and the growth of the core nanocrystals via thermal decomposition.[37, 38, 42] These syntheses involved heating and degassing trioctylphosphine oxide

(TOPO) under an inert gas at *ca*. 300-320 ºC. Selenium shot is first dissolved in trioctylphosphine (TOP) to form the TOPSe chalconide precursor followed by the simultaneous injection of TOPSe and $Cd(CH_3)_2$ into the vigorously stirred hot matrix. At these temperatures, the precursors decompose and cause a homogenous precipitation of CdSe seed crystals.[38] The temperature is maintained above 300 ºC to afford growth of the crystallites to the desired sizes. The growth time is relatively short; on the order of seconds-to-minutes depending on the desired size range of the QDs and the temperature of the reaction. The precipitation is initiated as a broad distribution of different sized crystallites, where focusing of the population to a Gaussian distribution takes place as the nanocrystals grow to larger sizes. For smaller sized CdSe nanocrystals, distributions as measured by the full-width-at-half-maximum (FWHM) of the PL emission band are *ca.* 30-35 nm while larger QDs have peak PL FWHM between 25-30 nm. The focusing of size distributions as governed by the kinetics of the reaction have been described elsewhere.[49] In the growth phase of the reaction, smaller unstable nanocrystals join to form larger crystallites. This phenomenon is known as *Ostwald ripening* and is in part responsible for the narrowing of QD size distributions during the reaction.[37] To obtain QDs with desired PL emission, the reaction can be quenched one of two ways. Aliquots may be removed during the growth phase at time intervals and immediately injected to a large volume of nonflammable solvent such as chloroform. If the entire batch is desired for a single QD sample, then a copious amount of cooled TOP can be injected into the reaction mixture to stop the crystallite growth. To improve the size distributions of QD samples, size-selective precipitation techniques can be integrated during core purification.[38] Core QDs are often purified by centrifugation and stored in toluene or butanol at 4 ºC. The pyrophoric nature of the $Cd(CH_3)_2$ carbene requires that synthetic preparation be conducted under inert conditions and requires use of a glovebox. More recent synthetic procedures have utilized more stable, oxidized forms of cadmium such as CdO and cadmium acetylacetonate.[50, 51] A typical procedure involved heating and degassing CdO in a mixture of TOPO, hexadecylamine (HDA), and stearic or oleic acid under inert conditions. HDA acts as an additional coordination ligand while stearic acid aids in dissolution of the CdO crystals. The mixture is often degassed multiple times followed by purging with N_2 or Ar until the white opaque mixture becomes transparent. At this point the TOPSe is rapidly injected into the Cd precursor to facilitation nucleation of the crystallites.[50]

The core CdSe QDs are capped with ZnS in a separate step although similar to the core synthesis. Cores are initially synthesized with Cd in slight excess (1.3×) to afford Cd rich cores that are primed initially with S to initiate ZnS shell growth. The formation of a CdS monolayer prior to growth of a ZnS is in attempt to minimize the discontinuity between the core and shell by minimizing the lattice mismatch between the two crystal (discussed in detail later). The CdSe QDs dissolved in chloroform are dispensed into a solution of TOP/TOPO degassed in a three-neck flask at temperatures greater than 150 ºC. Shell precursors include diethylzinc and hexamethyldisilathiane (TMS-S) which are first dissolved in TOP and then mixed together. The precursor mixture is then added drop wise with vigorous stirring to the dispersed solutions of core QDs. The temperature is maintained at *ca.* 200 ºC to afford annealing of the shell precursors to the cores while maintaining a steady but slow addition so as to not begin precipitation of ZnS QDs. After addition of the shell precursor solutions, the mixture is further stirred overnight to afford homogenous shell coating.[37] Alternate routes for shell formation include one pot synthesis, where core QD growth is quenched by injection of cold TOP followed by equilibration of the solution temperature to *ca.* 250 ºC. The Zn and S precursors are then injected drop wise and in sequential aliquots to avoid precipitation of ZnS QDs at the higher temperature.[42] Both routes are viable and have reported the synthesis of highly luminescent CdSe/ZnS QDs. As described earlier shell structures are melded to those of the core regardless of the preferred unit cell. Shells are also grown with Zn in slight excess (1.2×) to afford coordination of the stabilization ligands. The long aliphatic carbon chains of the coordination solvent prevent nanocrystal aggregation in nonpolar media by steric occlusion. In a comprehensive study by Dabbousi et al.[37] 1.4 atomic layers of ZnS afforded the strongest luminescent CdSe/ZnS core-shell QDs. Incomplete atomic layers often results from the nucleation of the shell material as islands on the nanocrystal interface and often causes inhomogeneous growth of the shell around the core. Additional growth of shell resulted in decreased PL intensities as the ZnS begins to grow with bulk lattice parameters. Incoherent growth of ZnS around the CdSe core results at increased shell thickness, leading to strain induced dislocations in the structure that afford nonradiative recombination of the exciton.[37] Alloyed QDs with a gradient transition to pure shell materials have alleviated the detrimental effects to QD PL from thick shells by minimizing lattice mismatches.[52] To determine the concentration of QDs in the synthesized sample, a study by the Peng group investigated the scaling of the position of first absorption peak with the size of the QD.[53] In this work, the molar extinction coefficients were determined by fitting the energy of

the bandgap as described by the first exciton peak with the diameter of the nanocrystal to a power function.[53]

1.4.2 Photophysics of Quantum Dots

For most NPs, the characteristic size, shape, and structure define the unique physical properties. Of these parameters it is predominantly the size-scale of QDs that enables quantum confinement effects to govern the intrinsic size-tunable PL that has afforded the integration of QDs into many optical applications. To understand the fundamental principles of QD photophysics, it is necessary to first introduce the concept of bonding in metals and semiconductor materials.

1.4.2.1 Band Theory in Metals

The term band theory refers to the bonding in bulk metals where the molecular orbitals are described as continuous bands. The origin of bands can be explained by considering a 1-D solid of an infinite line of bonded atoms.[54] Considering that each atom has a single S orbital available for bonding, the joining of two atoms by a single bond creates one bonding and one antibonding molecular orbital. Considering a bonded sequence of *N* atoms, *N* molecular orbitals are created where the bonding orbitals reside at a lower energy than the antibonding orbitals. While the molecular orbitals appear as a continuous *band*, they exist as *N* individual orbitals where the energy spacing between neighboring orbitals is infinitely small. For transition metals and elements with P orbitals, both an S band and P band exist, where the energy difference between the two bands is known as the *band-gap*. For most metals, the P band is also continuous and is the origin of conductivity.[54] The S band and P band are often referred to as the *valence band* and *conduction band*, respectively.

In the description of conductors, semiconductors, and insulators it is the positions of bands and the relative occupancy of electrons in each band that determine the level of conductivity in the material. Considering an alkali metal where each atom contributes one bonding electron, *N* electrons will occupy the aforementioned bands. The occupancy of electrons is temperature dependent, where at 0 K the electrons will reside in *½N* molecular orbitals because electrons are *Fermions* and cannot all reside in the lowest energy level. For such a system, the HOMO is often referred to as the *Fermi level*. As the temperature is increased, thermal energy is transferred to the systems and electrons can be excited to higher energy levels, specifically those that reside in

the Fermi level as they are the most mobile. The population, *P* of the molecular orbitals by electrons is described by the Fermi-Dirac distribution (Eqn. 22), which is a modified form of the Boltzmann distribution that takes into account the Pauli Exclusion Principle.[54]

$$P = \frac{1}{\left(e^{\frac{E-\mu}{k_B T}} - 1\right)} \tag{22}$$

In Eqn. 22, E and μ, represent energy and chemical potential, respectively, where the latter is equal to the energy at $P = 0.5$, k_B is the Boltzmann constant and T is the temperature in Kelvin. The distribution resembles an exponential decay with increasing energy, where increasing the temperature shifts the distribution to higher energy levels with a larger exponential tail.[54] For a conductor, overlap between the conduction and valence band exists with the Fermi level residing at a position between the areas of overlap. As a consequence of the overlap and position of the Fermi level, the available energy as described by k_BT is sufficient to promote electrons into the continuum of molecular orbitals of the conduction band and is the nature of electrical conductivity in most metals. For an insulator or dielectric material, the Fermi level resides in the valence band and the bandgap energy is significantly larger compared to k_BT and prevents transitions of electrons into the conduction band. In semiconductors, the Fermi level is positioned between the valence band and conduction band where the energy difference between the conduction band and the Fermi level is small compared to k_BT. As the temperature is increased, the tail-end of the Fermi-Dirac distribution extends across the band-gap where electrons populate the conduction band and holes are left in the valence band. It is the mobility of the electrons and holes that provide for conductivity in a semiconductor.[54]

1.4.2.2 Quantum Confinement

The size-tunable PL exhibited by QDs is due to quantum confinement effects that dominate as a result of NP size scale and the intrinsic spacing of energy levels. Confinement effects become prominent when the radius of the NP is on the order of the characteristic Bohr-exciton radius for the material, which is the preferred separation distance of the electron-hole pair or *exciton*; for CdSe this is *ca.* 5.6 nm.[55] The discreteness of energy levels of clusters on the order of 10^3-10^4 atoms lies intermediate between that of the bulk and atomic limits as shown in Figure 6.[39] For nanostructures of these size dimensions, the interior molecular composition is similar to the bulk

lattice although a significant proportion of the atoms reside on the surface where these structures are commonly referred to as nanocrystals.[47]

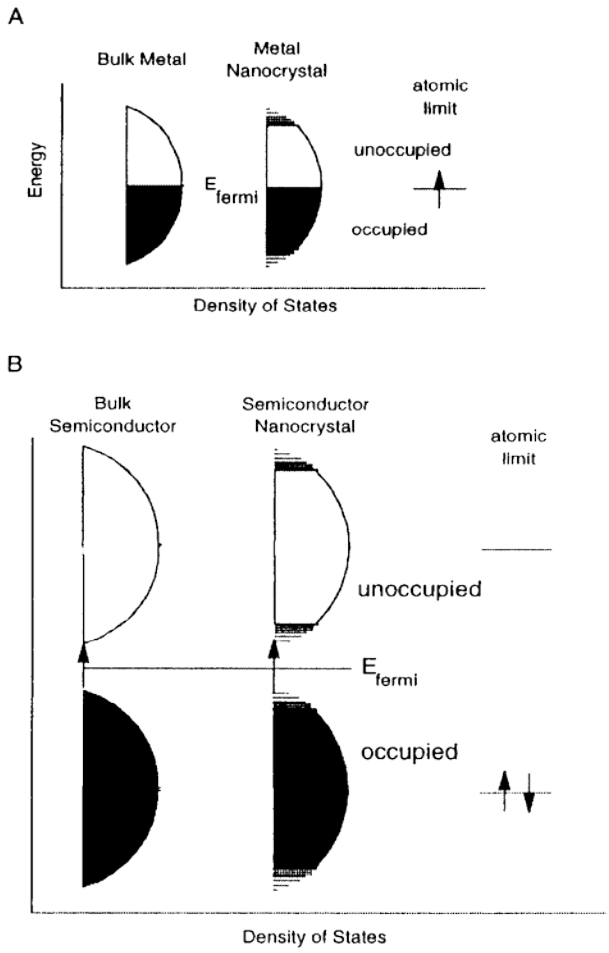

Figure 6. Development of conduction (white) and valence (black) bands in metals (A) and semiconductors (B) through a linear combination of the atomic orbitals. The relative position of the bands in energy is shown along with the density of states from the onset of the atomic limit to that of the bulk material. The nanocrystal regime resides intermediate of the two extremes for clusters on the order of thousands to tens of thousands of atoms where quantum confinement effects dominate the energetics. The Fermi level is also depicted in each diagram, where it is found directly in the center of overlapping bands in metals and in the band-gap in semi-conductors. The discreteness in the energy levels at the edges of bands is visible in the nanocrystal size scale. Band-edge transitions from the Fermi level are the basis for optical transitions in QDs. Reprinted with permission from ref.[39]. Copyright 1996 American Chemical Society.

For metal and semiconductor nanocrystals, the optical properties differ as a result of the overlap between bands as described in the previous section (Figure 6). Since bands or the density of states develop from the initial position of the atomic orbitals, the centers are developed prior to the edges. Even for metal nanocrystals of the same clusters sizes as QDs, the Fermi level resides in the center of the bands and thus optical transitions are similar to those seen in bulk molecular size scales. On the contrary, for semiconductor nanocrystals, the Fermi level resides between the

valence band and conduction band, where optical transitions across the band-gap are referred to as *band-edge* transitions. As the size of the nanocrystal increases, bands become wider and the energy of resonant transitions across the band-gap decreases.[39] As the size of the cluster approaches quantum confined regimes, the band-gap energy dramatically changes, where for CdSe QDs the band gap energy can vary from 2.4 eV to 1.7 eV, where resonant transitions are characteristic of green and red photons, respectively. Furthermore, smaller sized nanocrystals have high oscillator strength as a result of less developed band edges as described by the relationship between position (x) and momentum (p) as given by Eqn. 23.

$$\Delta p \Delta x \geq \hbar/2 \tag{23}$$

Considering free vs. confined particles in a crystal material, the energy of the free particle and the crystal momentum ($\hbar k$) can be described, where $\hbar$ is equal to Planck's constant over 2π. However, the position of this free particle is uncertain. As the size of the nanocrystal decreases, the particle becomes confined and more is known about position. At the same time, the energy may still be known but the uncertainty in momentum has now increased substantially. A superposition of bulk wavevector (k) states is used to describe the energy of the system where the relationship between energy and momentum can be explained as a first approximation by considering the quadratic dependence of energy on k (Eqn. 24).[39] In Eqn. 24 m, is the effective mass or reduced mass of the electron which is inversely proportional to the width of the band.[39]

$$E = \hbar k^2/2m \tag{24}$$

From these relationships, the energy dependence on band width or the size of the crystallite scales as $1/r^2$ as described by the particle-in-the-sphere model where r, is the radius of the nanocrystal which is approximated as a sphere.[39, 55] This description is sufficient for larger QDs but the model breaks down in describing smaller QDs.[39] For smaller nanocrystals it is necessary to consider the *tight binding model* that is used to describe the self-assembly of atoms in crystallites, the electron eigenvalues describing the energy as a function of k is given by Eqn. 25,[39, 56] where $k = 2\pi/\lambda$ and α is the energy associated with the linear combination of atomic orbitals and β is the width of the resultant band.

$$E = \alpha + 2\beta \cos(ka) \tag{25}$$

The distance between neighbouring atoms in the linear chain is given by *a*. For discrete eigenvalues in nanocrystals, the wavevectors have nodes at the ends of the crystal. For high energy molecular orbitals, more nodes exist within the crystal and can reside on atomic nuclei. The wavefunctions of the electron are essentially standing waves where the electron simultaneously senses both ends of the nanocrystal.[56]

1.4.2.3 Optical Transitions in the Bandgap of CdSe Quantum Dots

The relationship between the energy of molecular orbitals and nanocrystal size clearly illustrates how quantum confinement effects provide for the size-tuneable PL seen in QDs. Nonetheless to explain the specific energy of transitions seen in both the absorption and PL spectra of CdSe QDs, it necessary to describe the formation of the CdSe band gap from the atomic molecular orbitals. For CdSe the LUMO consists of Cd 5s atomic orbitals (conduction band) and the HOMO is comprised of Se 4p orbitals (valence band) that are 3-fold spatially degenerate.[55] The transitions across the bandgap consider both the wave functions of the electron (*e*) and hole (*h*). In this description, only the total angular momentum *J*, where $J = L + S$ (orbital + spin) is considered a good description of the molecular orbitals when the total Hamiltonian of the hole is used.[56] Furthermore, the strong spin-orbit coupling in CdSe and the crystal field splitting from the wurtzite unit cell splits the Se 4p HOMO.[55] While the band gap energy associated with the first excitonic transition can be described using Eqn. 24, it is insufficient in explaining the additional absorption shoulders seen throughout the spectrum and the excitation independent Stokes shift and PL emission. Further splitting of the HOMO levels is due to the *e*-*h* exchange or "mixing" of the wavefunctions. The quantum confined wavefunction of the exciton is shown by Eqn. 26:

$$E(r) = E_b + \frac{\hbar^2 \pi^2}{2r^2}\left[\frac{1}{m_e} + \frac{1}{m_h}\right] - \frac{1.8e^2}{\varepsilon_\infty r} \tag{26}$$

where the band gap energy of the bulk material is given by E_b and m_e and m_h are the masses of the electron and hole, respectively, and ε is the dielectric constant of the material.[56] In Eqn. 26 the Coulombic interactions between the electron and hole are considered, where in confined nanocrystals the overlap between wavefunctions increases as a function of decreasing *r*. The splitting of the valence band is shown in Figure 7(a). These transitions are collectively referred to as the *exciton fine structure* of the band-edge transition. The band-edge absorption is the lowest

energy excitonic transition denoted by $1S_e1S_{3/2}$ where S_e and $S_{3/2}$ refer to the orbital occupied by the electron and hole in the first (1) quantum confined energy state, respectively.[55] For CdSe QDs any asymmetry in the structure further splits these states and as a result 5 orbitals exist with some degeneracy as shown in Figure 7(a). The orbitals are labeled by the total angular momentum where the ±2 and 0^L are optically inactive and excitation to these states is forbidden.

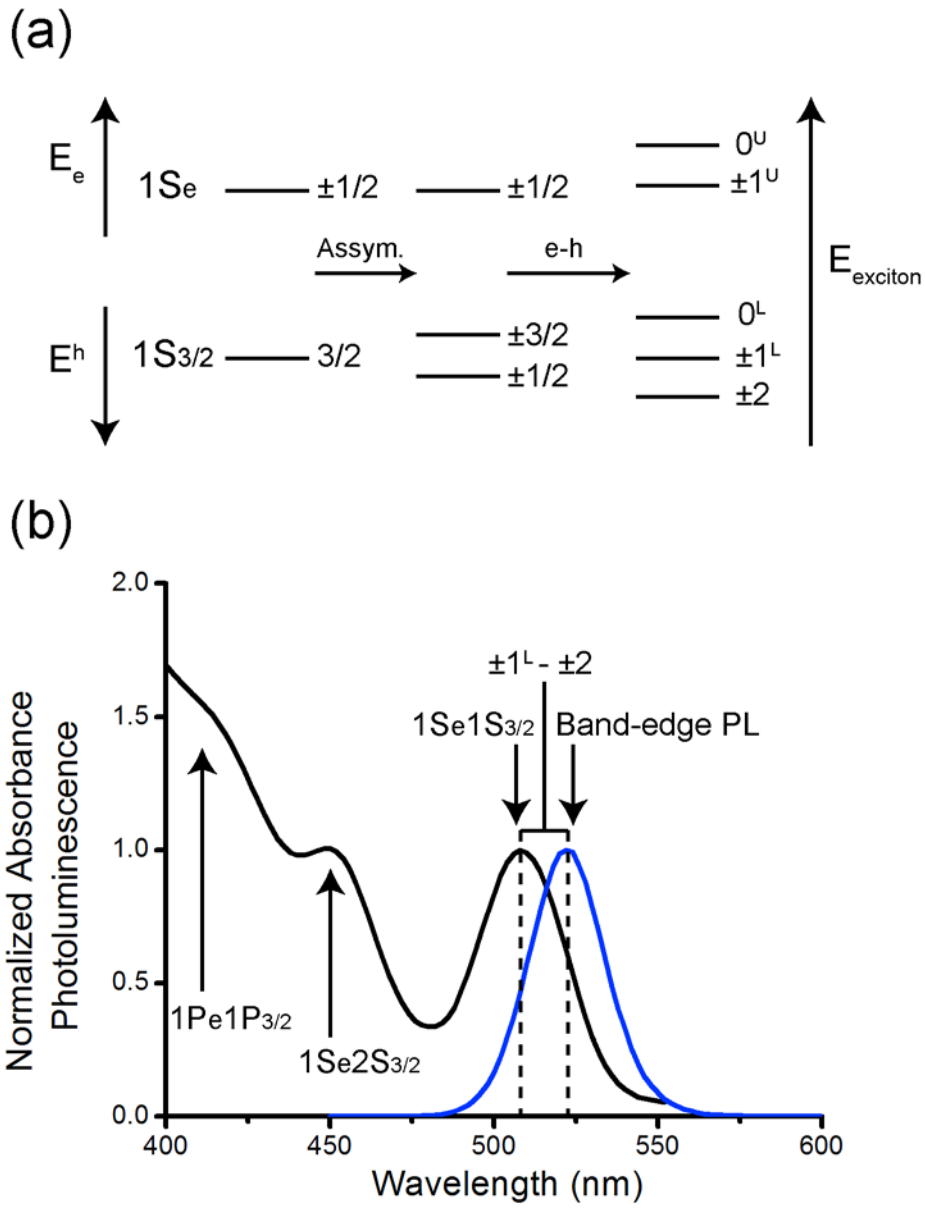

Figure 7. (a) Energy level description of the exciton fine structure in the $1S_eS_{3/2}$ exciton transition. Through a combination of crystal field, crystallite asymmetry and e-h exchange, the energy levels of the valence band are split into 8 states with three doubly degenerate as denoted by the total angular momentum. The ±2 and 0^L states are dark states and are optically inactive. Adapted from ref.[55]. Copyright 1999 American Chemical Society. (b) Normalized absorbance (black) and PL (blue) spectra for a sample of gQDs. The first absorption peak shown at *ca.* 510 nm is the

$1S_e1S_{3/2}$ transition and is also referred to as the first exciton peak. Additional absorption shoulders are visible at *ca.* 450 nm and 415 nm and correspond to higher order $1S_e2S_{3/2}$ and $1P_e2P_{3/2}$ transitions, respectively. The Gaussian band-edge PL is shown at 525 nm where the band width is characteristic of the size distribution of nanocrystals in the sample. The well-defined Stokes shift between the first absorption peak and the band-edge PL is a result of phonon mediated relaxation of the exciton from the $\pm1^L$ to the ±2 dark state followed by subsequent PL from electron-hole recombination.

The U and L superscripts indicate upper and lower energy orbitals, respectively.[57] Transitions through band-edge excitation cause occupancy of the ±1 which is the predominant optically active excitonic state.[55] Recall that in discussion of molecular fluorescence, the Stokes shift results from efficient vibrational relaxation after excitation and the appearance of the fluorescence spectrum is independent of the excitation wavelength. For optical transitions in QDs, similar vibrational deactivation takes place and is attributed to longitudinal optical (LO) *phonons*; quantized vibrations in the crystal lattice.[57] Furthermore, the PL emission is a result of a population of different sized nanocrystals with distinct band gap energies. In experiments probing the resonant PL Stokes shift, QDs were excited on the red end of the first exciton transition and exhibited narrow PL emission at 10 K.[57] A Stokes shift of the zero LO phonon line was observed. The exciton fine structure and the splitting of energy levels in the valence band sufficiently explained this phenomenon. While the $\pm1^L$ optically active resonant transition was excited, thermal relaxation of the exciton to the dark ±2 state accounts for the Stokes shift seen in the QD PL from the first absorption peak. Furthermore, luminescence from the ±2 state proceeds through phonon based electron-hole recombination or a spin-flip relaxation mechanism.[57] Moreover, the Stokes shift is also size-dependent, and increases with decreasing QD size even at excitation wavelengths higher in energy that the first absorption peak. Stokes shifts have ranged between *ca.* 100 meV to 25 meV for small to large CdSe QDs and the explanation is two-fold. Firstly, the probability for an optical transition is directly proportional to the nanocrystal volume where the larger crystallites have higher excitation probability. The resulting PL emission maximum is dominated by this region of the nanocrystal distribution and since the band gap energy of these particles of the ensemble is relatively lower, a distribution based Stokes shift is inevitable. Secondly, the confinement induced mixing of energy levels in the valence band results in concentration of oscillator strength in the higher optically allowed transitions. This stems from the superposition of bulk *k* states in the quantum confined regime. For smaller nanocrystals, the exciton fine structure reduces to the higher energy bright states. Phonon mediated relaxation returns the exciton to the dark state followed by subsequent PL emission. The difference in energy between the higher bright state and the dark state is relatively larger and

translates into a more pronounced Stokes shift for smaller QDs.[57] In the blue end of the excitation spectrum shown in Fig. 8 (b), additional absorption shoulders are present and are referred to as the subsequent second and third exciton peaks. These distinct features are characteristic of the excitonic transitions $1S_e2S_{3/2}$ and $1P_e1P_{3/2}$, listed in order of increasing energy.[58] Additional excitonic transitions can be seen in the full absorption spectrum with increasing ε until *ca.* 300 nm, although these are less pronounced for smaller QDs as a result of higher oscillator strength; for detailed discussion the reader is referred elsewhere.[58] It is important to note that the *k* states throughout the CdSe nanocrystal are all in phase as the dipoles from each individual unit cell are aligned. Since the wavelength of the incident photon is much larger than the nanocrystal dimensions, it causes alignment of all transition dipoles such that the overall excitation process has no change in *k*; this is referred to as a direct band gap material.[39]

Recall that the width of the PL band of QDs is an indication of the polydispersity in the sample. While the PL emission can be modeled by a Gaussian distribution it is sometimes asymmetric or tailed depending on the kinetics during the synthesis. As in molecular fluorescence, the PL emission band has an intrinsic line width and considering the single molecule spectroscopy of QDs, the FWHM is *ca.* 13 nm.[59] Luminescence in QDs has been suggested to occur from the ±2 dark state after phonon mediated relaxations within bands and the radiative recombination of the exciton was thought to be influenced by the surface of the nanocrystal. Radiative relaxation was confirmed to be independent of the surface ligands and evidence for this theoretically and experimentally was described in a study by Kuno et al.[60] Since transitions from the dark exciton ground state are dipole forbidden this can describe the longer PL lifetime seen in QDs where recombination from the optically active states is *ca.* 100 times faster.[60] Despite changing surface ligand composition, no direct effect on the electron-hole recombination mechanism was noted, and it was concluded that an internal exciton mediated relaxation explained the band-edge PL emission. Moreover it was noted that surface defect sites in the crystal enhanced nonradiative relaxation rates and resulted in band gap emission.[60] Band gap emission is characteristic of a broad PL peak that is bathochromic relative to the band-edge PL. Defect sites at the surface of the nanocrystal result in orbitals of energy intermediate of that of the band gap energy where radiative recombination of the electron-hole at these states cause this broad red shifted PL emission to appear.

The above discussion of optical transitions has been tailored to core CdSe QDs. While as a first approximation the quantum confined *k* states are said to have nodes at the surface of the nanocrystal, this applies only for a particle confined to a box with an infinite potential well. For QDs the appropriate model considers a particle inside a box with barriers of finite potential. Computing the expected Hamiltonian for this system reveals that a small percentage of the wavefunction lies outside the box as the electron effectively can tunnel through the barrier. Considering the probability distribution of finding the electron outside the box, the percentage decreases with an increasing energy barrier.[29] The resultant implications on QD PL are negative as the exciton can sample the nanocrystal interface, enhancing nonradiative or unfavorable radiative decay rates. These principles illustrate how a few atomic layers of a material of higher band gap (e.g. ZnS) results in improvement of the rate of band-edge PL by confining the exciton in the core of QD. Furthermore, the shell also protects the core from oxidation and or degradation by chemical agents which can also introduce defect sites into the crystallites as to create "trap" states that promote nonradiative relaxation of the exciton. While cores can be isolated without defect sites introduced from the synthesis, to preserve the integrity of the core structure it is critical that the QDs are capped immediately to prevent degradation. Shell passivation also does not influence the mechanisms of radiative electron-hole recombination but the chemistry of the shell and the intrinsic band gap has consequences on the location of the exciton within the nanocrystal. The chemistry and energetics of CdSe/ZnS renders them as type I QDs. In type 1 QDs the band gap energies between the core and shell have the valence band and conduction band of the core material residing between the valence band and conduction band of the shell. For type II QDs, the differences in band gap energy are offset between the core and the shell, where the valence and conduction bands of the core material are shifted higher or lower in energy than those of the shell. Exciton confinement is different in these materials where each charge carrier is localized to either the core or shell.[61] The reduced confinement of the exciton allows for tuned emission well into the NIR region.[62]

1.4.3 Quantum Dot Coatings and Bioconjugation

The impact of QDs in nanotechnology, and in bioanalytical analyses, could not have been realized without functional coatings to provide water solubility. The first translation of QDs from hydrophobic media into aqueous buffers utilized mercapto-alkyl carboxylic acid ligands.[63] The bifunctional nature of these ligands provided water solubility through chelation of the native Zn

atoms at the QD interface by thiol coordination. The carboxylic acid terminus ionized at physiological pH conditions to provide colliodal stability through repulsion since all nanocrystals have a net negative charge. The reaction is termed a ligand-exchange as the native hydrophobic alkane terminated phospine and phosphine oxide ligands are displaced from the QD surface. The exchange is driven by the higher affinity and bond strength of the Zn-S coordinate bond. Other chelating ligands include amines which also bind more strongly than the native phosphorus based ligands used in synthesis. Alternate strategies have incorporated the native hydrophobic ligands to impart aqueous solubility where the nanocrystals are overcoated with an amphilic polymer or block co-polymer.[64, 65] The structure is typically based on a polyacrylic acid oligomer backbone and 25-30% of the carboxylic acid backbones are derivatized with alkane chains varying from 12-18 carbons. These alkane chains intercalate with the native hydrophobic ligands on the surface of the QDs through van der Waals interactions and the polar carboxylic acids reside at the termini. Upon phase transfer to aqueous media, the carboxylic acids provide the solubility and colloidal stability while the QD remains encapsulated in a relatively hydrophobic environment. Since the surface of the nanocrystal is not in direct contact with the aqueous solvent, these QDs generally have higher quantum yields. While these two coatings strategies are widely used, a multitude of ligands with a myriad of terminal function groups have been described in the literature. For thiol based ligands, monodentate and bidentate ligands based on lipoic acid have been appended with polyethylene glycol (PEG) and PEG derivatives with amino, carboxyl, or alcohol terminal groups.[66-68] Mixtures of PEG ligands have also been reported, where a percentage are terminated with biotin to facilitate assembly of avidin derivatives.[68] Moreover, similar PEG derivatives can be tagged to the amphiphilic polymer backbone using standard carbodiimide chemistry to afford a stable amide linkage.[64] Zwitterionic coatings have also been reported and offer the ability to ameliorate nonselective adsorption of biomolecules to the surface of the QDs.[69, 70] QDs can be purchased commerically with different surface ligands and tethered bioconjugates. Life Technologies offers a variety of CdSe/ZnS QDs from hydrophobic post-synthesis nanocrystals to aqueous QDs functionalized with streptavidin (SAv).[71] Coating chemistries are also important from the standpoint of *in vivo* toxicity, where cytotoxicity has been linked to Cd^{2+} ion leaching from the core under continuous UV illumination and subsequent core oxidation.[72] While greener and heavy metal free QDs exist, designing biocompatible coatings that allow rapid excretion of QDs and that prevent bioaccumulation may still afford use of these nanocrystals *in vivo*.

Self-assembly of biomolecules on QDs has relied on a variety of surface ligands to facilitate tethering. Recent reviews have highlighted the myriad of bioconjugation strategies that have facilitated the use of QDs in bioanalyses.[73, 74] More recently, efforts toward orthogonal coupling strategies have accelerated to enable the selective and simultaneous immobilization of different classes of biomolecules at the QD interface.[74, 75]

1.4.4 Quantum Dots as Donors in FRET

The predominant role of QDs in FRET-based assays has been that of energy donors, [76, 77] although configurations where QDs are energy acceptors are described in section 1.4.5.3. Several of the unique optical properties of QDs make them excellent donors for FRET configurations. These include high quantum yield, long PL lifetimes, broad absorption spectra and narrow, symmetric, size-tunable emission.[63, 68] Here, some of their key advantages are summarized in the context of Eqn. 27 which was initially introduced in section 1.3.1.

$$E = \frac{aR_0^6}{aR_0^6 + r^6} = \frac{a\left[C\Phi_D J(\lambda)\right]}{a\left[C\Phi_D J(\lambda)\right] + r^6} \tag{27}$$

In recap, E is FRET efficiency, R_0 is the Förster distance (characteristic of a donor-acceptor pair), r is the donor-acceptor separation distance, a is the number of acceptors interacting with a QD donor, Φ_D is the QY of the donor, $J(\lambda)$ is the spectral overlap integral, and C is a constant collecting several parameters generally assumed to be constant.

- The potentially high QY, Φ_D, of QD donors helps to maximize energy transfer rates.
- The size-tunable QD PL permits optimization of the overlap, $J(\lambda)$, with the acceptor absorption spectrum to improve energy transfer rates while the narrow PL bandwidth minimizes crosstalk with acceptor emission.
- The surface area of the QD permits the assembly of multiple (equivalent) acceptors, a, per donor, increasing the net rate of energy transfer from the QD donor.
- The broad absorption spectrum and large effective Stokes shift of QDs permits judicious selection of donor excitation wavelength to minimize direct excitation of acceptors. Since acceptor molecules must be in their electronic ground state to function as an acceptor, the absence of direct excitation maximizes acceptor efficacy ($a_{\text{nominal}} \approx a_{\text{effective}}$).

The different means by which QD donors can enhance energy transfer rates are important given the inverse sixth power dependence on the D-A separation distance. Typically, oligonucleotide probes are 10–20 nucleotides, corresponding to extended lengths between *ca.* 3–7 nm. Since D-A separations must be measured from the center of the QD [76], an additional 2–6 nm contribution from the radius of the QD nanocrystal and its coating must also be considered. Typical Förster distances range from R_0 of 3–6 nm and virtually no energy transfer is observed for D-A separations with $r > 1.5R_0$. Fortunately, the highly favourable optical properties of QDs are frequently (but not always) able to offset this drawback for FRET, either through arraying multiple acceptors per QD or through above average R_0 values (*e.g.*, R_0 = 7.5 nm has been reported for a QD-dye FRET pair).[78] Moreover, QD donors still provide unique advantages for optical multiplexing and opportunities for interfacial design and bioconjugation that are unavailable with molecular donors.[74, 76] One highlight of the interfacial or solid-phase format that should not be overlooked is the potential for improvements in assay sensitivity arising from enhanced FRET efficiencies at an interface. It is thought that higher FRET efficiencies arise from a multitude of energy transfer pathways between donors and acceptors when both are assembled at high density at the interface.

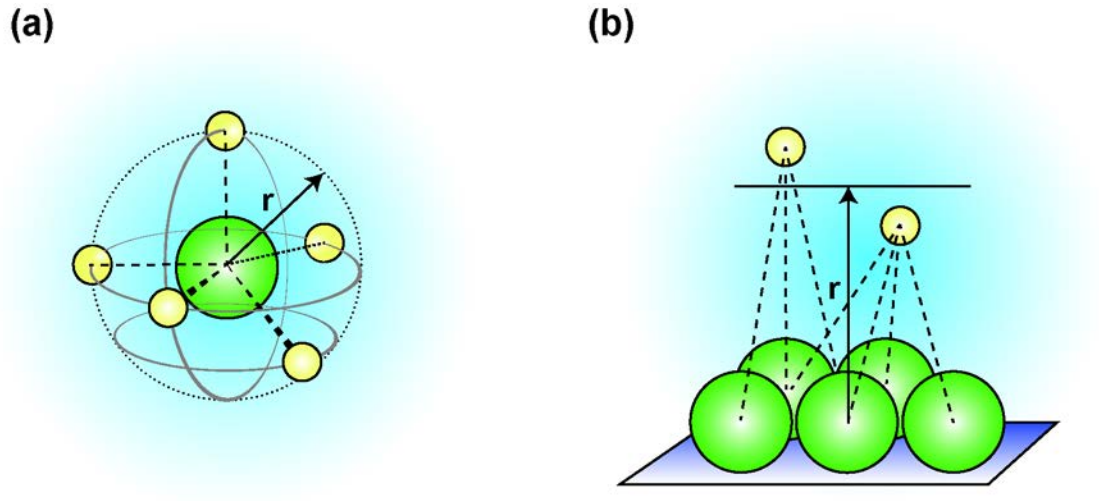

Figure 8. Possible energy transfer configurations for QD-FRET where (a) depicts a single QD-donor with a centrosymmetric orientation of acceptors and (b) multiple QD-donors interacting with multiple acceptors at an interface, the immobilization of QDs enable an increased number of pathways for energy transfer.

This effect is analogous to arraying multiple acceptors per QD donor in bulk solution (Figure 8(a)), except that each acceptor may now also interact with multiple donors (Figure 8(b)). In contrast to bulk solution, there are no discrete FRET pairs at the interface. The

multitude of FRET pathways appears to be sufficient to more than compensate for the loss of acceptor-accessible QD surface area upon immobilization (due to occlusion by the solid substrate and, presumably, neighbouring QDs) [79-81].

Given an appreciation for the optical properties of QDs and how these properties benefit FRET, it is worthwhile to briefly consider how an assay may be built around the combination of QDs and FRET. Indeed, QD-FRET assays have been reported for a myriad of analytes ranging from metabolites [82-84] and other small molecules [85, 86] to enzymes [87, 88] and other proteins [89, 90] to nucleic acids. Recent reviews have highlighted the more general use of QDs in bioanalysis [31, 76, 91]. These developments have been aided by the refinement and expansion of methods for functionalizing and bioconjugating QDs.[92] The basic blueprint for building an assay around a QD with FRET signaling (abbreviated QD-FRET) is as follows:

1) The core QD nanocrystal with the desired optical properties is passivated and protected with a thin shell of higher bandgap semiconductor. In most assay applications to date, CdSe/ZnS core/shell QDs have been utilized.
2) The surface of the QD is modified with a bifunctional ligand or polymer that imparts aqueous stability and provides reactive groups for covalent bioconjugation or an accessible interface for self-assembly of derivatized biomolecules.
3) The QD is conjugated with a probe capable of selectively interacting with the biological target of interest. This probe is typically but not always a biomolecule itself.
4) A fluorescent dye or other suitable acceptor for pairing with the QD donor is directly or indirectly associated with the above biomolecular interaction such that FRET is turned 'on' or 'off' in the presence or absence of target (or *vice versa*).

1.4.5 Nucleic Acid Diagnostics Based on QD-FRET

1.4.5.1 Hybridization Assays

One of the first and most successful of QD-FRET strategies for DNA detection was reported by Zhang et al., who developed a method based on the analysis of single QD-nanosensors [93]. In this method, streptavidin (SAv)-coated QDs were used as a scaffold for assembling a "sandwich" of biotinylated capture oligonucleotide probes and Cyanine 5 (Cy5) acceptor-labeled reporter oligonucleotides in the presence of DNA targets. Only in the presence of target DNA was energy

transfer from the SAv-QD_{605} to the Cy5 possible. Photon bursts from FRET-sensitized Cy5 PL were used to transduce hybridization events, with the number of these bursts correlated to the amount of target. Up to 54 duplexes could be self-assembled onto an individual QD, giving rise to substantial energy transfer efficiencies despite the large separation between QD donor and Cy5 acceptor. In an oligonucleotide ligation assay with clinical samples, the nanosensor was able to detect as little as 50 copies of a gene with a point mutation characteristic of ovarian cancer [93]. To permit measurement of single QDs, these assays were conducted under capillary microfluidic flow, which was later found to enhance energy transfer efficiency when compared to analyses in bulk solution [94]. The average donor-acceptor separation distance decreased by ca. 20% (from 12.0 nm to 9.6 nm) as a result of flow-induced deformation of the dsDNA-QD conjugates, resulting in higher assay sensitivity [95]. Zhang et al. have also used single QD-FRET nanosensors for the detection of microRNA (miRNA) after two-step isothermal exponential amplification reaction. [96] The first step in this assay was amplification of the target miRNA to complementary oligonucleotides, which served as a primer to produce a target oligonucleotide in the second step. As above, the oligonucleotide target hybridized with probe and reporter oligo sequences tagged with biotin and Cy5 (i.e., sandwich assay), respectively, and was captured by the SAv-QD_{605}. FRET-sensitized Cy5 PL was used to quantify the miRNA with an LOD of 0.1 aM [96]. Zhang et al. have further shown that multiplexed DNA detection is possible in a single QD-FRET format by using three-colour fluorescence coincidence detection [97]. Biotinylated capture probes complementary to the HIV-1 and HIV-2 genes were annealed to their respective target sequences, and REPs labeled with Alexa Fluor 488 (A488; for HIV-1) and Alexa Fluor 647 (A647; for HIV-2) were added to the mixture along with SAv-QD_{605} to capture the dsDNA. Single QDs were interrogated under capillary microfluidic flow using a 488 nm laser for excitation. Coincident photon bursts from the QDs, A488 (direct excitation) and A647 (FRET-sensitized) PL provided the signals to transduce the presence of HIV-1 and HIV-2 target genes [97].

In addition to single-particle methods, ensemble compatible QD-FRET hybridization assays have been described by our group[98, 99] and many others [100-104]. For example, Zhou et al. have reported an ensemble QD-FRET assay for nucleic acid detection using QD_{553} coated with a 2:1 mixture of 11-mercaptoundecyl-tri(ethylene glycol) alcohol and 11-mercaptoundecyl-tri(ethylene glycol) acetic acid ligands [105]. The latter ligands were conjugated with amine-terminated probe

oligonucleotides via carbodiimide activation, while the tri(ethylene glycol) (TEG) alcohol surface prevented the nonspecific adsorption of non-complementary (NC) targets. Hybridization with Alexa Fluor 594 (A594) labeled targets gave rise to FRET-sensitized A594 PL upon excitation of the QD. To avoid labeling targets with fluorescent dye, it was possible to use ethidium bromide (EB) as a FRET acceptor for the QD donor [98, 105]. EB selectively intercalates into dsDNA and exhibits a large fluorescence enhancement [106]. Hybridization of QD-probe conjugates with unlabeled fully complementary (FC) targets permitted intercalation of EB into the duplex, creating the necessary proximity for energy transfer from the QD and the necessary environment for EB fluorescence. Quantitative transduction of oligonucleotide targets was possible with a LOD of 1 nM [105]. More recently, Zhang and Zhou have described an oligonucleotide hybridization assay where the QD and intercalated EB acted as dual FRET donors for dye-labeled targets [107]. Energy transfer from the QD to an Atto 647 (At647) acceptor label on DNA targets was enhanced when EB was added to the system. Despite the relatively small spectral overlap between the QD_{550} and At647, a sub-nanomolar LOD was possible because EB molecules intercalated at multiple sites along the dsDNA were able to serve as relay sites for higher overall energy transfer efficiency [107].

1.4.5.2 QD molecular beacons

Molecular beacons (MBs) are perhaps the best known FRET technology for nucleic acid detection [108]. As such, the potential of QD-based MBs has been widely investigated. One of the first QD-MBs, reported by Kim et al., utilized mercaptoacetic acid (MAA)-coated QDs conjugated with 25 nt hairpins labeled with 4-((4-(dimethylamino)phenyl)azo)benzoic acid (DABCYL) quencher [109]. Molecular modeling suggested center-center separation distances of 3.3 nm and 5 nm between QD and dye for two hairpin conformations, giving rise to FRET efficiencies of 54% and 9%, respectively. A minimal increase in QD PL was observed upon exposure to NC target whereas a 6-fold increase was observed upon exposure to FC target, indicating that the hairpin sequence retained its function on the surface of QDs. In comparison to a MB based on molecular dyes, the QD-MB offered a 3-fold improvement in the spectral overlap integral and superior resistance to photobleaching [109]. However, the primary obstacle to use of the QD-MBs was the larger donor-acceptor separation imposed by the dimensions of the nanocrystal, which limited the maximum energy transfer efficiency.

In a study by Cady et al., the effect of oligonucleotide hairpin conjugation chemistry on the analytical performance of QD-MBs was evaluated [110]. Commercially available SAv-QDs and carboxyl QD donors were paired with Black Hole Quencher-2 (BHQ-2), Iowa black FQ (IaB), and 1.4 nm Au NPs as energy acceptors. Carboxyl QDs exhibited a larger relative increase in PL upon addition of target DNA than SAv-QDs, where the quenching efficiency in the hairpin conformation was limited by the dimensions of both the nanocrystal and the SAv layer [110]. To some degree, the extra distance imposed by the SAv layer can be compensated by arraying multiple hairpins around a QD. For example, Kim et al. have reported QD-MBs with 12–15 biotinylated BHQ-2-labeled hairpin probes per QD (QD_{525}, QD_{565}, or QD_{605}), although the FRET efficiency only reached 35% [111]. Alternatively, Li et al. have shown that electrophoretic separation of QD-MB constructs after hybridization can greatly reduce the background signal associated with incomplete QD quenching from QD-MBs in the native hairpin state [111]. Multiplexed analysis of two targets differing by a 1BPM was possible, with detection limits as low 14 nM, (Figure 9(a)) using capillary electrophoresis in conjunction with a two-colour QD-MB system comprised of QD_{585} and QD_{650} with hairpin oligonucleotides terminated with BHQ-2 [112].

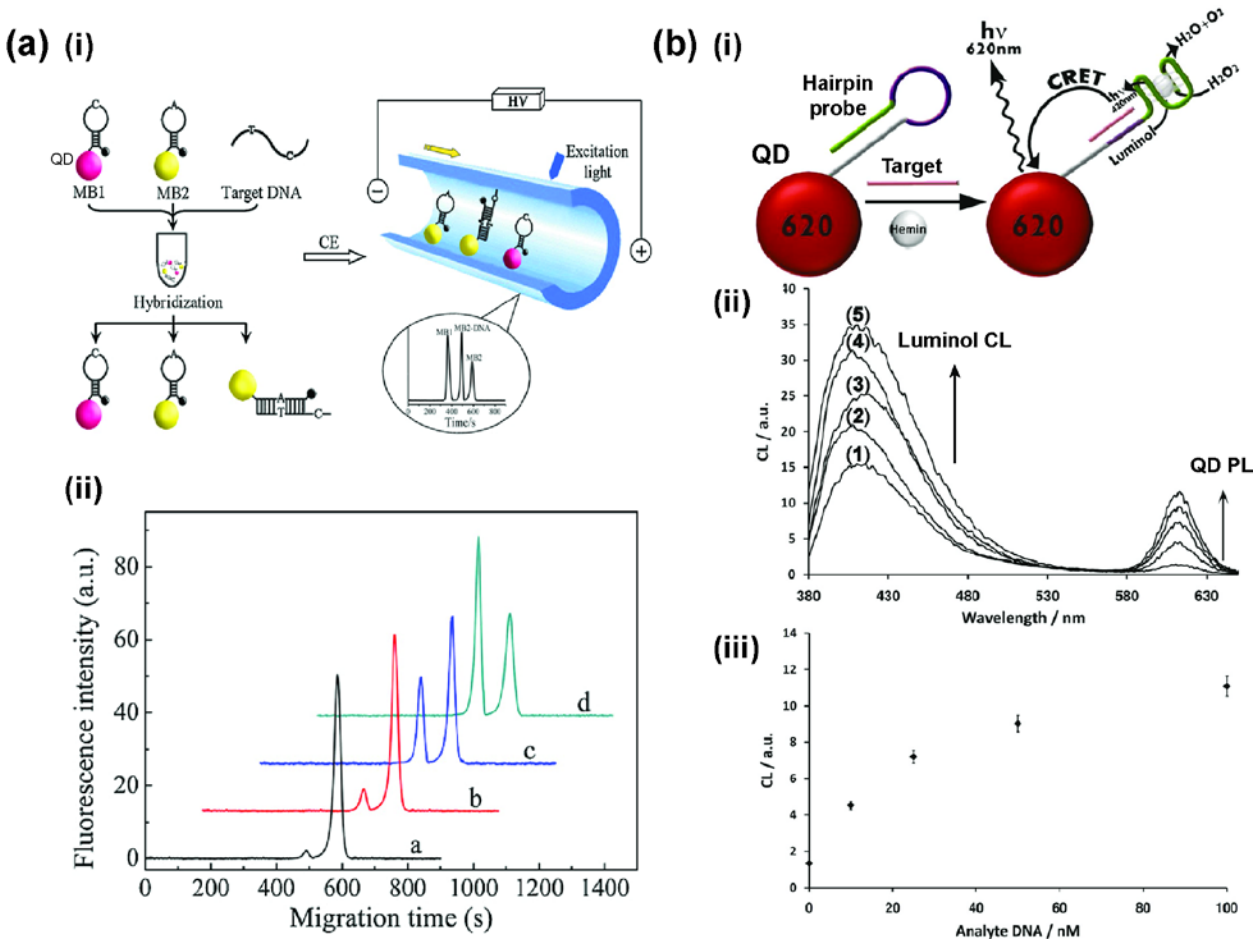

Figure 9. (a) (i) Principle of DNA detection with two QD-MBs where each hairpin probe is characteristic of a specific 1BPM. CE enables electrophoretic separation of the native probes and dsDNA hybrids as result of mobility changes. (ii) An electrophoregram displaying the quantitative response of a single QD-MB to (a) 14 nM, (b) 42 nM, (c) 168 nM, and (d) 336 nM of FC target. The leading band is seen to increase as a function of target concentration since the presence of dsDNA increases the mobility of the QD-MB conjugate. (b) (i) Illustration of the QD-CRET probe for transduction of DNA. Target oligonucleotide and hemin binding initiates the assembly of the G-quadruplex DNAzyme which catalyzes the chemiluminescent (denoted CL) oxidation of luminol and enables CRET to the QD. (ii) Emission spectra for the response of the probe to 0 nM, 10 nM, 25 nM, 50 nM, and 100 nM of target oligonucleotide denoted by (1-5), respectively. (iii) Response curve of the assay generated by using CRET sensitized QD PL to the concentrations listed in (ii). Adapted with permission from [113]. Copyright 2013 Elsevier.

In addition to SAv-biotin, several chemistries have been used to assemble QD-MBs. For example, Wu et al. reported covalent coupling of IaB quencher labeled hairpins to silica-coated QD_{535}.[114] The silica coating enabled analyses over a broad range of pH and DNA detection with 1BPM discrimination and an LOD of 100 pM. Medintz and coworkers have demonstrated that QD-MBs can be prepared via the self-assembly of a hexahistidine tagged oligonucleotide hairpin probes to QDs coated with dihydrolipoic acid (DHLA). [100] This strategy was adopted by Yeh et al. for the preparation of QD_{540}-Au NP MBs suitable for real time detection of viral replication in living cells.[115] Au NP hairpin probes were self-assembled on DHLA-coated QDs via a

hexahistidine tag. QD PL quenching efficiencies up to 91% were noted when six hairpin probes were immobilized per QD. Upon addition of complementary target, a >7-fold increase in QD PL was observed. TAT, the cell-penetrating peptide derived from HIV-1, was used to facilitate intracellular delivery of QD-MBs. QD PL was visible within cells 1 h post-delivery and it was possible to monitor spreading of the virus to adjacent cells in the media [115]. Wu *et al*. used an alternate method of self-assembly to prepare QD-MBs for the detection of β-Lactamase genes in *E. coli* by fluorescence in situ hybridization (FISH).[116] Thiol terminated hairpin oligonucleotides labeled with BHQ-2 were self-assembled on MAA-coated QDs, resulting in 74% quenching of QD PL. Analogous to MBs prepared via polyhistidine self-assembly, the relatively high quenching efficiency was a result of the compactness of the ligand coating and the direct binding of the hairpin to the QD. Upon addition of target oligonucleotides, a ca. 4-fold increase in QD PL resulted. The QD-MBs were successfully applied within bacterial cells and specifically targeted transcribed β-Lactamase genes. Although adsorption of the MBs to the outer cell membrane was observed, the adsorbed QD-MBs offered minimal background since the PL was quenched. This non-interference is in contrast to the use of non-hairpin QD-oligonucleotide probes, which yielded high background signals when adsorbed. [116]

With an eye toward possible *in vivo* applications, Liu et al. took advantage of the large two-photon absorption cross-section of QDs to demonstrate interrogation of QD-MBs using two-photon excitation with a NIR source [117]. This approach is attractive for the *in vivo* detection of nucleic acids since the QD-MBs do not require a reporter probe (cf. sandwich assays), and since NIR excitation largely eliminates autofluorescence background from biological samples while offering greater tissue penetration.

1.4.5.3 Special cases with QD acceptors

There are limited reports on the use of QDs as acceptors in FRET-based assays because there are only a few select types of luminophore that can effectively donate energy to a QD acceptor.[31] This challenge arises from the broad absorption spectrum of a QD since any wavelength suitable for excitation of a potential donor for a nominal QD acceptor will also directly excite the QD. The use of luminescent lanthanide complexes with long excited state lifetimes (10^{-5}–10^{-3} s) as FRET donors, in conjunction with time-gated PL measurements, permits effective use of QDs as FRET acceptors, as reviewed elsewhere [118]. Another possible mechanism of using QDs as

acceptors is to avoid optical excitation altogether. That is, by generating an excited state donor via chemiluminescence, electrochemiluminescence or bioluminescence. In the absence of optical interrogation, QDs remain in their ground state and are excellent acceptors. These processes are referred to as CRET and bioluminescence resonance energy transfer (BRET), respectively.

Willner's group has developed QD-CRET sensors for DNA detection based on the hemin/G-quadruplex horseradish peroxidase (HRP) mimicking DNAzyme [113]. This DNAzyme catalyzes the oxidation of luminol by H_2O_2 with concomitant chemiluminescence in the blue region of the spectrum (max. PL at 430 nm), providing large overlap with the absorption spectrum of QDs. Thiol-terminated oligonucleotides incorporating the G-quadruplex sequence were self-assembled on glutathione (GSH)-coated QDs and the addition of hydrogen peroxide, hemin, and luminol resulted in localization of the chemiluminescent reaction to the QD with efficient CRET from the excited state luminol oxidation product to the QD as displayed in Figure 9(b). While DNAzymes have mainly found utility as labels that are capable of providing signal amplification, this CRET scheme had the advantage of significantly reducing background signals arising from the catalysis of luminol by hemin. Since the analytical signal from CRET is distance dependent, there is little energy transfer from the chemiluminescence of luminol that diffuses through solution [113]. Multiplexed detection of nucleic acid targets was demonstrated by immobilizing three different nucleic acid hairpin probes on QD_{490}, QD_{560}, and QD_{620}, respectively. The probes were designed such that the stem duplex contained the DNAzyme sequence while the loop structure was complementary to the target sequence. This configuration enabled formation of the hemin/G-quadruplex structure and evolution of CRET only in the presence of the target nucleic acid sequence. Nanomolar LODs were reported and the inherent selectivity of the hairpin probes permitted parallel analysis of nucleic acid targets [113]. More recent work by the Willner group has shown that the aforementioned QD-CRET DNAzyme can be used in photoelectrochemical schemes for DNA detection and for following the activity of DNA machines [119, 120].

Deo's group has reported QD-BRET-based assays for nucleic acid detection [121, 122]. Renilla luciferase (Rluc), which catalyzes of the oxidation of coelenterazine with blue bioluminescent emission (max. PL at 485 nm), was used as the donor. In one format, nucleic acid probes were immobilized on QD_{705} while target was tagged with Rluc [121]. Hybridization provided the necessary proximity for BRET from Rluc to the QD_{705} upon addition of coelenterazine. A competitive binding assay format was used in practice so that target endogenous to a sample

would not need to be labeled with Rluc, but would complete with Rluc-labeled exogenous target. Progressive increases in the Rluc/QD (485 nm/705 nm) PL intensity ratio with increasing amounts of target permitted quantitative transduction. The LOD was as low as 4 pmol (~20 nM) and the assay was amenable to analyses in complex matrices [121]. Further work by the same group has included a QD-BRET sandwich assay with Rluc-labeled REP sequences [122]. A 15 nt spacer between the target sequence segments where probe and REP hybridized was found to improve BRET due to reduced steric hindrance between Rluc and the QD. Using the BRET sensitized PL as the analytical signal, a dynamic range greater than two orders of magnitude was realized and as little as 0.54 pmol (~3.5 nM) of target oligonucleotide could be detected. Discrimination against 1BPMs was demonstrated and the robustness of the assay was demonstrated by detecting nucleic acid targets in *E. coli* cell extract [122].

1.5 Microfluidics as a Platform for Bioanalysis

Microfluidics is defined as a technology used to manipulate fluids on the order of nL to aL in channel frameworks that are on the order of tens to hundreds of micrometers in dimension.[123] Such miniaturized fluidic platforms have garnered much interest from the analytical community for sample manipulation and the building of lab-on-a-chip (LOC) integrated analysis devices. The current impact of microfluidics was realized by widespread interest from four scientific fields: the microanalytical community set the foundation, application in molecular biology, biodefence sensors, and microelectronics provided the momentum.[123] With the largest impact on the area of separation science, microfluidic technologies and more specifically capillary electrophoresis (CE) systems enabled high resolution separations with speed suitable for high throughput analysis. For molecular biology, nucleic acid analysis techniques such as PCR and genomic sequencing methods were well suited to miniaturization.[124, 125] The US department of defense also stimulated the growth of the field into the chemical and biosensor field to provide on-demand sensors for transduction of chemical and biological warfare agents. The success of photolithographic techniques in microchip fabrication immediately translated to microfabrication of fluidic systems based on glass or silicon based materials.[123] Currently soft lithography techniques have dominated the device fabrication and are discussed in Section 1.5.1. Nonetheless photolithographic techniques are still required for microfluidic master fabrications used in soft lithography.

Microfluidic systems can be classified under three different fluid handling methods – channel, droplet, and digital microfluidics. The naming system identifies the way the fluids are manipulated, while the former two are conducted in channels as the name suggests, fluid streams are continuous and in droplet form[126], respectively. However droplet fluid handling bridges into the third type of microfluidic technology which involves manipulation of microliter droplets on a Teflon surface with sequential patterned electrodes.[127, 128] Application of voltages to the microelectrodes enables droplet movement over the dielectric.[129] All types of fluidic systems are advantageous from the stand point of LOC bioanalyses. Microfluidic systems are attractive since they are low cost, portable, require reduced sample and reagent volumes, are amenable to POC diagnostics, and offer faster reaction kinetics. Furthermore, each specific classification has additional advantages, channel-based systems offer laminar flow and under electrokinetic control, plug based sample dispensing is possible.[123] For droplet-based flow, rapid kinetics are afforded in each droplet "reactor" and pneumatic assisted methods for droplet splitting and fusion offer greater sample manipulation.[126] For digital microfluidics, electrowetting-on-dielectric (EWOD) droplet manipulation offers complete automation and full realization of the LOC concept.[129] All fluidic handling methods have found great utility as platforms for bioassays and biosensors. The interest in fluidic platforms for bioanalysis is exemplified by the continuous emergence of LOC biosensors and bioassays in the literature for the transduction of peptides,[130] nucleic acids,[131-133] small molecule toxins,[134, 135] bacteria species,[136] cancer cells,[137] and protein markers.[138, 139] Moreover, chip based platforms are amenable to optical,[137] electrochemical,[140] and piezoelectric[141] transduction methods offering greater versatility to biosensor design. Although some challenges with optical based transduction are the requirement for excitation and detection hardware along with band sorting filters or monochromators, recent advances in integrating waveguides on-chip have facilitated optical detection in LOC bioassays.[142] In recent work, paper based fluidic systems have also become attractive from the standpoint of cost, ease-of-use and the use of active wicking of materials to avoid the requirement of external pumps or power supplies.[143] The impact of chip based diagnostics have been highlighted in recent reviews,[144, 145] although the advances of microfluidics into many diverse fields owes much tribute to the robust prototyping offered by soft lithography methods.

1.5.1 Soft Lithography for Rapid Device Prototyping

Much of the early foundations of microfluidics utilized the well-established methods of photolithography, where chips were fabricated entirely of silicon or glass. While these chips are robust and are fabricated with excellent precision, the cost of fabrication along with the need for a cleanroom facility limits the throughput of prototype fabrication.[146] Furthermore, for many diagnostic assays, reusability may not be possible which further increases costs. Polymer prototypes alleviate these issues as they are casted by molding or embossing techniques rather than etching protocols with highly reactive and toxic solutions such as hydrofluoric acid. The only disadvantage of these materials is the limited applicable solvents for compatibility while channels comprised of glass can tolerate most organic solvents.[147] However, the impact of this challenge is minimized for bioanalytical applications which mainly require aqueous buffer solutions. A multitude of suitable polymer materials exist for device fabrication, these include: polyurethanes, polyphenol-formaldehydes, polyimides, and siloxane rubbers.[148] Perhaps the most commonly used material is poly(dimethylsiloxane) (PDMS).[149] The interest in this material arises from the many advantages it can offer that enable use of PDMS microfluidic devices for a variety of applications.[147] First and foremost, PDMS can replicate molds with micrometer precision and this is an ideal characteristic for microfabrication. PDMS cures at temperatures of *ca.* 100 ºC, is optically transparent well into the short UV wavelength range (280 nm), is biocompatible, non-toxic and can be used to culture cells, and the crosslinked form affords a reversible deformable modulus that is easily lifted from the template design. While the cured polymer is hydrophobic in nature, it is easily rendered hydrophilic through oxidation either by treatment with extremely alkaline solution or by oxygen/air plasma oxidation. This amphiphilic control of surface patterning enables either reversible or irreversible sealing with hydrophobic or hydrophilic planar surfaces, respectively. The elastomeric nature of PDMS also enables it conform to smooth surfaces.[147]

The chemistry of PDMS has been extensively characterized and developed to enable facile fabrication of polymer molds. PDMS is readily available commercially from Dow Corning and is supplied as a two component kit. A prepolymer elastomer and curing agent are combined in a 10:1 ratio and mixed vigorously to initiate crosslinking of the elastomer. Crosslinking proceeds via a Pt^0 catalyzed hydrosilylation reaction to build the carbon-silicon framework of the cured PDMS. The elastomer is supplied as a vinyl-terminated siloxane monomer while the curing agent

contains a Pt^0 complex mixed in with copolymers of a mixture of siloxanes, but importantly hydrosiloxanes.[148] Initial reports of Pt^0 catalyzed hydrosilylation utilized cyclic olefin-Pt complexes that proceeded through formation of Pt colloids to afford siloxane polymer growth.[150] Refining of the ligands of the Pt catalyst have afforded cross-couplings that avoid formation of colloidal Pt in hydrosilylation reactions.[151] Nonetheless, both reported methods offer efficient, high yield, hydrosilylation at room temperature. The mechanism first requires coordination of the olefin to the Pt center along with the hydrosiloxane. Formation of the new Si-C bond at the Pt center generates H_2 where cessation of this evolved gas offers a qualitative indication that the reaction is complete. If left at room temperature the solution will naturally cure on after a few hours. Pouring of the mixture on a template and baking at 100 ºC offers formation of cured PDMS stamps within 20 min that are ready for device assembly. Soft lithography techniques all require microfluidic master molds that are fabricated using traditional photolithographic techniques in clean room facilities. These templates are fabricated using photocurable epoxy materials (SU-8-5) that are spin coated on planar glass slides at micron thicknesses.[147] Photomasks with microchannel designs enable generation of positive photo reliefs after film development. The use of computer aided design (CAD) programs can produce high quality photomasks with micron resolution that enable the user to draft any microchannel template.[147] CAD programs for photomask design and photolithographic techniques are a convenient approach to robust microfluidic masters that can offer reproducible PDMS stamps for months at a time. More recently, advances in 3D-printer technology have afforded the development on fully functional microfluidic systems and offer a more convenient approach to in-house template and microfluidic master design.[152, 153]

1.5.2 Fluid Dynamics in Microchannels

In addition to the advantages microfluidic systems provide as platforms for bioassays and biosensors, fluid dynamics in channel offer interesting phenomena such as laminar flow.[123] The two common fluid driving forces are hydrodynamic and electrokinetic methods. The former is characterized by parabolic shape flow.[154] The latter offers flat “plug” like fluid profiles and is described in detail in section 1.5.3. In both forms of solution transport, microfluidic phenomena exist and are often characterized by dimensionless numbers used to describe fluid flow.[155] Two of the fundamental parameters in describing fluid dynamics are the density (ρ) and shear viscosity (η) or resistance to flow. The dimensionless Reynolds number (Re) which is defined as

the ratio of inertial to viscous forces is used to describe fluid flow in microchannels. The Reynolds number is given by Eqn. 28 where U_0 and L_0 are the fluid velocity and a length scale of force density, respectively.[155]

$$Re = \frac{\rho U_0 L_0}{\eta} \tag{28}$$

For a Newtonian fluid, its flow velocity is governed by Navier-Stokes theory; derivations can be found elsewhere. In microfluidics the Reynolds number is low and often below 10, inertial forces negligible and viscous forces dominant the flow profile. At low Reynolds number, the nonlinear component of the Navier-Stokes equation can be ignored and the fluid velocity is described by Stokes flow. In this description, the fluid flow is *laminar* and flows linearly throughout the microchannel with no turbulence. Inertial forces become significant when the Reynolds number exceeds 2000 and turbulent flow results.[155] In laminar flow, delivery of solution and more importantly analyte to areas perpendicular to the plane of flow is dominated by diffusional mass transport. Diffusion is the major driving force of mixing in laminar flow regimes and the relationship between convection and diffusion is described by the Peclet number as shown by Eqn. 29, where w is the width of the channel and D is the diffusivity of the molecule.[155]

$$Pe = \frac{U_0 w}{D}$$

The Peclet number is also dimensionless and can be understood by considering a T-shape microchannel junction where two independent fluid streams meet at the junction point. The Peclet number describes effectively the number of channel widths required for the two solutions to completely mix. The desired fluid dynamics in microchannels are ultimately application based where laminar and turbulent flows have each found specific niches.[155, 156]

1.5.3 Electrokinetic Phenomena

Alternate fluid driving forces in microchannels include electrokinetic flow, which is defined as the coupling of electric current and fluid dynamics in a solution containing electrolyte.[157] Requirements for electrokinetic fluid transport include a charged interface, since it is the electrical double layer (EDL) and more importantly the Debye layer that is responsible for driving fluid flow and an electrolyte solution. Since the microfluidic channels introduced thus far

have been most commonly comprised of silicon or siloxane materials, discussion of electrokinetic phenomena will be in reference to these surfaces. At a channel surface composed of glass or oxidized PDMS, silanols exist along the interface. The pKa of a silanol is *ca.* 4 and thus as described by the Henderson-Hasselbalch equation, solutions of pH of 5 and higher result in > 95% of the silanols ionized. This renders the entire channel interface with a dominant net negative charge. In the presence of buffer or electrolyte solutions containing NaCl or KCl the negatively charged surface is negated by positively charged Na^+ or K^+ counter ions as shown in Figure 10 and the outside boundary of these ions is known as the outer Helmholtz plane (OHP).[158] The layer of adsorbed ions is also known as the *Stern layer*, and while the solution in the channel is electrically neutral, a charge density profile exists at the interface which decays exponentially until the neutrality of "bulk" solution. This *diffuse layer* is the second component of the EDL where the charge amplitude of both components of the EDL is identical to that of the surface but of opposite polarity. The length of the diffuse layer varies with an inverse square root dependence on the concentration of electrolyte and typically extends *ca.* 1-100 nm from the surface depending on the ionic strength.[157] The compact layer as the name suggests is not mobile, although has been postulated to have lateral movement away from the surface.[158] It is the diffuse layer that is responsible for electrokinetic flow. As an electric field is applied across the channel filled with conductive liquid a current is established although the solution remains neutral. There is a potential (Ψ) that extends from the OHP through the diffuse layer, and the ions in this layer are mobile. For a negatively charged surface, a net force drives the cations toward the cathode (negative electrode) and creates a plane of shear at the interface. The movement of these ions in the diffuse layer "drags" the bulk solution in the channel along with it, the net movement of the fluid is known as *electroosmotic flow* (EOF).

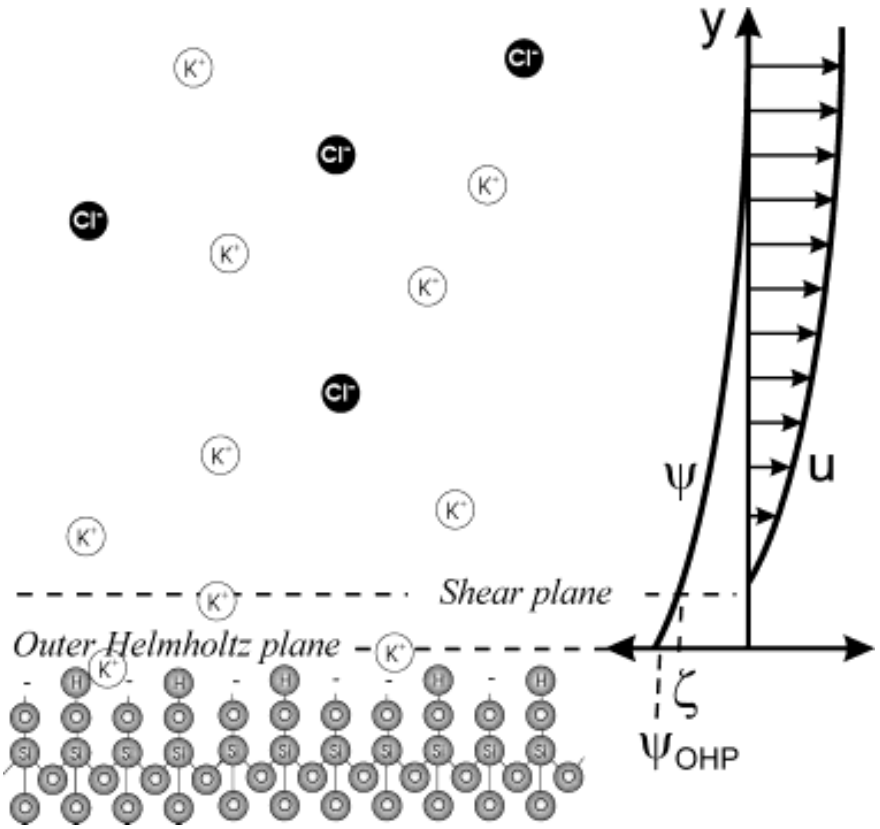

Figure 10. Formation of the EDL at a silanol interface and the origin of electroosmotic flow. A layer of potassium cations known as the Stern layer bounded by the outer Helmholtz plane (OHP) is electrostatically attracted to the net negatively charged silica surface. The diffuse layer is comprised of predominantly potassium ions with some chloride counter ion creating a local potential (Ψ) that decays exponentially from the surface. Application of a potential across the microchannel causes a net force that drives the cations in the diffuse layer toward the cathode where the movement of the diffuse layer creates a plane of shear. The diffuse layer causes the entire solution to move throughout the microchannel, this is known as electroosmotic flow (EOF) and the velocity (u) increases from the surface until the edge of the diffuse layer. The zeta potential (ζ) is defined as the charge from the surface at the shear plane. Reproduced with permission from ref.[158]. Copyright 2004 WILEY-VCH Verlag GmbH & Co.

The EOF velocity (u) increases from the surface to the edge of the diffuse layer, where the charge at the plane of shear is known as the zeta potential (ζ). The EOF velocity at an applied external electric field (E) is given by the Smoluchowski equation (Eqn. 30), where ε and ε_0 are the relative dielectric constant and the permittivity of vacuum respectively and μ is solution viscosity.[159]

$$u = \frac{\varepsilon\varepsilon_0\zeta}{\mu}E \tag{30}$$

The EOF velocity is directly proportional to the applied field strength and the zeta potential. While the former can be controlled using a power supply, the latter is influenced by both the pH and ionic strength and is described in detail elsewhere.[158] Since the zeta potential of the interface

is directly a combination of the degree of ionization and the abundance of electrolyte, an intricate balance is required. A high enough pH facilities suitable surface silanol ionization and sufficient electrolyte provides conductivity and a diffuse layer. At low ionic strength, the solution is poorly conductive, and at high electrolyte concentrations the surface charge is significantly screened and there is increased local Joule heating of the fluid in the presence of an applied field. Since the fluid adjacent to the interface is responsible for the net force that drives fluid movement, the fluid front appears as a flat profile in comparison to the parabolic flow dynamics in hydrodynamic flow. This characteristic of EOF has enabled higher resolution separations by minimizing band overlap. Moreover stacking of bands in channel has afforded high sensitivity using fluorimetric detectors.[160, 161] The relative size of the EDL in comparison to the channel dimensions can be perceived as the thickness of a layer of paint on the walls of a rectangular room. Because of this contrast, the fluid appears to "slip" along the channel surface as the EOF velocity at the interface is effectively zero.[157] Furthermore, it is important to note that the zeta potential at the channel interface is independent of the channel dimensions and thus reproducible experimental methods for determining the zeta potential can be applied to many microfluidic systems. One such method involves monitoring the slope of the current-time relationship in EOF and the resultant modified form of the Smoluchowski equation.[159] A capillary or microchannel along with one inlet reservoir is filled with a buffer solution of known ionic strength. A second buffer of slightly higher ionic strength *ca*. 5 % is placed in the opposite reservoir and a potential is applied across the channel. EOF will carry the higher ionic strength buffer into the channel and the current will increase until the entire channel is equilibrated with buffer and then will remain constant. Since the difference in ionic strength between buffers is small, the slope is linear. The slope of the current-time (m_{IT}) relationship can be related to the average EOF velocity and the zeta potential of the microchannel as shown by Eqn. 31.[159]

$$\zeta = \frac{\mu m_{IT} L}{\varepsilon \varepsilon_0 E^2 A_{cross} (\lambda_{b2} - \lambda_{b1})} \tag{31}$$

In Eqn. 31, L is the length of the microchannel and A_{cross} is the cross-sectional area. The difference in bulk conductivity between the higher ionic strength buffer and that of the lower is given by λ_{b2} - λ_{b2}. This method offers higher accuracy as it avoids ambiguity introduced in determining exactly when buffer is displaced in the microchannel.[159]

In electrokinetics, EOF is not the only driving force for analyte migration in capillaries or microchannels. Charged analytes also experience an acting electrophoretic force (EPF) attracting them to oppositely charged electrodes. The migration velocity (v) for a charged analyte is given by Eqn. 32, where μ_e is the characteristic electrophoretic mobility and is indirectly proportional to frictional forces and directly proportional to the charge of the analyte.[27]

$$v = \mu_e E \tag{32}$$

EPF and EOF may act cooperatively or oppositely, and the resultant net mobility is a combination of these processes. Treatment of a channel wall with NaOH and plasma oxidation can provide for high EOF velocity where all analytes and bulk solution travel via EOF. Alternatively, conditions can be selected to have weak EOF, and then EPF and EOF can allow for movement of analytes across the microchannel in different directions. For cathodic EOF using negatively charged surfaces of microchannels, positively charged analytes may have increased mobility as EOF and EPF vectors are aligned. On the contrary, for negatively charged analytes the EPF migration opposes the direction of EOF. Surface derivatization methods including silane chemistry and photo mediated modifications[162, 163] can pattern the surface with positively charged functional groups such as amines and reverse the direction of EOF toward the anodic reservoir. Alternative methods for EOF manipulation include dynamic coating with charged polymers. Polybrene is one example of a positively charged polymer and can be added to buffers in small percentages to reverse the direction of EOF without the need for surface modification in the microchannel.[164] In CE applications EOF is often unfavorable as analyte separation is facilitated by charge or differences in frictional forces.[27] Methods to eliminate EOF *in situ* are similar to those that reverse direction. Neutral surfactant polymers such as poly(vinylpyrrolidone) (PVP) can be incorporated as 1% v/v additives to buffers to dynamically coat the walls of the microchannel. Since this prevents formation of the EDL, EOF is suppressed to insignificant levels.[165]

1.6 Contributions of this Thesis

This thesis is organized into a total of six chapters including this introductory chapter and a conclusion. The research contributions are organized over four chapters in the order in which the studies were conducted. The foundation of this work was built by earlier members of Krull's team. In particular the contributions from Erickson and Krull[166, 167] in the advantages offered by

miniaturization of nucleic acid hybridization assays in an electrokinetically controlled biochip and the pioneering work by Algar and Krull[168] in the development of the QD-FRET mechanism to transduce nucleic acid hybridization.

Earlier work by Erickson et al. explored the utility of microfluidics as an assay platform for nucleic acid hybridization assays. The design incorporated immobilized oligonucleotide probes on fused silica substrates that had been modified with 3-glycidoxypropyl trimethoxysilane (GOPS) to facilitate coupling of amine terminated probes. The probe nucleic acids were grafted on to the surface in defined regions or pads in a separate immobilization step prior to chip assembly. Microfluidic channels comprised of PDMS were aligned over the pad locations on the glass slides during chip assembly. Electrokinetic injection of dye labeled target oligonucleotides resulted in hybridization with the interfacial probe nucleic acids. Line scans along the channel provided fluorescent signals from locations where hybridization occurred. Hybridization kinetics were on the order of minutes as provided by the efficient mass transport of target to the glass interface. It was noted that probe pads adjacent to the inlet reservoir initially became saturated with targets prior to subsequent hybridization with probe sites down-stream. This observation suggested that the length of channel that was covered with hybrids could be used to quantify the amount of nucleic acid present in a given sample. Analysis was performed by integrating the area under a fluorescence profile to quantitatively assess oligonucleotide samples. This was the first indication that *spatial profiles* may offer a new strategy for quantification. Moreover, the electrokinetically controlled assay platform offered significant advantages for SNP discrimination without the need for added denaturants or chaotropic agents. Control of the applied electric field strength was shown to provide a method to increase stringency conditions for interfacial hybridization, and higher voltages were used to selectively destabilize a SNP hybrid while a FC hybrid remained. The stringency control resulted from the combination of a continuous applied EPF on the DNA and contributions from Joule heating as a result of use of a high ionic strength buffer. The effectiveness of this platform toward rapid and selective nucleic acid analysis motivated the further development of microfluidic assays for the QD-FRET transduction pioneered by Krull's team.

Algar and Krull were one of the first groups to develop QD-FRET assays for the detection of nucleic acids. In their earliest work, multiplexing was demonstrated using probe oligonucleotides that were conjugated to green- and red-emitting thioalkyl acid-coated CdSe/ZnS QDs.[169] The

modified QDs were then hybridized with Cy3 and Alexa Fluor 647 labeled target oligonucleotides, such that each dye formed a FRET pair with the green and red QDs, respectively. Hybridization at the surface of the QD provided the proximity for FRET, and sensitized acceptor emission was used to transduce nucleic acid hybridization. While multiplexed and sensitive transduction of nucleic acids was possible with nanomolar detection limits, nonspecific adsorption and the need to maintain colloidal stability were some of the drawbacks of solution-based assays. The desire to overcome these challenges motivated development of solid-phase hybridization assays where QDs were immobilized on glass beads and optical fibers.[168, 170-172] In this format, multiplexed transduction was extended to the concurrent detection of up to four targets with high selectivity using a combination of FRET and direct excitation of fluorescence.[173] The methods were ensemble compatible and did not require spatial registration, sorting or multiple excitation sources—advantages that are highly amenable to miniaturization.

While the excellent research provided by earlier members of Krull's team outlined the foundation for this work, this thesis presents a new contribution to the field of bioanalytical chemistry in the area of bioassays and biosensors. Moreover, the investigation of semiconductor QDs has offered new insights into the effect of different sized QDs on biomolecular interactions. The novelty of this work is highlighted by the spatial transduction strategy used to quantify the amount of nucleic acid present in a sample. The microfluidic assay platform has proven advantageous in comparison to previous solid-phase assay formats due to the combination of the fluidic control and the spatially based quantitative measurement strategy. These concepts are explored in Chapters 2, 3, and 5. Chapter 4 investigates interfacial nucleic acid hybridization on QDs in bulk solution format.

In Chapter 2, the framework for this thesis was built as the two most integral components to a biosensor were realized: a selective biorecognition element and a novel transduction mechanism. Although it can be argued that from a fundamental standpoint that the inherent selectivity of nucleic acid hybridization and the FRET based detection strategy comprise these two concepts, these alone were insufficient to realize the full potential of the assay. While hybridization is a highly selective biomolecular interaction, the nature of the channel surface and more importantly the QD surface has been shown to be susceptible to nonspecific adsorption of nucleic acids and proteins. For analysis of labelled oligonucleotide targets and even for unlabeled target using sandwich assay formats, this can lead to the generation of false positives. The effects of

adsorption can be ameliorated by careful selection of the QD surface ligand or by additional passivation. For solid-phase assays, diminishing adsorption must be considered alongside finding suitable immobilization chemistry to build the selective biorecognition element. Earlier work that aimed at minimizing nucleic acid adsorption utilized a passively adsorbed layer of SAv.[170] Biotinylated oligonucleotide probes were subsequently conjugated to the interface. SAv-biotin interaction is one of the strongest non-covalent bonds with a dissociation constant on the order of 10^{-15} M^{-1}. This immobilization strategy simplified the in-channel interfacial assembly as this interaction could both immobilize QDs and offer subsequent conjugation of probe oligonucleotides. The constant EOF and EPF in-channel necessitate strong interfacial bonding to achieve physical stability of the immobilized QDs and probes. Preliminary work using MPA coated QDs and tetradentate thiolated ligands displayed poor stability on-chip and the QD surface was prone to nonselective adsorption. In addition to finding a suitable interfacial chemistry, Chapter 2 also explores the utility of the chip platform in a novel spatial detection strategy. This quantitative transduction strategy was realized due to the nature of the assay; the interfacial recognition chemistry was built throughout the entire channel length as opposed to defined regions as reported by Erickson et al. Thus, in order to realize the full potential of the assay it was necessary to find a suitable method to quantify the total amount of nucleic acid transduced at the interface. This was also necessary since different nucleic acid concentrations had similar FRET ratios from the channels which signified that mass transport to the interface first saturated immobilized probe adjacent to the inlet prior to delivery of target to subsequent probe sites. It was postulated that an integrated measurement of PL from the entire channel would enable quantitative analysis, but this would require a more sophisticated analysis method and rather a simple *length* measurement. In Chapter 2, assay selectivity is also considered and it is shown that resolution of a target sequence containing a 3BPM was possible. Furthermore, the assay also displayed resistance to nonselective adsorption as transduction was possible in matrices containing a 5-fold excess of similar noncomplementary oligonucleotide sequences.

Chapter 3 illustrates one significant advantage of using QDs; *multiplexing*. QDs are advantageous for multiplexed analysis as a single excitation wavelength can be used to excite multiple colours of QDs as the absorption spectrum is broad and the Stokes shifts are on the order of 100 nm. Moreover, the size-tunable symmetric emission enables facile pairing with dye acceptors. The on-chip assay format displayed improvements in multiplexed analysis by

overcoming issues associated with donor dilution effects that reduced assay sensitivity. This results from the method of assembly of a mixture of probes onto a mixture of QDs. The same chemistry for immobilization is used to functionalize different QDs with different probe nucleic acids. There is no control over which probe is immobilized on a mixture of different QDs. This results in numerous mismatches where the spectral overlap is not suitable for FRET. Where more different oligonucleotide sequences are concurrently used there is more of this dilution effect. When analyzing a FRET ratio, this reduces sensitivity by limiting the number of pathways to permit energy transfer. In spatially based quantification, the sensitivity actually increases, as multiple probes dilute the density of a given probe in comparison to single colour measurements. Thus a given spatial profile for a specific quantity of nucleic acid *ca.* will be physically extended in a multiplexed format. Thus, similar detection limits to single-colour assays were realized even from a multiplexed system. Concurrent transduction of tens of femtomole amounts of two targets was demonstrated and the assay also retained excellent selectivity.

In Chapter 4, nucleic acid hybridization at the interface of two differently sized QDs is investigated through a series of steady state and time-resolved PL measurements. Although Chapter 4 considers analysis of assay formats outside of the theme of microfluidics, the work was integral to this thesis as it provided a fundamental understanding of QD-FRET using commercial SAv-QDs. Despite the large size hydrodynamic radius of both the gQD and rQD, energy transfer efficiencies reaching *ca.* 80% were possible for both the gQD-Cy3 and rQD-A647 FRET pairs even though donor-acceptor distances were estimated to be between 9-12 nm. The enhancement in FRET efficiency was a result of the ability to deposit *ca.* 50 and 70 Cy3 and A647 acceptors on the gQD and rQD, respectively. Differences in assay selectivity using an oligonucleotide duplex demonstrated that the QD interface, and specifically the effective charge of each QD-probe conjugate, influenced assay selectivity. SNP resolution was possible when the assay utilized rQDs and could be achieved without any added denaturant. On the contrary, no discrimination of SNPs was possible using the gQDs. Chapter 4 provides fundamental insights into the effects of differently sized nanocrystals toward interfacial DNA hybridization. These results were utilized in optimization of the in-channel assay to move towards SNP discrimination.

Chapter 5 builds on the results obtained in Chapter 4 for implementation in the microfluidic assay format. Given the higher selectivity at the rQD interface toward SNP discrimination,

assembly of the on-chip assay made use of rQDs. SNP resolution was possible with contrast ratios exceeding two-orders of magnitude. Moreover, less formamide was required to melt the SNP duplex on-chip due to the higher stringency of hybridization in the presence of an applied electric field. Assay regeneration was also possible enabling three cycles of transduction prior to degradation of the interfacial chemistry. Chapter 5 also explores the applicability of the on-chip assay for analyses of real nucleic acid samples as might be encountered in clinical or pathogen analysis. The work presented in Chapters 2-4 considered transduction of short, dye labeled nucleic acid targets. Although such analytes are integral to assay development and optimization, these oligonucleotides are not representative of real-world samples. Most nucleic acid targets of interest such as mRNA or genomic DNA are often greater than *ca*. 100 bases in length. Many ensemble assays including the one described herein, require amplification steps prior to transduction and target strands are not intrinsically labeled with fluorescent dye. To demonstrate application of the solid-phase QD-FRET assay to real sample analysis, a sandwich assay approach was implemented in-channel. Short nucleic acid probes were first hybridized to a longer nucleic acid target generating a duplex with an overhang. A reporter oligonucleotide tagged with A647 subsequently hybridized with the overhang enabling FRET from the immobilized QD. Despite the larger donor-acceptor distance, the spatial measurement demonstrated no loss in sensitivity or detection limits. This can be understood by considering that even a weak FRET signal above background can be translated to a spatial measurement. Furthermore, the lower hybridization efficiency of the longer targets to the short immobilized probes resulted in longer spatial profiles, resulting in the improvement of sensitivity. SNP discrimination was also possible in this format, and was achieved in assays done using complex matrices consisting of a large excess of salmon sperm DNA and BSA. Integration of highly efficient isothermal amplification methods with the on-chip transduction is demonstrated in Chapter 5 and may ultimately provide a robust, POC assay platform for on-demand nucleic acid diagnostics.

2 On-Chip Transduction of Nucleic Acid Hybridization Using Spatial Profiles of Immobilized Quantum Dots and Fluorescence Resonance Energy Transfer

The results and data presented herein have been published and can be found in the citation below. The interfacial assay chemistry and chip-based assembly was designed and optimized by AJT. Solution based FRET experiments and initial selectivity experiments were designed, analyzed and interpreted by AJT. MON's expertise in microfluidics enabled outstanding contribution to design, interpretation and analysis in quantitative hybridization experiments. MON also contributed toward optimization of conditions for 3BPM selectivity along with interpretation of the data. CHV is thanked for collecting data in complex matrices and WRA's contributions to quantitative data analysis in spatial based transduction and FRET modelling were invaluable.

> Tavares, A.J.; Noor, M.O.; Vannoy, C.H.; Algar, W.R.; Krull, U.J., *Anal. Chem.* **2011**, 84, 312-319.

2.1 Introduction

The success of solid-phase QD-FRET assays on glass beads and optical fibers motivated efforts toward miniaturization of such assays into an electrokinetically controlled microfluidic chip. Fast reaction kinetics, minimal reagent consumption, robustness, and portability are some of the advantages microfluidics offers towards bioanalysis. Given that the QD-FRET transduction mechanism for nucleic acid hybridization was amenable to miniaturization, this offered ease of integration of assays with the chip based format. The initial challenge was finding a suitable immobilization chemistry to offer a selective and stable interfacial recognition element in the presence of EOF and EPF.

In Chapter 2, a solid-phase strategy for the transduction of nucleic acid hybridization using immobilized QDs and FRET in an electrokinetically controlled microfluidic chip is described. A schematic of the design is displayed in Figure 11. Commercial streptavidin coated green-emitting CdSe/ZnS QDs (peak PL *ca.* 525 nm) were delivered into microfluidic channels by electroosmotic flow (EOF). The glass surface of a glass-polydimethylsiloxane (PDMS) microfluidic chip was derivatized with biotin for immobilization of QDs by the streptavidin-

biotin interaction. Further bioconjugation of the immobilized QDs was accomplished through electrophoretic deposition of biotinylated probe oligonucleotides. Hybridization with Cy3 labeled target nucleic acid generated FRET sensitized Cy3 acceptor emission upon excitation of the immobilized QD-probe conjugates (Figure 11).

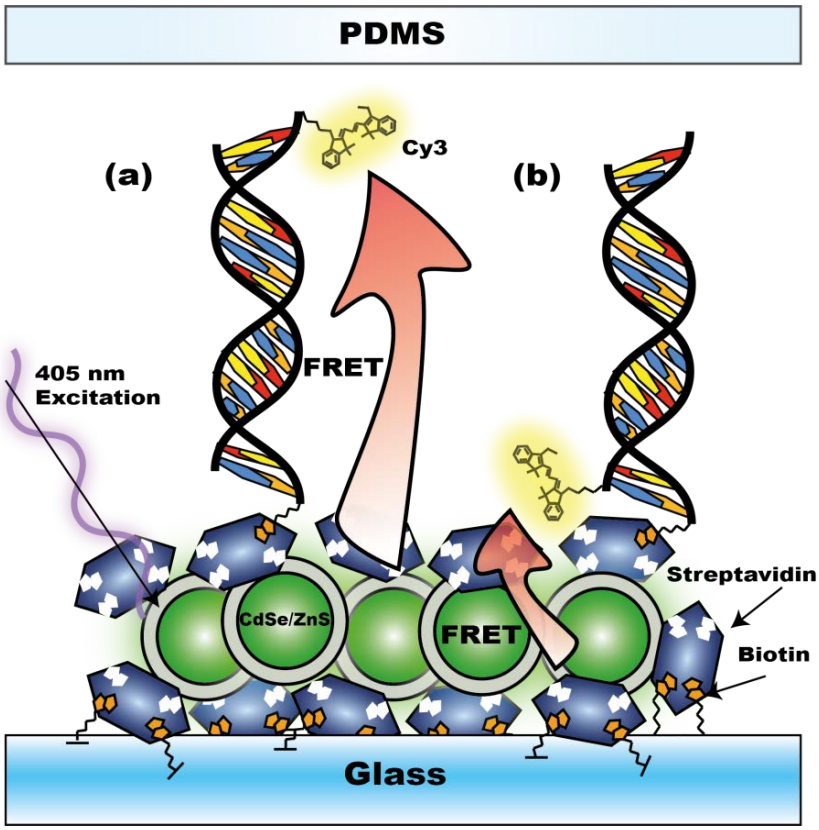

Figure 11. Cross-section of a microfluidic channel as part of an assay for the transduction of nucleic acid hybridization using FRET. Streptavidin conjugated CdSe/ZnS QDs are immobilized on a biotin derivatized glass surface, and are conjugated with biotinylated probe oligonucleotides. Hybridization with either (a) distal 5' or (b) proximal 3' Cy3 labeled target provides the necessary distance for energy transfer, and yields FRET sensitized Cy3 emission upon excitation by a 406 nm laser.

The function of the QD-oligonucleotide-Cy3 FRET pairs was characterized using bulk solution measurements. The in-channel, dynamic transduction of femtomole levels of nucleic acid was possible, and could be achieved within minutes rather than hours, as typically required in previous assay designs. This can be attributed to the increased hybridization kinetics offered by the microfluidic assay format. This rapidity provides the potential for on-demand assay assembly. Moreover, the increased mass transport of oligonucleotide targets to the in-channel QD interface enabled the quantitative transduction of target nucleic acid by measuring the length of the microfluidic channel that exhibited FRET sensitized Cy3 PL. This novel, spatial method of

concentration analysis is in contrast to virtually all other QD and FRET methods, which rely solely on PL intensities for quantification.

2.2 Experimental Section

Detailed experimental procedures, materials and reagents, buffers, and a description of the instrumentation used are given in Appendix 1.

2.2.1 Preparation of QD-Probe Conjugates and Solution Hybridization Experiments.

Oligonucleotide sequences used in the assay are listed in Table 2. The SMN1 sequence is diagnostic of spinal muscular atrophy. Streptavidin (SAv) coated QDs (SAv-QDs) were mixed with a 10-fold excess of biotinylated SMN1 probe in tris-borate (TB) buffer, agitated using a vortex mixer, and placed on a shaker for 2-3 h. The SAv-QD-probe conjugates were purified from excess oligonucleotides by centrifugation twice using an Amicon Ultra-0.5, Ultracel-50 Membrane, 50 kDa centrifugal filter (Millipore Corporation, Billerica, MA) at 8000 RPM. These were then resuspended in TB buffer. Purified SAv-QD-probe conjugates were mixed with fully complementary target oligonucleotides labeled with Cy3 at either the 3’ or 5’ end, which are referred to throughout the text as FC-P TGT (i.e., proximal) and FC-D TGT (distal), respectively. The solutions were agitated using a vortex mixer and placed on a shaker for 24 h; the final concentration of QDs in the hybridization samples was 50 nM. The PL of the samples was measured at both 12 and 24 h, and no changes in FRET intensities were visible after 12 h within experimental precision. For all steady-state measurements, the samples were excited at 406 nm and the resulting PL was scanned from 450 - 700 nm.

Table 2. Oligonucleotide sequences

SMN1 Probe	BiotinC6 - 5’ - ATT TTG TCT GAA ACC CTG T - 3’
FC-P TGT	Cy3 - 3’ - TAA AAC AGA CTT TGG GAC A - 5’
FC-D TGT	3’ - TAA AAC AGA CTT TGG GAC A - 5’ - Cy3
NC TGT	Cy3 - 3’ - TGT CCC AAA GTC TGT TTT A - 5’
3BPM TGT	3’ - TGA AAC AGG CTT TGG GAT A - 5’
CM 1	3’ - GTA GAC AAA TGG CCC GTA T - 5’ - $C_{12}H_{24}NH_2$
CM 2	3’ - TTT CTT TAG TAC CTT CAT TC - 5’ - $C_{12}H_{24}NH_2$

TGT = target; FC-P = fully complementary proximal; FC-D = fully complementary distal;
NC = non-complementary; BPM = base pair mismatch; CM = complex matrix; BiotinC6 = biotin conjugated via a six-carbon linker. Mismatches are bolded and underlined in the 3BPM sequence.

2.2.2 Microfluidic Chip Preparation and In-Channel Assembly of QD-Probe Conjugates.

Glass microscope slides or coverslips were etched using a two-step RCA cleaning protocol (successive treatment with strong base and acid, in the presence of peroxide, to yield surface silanol groups).[174] Silanol terminated slides were then derivatized with 3-aminopropyltrimethoxysilane (APTMS) and further coupled with biotin using a previously reported method.[175] Assembly of the PDMS-Glass microfluidic substrates was done using standard soft lithography techniques.[146] Cured PDMS substrates were oxidized in air plasma for 30 s at 10.5 W and then were physically sealed to the derivatized glass substrates by application of moderate pressure. Sealed channels were immediately filled with pH 9.25 borate buffer (BB). Preparation of in-channel selective chemistry (which comprised immobilized QD-probe oliognucleotide conjugates) and the introduction of samples containing target oligonucleotides were done in the stepwise manner described in Table 3. The applied field strength was fixed at 200 V cm^{-1}. Elevation of the field strength to, or beyond, 500 V cm^{-1} caused removal of QDs and probe conjugates from the channel. Preconditioning of the channels was necessary to ensure that

any adsorbed impurities were flushed from the channel interior and would not impede immobilization steps.[159, 176] Preconditioning also enabled equilibration of the pH inside the microchannel, prior to delivery of reagents. Prior to preconditioning, chips were examined under a microscope to confirm the absence of contaminants or debris that could block flow. After conditioning, a combination of (EOF) and electrophoretic force (EPF) was used to deliver reagents and assemble the immobilized QD-bioconjugates. The EOF velocity at 200 V cm^{-1} was determined to be *ca.* 5×10^{-2} $cm\cdot s^{-1}$ using the current monitoring method reported elsewhere.[176] Both the SAv-QDs and oligonucleotides had positive electrophoretic mobilities (see Appendix 1), and the delivery method reflected the process that dominated their net mobility.

Table 3. Assembly Steps for the Solid Phase Microfluidic Assay

Assembly Step	Concentration	Delivery Method	Incubation	Washing
Preconditioning	-	EOF/pH 9.25 BB 2 min	-	-
QD Immobilization	100 nM	EOF/pH 9.25 BB 20 min	5 min	5 min/pH 7.44 TB buffer
Probe Conjugation	3.0 µM	EPF/ pH 7.44 TB buffer 5 min	5 min	5 min/pH 7.44 TB buffer
Target Injection	0.25 – 2 µM	EPF/ pH 7.44 TB buffer 5 min*	5 min	2 min/pH 7.44 TB buffer*

*In 3BPM selectivity experiments, 20% formamide was added to the buffer composition.

2.2.3 On-Chip Hybridization Experiments.

Conditions for target delivery are listed in Table 3. Field strengths were maintained at 200 V cm^{-1}. In experiments that investigated the selective discrimination of FC and 3BPM targets, the targets oligonucleotides were in TB buffer containing 20% v/v formamide. In these cases, preconditioning of the channels was also done using 20% formamide in TB buffer.

For experiments that investigated the quantification of hybridization, both the applied field and injection time were kept constant, and each concentration was measured in triplicate. The length of a fluorescent region in a channel at any given concentration was measured from the edge of the inlet reservoir to the position where the FRET sensitized acceptor PL signal dropped below a threshold of 50% of the maximum Cy3 PL signal (alternative analyses are discussed later). To determine the amount of oligonucleotide target injected, the electrophoretic mobility of the target sequence was first calculated; Cy3 PL was monitored at a fixed point at the end of the microfluidic channel (initially only background signal), and the amount of time needed for the target sequence to travel the specified length (indicated by a sudden increase in signal) was recorded as a function of applied voltage. The net mobility of the FC-D TGT was determined to be 8.4×10^{-4} cm^2 V^{-1} min^{-1}. The electrophoretic mobility, concentration of the target, and the total time for injection was then used to estimate the amount of target oligonucleotide injected. The injection volume was estimated to be 19 nL for an injection time of 5 min under the applied field of 200 V cm^{-1}.

2.2.4 Data Analysis.

PL spectra from solution and on-chip experiments were background subtracted, normalized to the peak QD PL, and a FRET ratio was calculated for each spectrum. The details of these calculations can be found in the Appendix 1. Calculations of the spectral overlap integral and Förster distance are also described therein. Epifluorescence images were all background subtracted, false-colored, and the contrast optimized for viewing. These image processing steps were not applied to the raw numerical data that was extracted from the original images and used for quantitative analysis.

2.3 Results and Discussion

2.3.1 Solution Hybridization Experiments.

Prior to use in the proposed microfluidic assay format, the QD-Cy3 FRET pair was first characterized using steady state and time resolved PL measurements in bulk solution. The spectral overlap of the QD-Cy3 FRET pair was determined to be 3.03×10^{-10} mol^{-1} cm^6 (see Appendix 1, Eqns. A1.1-1.2, Figure A1.3), and this value is consistent with previously reported values for similar QD donors paired with Cy3.[169] The Förster distance was calculated to be 4.6 nm, which is *ca.* 1-1.5 nm larger than values we have previously reported for ligand-coated QD donors and Cy3 acceptor FRET pair.[169] This is ascribed to the larger quantum yield of the polymer coated QDs.[177]

In order to gain insight into sensitivity and selectivity, the FRET efficiency and resistance of the SAv-QDs to the nonspecific adsorption of nucleic acids was evaluated using solution based measurements. In previous studies, the nonspecific adsorption of nucleic acids on thioalkyl acid coated QDs was a prominent issue.[178] This was extensively characterized, and the phenomenon was found to be consistent with a process driven by hydrogen bonding between the nucleobases and neutral carboxylic acid groups associated with the QD surface coating.[178, 179] This issue was resolved by physisorption of a layer of NeutrAvidin and bovine serum albumin.[170] Given that the QDs used in this study were coated with SAv, it was expected that the adsorption of NC oligonucleotides should be minimal. However, this was not guaranteed since the SAv was coupled to the carboxylic acid groups of an underlying amphiphilic polymer coating on the QDs. Depending on the orientation and surface coverage of the protein on the QD, accessible carboxylic acid groups could potentially promote nonspecific adsorption. SAv-QDs were conjugated with nucleic acid probes and incubated with excesses of NC, FC-P, and FC-D TGTs labeled with Cy3. The resulting PL spectra (normalized to the QD emission) are displayed in Figure 12(a). No significant nonspecific adsorption of NC TGT was visible above the QD PL. This result was consistent with previous observations that a layer of avidin can passivate the QD surface.[93, 168] Quantitatively analyzing the data in Figure 12(a), the FRET ratios (see Eqn. A1.5) were 0.01, 0.1 and 0.49 for the NC, FC-D, and FC-P TGTs, respectively. Greater FRET efficiency was noted for hybridization of the FC-P TGT compared to the FC-D TGT. This was expected *a priori* since the probe sequence was conjugated to the SAv-QDs via a 5' biotinylated

linker. Therefore, the 3'Cy3 of the proximal target should, on average, have been closer to the QD than the 5'Cy3 of the distal target.

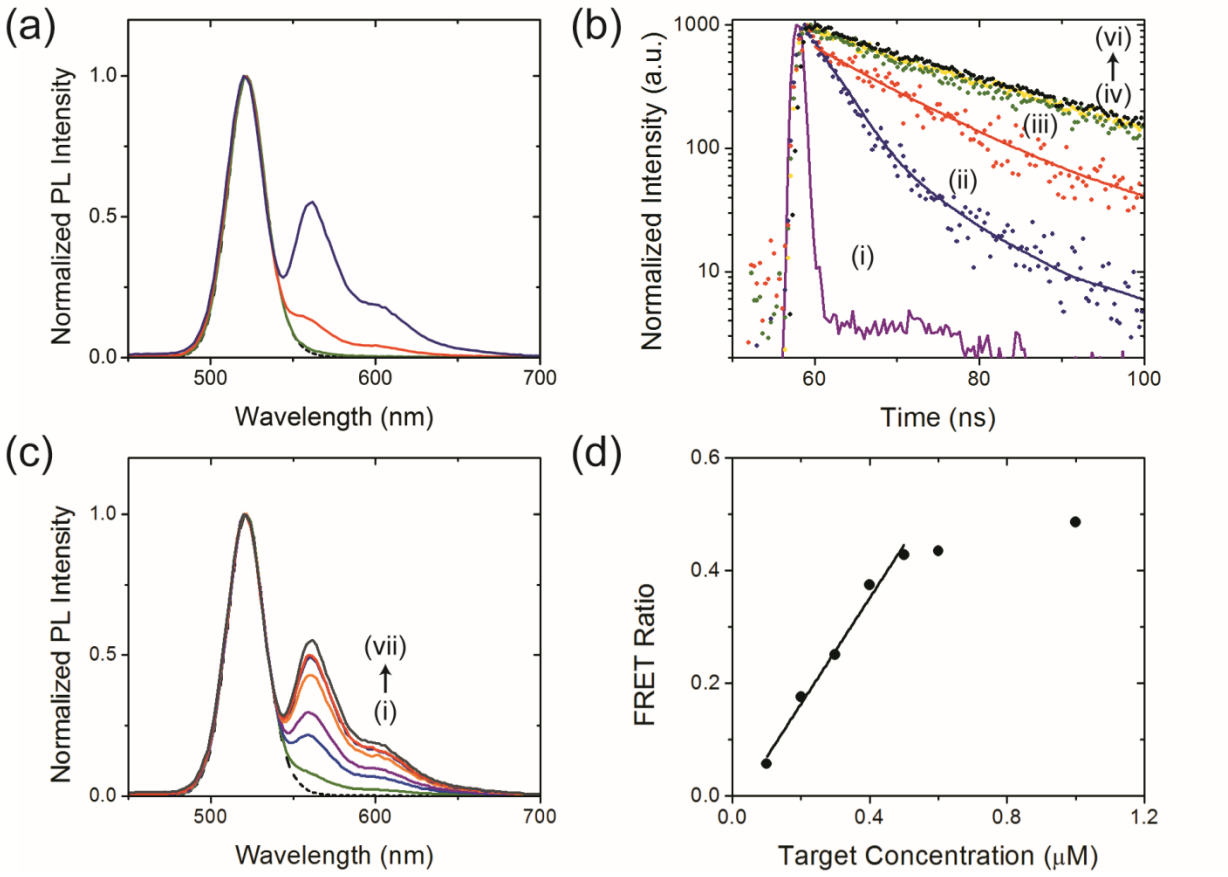

Figure 12. (a) Normalized solution-phase PL spectra for the response of the QD-probe conjugates (dashed black line) to 1 μM of NC TGT (green), FC-D TGT (red), and FC-P TGT (blue). (b) Normalized PL decay curves against the (i) instrument response function for: SAv-QD probe conjugates in the presence of 1 μM of (ii) FC-P TGT and (iii) FC-D TGT, (iv) NC TGT, (v) no TGT and (vi) only SAv-QDs. Curve fits for (ii) and (iii) are shown as solid colored lines. The concentration of QDs in all samples was 50 nM. (c) The response of the assay to (i) 100, (ii) 200, (iii) 300, (iv) 400, (v) 500, (vi) 600, and (vii) 1000 nM of proximal FC TGT. The dashed black line is the initial PL spectrum. The final concentration of QDs in all samples was 50 nM. (d) The FRET ratios corresponding to the PL spectra in (c), the relative standard deviation for each data point is ≤ 2%.

PL decay curves collected for SAv-QDs, SAv-QD-probe conjugates, and SAv-QD-probe conjugates after exposure to FC-P, FC-D and NC TGTs are shown in Figure 12(b). The lifetimes of SAv-QDs and SAv-QD-probe conjugates were determined to be 19.0 ± 0.8 and 17.3 ± 1.1 ns, respectively. The SAv-QD-probe conjugate lifetimes after exposure to NC, FC-D, and FC-P TGTs were 17.2 ± 2.3, 11.2 ± 2.9 and 3.8 ± 0.5 ns, respectively. Importantly, no changes in QD lifetime were observed within experimental precision upon conjugation with probe and exposure to NC TGT. This indicated that the amphiphilic polymer coating provided a barrier against the

influence of the local environment, and further confirmed that the SA offered excellent resistance to nonspecific adsorption. In contrast, significant changes in lifetime were visible after hybridization with the FC-D and FC-P TGTs. The corresponding FRET efficiencies were determined (using Eqn. A1.3) to be 35% and 78%, respectively. From Eqn. A1.4, these values correspond to average QD-Cy3 separation distances of 7.5 and 5.5 nm for the FC-D and FC-P TGTs, respectively. Two important insights can be gained from this data. First, the distinct difference in FRET efficiency between the distal and proximal FC TGTs is in contrast to the nearly identical efficiencies that were previously observed in systems prone to nonspecific adsorption.[170, 178] This further indicates strong resistance to nonspecific oligonucleotide adsorption, while also suggesting that the probe oligonucleotides adopted a conformation independent of the QD surface and were available for hybridization with target. Second, the difference in donor-acceptor separation distance between the distal and proximal FC TGTs was *ca.* 2 nm, which is significantly shorter than the 6.5 nm linear extension predicted for a 19-mer of double-stranded DNA in addition to the immobilized SAv and intrinsic nanocrystal size. This indicated that the probe/target hybrids did not extend radially from the QD surface, in agreement with previous observations reported for commercial SAv-QD-oligonucleotide conjugates.[180] Considering our data, a basic geometric model (Figure A1.5) suggested that the probe/target oligonucleotide duplexes had a time- and ensemble-averaged extension angle of about 100˚ to the normal to the QD surface.

The response of the SAv-QD-probe conjugates to an increasing quantity of proximal FC TGT is displayed in Figure 12(c-d), and demonstrates that the magnitude of FRET-sensitized Cy3 emission was suitable for quantitative detection. This was conveniently reduced to a FRET ratio that reflected the degree of QD quenching and sensitization of Cy3, without being dependent on the measurement of absolute PL intensities (*cf.* a FRET efficiency derived from only QD donor quenching). The FRET ratio was also analytically useful, exhibiting a linear response up until saturation at approximately 10 proximal FC TGTs added per QD. This value correlated well with the expected number of SAv proteins (5-10) conjugated per QD, and between 1-2 probe oligonucleotides were bound per SAv protein. Note that 10 equivalents of probe were added to prepare the conjugates, suggesting nearly quantitative hybridization at these concentrations.

2.3.2 In-Channel Assay Assembly and Hybridization Experiments.

The hybridization assay was implemented in an electrokinetically controlled microfluidic chip that offered simple assembly, minimal reagent consumption, and miniaturization. The PDMS component of the microfluidic chip was assembled after biotinylation of the glass surface, and EOF was used to deliver QDs in-channel. Less than 10% variation in QD PL intensity was visible throughout a channel, and also between different channels on the same chip. Immobilization of QDs was efficient to the degree that, without an excess of QDs, no visible QD PL could be seen in the exit reservoir. Since only nL volumes of QDs actually entered the channel thus, the remaining volume of QD solution in the injection reservoir was discarded after immobilization. EPF was then used to deliver probe and target oligonucleotides. This approach enabled QD immobilization and bioconjugation in less than 1 h, which was much faster than the overnight QD immobilization and *ca.* 3 h bioconjugation used to assemble analogous fiber optic assays.[168, 170] The timeframe for assembly is suitable for the on-demand fabrication of chips for hybridization assays.[181]

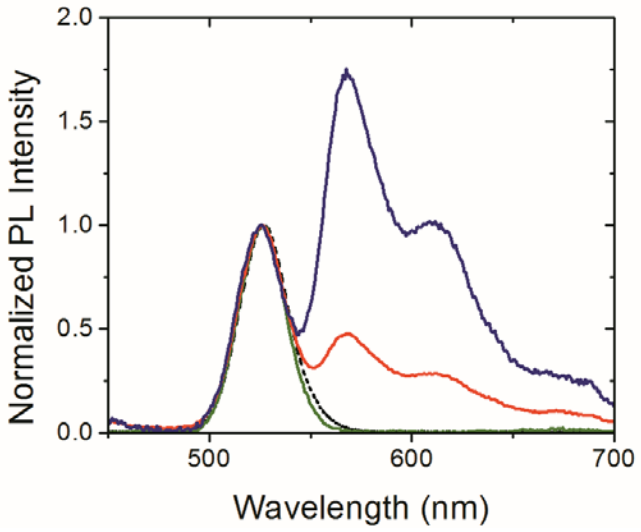

Figure 13. Normalized PL spectra for the in channel assay response to the injection of 1 µM NC TGT (green), distal FC TGT (red), and proximal FC TGT (blue) for 5 min, followed by washing of the channel for 2 min. The dashed black line is the initial PL spectrum of immobilized QD-probe bioconjugates.

Following probe conjugation, the system was tested using the EPF delivery of 1 µM NC, FC-P, and FC-D TGTs. PL spectra averaged from four points along the channel were normalized to the

initial QD peak and are shown in Figure 13. The FRET ratios for the FC-D and FC-P TGTs were 0.5 and 1.8, respectively. There was no detectable FRET sensitized emission from NC TGT, suggesting amelioration of nonspecific adsorption. The apparent FRET efficiencies associated with solid-phase assay on-chip were calculated to be 76% and 94% for the distal and proximal targets, respectively. It should be noted these are only *apparent* efficiencies since there are no discrete donor-acceptor assemblies in the solid-phase format, but rather two quasi-continuous layers of donor QDs and (via hybridization) Cy3 acceptors. The apparent FRET efficiencies in the solid-phase format were calculated from the measured Cy3/QD PL ratio, using parameters estimated from the solution-phase data (Eqn. A1.6). Relative to solution-phase assays using FC-P and FC-D TGT, *ca.* 4-fold and 5-fold enhancements in FRET sensitized acceptor emission were observed in-channel, and relative enhancements in FRET efficiency were 21% and 117%, respectively.

Enhancements in FRET efficiency have been observed in previously reported solid-phase assays and may be due to a greater number of energy transfer pathways.[31] For solution-phase measurements, the ensemble consists of a single QD donor surrounded by multiple dye acceptors, where multivalent acceptors enhance the efficiency of energy transfer. However, each acceptor can only interact with one donor. At an interface of high enough QD density, each QD donor remains in close proximity to several acceptors, but now each acceptor is also in close proximity to several donors. This physical arrangement gives rise to additional pathways for energy transfer. In contrast to the observation by Zhang et al., where higher FRET efficiencies were reported due to double-stranded DNA deformation under microfluidic flow,[182] all PL measurements were made in the absence of flow. Thus, deformation of double-stranded DNA was not expected, and the FRET enhancement is attributed to the solid-phase format. Another factor that may contribute to the FRET enhancement may be the seemingly tangential conformation of oligonucleotide probes conjugated to the SAv-QDs, assuming such a conformation is maintained in the solid-phase format. The apparent solid-phase FRET enhancement is highly advantageous for assay development due to the greater analytical sensitivity.

It is noteworthy that the PL spectra in Figure 13 were obtained 7 min after initial target injection. Similar assays done in bulk solution required 1–3 h to reach equilibration following mixing with target. Considering this rapidity in conjunction with the < 1 h assay fabrication time, it is clear

that this microfluidic format has potential for on-demand QD-FRET assay fabrication and analysis.

2.3.3 Quantitative On-Chip Transduction.

To quantify nucleic acid hybridization via QD-FRET, a different approach was taken than the conventional fluorescence intensity measurements previously used by our group and others in QD-FRET based assays.[68, 93, 173, 183-186] Instead, a spatial profile of fluorescence generated from rapid, in-channel nucleic acid hybridization was used. The premise is that, in the microfluidic channel, the immobilized QD-probe conjugates closest to the sample injection reservoir will always experience longer exposure to target during a continuous injection. As target injection proceeds, additional probe sites further along the channel will become saturated until: (i) the entire recognition surface has been completely covered and probe sites are saturated; (ii) mass transport of target is saturated; or (iii) quantitative capture of all target oligonucleotides from the sample has occurred. Erickson *et al.* studied and modeled this type of rapid DNA hybridization in an electrokinetically controlled biochip using only immobilized nucleic acid probes.[166, 167, 187] Although it is not yet clear how the immobilized SAv-QDs will influence the in-channel hybridization mechanism in our current study, it is not anticipated to be dissimilar to the mechanism elucidated previously. Our assays were done with the immobilized SAv-QD-probe conjugates using FC-D TGT. Despite the larger FRET efficiency associated with FC-P TGT, the FC-D TGT was used to better mimic the position of a Cy3 acceptor in a sandwich assay. Sandwich assays use a labeled reporter oligonucleotide that binds to the target at a site adjacent to the probe oligonucleotide (Appendix 1, Fig. A1.6); this configuration could be used to avoid direct labeling of target in future work, and has been presented elsewhere.[172] Here, however, the simplicity of the directly labeled probe was more amenable to the goal of the current study: to demonstrate that rapid hybridization within a microfluidic channel would enable quantitative transduction based on the length of a spatial profile of PL from QD-FRET.

Epifluorescence images of a 3-channel microfluidic chip showing signals for Cy3 PL, QD PL, and a composite of the two are presented in Figure 14(a-c). The intensity profiles for both Cy3 and QD PL are also illustrated for each channel. The channels at the top, middle, and bottom of the image display the assay response to the injection of 9.5, 19 and 28.5 fmol of FC-D TGT, respectively. The FRET ratio along each of these channels is shown in Figure 14(d). The critical

result was that FC-D TGT resulted in a discrete length of FRET-sensitized Cy3 PL along the length of the channel, and that this length increased with the amount of target. This provided clear evidence that target was hybridizing nearly quantitatively. The length of the FRET-sensitized Cy3 PL zone in the channel was suitable for generating a calibration curve for quantification of target in the sample. Figure 14(e) displays the Cy3 PL coverage length for a range of target concentrations. Without any manipulation of flow conditions, the dynamic range was, at minimum, between 5-45 fmol for in-channel delivery. To extend the dynamic range to lower quantities, increases in the injection time (or volume) would afford delivery of a larger quantity of oligonucleotides to the interface, extending the coverage length within the channel. The upper limit of the dynamic range was estimated by extrapolation of the data in Figure 14(e) to the limit of the channel length. The dynamic range could potentially be improved by manipulation of injection conditions, probe densities, and the use of longer channels (*e.g.* a serpentine design on the same sized chip). Nonetheless, the dynamic range in this work is comparable in magnitude to those typical of intensity-based, ratiometric FRET assay formats.[169, 188] The LOD is limited by the ability to resolve low FRET efficiencies (*e.g.* < 5-10%) and small amounts of sensitized acceptor PL on a background of bright donor PL. Importantly, the 5 fmol of target detected herein is approximately 500-fold better than the 1 pmol limit of detection (LOD) reported previously for optical fiber assays.[168] This improvement from miniaturization is in good agreement with the superior LOD predicted from a recent study that used glass beads to discretely control active sensing areas.[172]

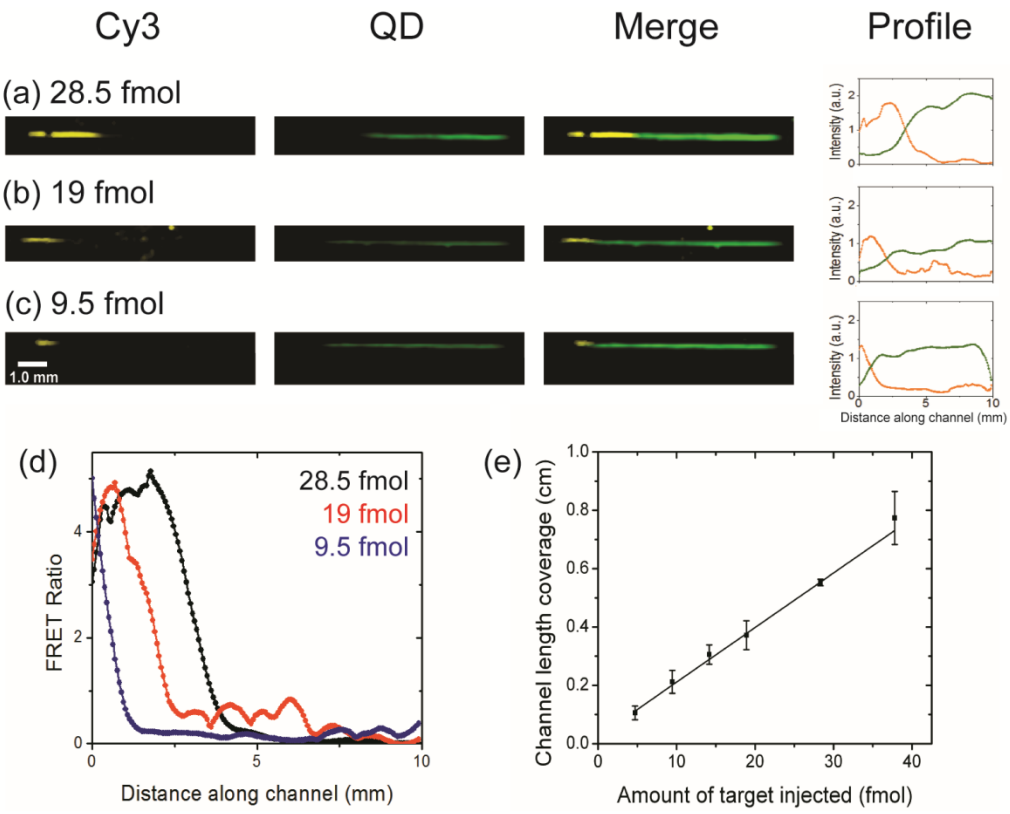

Figure 14. Epifluorescence image of FRET sensitized Cy3 PL, QD PL, PL merge, and corresponding Cy3 and QD channel intensity profiles (Cy3: orange, QD: green) for the injection of (a) 28.5 fmol (b) 19 fmol (c) 9.5 fmol of Cy3 labeled FC distal TGT. The images have been background corrected for contributions from QD PL. (d) In-channel FRET ratio profiles for the injection of 28.5, 19.0, and 9.5 fmol of FC distal TGT. (e) Quantitative transduction of nucleic acid hybridization as a function of the length of channel covered by Cy3 PL. The channel length coverage was determined from a point where the Cy3 acceptor PL had decayed to 50% of the initial intensity for that respective concentration. The target concentrations injected were 0.25, 0.50, 0.75, 1.0, 1.5, and 2.0 μM at a fixed volume of 19 nL.

An intriguing aspect seen in the data of Figure 14 is that the two PL zones along the channel length—hybridized FRET "on" Cy3 PL and unhybridized FRET "off" QD PL—could provide a means of a self-referencing that compensates for fabrication variations in channel length or placement on-chip. Less than *ca.* 5% variation in capture length was seen for the same sample concentration between channels on the same chip, or between chips from the same batch of surface modification (Figure 14(e)). Variations closer to 10% were seen between different batches of chips. Variability associated with the amount and quality of APTMS deposited in the silane step can alter the amount of QD that is immobilized. By developing a method that references signals to the QD PL, it may be possible to correct for these chip-to-chip and channel-to-channel variations.

The most interesting and important aspect of this work is that the microfluidic channel format enabled a QD-FRET assay with quantitative detection capability that only relied on spatial resolution of FRET on/off states, aided by a ratiometric format, rather than highly precise measurements of FRET efficiency or small changes in acceptor/donor PL ratios. While our primary analysis was based on a straightforward "on/off" threshold (*i.e.* half maximum) for FRET-sensitized Cy3 PL, other analysis methods are possible. For example, the length of the spatial profile can also be estimated from the "crossover" between the QD and Cy3 PL intensities. Considering the data in Figure 14(a-c), the slope of response toward the three quantities of FC-D TGT was 0.13 cm $fmol^{-1}$ using both the on/off Cy3 PL threshold and the crossover method. A second alternative approach to data analysis is the use of the area under the FRET ratio profile. While this parameter is no longer strictly a length measurement, it should be directly proportional to the profile length. The relative areas for this method were 1:1.8:3.1, which was in poor agreement with the 1:2.9:4.6 length ratio from the Cy3 threshold measurements. The discrepancy may be due to the inclusion of noise from the profiles for 9 and 19.5 fmol FC-D TGT (see Figure 14(b)), or complex changes in binding kinetics associated with the descending slope of the FRET ratio profile as the TGT concentration is rapidly depleted. Overall, the data analysis methods based on the Cy3 PL on/off threshold (Figure 14(e)), or the crossover between Cy3 and QD PL, appear to be the most robust toward noise.

2.3.4 Assay Selectivity and Stringency.

To examine the selectivity of the assay, a more complex sample mixture containing 1 µM of FC-D TGT and a 5-fold excess of two additional oligonucleotides (CM 1 + CM 2) was injected. This sample yielded 90% of the response associated with a sample containing only 1 µM of FC TGT in buffer (data not shown). It was speculated that the 10% decrease was due to a decrease in the capture efficiency of target to the assay interface. Regardless, it was clear that the added NC oligonucleotides did not induce any false positive signals.

Tuning of assay stringency in-channel was demonstrated by discrimination of a Cy3 labeled 3BPM TGT oligonucleotide. In previous solid-phase QD-FRET assays based on optical fibers, a fixed percentage of formamide was added to aqueous sample solution to suppress the melt temperature of mismatched sequences below ambient.[168, 170] This methodology was adopted for application in the microfluidic channels. Figure 15 displays the response of the assay to FC-D

and 3BPM TGTs in the absence and presence of 20% v/v formamide at room temperature. Without any formamide, the FRET ratios for FC-D and 3BPM TGTs were indistinguishable. However, when the target sample buffer contained 20% v/v formamide, with washing under the same conditions, the FRET signal for the 3BPM TGT was reduced by 80%. The absolute loss in FRET ratio for the FC-D TGT was only 5%, resulting in a contrast ratio of 4:1 over 3BPM TGT. In addition to the absence of signal from NC, this set of experiments clearly established the capacity for selective detection and tuning of stringency within the framework of this new detection method.

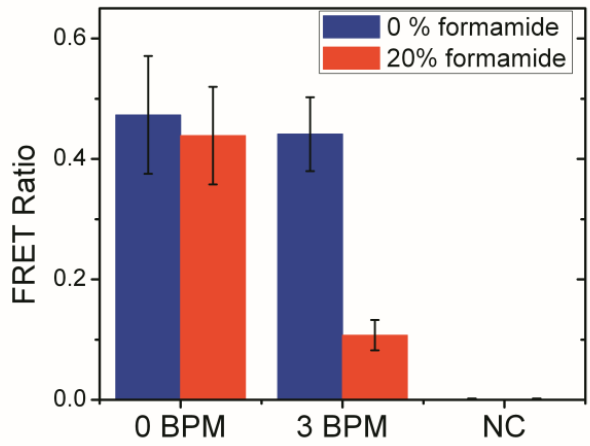

Figure 15. Discrimination of 3BPM from FC-D TGT using 20% v/v formamide in TB buffer. The amount of each sequence injected was 19 fmol.

2.4 Conclusions

In this work, the viability of integrating a solid-phase QD-FRET nucleic acid hybridization assay into an electrokinetically controlled microfluidic platform was investigated. SAv-QDs were immobilized and were then further bioconjugated with biotinylated probe oligonucleotides along the length of one interface of the channel interior. Subsequent delivery of Cy3 labeled target nucleic acid resulted in hybridization providing the necessary proximity for energy transfer from the QD to the Cy3. This enabled transduction via Cy3 FRET sensitized PL. The microfluidic system offered the ability for in situ assay fabrication, rapid reaction kinetics, and minimal reagent consumption. Transduction of hybridization was possible within minutes after target injection, with no appreciable nonspecific adsorption of noncomplementary sequences. The microfluidic-based QD-FRET assays enabled the detection of as little as 5 fmol of target, which

was a 500-fold improvement from previous solid-phase assays developed by our group. Concurrently, detection times of these assays were reduced from hours to minutes. The robustness of the assay was further tested in a complex matrix containing a 5-fold excess of two additional sequences and recovery of up to 90% of target relative to a purified sample was demonstrated. Discrimination against a sequence containing a 3BPM was possible with a contrast ratio of 4:1. Hybridization kinetics were sufficiently rapid that transport of target oligonucleotides to the interface enabled the quantitative capture of target by measuring the length of the FRET-sensitized PL zone within the channel interior. Further optimization of this novel quantitative hybridization method should enable spatial and multiparametric detection of nucleic acids in future studies. This work provides an important foundation for the future development of solid-phase QD-FRET hybridization assays with microfluidics that are well suited to multiplexing formats.

3 On-Chip Multiplexed Solid-Phase Nucleic Acid Hybridization Assay Using Spatial Profiles of Immobilized Quantum Dots and Fluorescence Resonance Energy Transfer

The data presented in Chapter 3 has been published prior to formatting this thesis and can be found in the citation below. While the first report of this work was developed by AJT, MON designed and optimized the in-channel assay toward multiplexed analysis in all aspects from QD immobilization density, FRET pairs, and conditions for concurrent target transduction. AJT and MON designed, analyzed and interpreted all single-colour quantitative hybridization experiments in-channel. MON designed and analyzed all selectivity experiments. MON and AJT developed and interpreted solution hybridization experiments to determine differences in QD probe loading capacities as to provide insight into differences in spatial responses from the two targets.

Noor, M.O.; Tavares, A.J.; Krull, U.J., *Anal. Chim. Acta* **2013**, 788, 148-157.

3.1 Introduction

Building on Chapter 2 where a solid-phase nucleic acid hybridization method using a novel spatial detection strategy was presented, the work was extended to immobilize a mixture of QDs to acheive multiplexing capacity. Earlier solid-phase assays reported by our group demonstrated detection of up to four targets in a given sample using a single excitation source. It was postulated that immobilization of two colours of QDs on a microfluidic chip would provide for multiplexed detection using the spatial detection method for quantification.

Only a limited number of studies have reported the integration of QD-based multiplexed solid-phase assays within microfluidic systems [189, 190]. Typically QDs have been used as labels, and the fluidic network offers containment of sample solution to achieve proximity with selective chemistry that is immobilized on the surface of microsphere beads. For example, Jokerst and coworkers [190] reported on the implementation of sandwich-based multiplexed immunoassay within a microfluidic chip using multicolor QDs as labels for the detection of three cancer markers. The selective chemistry was immobilized on agarose beads and captured within a chip using microstructures, where the spatial registration of the agarose beads provided multiplexing capability. In another example, Hu and coworkers [189] used microfluidics for surface patterning of

capture antibodies and QD-labeled secondary antibodies for selective and sensitive multiplexed detection of femtomolar concentrations of two cancer biomarkers in serum. Multiplexed detection of nucleic acid hybridization using QDs as labels and integration with on-chip detection has also been demonstrated using spectral barcoding, where microbeads were infused with multicolor QDs at different ratios to yield a distinctive spectral signature for each analyte [191]. The utility of QDs in microfluidics has been limited to only labels for solid-phase assays and no examples of multiplexed solid-phase QD-FRET assays integrated within microfluidics have been described.

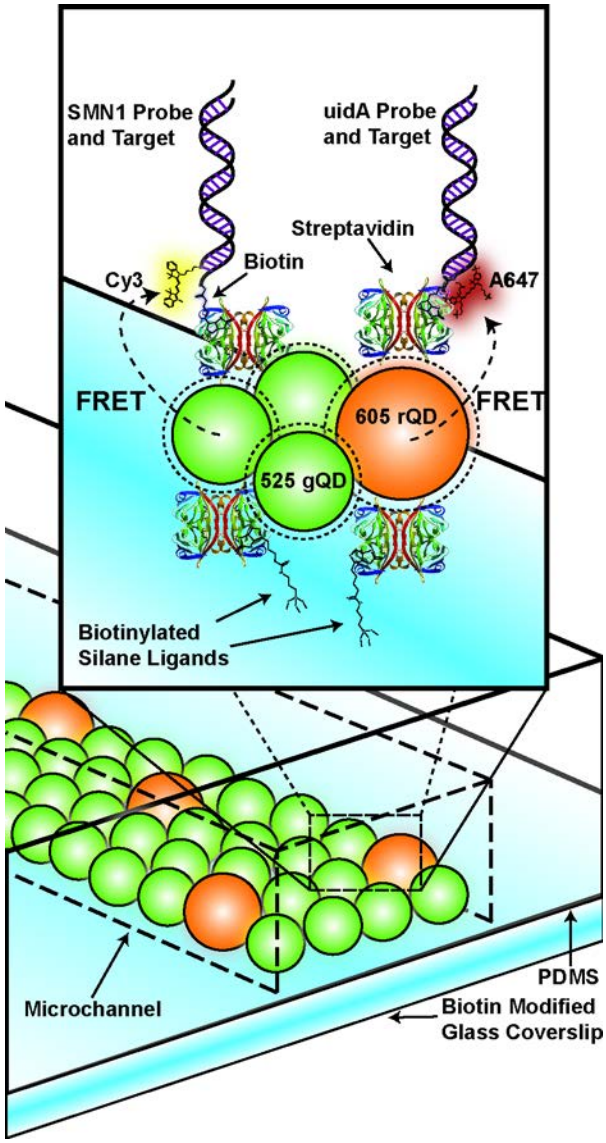

Figure 16. Representation of a cross-sectional area of a hybrid glass/PDMS based microfluidic channel showing the design of the solid-phase multiplexed nucleic acid hybridization assay using immobilized multicolor QDs as donors in a FRET based transduction scheme. SAv conjugated gQDs and rQDs were immobilized on a biotin modified

glass surface, and subsequently conjugated with two types (SMN1 and uidA) of biotinylated probe oligonucleotides. Hybridization with Cy3 labeled SMN1 and A647 labeled uidA target oligonucleotides provided the proximity for FRET sensitized emission from Cy3 and A647 dyes upon excitation with a 402 nm diode laser.

The work described in Chapter 3 builds on the fundamental on-chip assay presented in Chapter 2 which utilized a single QD-FRET system to transduce oligonucleotide targets [192], and investigates a solid-phase assay for the multiplexed interrogation of nucleic acid hybridization within an electrokinetically operated microfluidic chip. The design of the transduction interface is depicted in Figure 16. The glass surface of a hybrid glass/PDMS microfluidic chip was chemically modified with a biotin functionality to immobilize SAv-gQDs and SAv-rQDs. The in-channel delivery of the two colors of QDs was done EOF. The surface of the QDs were subsequently bioconjugated with two types of biotin terminated oligonucleotide probe sequences (SMN1 and uidA) using electrophoretic injection for in-channel delivery. The assembly of the biorecognition interface was possible within minutes. The electrophoretic injection and subsequent hybridization of the acceptor labeled target oligonucleotides provided the proximity for FRET sensitized dye emissions upon excitation of the QD-probe conjugates. Cy3 was used as the acceptor for gQDs and A647 was used as the acceptor for rQDs (see Appendix 2, Figure A2.2). The electrokinetic flow mediated active transport of target oligonucleotides to the transduction interface. This allowed nucleic acid hybridization to occur within minutes, resulting in femtomole detection levels of the target oligonucleotides with improved sensitivity using a FRET response associated with spatial channel length coverage [192].

3.2 Methods and Materials

A detailed description of the experimental procedures and instrumentation used, including data analysis, can be found in Appendix 2.

3.2.1 Reagents

Green emitting CdSe/ZnS Qdot® 525 ITK™ Streptavidin conjugates (gQDs), red emitting CdSe/ZnS Qdot® 605 ITK™ Streptavidin conjugates (rQDs) and quantum yield reference dye sampler kit were obtained from Invitrogen Life Technologies (Oakville, ON, Canada). Redistilled *N*,*N*-diisopropylethylamine (DIPEA, 99.5%), *N*-hydroxysuccinimide (NHS, 99%), *N*,*N* diisopropylcarbodiimide (DIC, 99%), 3-aminopropyltrimethoxysilane (APTMS, 97%), anhydrous toluene (99.8%), anhydrous *N*,*N*-dimethylformamide (DMF, 99.8%), biotin (99%) and formamide (F, ≥ 99.5%) were from Sigma Aldrich (Oakville, ON, Canada). Ammonium

hydroxide (30%), hydrochloric acid (16 M) and hydrogen peroxide (30%) were from EMD Millipore Chemicals (San Diego, CA). Methanol, dichloromethane, diethylether and isopropanol were reagent grade or better, and were obtained from Caledon Laboratories (Georgetown, ON, Canada). All buffer solutions were prepared using a deionized Milli-Q water purification system with a specific resistance of 18 $M\Omega cm^{-1}$ (Millipore Corporation, Mississauga, ON, Canada). All buffer solutions were autoclaved for sterilization. The buffer solutions included 50 mM borate buffer (BB, pH 9.25) and 100 mM Tris-Borate buffer (TB, pH 7.44, 20 mM NaCl). The buffer solutions were also filtered through a 0.2 μm syringe filter from Pall Corporation (Ann Arbor, MI) prior to their application in microfluidics. Microscope glass coverslips with dimensions 22 mm × 22 mm × 0.25 mm were from Fischer Scientific (Pittsburgh, PA). P-type boron doped silicon wafers, diameter × thickness (100.0 ± 0.5 mm × 515 ± 30 μm), were obtained from Empak (Chanhassen, MN). Polydimethylsiloxane (PDMS) Sylgard 184 silicone elastomer kit was obtained from Ellsworth Adhesives Canada (Stoney Creek, ON, Canada). Su 8 3010 photoresist used in fabrication of positive relief microfluidic templates was from MicroChem (Newton, MA).

Table 4. Oligonucleotide Sequences.

gQD/Cy3 FRET pair (SMN1 sequences)	
SMN1 probe	Biotin-C6 – 5'– ATT TTG TCT GAA ACC CTG T – 3'
SMN1 FC TGT	Cy3 – 3'– TAA AAC AGA CTT TGG GAC A – 5'
SMN1 3BPM TGT	Cy3 – 3'– T**G**A AAC AG**G** CTT TGG GA**T** A – 5'
SMN1 NC TGT	Cy3 – 3'–TGT CCC AAA GTC TGT TTT A – 5'
rQD/A647 FRET pair (uidA sequences)	
uidA probe	Biotin-C6 – 5'– CTT ACT TCC ATG ATT TCT TTA ACT – 3'
uidA FC TGT	A647– 3'– GAA TGA AGG TAC TAA AGA AAT TGA – 5'
uidA NC TGT	3'– TTG TTA TAA CAG AAC TAA TCA GTA – A647 – 5'

TGT = target; FC = fully-complementary; 3BPM = 3 base pair mismatch; NC = non-complementary; Cy3 = Cyanine 3; A647 = Alexa Fluor 647. The mismatch bases are bolded and underlined in the 3BPM TGT.

Oligonucleotide sequences were from Integrated DNA Technologies (Coralville, IA) and were HPLC purified by the manufacturer. The oligonucleotide sequences used in the hybridization assays are given in Table 4. Oligonucleotide sequences were dissolved in sterile Milli-Q water and stored at −20°C.

3.2.2 Fabrication of Microfluidic Chips

The fabrication of PDMS covers of the hybrid glass/PDMS based microfluidic chips was based on soft lithography introduced by the Whitesides' group [193]. The fabrication of the positive relief microfluidic template was based on a rapid prototyping technique as described elsewhere [194]. Positive relief microfluidic templates containing a design pattern for three straight channels connected by two end channel reservoirs were used for replica molding of PDMS covers for the hybrid glass/PDMS based microfluidic chips.

Briefly, PDMS base and curing agent were mixed in 10 to 1 ratio respectively and the mixture was degassed under vacuum. The degassed mixture was then poured (*ca*. 3.2 g) on the microfluidic template and baked in the oven at 120°C for 20 min. The PDMS was then trimmed to the dimensions of *ca*. 20 mm × 20 mm and end channel reservoirs were made using a metal borer. The length, width and height of the microfluidic channels were 1.2 cm, 250 μm and 11 μm, respectively. PDMS cover was bonded to the biotin modified glass coverslips by air plasma oxidation using a Harrick PDC-32 G plasma cleaner (Ithaca, NY) at 10.5 W for 30 seconds. The details for the chemical modification of glass coverslips with biotin can be found in Appendix 2 along with a schematic of the microfluidic chip.

3.2.3 Assembly of the biorecognition interface

The steps involved in the assembly of the assay are given in Table 5. As reported in our previous study, combinations of EPF and EOF were used to deliver reagents (QDs and oligonucleotides) inside a hybrid glass/PDMS microfluidic channel to facilitate *in situ* assembly of the biorecognition interface [192]. An electrokinetic-based delivery of reagents offers many advantages as compared to a pressure-based delivery of reagents. These advantages include ability to handle, control and dispense small volumes of reagents (nL) without the need for the integration of valves and pumps, which can otherwise complicate the device fabrication process [195]. In contrast with a pressure-based injection, electrokinetic-based injection of reagents is also compatible with

a less-durable seal of a microfluidic chip. This was the case in this work as plasma oxidized PDMS cover was bonded to a non-oxidized biotinylated glass coverslip, which renders the seal as less durable (see Appendix 2 for details).

The QDs were delivered inside the microfluidic channel via EOF with a net mobility in the direction of the cathode. Oligonucleotide probes and targets were introduced inside the microfluidic channel using EPF with a net mobility in the direction of the anode. The injection voltage was kept constant at 200 V for in-channel delivery of all the reagents. In-channel assembly is useful from the standpoint of minimal reagent consumption [192] and fast immobilization kinetics [196] to allow on demand assembly of the biorecognition interface for nucleic acid hybridization assays.

Table 5. Steps for the In-Channel Assembly of the Solid Phase Assay

Assembly Step	Concentration	Delivery Method	Incubation	Washing
Preconditioning	-	EOF/pH 9.25 BB 2 min	-	-
QDs delivery and Immobilization	200 nM[a] 360 nM (gQDs) and 30 nM (rQDs)[b]	EOF/pH 9.25 BB 10-15 min	5 min	5 min/pH 9.25 BB
Probe(s) delivery and bioconjugation	3 μM[a] 1.5 μM (SMN1) and 1.5 μM (uidA)[b]	EPF/pH 7.44 TB 5 min	5 min	5 min/pH 7.44 TB
Target(s) delivery and hybridization	0.25 μM – 3 μM	EPF/pH 7.44 TB 3 min	5 min	1 min/pH 7.44 TB

[a]for single-color experiments, [b]for multicolor experiments. **Note:** for 3BPM discrimination experiments, all the steps associated with the assembly of the biorecognition interface and targets injection were done in pH 9.25 BB.

3.3 Results and Discussion

3.3.1 The FRET Pairs

The gQD/Cy3 (donor/acceptor) and rQD/A647 (donor/acceptor) FRET pairs used in this work were characterized in solution using absorbance and steady state PL measurements. The absorption and PL spectra of the two FRET pairs are shown in Appendix 2 (Figure A2.2). The spectral overlap integrals for the gQD/Cy3 and rQD/A647 FRET pairs were 6.31×10^{-10} and

1.55×10^{-9} cm^6mol^{-1}, respectively. The solution-phase quantum yields of gQDs and rQDs were 0.48 and 0.89, respectively. Using the Förster formalism and assuming a refractive index of n = 1.33 and an orientation factor of $\kappa^2 = 2/3$, the corresponding Förster distances for the gQD/Cy3 and rQD/A647 FRET pairs were calculated to be 6.2 nm and 8.0 nm, respectively. Considering the dimensions of streptavidin coated QDs (radius 4-5 nm) and the calculated Förster distances, it was deduced that the implementation of streptavidin coated QDs was a suitable choice for the development of FRET based assays.

3.3.2 Single-Color Hybridization Assays

The functionality of the gQD/Cy3 and rQD/A647 FRET pairs for a quantitative transduction of SMN1 and uidA oligonucleotide targets, respectively, was investigated using single-color hybridization assays within microfluidic channels. The SMN1 sequence is a genetic marker for diagnosis of the neuromuscular disease spinal muscular atrophy, while the uidA sequence is diagnostic of *E. coli* [168]. This multiplexed detection builds on the results presented in Chapter 2 where a novel quantification method for a solid-phase QD-FRET nucleic acid hybridization assay that is based on spatial channel length coverage of target DNA within a microfluidic channel [192]. In this spatially-based quantification method, the amount of target DNA delivered into a microfluidic channel can be determined by measuring the length of a microfluidic channel that exhibits a “turn-on” signal from the FRET sensitized acceptor dye emission, or a “turn-off” signal due to the loss in the emission of immobilized QD donors upon hybridization of dye-labeled target DNA. The cross-over position along the length of a microfluidic channel of these signals enabled a useful and reproducible point of reference to provide for quantitative transduction of hybridization. This spatial channel length quantification method was used in this work, and the results for single-color hybridization assays are shown in Figure 17.

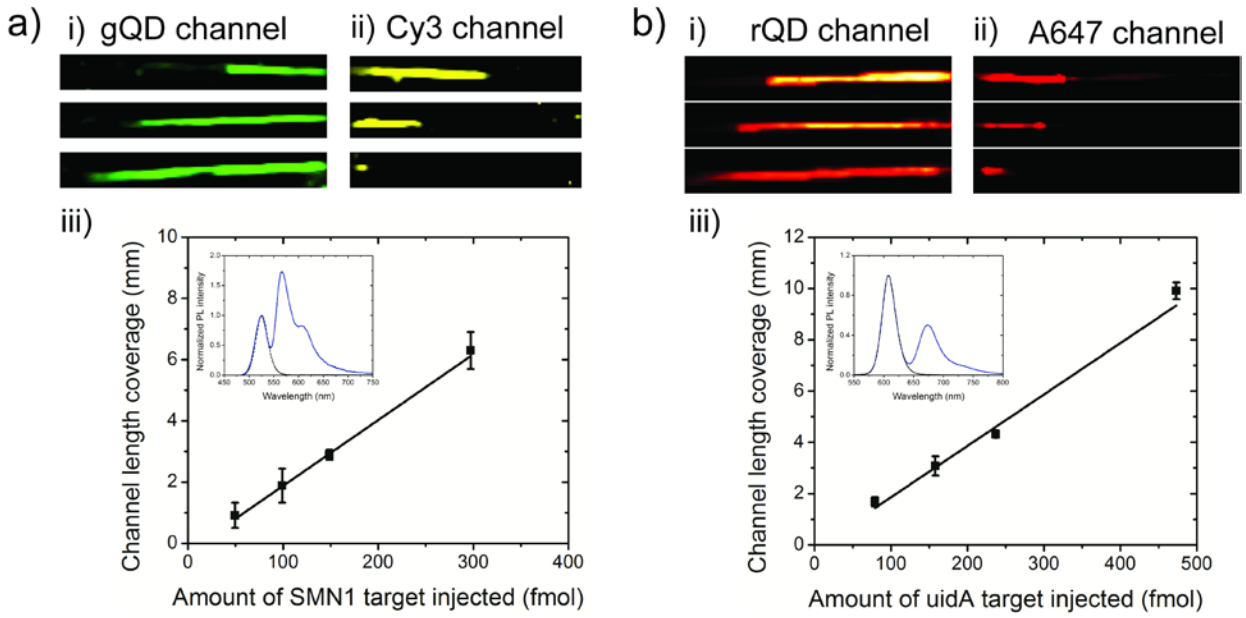

Figure 17. Single-color hybridization experiments with (a) gQD/Cy3 FRET pair and (b) rQD/A647 FRET pair showing the applicability of the assay to quantitatively transduce nucleic acid hybridization using a spatial channel length coverage response of donor PL and acceptor PL. (a) Pseudocolor epifluorescence images of (i) gQD donor PL and (ii) Cy3 acceptor PL for the injection of 297 fmol (top channel), 149 fmol (middle channel) and 49.5 fmol (bottom channel) of SMN1 FC TGT. (b) Pseudocolor epifluorescence images of (i) rQD donor PL and (ii) A647 acceptor PL for the injection of 237 fmol (top channel), 158 fmol (middle channel) and 78.9 fmol (bottom channel) of uidA FC TGT. (iii) Calibration curves showing the channel length coverage response of the two targets as a function of the amount of target DNA injected into microfluidic channels. (Inset) Normalized PL spectra in the absence (black dashed line) and presence (blue line) of the DNA targets.

Hybridization of dye-labeled target oligonucleotide to immobilized QD-probe conjugates provided the necessary proximity for energy transfer from the QDs resulting in FRET sensitized acceptor PL. The zone along the channel interior that was covered with a dye-labeled target DNA exhibited a “turn-on” signal from the acceptor dye emission (Figure 17a and b (ii)), and concurrently the same length of a microfluidic channel exhibited a “turn-off” signal from the loss in QD PL signal due to energy transfer (Figure 17a and b (i)). Figure 17a shows the PL image profiles for (i) gQD donor and (ii) Cy3 acceptor detection channels for the gQD/Cy3 FRET pair for the injection of 297 fmol, 149 fmol and 49.5 fmol of SMN1 FC TGT from the top to bottom channels, respectively. Figure 17b shows the PL image profiles for (i) rQD donor and (ii) A647 acceptor detection channels for the rQD/A647 FRET pair for the injection of 237 fmol, 158 fmol and 78.9 fmol of uidA FC TGT from the top to bottom channels, respectively. Hybridization resulted in a linear relationship between the amount of target oligonucleotide injected into a microfluidic channel and the length of the FRET sensitized PL zone from the channel interior (Figure 17a and b (iii)). The amount of target DNA delivered into a microfluidic channel was

determined by multiplying the injection volume by the concentration of target DNA added to the sample reservoir. The volume of target DNA delivered into a microfluidic channel was estimated by multiplying the net mobility of the target DNA by the cross-sectional area of the microfluidic channel. The net mobilities of SMN1 and uidA targets in the direction of the anode were determined to be 1.1×10^{-4} $cm^2 V^{-1}s^{-1}$ and 1.6×10^{-4} $cm^2 V^{-1}s^{-1}$, respectively. Since the injection voltage (200 V) and time (3 min) were kept constant in all the hybridization assays, it was determined that about 99 nL and 158 nL of SMN1 and uidA targets were delivered into a microfluidic channel, respectively.

Quantitative assessment of the length of a microfluidic channel that exhibited FRET sensitized PL from target hybridization was determined by a cross-over point analysis, i.e. the point in the microfluidic channel where the normalized PL intensities of the acceptor and donor crossed. An example of a cross-over point analysis for the determination of channel length can be found in Appendix 2 (see Figure A2.3). For a constant injection voltage of 200 V and time of 3 min, the limit of detection (LOD) of the SMN1 and uidA targets was determined to be 23 fmol. Similar detection limits in the fmol range have been previously reported for the nucleic acid hybridization assays conducted within a microfluidic channel (non QD-FRET based assays) [195, 197]. The LOD (based on a distance measured) was estimated by taking into account the spatial relationship of one imaged data point and the equation associated with the calibration curve of the corresponding target. One spatial data point correlated to a channel length of *ca.* 0.24 mm, considering that for imaging each chip, approximately 50 line scans were completed across the length of the channel which measured 12 mm.

For solid-phase QD-FRET assays that rely on the PL intensities of donors and acceptors, ratiometric analysis is commonly employed for quantification. For a ratiometric approach, the LOD is determined by the ability to resolve FRET sensitized acceptor PL against a bright background of donor PL, and the limit of linearity (LOL) is determined by either the saturation of the biorecognition element or by the threshold of the number of acceptors that results in the saturation of FRET efficiency response [198]. It is important to note that saturation of the FRET efficiency response as governed by the number of acceptors may occur prior to the saturation of the biorecognition element. The sensitivity of such assays is governed by changes in the FRET efficiency upon an increasing number of acceptors interacting with the donor QDs. For the spatially-based detection method described herein, the quantification is independent of the PL

intensities of donors and acceptors. The LOL is only governed by the saturation of the biorecognition element and is limited by the length of the microchannel. Furthermore, the sensitivity of this transduction method is not as dependent on changes in the FRET efficiency response and has the potential to improve the dynamic range of QD-FRET based assays.

3.3.3 Selectivity

The selectivity of nucleic acid hybridization assays was evaluated with single-color experiments by comparing the response of the assay to FC and NC targets. The results are shown in Figure 18. For the gQD/Cy3 FRET pair, hybridization assays conducted with SMN1 FC TGT yielded a FRET ratio response of 1.7 ± 0.2, while in the presence of SMN1 NC TGT, the FRET ratio response observed was 0.0015 ± 0.0003. This corresponds to a contrast ratio of 1143 to 1 for FC and NC targets respectively. In the case of the rQD/A647 FRET pair, hybridization with uidA FC TGT yielded a FRET ratio response of 0.58 ± 0.05, while uidA NC TGT yielded a FRET ratio response of 0.029 ± 0.007. This corresponds to a contrast ratio of 20 to 1 for FC and NC targets respectively. These results confirm that the assay design provided selectivity of nucleic acid hybridization and is consistent with the previous reports of resistance of streptavidin coated QDs to non-specific adsorption of oligonucleotides [192].

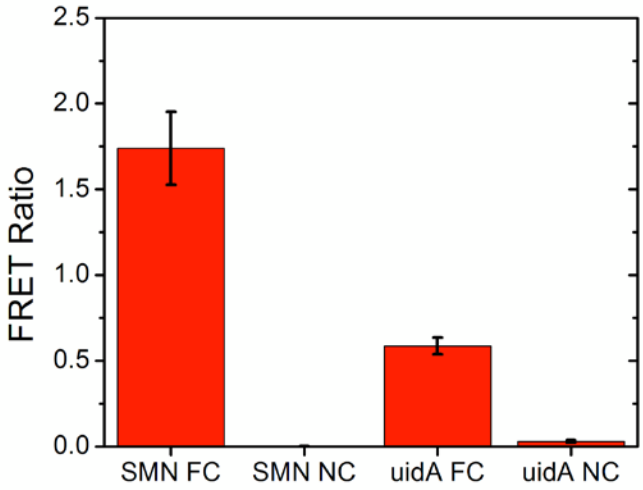

Figure 18. Single-color hybridization experiments showing the FRET ratio response of the assay in the presence of FC and NC targets.

3.3.4 Multiplexed Hybridization Assays: Two-Colour Immobilization of QDs

Co-immobilization of multiple colours of QDs is an important step towards the development of multiplexed solid-phase QD-FRET assays for nucleic acid detection without a need for spatial registration. In the previous QD-FRET based multiplexed assays that have relied on PL intensities of donors and acceptors for quantification, the optimization in terms of the relative molar concentration of the multiple colors of QD donors used was based on matching their PL intensities. This was done to account for differences in the absorption cross-sections and quantum yields of various populations of QDs, and also to minimize the overshadowing of one QD PL intensity by another QD PL intensity. [173, 199] The quantification method presented in this work is based on a spatially resolved detection of FRET sensitized emission from the acceptor dyes. Therefore, an optimization of the immobilization of multiple colors of QDs in terms of their relative proportions was done to yield a reasonable signal-to-noise ratio (S/N) for fluorescence imaging in each of the two QD donor (gQDs and rQDs) detection channels and the two acceptor (Cy3 and A647) detection channels. Tuning of the signal-to-noise in the Cy3 detection channel was particularly significant due to the background fluorescence of PDMS that spans the wavelength range of the Cy3 emission band [200]. There was also a limited wavelength separation (*ca.* 50 nm considering a FWHM of gQDs and rQDs) between the PL ranges of the two colors of QDs. An emission filter (570/20 nm) was used in order to minimize the crosstalk of the PL from the two QDs with the Cy3 detection channel. It was found that a gQD to rQD ratio of 12 to 1 generated a good S/N in the Cy3 detection channel (see Figure A2.4 in Appendix 2 for the associated PL spectrum). The PL images and the corresponding PL spectra showing co-immobilization of two colors of QDs are depicted in Figure 19. The images in Figure 19 correspond to the same microfluidic chip that was sequentially imaged using the (a) rQD and (b) gQD detection channels. The PL from the two colors of QDs were sufficiently spread apart spectrally such that no cross-talk was seen between detection channels and still enabled suitable spectral ranges for collection of acceptor PL. Less than 30% variation of peak PL intensity was seen between different microfluidic channels from different batches of biotin functionalized glass slides.

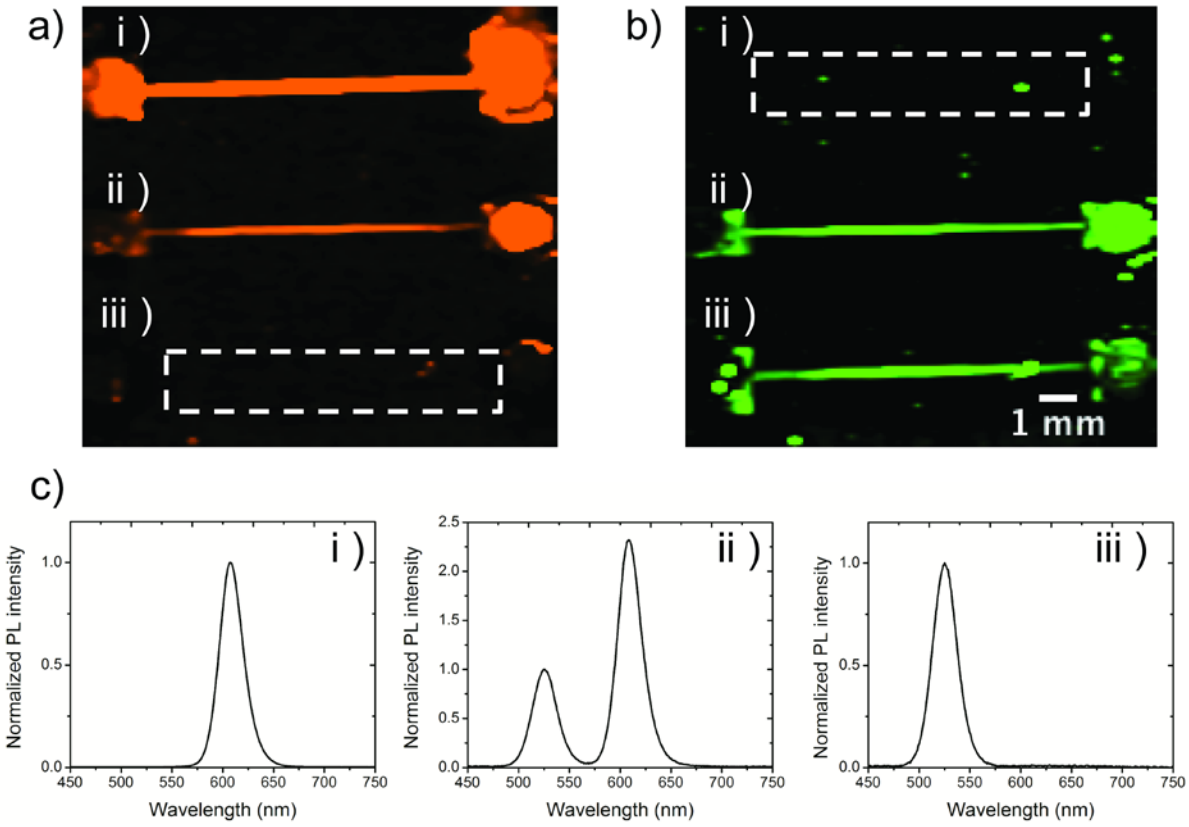

Figure 19. Pseudocolor epifluorescence images of a microfluidic chip showing co-immobilization of gQDs and rQDs under (a) rQD detection channel (b) gQD detection channel. Microfluidic channel (i) only rQDs, microfluidic channel (ii) gQDs and rQDs in 12 to 1 molar ratio, respectively, and microfluidic channel (iii) only gQDs. (c) PL spectra corresponding to microfluidic channels (i), (ii) and (iii). The dashed box in images (a) and (b) shows the channel area.

SEM imaging of the QDs immobilized within a microfluidic channel was done to determine if a 12 to 1 molar ratio of gQDs to rQDs that was injected into a microfluidic channel was reflected in the immobilization density of the interfacial QDs. A solution of gQDs and rQDs in 12 to 1 molar ratio was injected into a hybrid silicon wafer/PDMS based microfluidic chip, where the surface of the silicon wafer was modified with biotin in a same manner as the glass coverslips (see Appendix 2 for details). It should be noted that the interfacial chemistry on the glass coverslips and silicon wafers is expected to be similar as both substrates when subjected to the RCA (Radio Corporation of America) cleaning protocol offer the same functional group (silanol groups), which was subsequently modified with biotin. The conductive nature of a silicon wafer renders this substrate suitable for SEM imaging but incompatible for electrokinetic delivery. Therefore, vacuum-based injection was used to bring the solution of QDs into the microfluidic

channel. It is likely the case that an electrokinetic-based delivery and vacuum-based delivery of QDs provided similar immobilization densities of the two colors of QDs due to the incubation step that followed the QD injection step, which likely saturated the surface in terms of immobilization of QDs.

A representative SEM image of the immobilized QDs within a microfluidic channel and the associated PL spectrum are shown in Figure 20. The QDs were immobilized as a monolayer without any signs of aggregation. The difference in the size of green-emitting (diameter *ca.* 4 nm) and red-emitting (*ca.* 6 nm) CdSe/ZnS based QDs is distinctly visible in Figure 20(a). The immobilization density of gQDs was estimated to be $1.4(\pm 0.4) \times 10^{11}$ gQDs per cm^2, while the immobilization density of rQDs was estimated to be $1.2(\pm 0.2) \times 10^{10}$ rQDs per cm^2. This corresponds to a relative ratio of gQDs to rQDs of *ca.*12 to 1 in terms of the immobilization density, and is consistent with the relative molar ratio of gQDs to rQDs that was injected into the microfluidic channel. Evidence suggesting that the immobilization density of the two colors of QDs on a biotinylated glass slide (electrokinetic delivery) and on a biotinylated silicon wafer (vacuum delivery) was similar is provided by the peak PL intensity comparison of the two colors of QDs (cf. Figure 19c (ii) and Figure 20b). In the case of glass substrates, the ratio of the peak PL of rQDs to gQDs was observed to be 2.0(±0.6), while in case of silicon wafers, the ratio was found to be 1.9(±0.1). No statistically significant difference was observed in the peak PL ratios from the two colors of QDs regardless of the substrate used for immobilization.

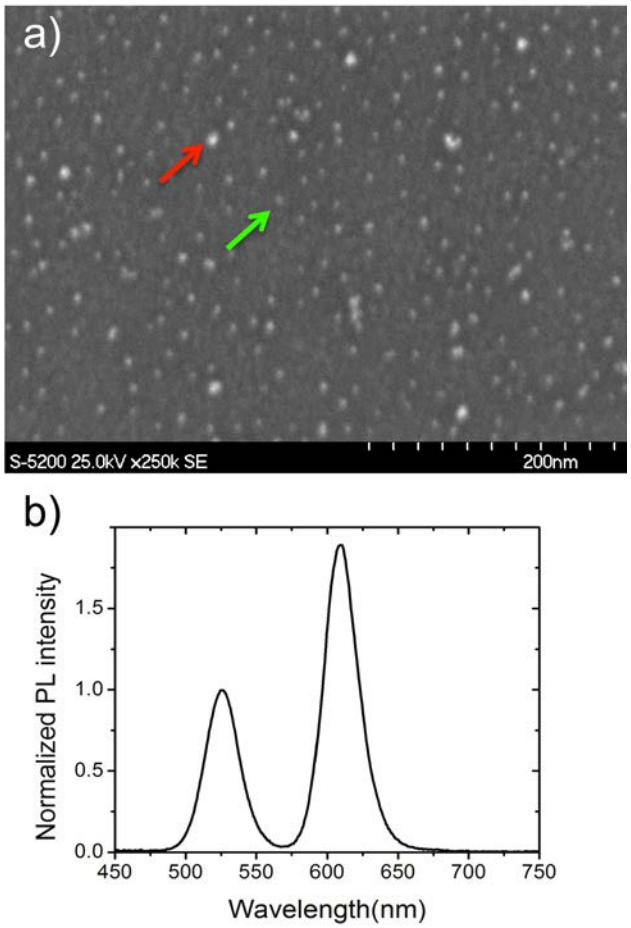

Figure 20. (a) SEM image showing co-immobilization of gQDs (green arrow) and rQDs (red arrow) in 12 to 1 molar ratio respectively on a silicon wafer. (b) PL spectrum corresponding to the SEM image shown in (a).

3.3.5 Two-Color Multiplexed Hybridization Assays

In previous solid-phase QD-FRET nucleic acid hybridization assays, a presence of mixed films of immobilized QDs and probe sequences in the multiplexed assay configuration resulted in a reduction of the assay sensitivity due to donor (QDs) and probe dilution effects [168]. Incorporation of up to four sequences in some assays caused a decrease in the number of acceptors for each FRET pair, reducing the extent of energy transfer in each detection channel [173]. Furthermore, since it was not possible to control the placement of a specific probe sequence onto a given QD, there was significant probability that acceptors could end up on QDs that could not serve as donors. While similar constraints on probe placement are apparent in the assay reported herein, spatially-based detection in the two-color multiplexed format did not suffer from the drawbacks of the donor and probe dilution effects in terms of assay sensitivity; rather an improvement in assay sensitivity was observed. Figure 21 shows epifluorescence images of (i) A647 and (ii) rQD

PL from a microfluidic channel for the injection of 79 fmol of uidA FC TGT in the (a) single-color assay format and in the (b) two-color assay format; images of the same microfluidic channel in the (iii) gQD and (iv) Cy3 detection channels are also shown for inclusivity of data. In the single-color assay format (rQDs and uidA probe only), the spatial length of a microfluidic channel exhibiting target hybridization was determined to be 1.68 ± 0.18 mm. In the two-color multiplexed format (both colors of QDs and both types of probes), the spatial length for the injection of same amount of target DNA was found to be 3.63 ± 0.35 mm, approximately a 2.2-fold increase in the spatial channel length coverage response in the two-color multiplexed assay format as compared to the single-color assay format. This difference was anticipated given that the spatial length of the FRET sensitized acceptor (A647) PL would increase since the probe density of each sequence at the interface was decreased by half in the two-color assay format relative to the single-color assay. In the multiplexed assay, fewer probe sites of each sequence are available for hybridization per unit area, which enabled an increase in the spatial coverage as targets could reach probe sites further along the length of the channel. In previous solid-phase FRET assays, transduction was accomplished by analysis of the FRET ratio based on changes in FRET sensitized acceptor PL. Multiplexed analysis reduced the extent of energy transfer in each detection channel and decreased assay sensitivity due to the dilution of donors and acceptors. The reduction in the FRET ratio response of the assay due to QD and probe dilution effects was seen in this work as well. For the rQD/A647 FRET pair, the FRET ratio dropped from 0.58(±0.05) to 0.31(±0.03) for the single-color (Figure 21a) and two-color (Figure 21b) assay formats, respectively. However, when quantification for a multiplexed format is based on a spatial occupancy of channel length, the reduction in the FRET ratio upon dilution does not affect the sensitivity of the assay. This increase in sensitivity in the multiplexed format highlights another advantage of the spatially-based detection for QD-FRET assays.

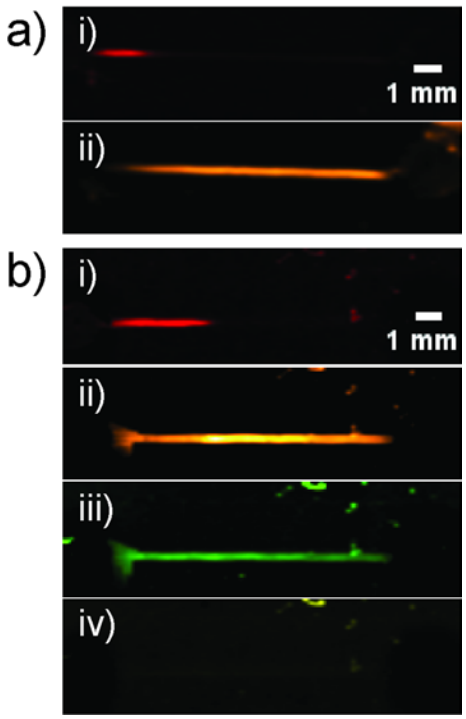

Figure 21. Pseudocolor epifluorescence images of microfluidic channels showing (i) A647 FRET sensitized acceptor PL and the corresponding (ii) rQD donor PL after the injection of 79 fmol of uidA FC TGT in the (a) single-color assay format and in the (b) multicolor assay format. Epifluorescence images of the same microfluidic channel in the multiplexed assay showing (iii) gQD donor PL and (iv) Cy3 acceptor PL are also shown in (b) for completion purposes. No visible Cy3 PL is seen in (iv) as no SMN1 FC TGT was injected in this channel.

The improvement in assay sensitivity was further illustrated by the response curve for the multiplexed concurrent transduction of both SMN1 and uidA TGTs as presented in Table 6. Figure 22a shows PL images for the detection of both targets in the (i-ii) gQD-Cy3 and in the (iii-iv) rQD-A647 detection channels. The FRET sensitized Cy3 PL images correspond to the injection of 49.5 fmol of SMN1 FC TGT in each channel and display reproducibility of spatial coverage of target DNA for the three replicate channels, with an average spatial length of 3.2 ± 0.6 mm. While the spatial profiles of Cy3 PL appear shifted in the Figure 22a, the use of the cross-over point between Cy3 and gQD PL emission zones greatly improves the precision of distance measurements. Further discussion about the significance of the cross-over point is was provided in Chapter 2 pg. 78 additional details can be found in Appendix 2 pg. 160 (Figure A2.3).

In the rQD and A647 detection channels, the PL images correspond to injection of 118, 78.9, and 39.4 fmol of uidA FC TGT from the top to bottom channels, respectively. The change in spatial profile displays a quantitative response of nucleic acid hybridization enabling transduction via channel length coverage in the multiplexed format. The concentration of the SMN1 FC TGT was held constant and the uidA FC TGT was varied. This suggested that the presence of one target did not influence the channel length coverage response of the other target. The response curves for both detection channels can be seen in Figure 22b. The increase in the coverage of each spatial profile was commensurate with a decreased FRET ratio as shown in Figure 22c as a result of dilution of both QDs and probes. Comparing the response curves for the two FRET pairs in the single-color and multiplexed hybridization experiments, the change in the response in terms of spatial channel length coverage was not identical for the two FRET pairs as shown in Table 6. In the case of the gQD/Cy3 FRET pair (SMN1 TGT), a 17% increase was seen in the slope of the multiplexed response curve when compared with the response curve for single-color experiments. For the rQD/A647 FRET pair (uidA TGT), a 95% increase was seen in the slope of the multiplexed response curve when compared with the single-color response curve. It should be noted the targets injection time and voltage were kept constant at 3 min and 200 V, respectively, for all the hybridization assays.

Table 6. Analytical figures of merit for the SMN1 and uidA TGTs in the single-color and two-color assay formats.

	Sensitivity (Slope of response curve) Channel length/amount of target DNA (mm fmol^{-1})	**y-intercept (mm)**
gQD/Cy3 SMN1 TGT (single-color assay format)	0.0219(±0.0006)	-0.25(±0.09)
gQD/Cy3 SMN1 TGT (two-color assay format)	0.0256(±0.0010)	1.95(±0.10)
rQD/A647 uidA TGT (single-color assay format)	0.0211(±0.0013)	-0.25(±0.35)
rQD/A647 uidA TGT (two-color assay format)	0.0413(±0.0056)	1.24(±0.48)

The small increase in the slope of gQD/Cy3 FRET pair (SMN1 TGT) can be ascribed to changes in hybridization efficiency as the slopes nearly mirror one another while the y-intercept is shifted

up due to probe dilution of the SMN1 sequences at the interface in the multiplexed assay format (cf. single-color assay format).

The substantial increase in the slope of rQD/A647 FRET pair (uidA TGT) is a result of the interfacial chemistry differences between the single-color and multiplexed assay formats. In the multiplexed design, the two colors of QDs were immobilized in a 12:1 (gQD:rQD) ratio. Thus the multiplexed assay assembly is similar to that of the gQD single-color assay format based on the number density of gQDs. This is significant due to the resulting probe density on the QD surface. The larger nanocrystal size of the SAv-rQDs as opposed to the SAv-gQDs (discussed in further detail in Chapter 4) enables an attachment of increased number of streptavidin protein molecules on the nanocrystal surface, and this allowed for an attachment of a greater number of probe molecules to the rQD surface as compared to the gQD surface. It was found by absorbance and fluorescence measurements that 68 and 46 probe sequences could be immobilized on rQDs and gQDs, respectively (see Appendix 2, Figure A2.5 and A2.6).

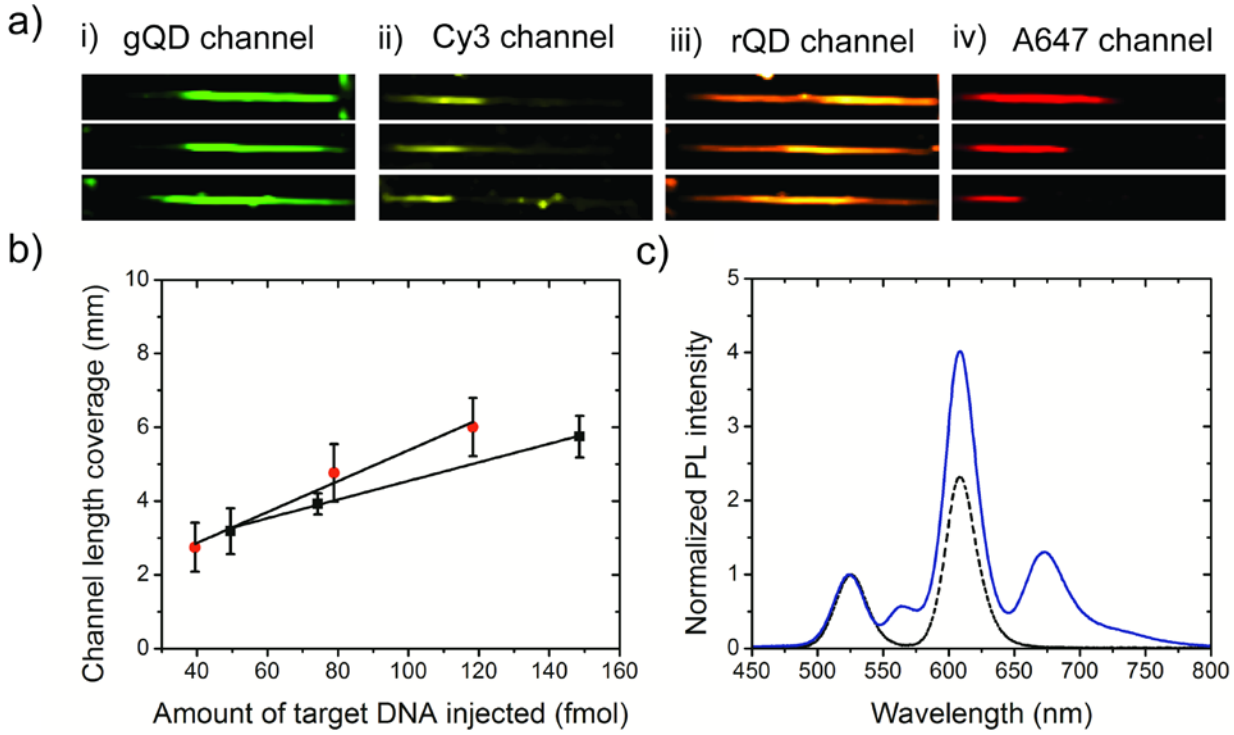

Figure 22. Two-color hybridization experiments showing the applicability of the assay to quantitatively transduce the SMN1 and uidA targets in a multiplexed format using a spatial channel length coverage response of donor and acceptor PL. (a) Pseudocolor epifluorescence images of (i) gQD donor PL, (ii) Cy3 acceptor PL, (iii) rQD donor PL and (iv) A647 acceptor PL for the injection of 49.5 fmol/118 fmol (top channel), 49.5 fmol/78.9 fmol (middle channel) and 49.5 fmol/39.4 fmol (bottom channel) of the SMN1/uidA targets. (b) Calibration curves for the SMN1 target (black square) and uidA target (red circle) displaying the channel length coverage response of each target as a

function of the amount of target DNA injected into the channel. (c) Normalized PL spectra in the absence (black dashed line) and presence (blue line) of the two DNA targets.

Hybridization experiments using Cy3 and A647 labeled TGTs confirmed that all bioconjugated probe sequences were available for hybridization. For a detailed discussion of probe loading capacity and hybridization efficiency, the reader is referred to Appendix 2 (Figure A2.6). The *ca.* 30% reduction in probe density experienced by uidA FC TGT in the multiplexed assay format (22 fewer probe molecules on gQDs as compared to rQDs) as compared to the single-color assay format (rQD/A647 FRET pair) explained the substantial increase in channel length coverage of uidA FC TGT in the multiplexed assay format. Furthermore, the 12:1 dilution of gQD compared to rQDs at the interface further enhanced the length of the spatial profile. The LOD of SMN1 and uidA targets in the multiplexed assay format are estimated by extrapolation to be ca. 3 fmol based on the improvement in assay sensitivity in the multiplexed assay format as compared to single-color assay formats.

In addition to improved assay sensitivity, the spatial transduction method enabled a simplified data analysis when compared to spectral analysis of absolute FRET ratios, the latter requiring deconvolution of spectra in previous assays. [168, 173] In this system, isolation of each PL signal by imaging was suitable to obtain the necessary information about a specific target analyte concentration, suggesting that this rapid detection method might be more suitable for point-of-care diagnostics.

The selectivity of the two-color multiplexed hybridization assays was demonstrated by discrimination against a 3BPM using sample solutions containing uidA FC TGT in addition to either SMN1 FC TGT or SMN1 3BPM TGT in a mixture. The mismatch discrimination was done at room temperature by using a combination of ionic strength and formamide as reported previously [201]. In order to induce the effect of ionic strength in providing selectivity for mismatch discrimination, the steps for the assembly of the biorecognition interface and target injection were done in BB (0 mM NaCl) instead of TB (100 mM NaCl). Lowering the ionic strength destabilizes a DNA duplex by preventing the charge screening associated with the negatively charged phosphate backbone of DNA [202, 203]. In addition, formamide serves as a hydrogen bond disrupter and resides at sites within the duplex that are normally occupied by water molecules. Ultimately the melt temperature of the DNA duplex is lowered and resolution of mismatched sequences can be achieved at room temperature [204]. The results for mismatch discrimination are

shown in Figure 23. Hybridization assays conducted in BB provided no selectivity between SMN1 FC and 3 BPM TGTs at room temperature. Increasing the stringency of nucleic acid hybridization by introduction of 20% (v/v) formamide in BB within microfluidic channels for 10 min at 200 V provided a contrast ratio of 8 to 1 for SMN1 FC to SMN1 3BPM TGT. In the presence of 20% (v/v) formamide in BB, the FRET ratio responses associated with the SMN1 and uidA FC TGTs were 75% of those for hybridization assays conducted in BB alone.

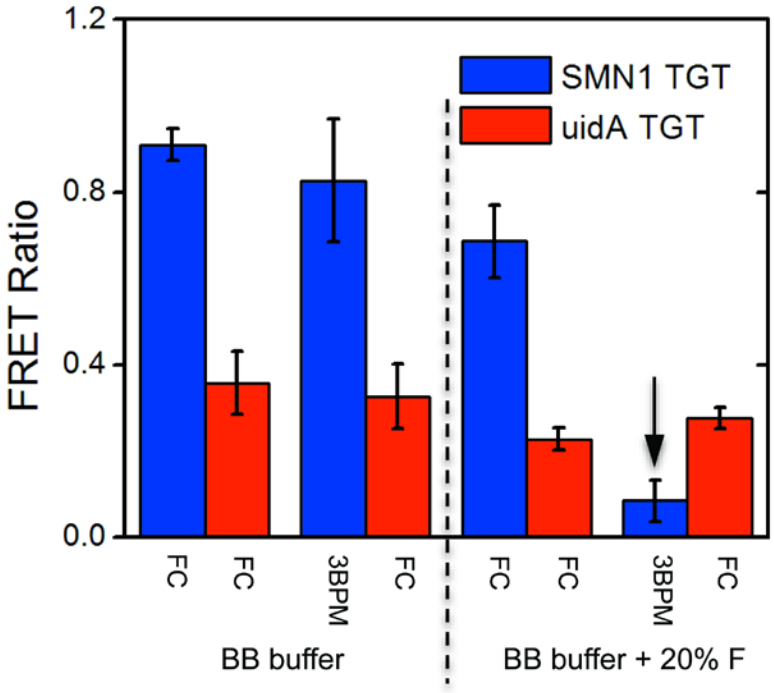

Figure 23. Mismatch discrimination between SMN1 FC and SMN1 3BPM TGTs in the multiplexed assay format. Addition of 20% (v/v) formamide into the channel enabled discrimination against a 3BPM TGT (black arrow) while 75% of the original FRET ratio response associated with the SMN1 and uidA FC TGTs was retained. The black arrow indicates 3BPM discrimination.

3.4 Conclusions

In this work, the implementation of solid-phase QD-FRET multiplexed assay for oligonucleotide detection within an electrokinetically controlled microfluidic chip was investigated. The interior of the biotin functionalized glass wall of hybrid glass/PDMS based microfluidic channels was decorated with streptavidin coated multicolor QDs. Two different oligonucleotide probe sequences were then delivered to immobilize with the QDs inside a microfluidic channel. These steps were completed within minutes to facilitate *in-situ* and on-demand assembly of the

biorecognition interface. Subsequent in-channel delivery and hybridization of dye-labeled oligonucleotide targets provided the proximity for FRET sensitized energy transfer from gQDs and rQDs donors to Cy3 and A647 acceptors, respectively. The emission from the acceptor dyes served as the basis on which an analytical signal could be determined. Electrokinetically mediated mass transport of target oligonucleotides to the biorecognition interface provided for completion of hybridization within minutes. Quantitative determination of femtomole quantities of the two oligonucleotide targets (SMN1 and uidA) was possible by measurement of spatial channel length coverage by the two oligonucleotide targets. The channel length coverage was dependent on “turn-on” PL profiles of the two acceptor dyes and “turn-off” PL profiles of the two donor QDs. As compared to other solid-phase QD-FRET nucleic acid hybridization assays that rely on the PL intensities of donors and acceptors for quantification, the spatially-based detection method provided improved sensitivity when subjected to similar constraints of dilution of donors and acceptors when operating in a multiplexed detection format. Hybridization assays showed excellent resistance to non-specific adsorption of oligonucleotides, and provided a contrast ratio of 8 to 1 for 3BPM discrimination by using a combination of ionic strength and formamide. This work provides an important precedent towards the integration of solid-phase multiplexed QD-FRET assays within microfluidics, where the spatially-based detection method enhances precision and simplifies data analysis.

4 Interfacial Nucleic Acid Hybridization on Streptavidin Coated Quantum Dots: Impact of Nanocrystal Size on the Sensitivity and Selectivity of Oligonucleotide Conjugates

The following content in Chapter 4 is unpublished at the present time. The hydrodynamic radii of both QDs were measured by Zhenfu Zhang from the Gradinaru Group at UTM using FCS. MON is also thanked for collection of the data set containing the effect of ionic strength on SNP selectivity. The remainder of the experiments, results, and data analysis was performed by AJT.

4.1 Introduction

Perhaps one of the most important characteristics of a nucleic acid bioassay or biosensor is the ability to resolve oligonucleotides with mismatches within a mixture of target sequences. The work reported in Chapters 2 and 3 developed assays in either single or multiplexed formats that have offered discrimination of duplexes containing a 3BPM. Ideally assays should offer selectivity for distinction of a 1BPM or a SNP, as single base insertion, deletions, or mutations can lead to disease as described previously in the case of spinal muscular atrophy. The intrinsic selectivity of hybridization can enable SNP resolution as the T_m of each duplex is different. Through a systematic evaluation of denaturation conditions it is possible to selectivity melt the SNP duplex prior to that of the perfectly matched duplex. The difference in probe loading capacities of gQDs and rQDs as observed in Chapter 3, which is likely a result of the different size scales of the QDs, has significant impact on selectivity. In an effort to find suitable conidtions for SNP selectivity, it was necessary to evaluate the stringency conditions for each QD. .

Previous work that has conjugated oligonucleotides to glass, fused silica and gold has demonstrated that surface propoerties such as charge and the density of probe immobilization must be considered as features that impact selectivity and sensitivity.[205-208] Chapter 4 evaluates the impact of QD size and the average number of conjugated oligonucleotide probes on the analytical performance of a FRET-based hybridization bioassay. The same SMN1 19mer probe-target oligonucleotide hybridization system was used on the gQDs and rQDs which had similar

chemistry but different size. The radius of hydration of the SAv-gQD and SAv-rQD were measured fluorescence correlation spectroscopy (FCS) to be 8.47 ± 0.14 nm and 12.74 ± 0.51 nm, respectively. Significant differences in selectvity were noted for the interfacial hybridization of SNPs with immobilized probes on the rQDs in comparison to those on the gQDs. This is presented by the schematic shown by Figure 24, where without any added denaturant, SNP discrimination was possible using the rQD. SNP discrimination was not achieved with the gQD system even when stringency was adjusted using a chaotrope. This effect is consistent with a higher effective charge on the rQD as compared to the gQD, which results from the ability of the rQD to accommodate more SAv molecules and oligonucleotide probes.[206]

Furthermore, insights into sensitivity were of interest. It was expected that the smaller size of the gQD would provide for higher energy transfer efficiency due to the inverse sixth power dependence of FRET on distance, but the additional acceptor loading capacity of the rQD could also provide for higher energy transfer efficiency. It was determined that the additional acceptor loading capacity of the rQD had a contributing effect in terms of the FRET intensity. The rQD had higher quantum yield than the gQD, and this appeared to be an influential factor. This study demonstrates the significance of bioconjugation density on QD surfaces, which impacts on both sensitivity and selectivity of QD-FRET bioassays and bioprobes.

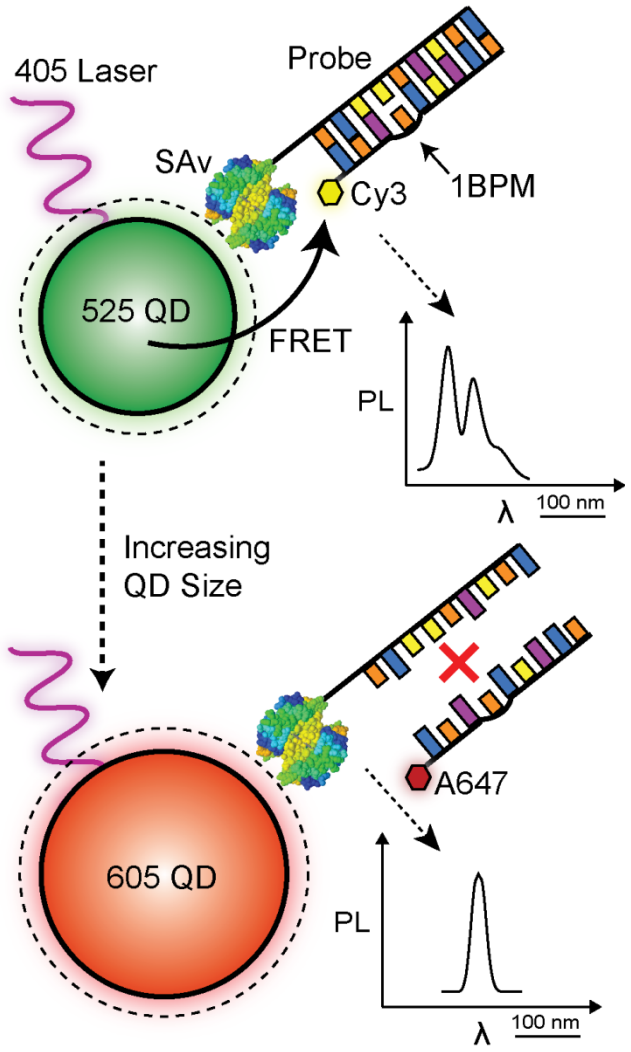

Figure 24. Schematic representation of the interfacial hybridization of a SNP target to SAv-gQDs and SAv-rQDs derivatized with probe oligonucleotides. Spectral discrimination of a SNP target was not possible for the assay using the gQD (excitation by a 405 nm laser), as indicated by emission from both the gQD and the Cy3 label. In contrast, the larger rQD was loaded with a greater number of oligonucleotide probes (not shown in the schematic) and provided discrimination of a SNP target due to improved electrostatic repulsion. Upon excitation, the rQD system produced minimal FRET sensitized A647 emission, with emission from the rQD being the predominant spectral feature.

4.2 Experimental Methods

4.2.1 Preparation of QD-SMN1 Probe Conjugates

The nucleic acid sequences used in this study are given in Table 7. CdSe/ZnS Qdot® 525 ITK™ and 605 ITK™ Streptavidin Conjugates (Life Technologies Oakville, ON, Canada) were incubated with an 100-fold excess of SMN1 biotinylated probe oligonucleotides (SMN1 probe) each in Tris-borate buffer (TB) and placed on an orbital shaker for 2 h.[207] A triethylene glycol (TEG) linker was incorporated between the biotin tag and the first nucleobase of the SMN1 probe. The QD SMN1 probe conjugates (QD-SMN1-PC) were purified from excess probe oligonucleotides using Amicon ultra-0.5 mL, Ultracel-100 Membrane, 100 kDa centrifugal filters (Millipore Corp., Billerica, MA) and centrifuged at 8000 RPM three times for 4 min in each wash, using 300 µL of fresh TB each time. For selectivity experiments, QD-SMN1-PC samples were washed with borate buffer (BB). Purified conjugates were resuspended in a total volume of 250 µL of TB (BB for selectivity experiments). Despite attempts to extensively wash the filter unit, residual QD PL was still observed from the filter matrix. In order to determine the effective concentration of the QD-SMN1-PC samples after purification, the percentage of conjugated QDs recovered was calculated using PL intensity measurements. The PL intensity from the unpurified solution was measured prior to centrifugation and after the purified conjugates were resuspended in the same amount of buffer. Integrating the resulting PL spectra, followed by ratiometric comparison of the integrated PL intensities allowed for the determination of the percentage of QD-SMN1-PC that were recovered. The recovery was *ca.* 80% for the gQDs and *ca.* 90% for the rQDs (data not shown). Conjugation of probe oligonucleotides to SAv-QDs was confirmed using gel electrophoresis and by analysis of the relative mobility shift compared to SAv-QDs (see Appendix 3 Figure A3.1). Solutions of SAv-QDs and QD-SMN1-PCs were loaded on a 2% w/v agarose gel in BB. Solutions were diluted 1.2 times with 20% w/v sucrose solution in deionized water prior to loading. The gel was run at a constant electric field of 3.6 V cm^{-1} for 2 hr and then imaged on a Gel Doc (Bio Rad) under QDOT 525 and QDOT 625 bandpass filters. The composite image overlay was produced using Image J software (National Institutes of Health, Bethesda, MD) from the two separate acquisitions. Oligonucleotide loading capacities for gSAv-QDs and rSAv-QDs were determined previously using UV-Vis absorption spectroscopy and through FRET PL responses with labeled oligonucleotide targets as shown in

Chapter 3. The gSAv-QDs and rSAv-QDs SMN1 PC loading capacities were 46 ± 1 and 68 ± 1 per QD, respectively.

4.2.2 Hybridization Experiments and FRET Efficiency

The purified gQD-SMN1-PCs and rQD-SMN1-PCs were mixed with increasing amounts of FC Cy3 and FC A647 TGT oligonucleotides, respectively, and the solutions were vortexed and allowed to stand at room temperature for 4 h.

Table 7. Oligonucleotide Sequences.

SMN1 probe	Biotin-TEG - 5’ - ATT TTG TCT GAA ACC CTG T - 3’
FC-Cy3 TGT	Cy3 - 3’ - TAA AAC AGA CTT TGG GAC A - 5’
SNP-Cy3 TGT	Cy3 - 3’ - TAA AAC A**C**A CTT TGG GAC A - 5’
FC-A647 TGT	A647 - 3’ - TAA AAC AGA CTT TGG GAC A - 5’
SNP-A647 TGT	A647 - 3’ - TAA AAC A**C**A CTT TGG GAC A - 5’

Biotin-TEG: biotin with a triethylene glycol linker; FC TGT: fully-complementary target; SNP: single nucleotide polymorphism. The mismatch location is bolded, underlined and colored in red.

Acquisition of steady state PL spectra was done using an excitation wavelength of 405 nm. The PL was scanned over the wavelength range of 450-700 nm for the gQD-Cy3 FRET pair and from 550-800 nm for the rQD-A647 FRET pair. FRET efficiencies were determined using time-resolved PL measurements, and each PL decay curve was an average of three acquired traces from the same sample. The concentration of the gQDs varied from 25-40 nM and the rQDs from 10-20 nM for the steady state and time-resolved measurements.

4.2.3 Selectivity of Hybridization and SNP Resolution

For all selectivity experiments, hybridization with FC and SNP TGTs was done in BB with no additional NaCl as to enhance stringency conditions, and at 15-20 fold excess of target relative to the number of probes immobilized. Formamide was added to BB to further enhance the stringency conditions. After addition of formamide, solutions were allowed to stand for 30 min and then PL spectra were collected using excitation at 405 nm. For selectivity experiments in goat serum, the FC and SNP target solutions were prepared in 50% v/v goat serum instead of neat buffer. In studies investigating the effect of probe density on selectivity, rQD-SMN1-PCs

with different amounts of immobilized SMN1 probe were incubated with a 10 fold excess of FC and SNP TGTs (relative to the amount of immobilized probe). In evaluating the effect of ionic strength on selectivity, sodium chloride was added directly to the hybridization solutions containing rQD-SMN1-PCs with FC and SNP TGTs. After an aliquot was added, the solutions were allowed to stand for 30 min and the PL was determined. Although continued additions diluted the samples, analysis via an assigned FRET ratio alleviated this issue.

4.3 Results and Discussion

4.3.1 FRET Efficiency and Sensitivity

The sensitivity of QD-FRET nucleic acid hybridization assays are often measured by the magnitude of the ratio of the FRET ratio which is defined as the ratio of acceptor to donor PL. This is influenced by the quantum yield of the acceptor and the efficiency of energy transfer as related to the number of donor-acceptors interactions at the QD interface. Two FRET pairs are considered herein; gQD-Cy3 and rQD-A647 and have been extensively characterized spectroscopically by our group. The quantum yields of the Cy3 and A647 dyes that are the labels on the target oligonucleotides have been previously determined to be 0.2 and 0.52, respectively.[209] Despite the *ca.* 2.5 fold brighter PL of A647 as compared to Cy3, the sixth power distance dependence of FRET and the energy transfer efficiency will also significantly influence the intensity of FRET sensitized acceptor PL as governed by the Förster formalism. The efficiency of energy transfer (E) is given by Eqn. 20 (previously defined in Chapter 1), where R_0 is the Förster distance and the donor-acceptor separation distance is given by r.

$$E = \frac{nR_o^6}{nR_o^6 + r^6} \tag{20}$$

These QD-dye FRET pairs have been extensively characterized spectroscopically by our group. The Förster distances for the gQD-Cy3 and rQD-A647 FRET pairs were determined to be 6.2 and 8.0 nm, respectively. The reasoning for the 1.3-fold larger Förster distance for the rQD-A647 FRET pair is two-fold. The donor-acceptor spectral overlap is much larger for the rQD-A647 FRET pair *cf.* 1.55×10^{-9} $cm^6 \cdot mol^{-1}$ vs 6.31×10^{-10} $cm^6 \cdot mol^{-1}$ than for the gQD-Cy3 FRET pair as determined in Chapter 3.[209] Furthermore, the quantum yield of the SAv-rQDs (Φ = 0.89) is also *ca.* 1.9-fold larger than that of the SAv-gQDs (Φ = 0.48). An increased Förster distance ultimately offers improved FRET efficiency for larger values of r. This can be

illustrated by dividing the right side of Eqn. 20 by R_0^6. In this form Eqn. 20 describes the energy transfer efficiency as function of (r/R_0) for a given FRET pair. This has important implications on QD-FRET since the donor PL emission is tuned by the size of the nanocrystal. Furthermore, it is noteworthy to mention that the Förster formalism considers the donor and acceptor as point dipoles, where the center-to-center distance is taken from the center of the QD.[210] The intrinsic size of different QDs will influence the efficiency of energy transfer. The CdSe/ZnS QDs nanocrystals that emit at 525 nm have an inorganic diameter of about 3 nm, whereas the 605 QDs had a diameter closer to 5 nm.[36] This 66% relative increase in size of the rQDs would have a negative impact on energy transfer efficiency given that the Förster distances for the two FRET pairs are identical. For the FRET pairs described herein, the larger Förster distance for the rQD-A647 FRET will likely compensate for the increased intrinsic size of the nanocrystal. Moreover, the surface chemistry of the QDs used herein consists of anamphilic polymer terminated with carboxylic acids. The QDs are further conjugated with SAv which adds considerable size.The diameters of the the SAv-gQDs and SAv-rQDs were reported to be 12 and 15 nm, respectively as measured by the manufacturer through size-exclusion chromatography. Using fluorescence correlation spectroscopy (FCS), we measured the radius of hydration of both colors of SAv-QDs. A value of 8.47 ± 0.14 nm was found for the SAv-gQDs and 12.74 ± 0.51 nm for the SAv-rQDs, Other reports in the literature have measured these same QDs to be indistinguishable in hydrodynamic radius within experimental precision using FCS, albeit the SAv-rQDs have a higher mean hydrodynamic radius.[211, 212] These data suggest that the proportional differences in intrinsic nanocrystal size are in fact lessened by both the amphiliphilic polymer and the immobilized SAv. Nonetheless, since these nanocrystals are prepared in batch synthesis, slight variations in size and resulting composition may result between different studies. In Chapter 3 it was determined that 46 and 68 nucleic acid probes could be immobilized on the SAv-gQDs and SAv-rQDs, respectively using a combination of absorbance and fluorescence spectroscopy. This occupancy of biotin binding sites at each QD interface is also consisten with what others have reported in the literature.[213] The ability to immobilize *ca.* and additional 20 probes on the SAv-rQD should also provide for improved energy transfer efficiency as displayed by Eqn. 1. It was anticipated that similar energy transfer efficiencies would be displayed in both FRET pairs.

Time-resolved fluorescence (TRF) measurements were used to determine the FRET efficiency (*E*) independent of acceptor quantum yields using Eqn. 21 (previously defined in Chapter 1).

$$E = 1 - \frac{\tau_{DA}}{\tau_D} \tag{21}$$

where τ_{DA} and τ_D are the lifetimes of the donor in the presence and absence of the acceptor, respectively. The lifetimes of both gQD and rQD probe conjugates obtained from fitting of the TRF data are shown in Table 8 for increasing amounts of Cy3 and A647 target oligonucleotides.

Table 8. PL lifetimes of the gSAv-QDs and rSAv-QD SMN1 PCs in response to increasing amounts of Cy3, and A647 labeled FC TGTs.

SAv-gQD – Cy3 Hybrids		SAv-rQD – A647 Hybrids	
Average No. of Acceptors	τ, ns	Average No. of Acceptors	τ, ns
0	18.9 ± 0.2	0	29.5 ± 0.6
25	8.6 ± 0.1	24	15.9 ± 0.1
50	3.4 ± 0.1	48	8.9 ± 0.1
75	2.6 ± 0.1	72	6.8 ± 0.1
		96	6.4 ± 0.1

The relationship between the energy transfer efficiency and the average number of acceptors on a QD is presented in Figure 25. The trend of the data indicates saturation of energy transfer efficiency at *ca.* 50 and 70 acceptors for the SAv-gQD and SAv-rQD, respectively. This is consistent with a the data presented in Appendix A2, pgs. 160-164.[209] The maximum energy transfer efficiences were 86 ± 3% for SAv-gQD-Cy3 SMN1 hybrids and 78 ± 2% for the SAv-rQD-A647 SMN1 hybrids.

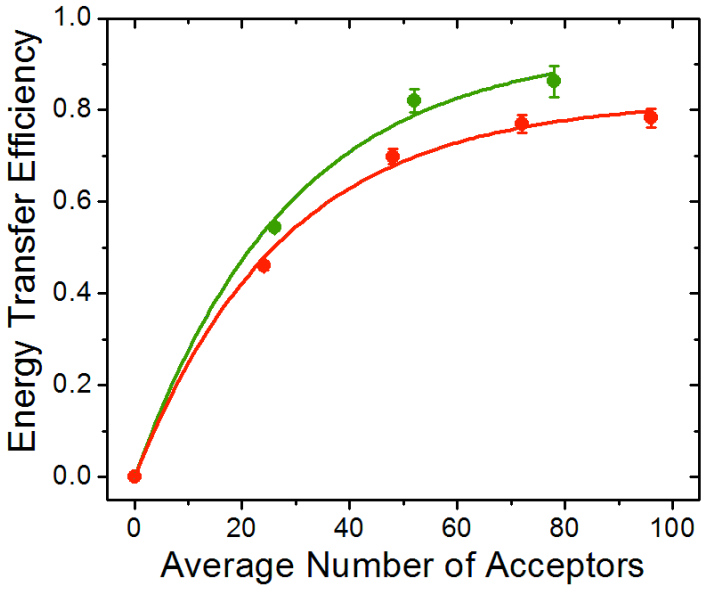

Figure 25. Efficiency of energy transfer as determined by changes in QD lifetime for the gQD (green curve) and rQD (red curve) SMN1 probe conjugates with increasing concentrations of FC Cy3 and A647 labelled TGTs, respectively. The concentration of the SMN1 gQD conjugates was 40 nM, and samples were incubated with 1, 2, and 3 µM of FC Cy3 TGT. The SMN1 rQD conjugate concentration was 18 nM, samples were incubated with 0.4, 0.8, 1.2, and 1.6 µM of FC A647 TGT.

The overall difference in efficiency of energy transfer was slightly less than 10%. The data presented in Figure 25 shows that when *n* is doubled in the regime well before saturation, the efficiency of energy transfer increases by a factor of 1.5 for both FRET systems. For hybridization with approximately 50 acceptors, energy transfer efficiencies were 0.82 ± 0.03 and 0.70 ± 0.02 for the gQD-Cy3 and rQD-A647 systems, respectively. A total of about 50 acceptors per QD provided energy transfer saturation for the gQD. For rQD hybridization, an additional *ca.* 15-25 acceptors results in a FRET efficiency of 0.77 ± 0.02, which represents saturation at a level of energy transfer efficiency that is within experimental precision of that seen for the gQD-Cy3 system. within experimental precision as seen in Figure 25. These results suggest that when the coating on a nanocrystal has dimensions that are on the order of (or larger than) the diameter of the core-shell QD, then the sixth power sensitivity to distance of the FRET process may become secondary and other aspects such as the acceptor loading capacity and the intrinsic photophysical properties may dominate the efficiency of energy transfer.

4.3.2 Transduction of Single Nucleotide Polymorphisms

The selectivity offered by each QD for the same SMN1 target was evaluated. Discrimination of mismatched sequences are often considered indicative of assay selectivity for nucleic acid hybridization. The probe-target combination used in this work is suitable for SNP determination in Spinal Muscular Atrophy, where the Survival Motor Neuron probe, SMN1, can ideally detect SNP that represents the disease state.[207] To optimize assay conditions for SNP selectivity, we first evaluated the selectivity offered by each QD-SMN1 conjugate in bulk solution as controlled by stringency conditions. The response of gQD-SMN1-PC and rQD-SMN1-PC to an excess (100-fold) of FC and SNP TGTs in BB with no added NaCl is shown in Fig. 26(a). No contrast was visible for FC and SNP Cy3 TGTs in the green channel. For the red channel, hybridization of FC and SNP A647 TGTs to the rQD-SMN1-PC displayed substantially different responses with FRET ratios of 0.86 ± 0.01 and 0.40 ± 0.01, respectively. The resolution of a SNP TGT was possible using the rQDs at a 9.8:1 contrast ratio, and was achieved without any added denaturant to increase stringency. The higher selectivity can in part be attributed to the immobilization of an additional *ca.* 25 oligonucleotides on the rQD. Assuming a spherical QD, the oligonucleotide density was determined to be 0.051 probes·nm^{-2} and 0.033 probes·nm^{-2}, on the gQD and rQD, respectively. The differences in hybridization efficiency between the FC and SNP TGTs may be a function of both the intrinsic charge of the SAv-QD and the overall particle zeta potential from the polyanionic immobilized oligonucleotide probes. Moreoever studies of interfacial hybridization assays on carboxylic acid terminated polystyrene beads have shown that carboxylate density and resultant charge are influential parameters to consider from the stand point of probe immobilization and hybridization efficiency.[214]

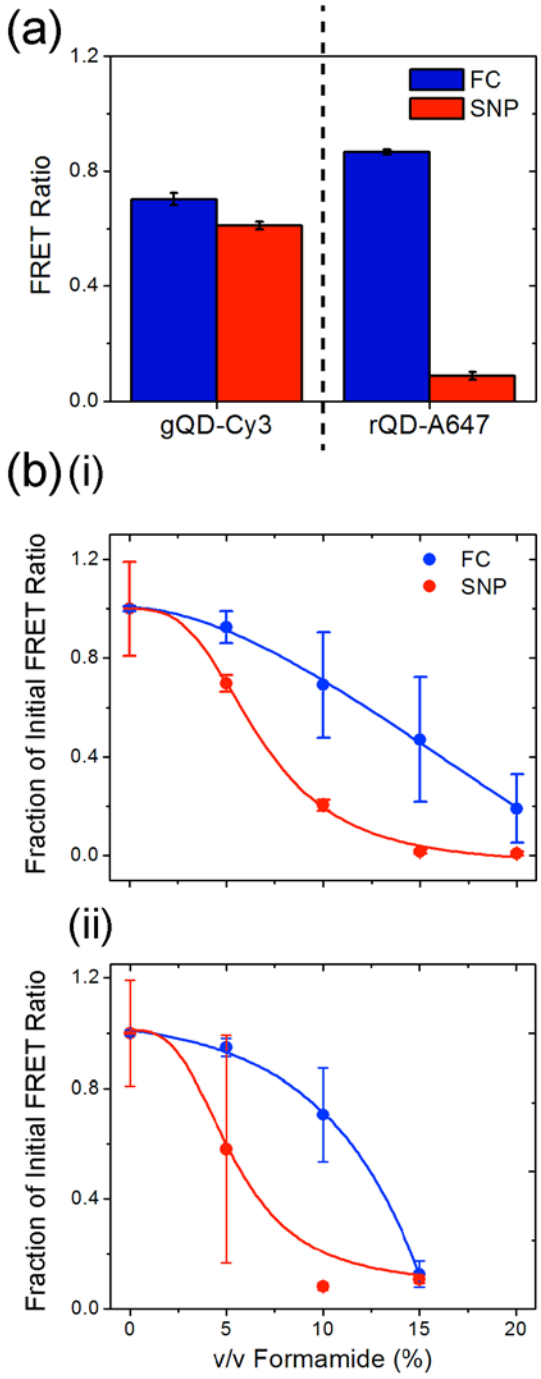

Figure 26. (a) FRET ratio response in the absence of formamide of the gQD-SMN1 PC (left) and rQD-SMN1 PC (right) to FC (blue) and SNP (red) SMN1 targets labeled with Cy3 and A647, respectively. Resolution of a target sequence containing a SNP was not discerned using the gQD-SMN1 PC (contrast ratio: 1.2:1), while a 9.8:1 contrast ratio was observed using the rQD-SMN1 PC (b) Denaturation of FC (blue) and SNP (orange) targets from rQD-probe conjugates and gQD-probe conjguates by addition of formamide. FRET ratios are normalized to the initial response observed for each target. Addition of formamide provided the stringency control for improved discrimination of the SNP, an additional *ca.* 5% v/v formamide was required to melt the SNP response to baseline signal at the interface of the gQD in comparison to the rQD.

To further improve the contrast between FC:SNP TGTs and to evaluate the difference in duplex stability at each QD interface, formamide (% v/v) was incorporated into the hybridization assay for the rQD-SMN1 PC with FC and SNP TGTs.[25] Figure 26(b) (i) and (ii) show the assay response to increasing amounts of formamide for FC and SNP TGTs on gQD and rQD-SMN1 hybrids. The respective FRET ratios are plotted as a percentage of the initial response for both targets to illustrate the degree of duplex denaturation at each increment of added formamide. In Figure 26(b) (i) an optimal contrast of 33:1 between FC and SNP TGTs at the gQD interface was observed at 15% v/v formamide in BB where the FRET ratios for the FC (0.33 ± 0.17) and SNP (0.010 ± 0.005) TGTs were reduced to 47% and 2% of their initial response, respectively. On the contrary, at the rQD interface only 10% v/v formamide in BB was required to achieve an optimal contrast ratio of 43:1 (Figure 26(b) (ii)). The response of the SNP TGT is reduced to 8% of its initial response with a FRET ratio of 0.012 ± 0.001, while the response from FC TGT is still large at 71% with a FRET ratio of 0.51 ± 0.12. Furthermore, differences in hybridization efficiency can be seen for the FC TGT at each respective QD interface. As shown in Figure 26(b) (i) 50% of the FC duplexes at the gQD interface are denatured at *ca.* 15% v/v formamide while only *ca.* 12.5% v/v formamide is required to achieve the same degree of denaturation on the rQD (Figure 26(b) (ii)).

4.3.3 Effect of Probe Number on Selectivity

To evaluate whether the higher stringency of hybridization at the rQD-SMN1-PC was in fact a result of overall conjugate charge and or a result of differences in the number of immobilized oligonucleotides, different amounts of SMN1 probe oligonucleotides were immobilized on the rQDs. The immobilization of different amounts of SMN1 probe on the rQDs was confirmed by gel electrophoresis (see Appendix 3 Figure A3.2) where increased probe number resulted in increased migration distances toward the anode. It was estimated that a maximum of *ca.* 46 SMN1 oligonucleotide probes could be immobilized on gSAv-QDs. If a similar number of SMN1 probes were immobilized on the rSAv-QD then a contrast of 1.2:1 between FC and SNPs TGTs would be expected given that the oligonucleotides were the predominant source of the charge difference between both sizes of QD.

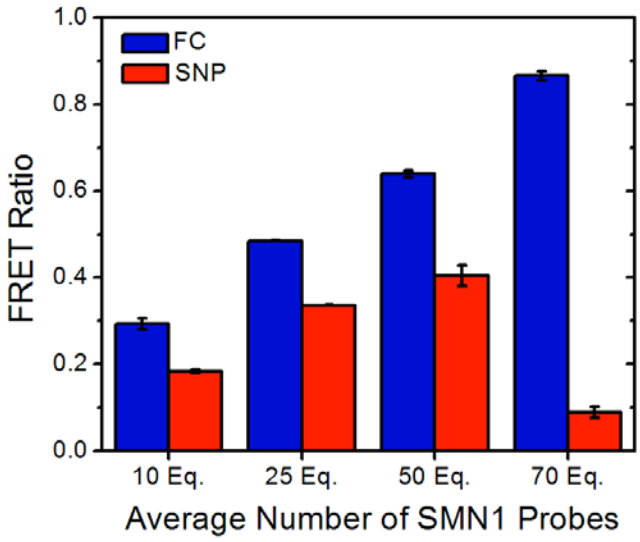

Figure 27. Immobilization of an increasing number of SMN1 probes on rQDs and the resultant response of the bioconjugates to FC and SNP TGTs. Despite only derivatization with 10 equivalents (Eq.) of SMN1 probe, contrast between FC and SNP TGTs is seen, with the highest contrast ratio (9.8:1) visible at saturation (67 probes per QD).

The response of the rSAv-QD with an increasing number of immobilized SMN1 probes to FC and SNP TGTs is shown in Fig. 27. Even at 10 immobilized SMN1 oligonucleotides per QD, improved contrast (1.5:1) between FC and SNP TGTs was visible where the FRET ratios for the FC and SNP TGTs were 0.29 ± 0.01 and 0.18 ± 0.01, respectively. A minimum of 10 Eq. of probe was chosen to avoid Poisson statistics governing the distribution of oligonuceotides on the SAv-rQDs which is often seen for biomolecule conjugates of 5 Eq. or less.[215] At 25 and 50 SMN1 probes per QD, the response to the FC TGT increased to 0.49 ± 0.01 and 0.64 ± 0.01, where the response to the SNP increased to 0.34 ± 0.01 and 0.40 ± 0.02, and respectively. At an average of 50 SMN1 probes immobilized per rQD these rQD-SMN1-PC have a similar probe valency to the gQD-SMN1-PC at saturation of immobilized probe, yet they display a slightly improved contrast ratio (*cf.* 1.6 vs. 1.2). These data suggest that the instrinsic charge of the QD may also influence the hybridization efficiency assuming that the increase in charge provided by the *ca.* 50 oligonucleotide probes would be consistent amongst both QDs. The isolectric point of immobilized monolayers of SAv has been reported to be *ca.* 5.5 and the resultant charge is dependent on ionic strength.[216] Since hybridization was conducted herein at pH 9.25, the SAv immobilized on both QDs are negatively charged and contribute to the overall effective charge of the QDs in addition to the underlying carboxylic acid coating on the QDs to which the protein is conjugated. The zeta potentials of the gSAv-QDs and rSAv-QDs were measured to be -20 mV

and -25 mV, respectively using Ferguson analysis of the electrophoretic mobility in agarose gels as described elsewhere[217] (details can be found in Appendix 3, see Figure A3.3). This 25% relative higher anionic charge of the rQD compared to the gQD can explain the reduced hybridization efficiency and kinetics of the SNP at the rQD interface despite the same number of SMN1 probe immobilized on each QD. While the optimal contrast ratio between FC and SNP TGTs was seen at saturation of SMN1 probe (68 probes per QD) at the rQD interface, the response to the SNP decreased rapidly to 0.09 ± 0.01 where the FRET ratio for the FC TGT increased to 0.87 ± 0.01. The additional oligonucleotides further increased the stringency of hybridization at the rQD interface and reduced the hybridization efficiency of the SNP as a result of charge repulsion between adjacent probes. The additional probe sites did not reduce the hybridization efficiency of the FC TGT, and rather hybridized with additional TGTs as displayed by the increase in the FRET ratio. In a study which investigated the effect of conjugation chemistry on the resultant DNA orientation, SAv-biotin mediated probe immobilization on the same QDs used herein displayed conjugates with no specific probe oreintation.[180] Distance dependent FRET measurements suggested that the oligonucleotides were extended from the QD interface in all directions as a result of the diverse orientation of the surface immobilized SAv. These findings provide insight into the mechanism responsible for the reduced hybridization efficiency of the SNP at maximum probe loading on the rQD-SMN1-PC, where repulsion between anionic phosphate backbones is prominent since the immobilized oligonucleotides are not oriented in a single direction to minimize steric repulsion. Moreoever, these effects are likely more pronounced as result of the low ionic strength buffers used herein for hybridization experiments.

4.3.4 Effect of Ionic Strength on SNP Resolution

It was hypothesized that the electrostatic repulsion between immobilized oligonucleotides at the QD surface with nucleic acid targets increased the stringency of hybridization. To confirm that this was responsible for the improved contrast between FC and SNP TGTs, it was expected *a priori* that if the ionic strength were increased, the added sodium would suppress the local charge and enable increased hybridization of the SNP TGT. Figure 28 shows the assay reponse to both targets (blue curves) as a function of increasing ionic strength by addition of sodium chloride. The contrast ratio between the two targets is also given by the black curve. Under conditions of no additional added sodium ion other than that from the 50 mM BB (i.e., 25 mM NaCl), the

contrast ratio for FC:SNP was 9.8:1. Increasing the ionic strength resulted in an exponential increase in the response of the rQD-SMN1 PC to the SNP as determined by the FRET ratio. At an added 30 mM NaCl in addition to the 25 mM NaCl contribution from the BB, the contrast between targets decreased rapidly to 1.2:1 and at 100 mM NaCl the response between targets was indistinguishable within the precision of the experiment.

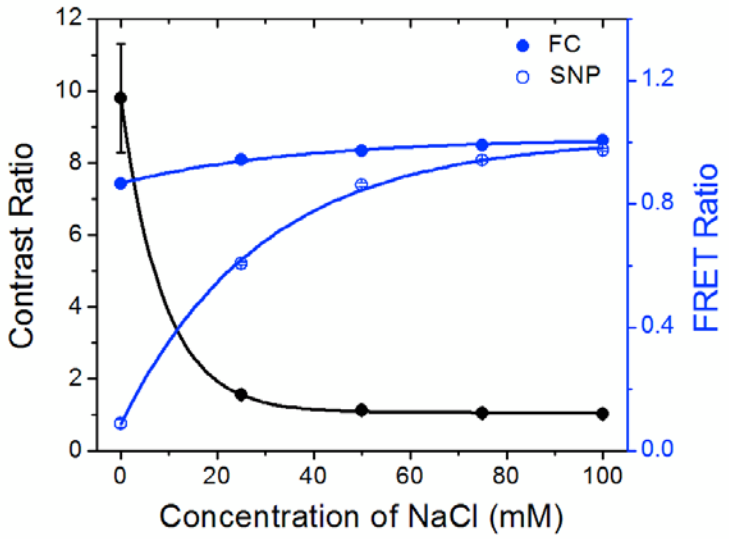

Figure 28. Response of the rQD-SMN1 PC to FC (filled blue dots) and SNP (open blue dots) TGTs with increasing concentration of NaCl. As additional NaCl is added to the solution, the contrast ratio (black curve) is reduced from 10:1 to 1:1 at 100 mM of NaCl, where the added sodium screens the charge of the rQD-SMN1 PC enabling hybridization of the SNP TGT. Note: an additional 25 mM NaCl contribution from the BB was also present in all the sample solutions.

The decreased contrast ratio is consistent with screening of the effective charge of the rQD-SMN1 PCs by the increase in ionic strength. While at a lower concentration of sodium, only perfectly matched duplexes are stable at the rQD interface.

4.3.5 Toward SNP Resolution in Complex Matrices

The previous analyses toward discrimination of SNPs were conducted in neat buffer solutions. A rigorous test of assay robustness and selectivity would afford analysis under more realistic sample conditions in a complex matrix. To further evaluate the robustness of the proposed QD-FRET hybridization assay reported herein, we evaluated whether transduction of SNPs could be conducted in 50% v/v goat serum utilizing the SAv-rQD-SMN1-PC given the higher selectivity of these conjugates relative those prepared using SAv-rQDs. The response of the assay is shown

by Figure X without any added formamide the response to the FC and SNP targets were 0.732 ± 0.001 and 0.54 ± 0.05. The reduced contrast (1.35:1) displayed between the FC and SNP in comparison to buffer was expected *a priori* as result of the higher ionic strength present in serum. To obtain higher stringency conditions and improved selectivity, formamide at 25% v/v was necessary to afford a 20:1 contrast ratio between the FC and SNP targets where the FRET ratio of the FC target reduced to 0.33 ± 0.07 while that of the SNP was 0.016 ± 0.001.

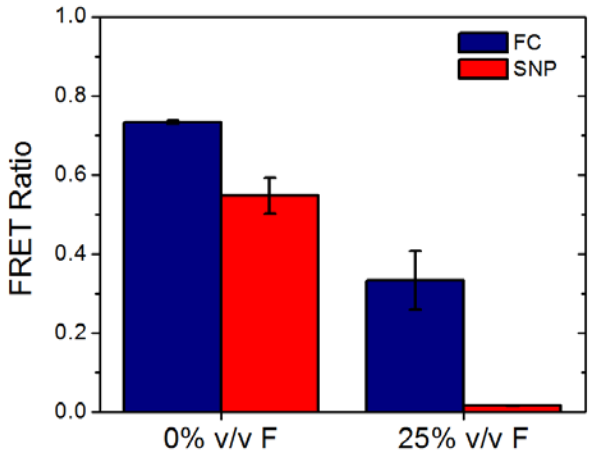

Figure 29. FRET ratio response of the SAv-rQD-SMN1-PC to FC (blue) and SNP (red) targets in 50% v/v serum at 0% and 25% v/v added formamide. At 25% v/v formamide, resolution of a SNP was possible with a contrast ratio of 20:1 as higher formamide was required to improve the assay stringency due to the higher ionic strength in serum.

These data are consistent with the ability for SAv to resist nonselective adsorption and maintain colloidal stability of the assay. Furthermore, the immobilized oligonucleotides also further passivated the core nanocrystal from adsorption of serum proteins to enable SNP resolution.

4.4 Conclusions

The impact of the selection of QD size in the design of QD-FRET hybridization assays was investigated to evaluate any differences in terms of selectivity and sensitivity. Despite the larger hydrodynamic diameter of rQDs compared to gQDs, the gQD-Cy3 FRET pair only offered 5% higher energy transfer efficiency. The larger sized rQD afforded immobilization of *ca.* 20 more oligonucleotide probes at saturation, where hybridization with A647 tagged targets provided a greater number of energy transfer pathways and improved FRET efficiency. Moreover, the additional immobilized probe strands and SAv created an overall higher effective charge and

increased the stringency of hybridization at the rQD interface enabling discrimination of a SNP target without any added denaturant. In contrast, resolution of a SNP was not possible when the assay was conducted with the gQDs. These results provide important insights about criteria for the design and optimization of QD-FRET bioassays and biosensors.

5 Transduction of Unlabeled Target Oligonucleotides and Resolution of Single Nucleotide Polymorphisms in an Electrokinetically Controlled Microfluidic Chip using Immobilized Quantum Dots and Fluorescence Resonance Energy Transfer

Of the following data presented in Chapter 5, MON collected and analyzed the in-channel regeneration data and contributed to acquisition of SNP resolution data. Dr. Ilya Gourevich is thanked for assistance with SEM imaging of the immobilized QDs. The remainder of the experiments and analyses of collected data were performed by AJT.

5.1 Introduction

In Chapter 4, the differences in selectivity between the two colours of SAv-QDs toward SNP discrimination provided insight into optimization of the on-chip assay. Up until this point, resolution of SNPs on-chip was not possible in both the single-colour or multi-colour assay formats presented in Chapters 2 and 3, respectively. Chapter 4 elucidated why this challenge existed. In single-colour assays with the gQD-Cy3 FRET as demonstrated in Chapter 2, SNP resolution would not be expected without added denaturant. The multi-colour assay format also reflected similar interfacial chemistry since the QDs were deposited in a 12:1 ratio of gQD:rQD and the interface resembled that of a single colour assay using gQDs. Furthermore, only a 15-fold (relative to the concentration dispensed) excess of oligonucleotide probe was deposited after initial QD immobilization. The investigation of QD loading capacities suggested that this was insufficient probe to offer the highest selectivity toward interfacial hybridization. With this knowledge it was anticipated that SNP resolution could be achieved on-chip with careful refinement of conditions for assay assembly and target hybridization and by utilizing a single-colour approach with the rQD-A647 FRET pair. This was realized and a contrast ratio between FC:SNP of 108:1 was possible at only half of the added formamide utilized in Chapter 4 for optimal SNP resolution. Moreover, assay regeneration was possible on-chip where a single channel could undergo up to three rounds of hybridization.

In reference to sensitivity of solid-phase assays, electron microscopy was performed on the immobilized QDs in-channel to evaluate the relative donor densities. As introduced in Chapter 1, enhancements in FRET efficiency on solid-phase formats arise as a result of the increased donor-

acceptor transfer pathways and are beyond traditional single donor – multiple acceptor formulations. Significant differences in QD surface densities between the SAv-rQDs and SAv-gQDs were not observed as both densities were of the same order of magnitude. Relating this result to those observed in Chapter 4, similar enhancements in sensitivity in both FRET pairs would be anticipated in translation to the solid-phase format.

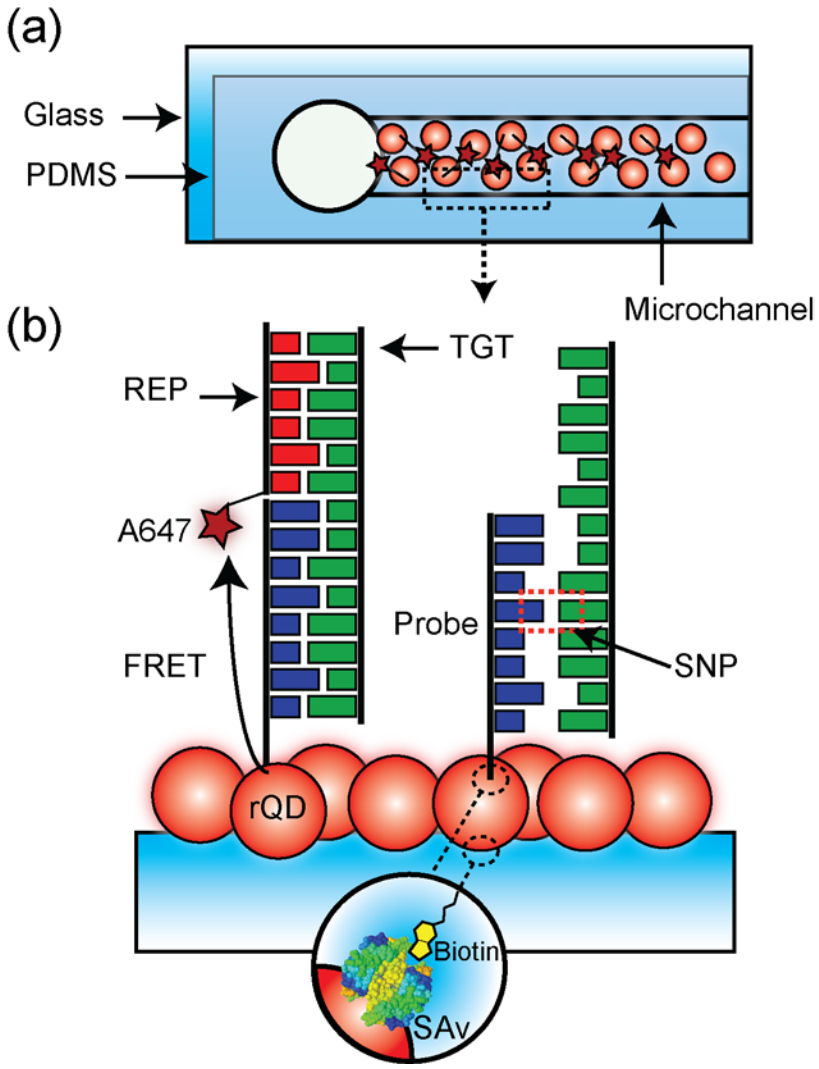

Figure 30. (a) Segment of a glass-PDMS microfluidic chip displaying a microchannel containing interfacial chemistry comprised of SAv-rQDs and immobilized probe oligonucleotides hybridized with A647 tagged targets. (b) Enhanced cross-section of the glass substrate containing the assay chemistry. Target transduction is mediated by a sandwich assay approach that depicts a longer oligonucleotide target (green) that hybridizes to short immobilized probe (blue). The single stranded portion is then subsequently hybridized with a REP oligonucleotide (red) tagged with A647 as to indirectly introduce the FRET acceptor and avoid an intensive labeling step. FRET sensitized A647 signal target hybridization and with increased stringency conditions, SNP resolution was also possible in this format. The same biotin-SAv interaction was utilized for both QD immobilization and probe bioconjugation as highlighted by the circular inset at the bottom of the figure.

A significant advantage of the chip based assay is the rapid hybridization times which are on the order of seconds to minutes. In all assays described thus far, transduction of hybridization of short labeled targets was presented. While these sequences are ideal for proof-of-concept and assay optimization, they do not reflect targets characteristic of real-world application. The need for labeling steps would diminish the impact of the fast hybridization kinetics offered by the microfluidic format and would reduce sample-to-answer response times. An alternate design strategy that does not require labeled targets and permits transduction of longer target sequences is a sandwich assay. This transduction scheme is shown in Figure 30, where a short oligonucleotide probe hybridizes to a longer target sequence in the first step. The extended ssDNA segment is then hybridized with a reporter oligonucleotide tagged with an A647 label. While the dye label extends further from the interface in a sandwich configuration, FRET sensitization of the A647 is still possible from the immobilized QDs and the A647 PL still serves as the analytical signal. This approach avoids a labeling step prior to detection and is amenable to target lengths exceeding 100 nucleotides. Through this approach fmol amounts of oligonucleotide target could still be detected and no loss in assay sensitivity was demonstrated. For traditional FRET assays relying on FRET sensitized PL intensity, a decreased sensitivity resulted from implementation of the sandwich assay format due to the larger separation distance between the QDs and the acceptor dye.[168] On the contrary, transduction using spatial FRET profiles only requires a FRET signal intensity higher than background, so that sensitivity is controlled by saturation of defined areas of interfacial chemistry and an unambiguous length measurement provides for quantification. The robustness of the assay was further tested in complex matrices containing large excesses of BSA and genomic DNA. Target transduction was still possible and with excellent selectivity.

5.2 Experimental Methods

5.2.1 On-Chip Assay Assembly

Glass substrates were functionalized with biotin using a previously published protocol,[218] and the details of the modification steps can be found in the Appendix 4. Negative relief PDMS stamps that served as a cover for PDMS-glass microfluidic chips were cast from a glass master that was fabricated using standard photolithography methods.[146] PDMS chips were oxidized in air plasma for 2 min and reversibly sealed to modified glass coverslips as described elsewhere.[209] The

microfluidic channels were immediately filled with 5 µL of 50 mM pH 9.25 BB that was dispensed in both reservoirs prior to application of a potential. A volume of 5 µL was utilized for all reagents and targets. An application of 200 V was used to inject oligonucleotides and QDs into microfluidic channels by EPF and EOF, respectively. While QDs have previously shown electrophoretic migration towards an anode in gel electrophoresis experiments,[192] the net mobility within microfluidic channels was in the direction of EOF under the buffer conditions and the applied field strength used herein. The EOF velocity within microfluidic channels was determined previously and found to be 5×10^{-2} cm·s^{-1} toward the cathode.[192] The length of the microfluidic channel was *ca.* 1.2 mm after boring of reagent reservoirs, therefore the electric field across the channel was 167 V·cm^{-1} and this field strength was used throughout all dispensing steps and for introduction of labeled TGT. The probe, TGT, UNL-TGT and REP oligonucleotide sequences are shown in Table 9.

Table 9. Oligonucleotide Sequences.

SMN1 probe	Biotin-TEG - 5’ - ATT TTG TCT GAA ACC CTG T - 3’
FC-A647 TGT	A647 - 3’ - TAA AAC AGA CTT TGG GAC A - 5’
SNP-A647 TGT	A647 - 3’ - TAA AAC A**C**A CTT TGG GAC A - 5’
FC-UNL TGT	3’ - TAA AAC AGA CTT TGG GAC ATT CCT TTT ATT TCC T - 5’
SNP-UNL TGT	3’ - TAA AAC A**C**A CTT TGG GAC ATT CCT TTT ATT TCC T - 5’
REP	A647 - 5’- AA GGA AAA TAA AGG A - 3’

Biotin-TEG: biotin with a triethylene glycol linker; FC TGT: fully-complementary target; BPM: base-pair mismatch. The mismatch location is bolded, underlined and colored in red.

The stepwise assay assembly is shown in Table 10. Preconditioning of the microfluidic channel with BB was done not only to equilibrate the interior pH, but to assess the quality of the bonding of the PDMS-glass chip by visually inspecting for leakage prior to reagent dispensing.

Table 10. In-channel Assay Preparation

Step	Concentration	Dispensing Method	Equilibration	Wash
Precondition	-	EOF – BB 2 min	-	-
QD Immobilization	200 nM	EOF – BB 10 min	10 min	BB + 20 mM NaCl – 5 min
Probe Delivery	10 µM[a]	EPF – BB + 20 mM NaCl 5 min	5 min	BB – 5 min
Target Injection	1 µM	EPF – BB 5 min[b]	-	BB – 5 min[b,c]
UNL TGT	0.50-3 µM	EPF-BB + 100 mM NaCl 10 min[d]	-	-[e]
REP	3 µM	EPF-BB + 100 mM NaCl 5 min[d]	-	BB + 100 mM NaCl - 2 min

a Selectivity experiments were also conducted using 3 µM probe, see Appendix 4 Figure A4.1. **b** For resolution of the 1BPM TGT, 5-20 % v/v formamide was added to BB during the target injection and washing steps. **c** Regeneration experiments for in-channel assays were facilitated by incorporation of 20 % v/v formamide in BB during the washing step. **d** BB contained 0.1 % PVP in all UNL TGT and REP injections as to supress EOF, reagents were dispensed at 84 $V \cdot cm^{-1}$. **e** For selectivity experiments 10 % v/v formamide was incorporated in BB and the channel was washed for 10 min at 167 $V \cdot cm^{-1}$.

5.2.2 On-chip Hybridization and Assay Regeneration

Parameters for target injection are included in Table 10. The concentration of FC and 1BPM TGTs was fixed at 1 µM and formamide (% v/v) was added to the target solutions to enhance stringency conditions. The percentage of formamide varied from 5-20 % v/v depending on the concentration of probe oligonucleotide used in assay assembly. After washing, the PL intensity from the channels was measured offline using an epifluorescence microscope. Acquisition of a PL spectrum was done by sampling the surface of a channel at three different positions along the channel length adjacent to the inlet reservoir. The resulting PL spectra were averaged into a single spectrum and this averaged PL spectrum served as one replicate for an in-channel assay response. For regeneration experiments, 20 % v/v formamide in BB was electrokinetically introduced inside the channels for 5 min, and then the PL from the channels was determined.

Prior to an additional hybridization cycle, the channel interior was flushed for 5 min using BB to remove the formamide from the previous regeneration cycle.

5.2.3 Unlabeled Target Hybridization Experiments.

For analysis of longer targets in sandwich assay format, flow injection parameters were tuned to afford optimal hybridization conditions. It was observed that the UNL TGT required higher ionic strength to improve the hybridization efficiency and thus 100 mM NaCl was added to the BB in all hybridization experiments. Furthermore, the added electrolyte resulted in substantially higher conductivity and thus the applied voltage reduced to 100 V so the injection time was doubled to 10 min. After dispensing UNL TGT, REP (3 µM) was injected on-chip for 5 min. The channels were then washed briefly in BB + 100 mM NaCl for 2 min prior to PL measurements. For selectivity experiments, BB containing 0-10 % v/v formamide was dispensed into the channel after initial FC-UNL and NC-UNL TGT capture and the field strength was increased back to 167 $V \cdot cm^{-1}$. This was followed by REP injection using the same aforementioned flow parameter conditions.

5.2.4 Data Analysis

PL spectra were first background subtracted and then normalized to the QD PL maximum at 605 nm. Assay responses were collected in triplicate or more, and the precision displayed represents one standard deviation of the replicates. A FRET ratio was assigned for quantitative comparison purposes, the details can be found in Appendix 4.

5.3 Results and Discussion

5.3.1 The Impact of QD Immobilization Density on Assay Sensitivity

In Chapter 4 it was observed that an incremental improvement in FRET efficiency was seen for the gQD-Cy3 FRET pair. While this could translate to higher sensitivity for solution based assays, for solid-phase QD-FRET assays the immobilization density of the QD donor has also been shown to increase the apparent FRET efficiency.[31] A high density packing of QDs at an interface provides a configuration where a hybridized dye labeled target can be excited by the QD directly bound to the dsDNA or by any adjacent QD within the vicinity that satisfies the criteria for FRET. The resulting enhancement represents an increased number of potential pathways for donor-acceptor dipole coupling and thus an overall increased probability for energy

transfer. In a mixed film of immobilized QDs, if one type of QD were to immobilize at a higher density, then this may enable higher efficiencies of energy transfer for that donor-acceptor system. The immobilization density of each color of QD that was immobilized in microfluidic channels was determined by SEM. Figure 31 shows representative SEM images of a microchannel containing immobilized SAv-gQDs and SAv-rQDs. EOF delivery of QDs to the interface enabled a homogenous distribution of immobilized QDs without aggregation for both colors of QD. QD immobilization densities were similar for both colors; it was found that the SAv-gQDs immobilized at densities of $1.13 \pm 0.16 \times 10^{11}$ QDs·cm^{-2}, and the surface density was $1.23 \pm 0.67 \times 10^{11}$ QDs·cm^{-2} for the SAv-rQDs.

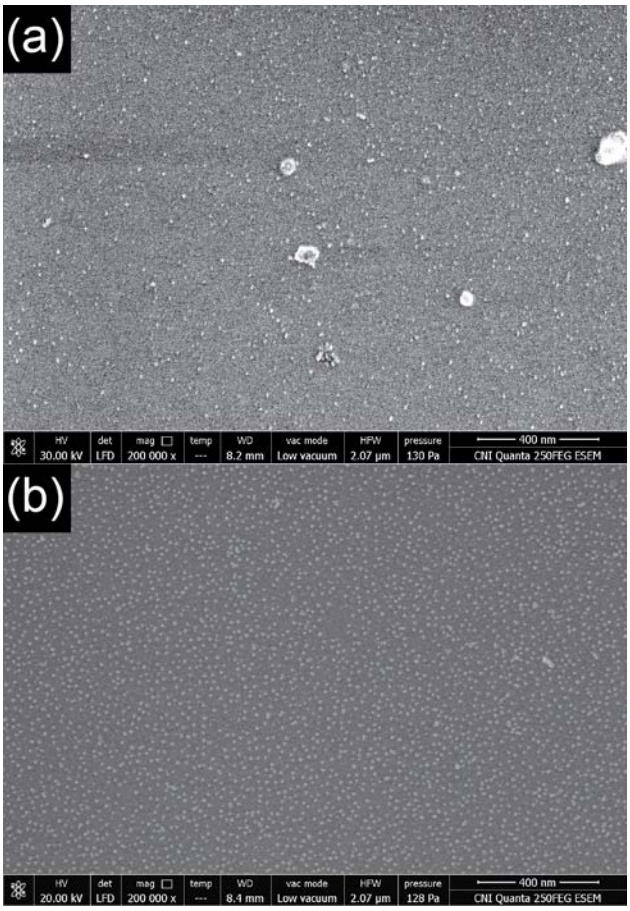

Figure 31. SEM images of in-channel immobilized (a) SAv-gQDs (b) SAv-rQDs on planar biotinylated glass slides (PDMS had been removed to expose the glass). EOF deposition of both types of QDs displayed homogeneous immobilization and no multilayer formation.

Given that both colors of QDs immobilized at almost the same density, it would not be advantageous to use one type of QD as opposed to the other in an attempt to maximize donor density and the resulting sensitivity of the on-chip assay.

As an additional consideration, it has been noted that autofluorescence from the PDMS layer coincided with the region of FRET sensitized Cy3 PL.[200, 219] This resulted in higher background signals within the green detection channel. Thus, using the rQD-A647 FRET pair is advantageous as this detection channel experiences less background in single color assays.

5.3.2 On-chip SNP Resolution

Given the higher stringency of hybridization at the SAv-rQD interface compared to that of the SAv-gQD as shown in Chapter 4 and marginal differences in sensitivity between the two FRET pairs, the in-channel hybridization assay assembled using the rQDs should offer improved selectivity. The in-channel format offers additional stringency control by electrokinetic control with a constant electrophoretic force acting on oligonucleotides within the channel and an elevation of local temperature due to Joule heating.[167] Because of these conditions, it was anticipated that less formamide would be required to offer high contrast between FC and SNP TGTs when a suitable voltage was applied across the microfluidic channel. In-channel hybridization of the FC and SNP TGTs in the presence and absence of formamide is shown in Figure 32. Without any added formamide, SNP resolution was possible with a contrast ratio of 4.2:1.

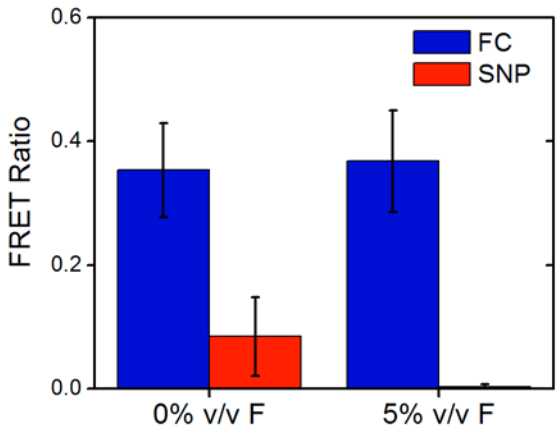

Figure 32. Response of the rQD-A647 in-channel assay to FC (blue) and SNP (red) targets in BB with 0% and 5% v/v formamide (F). After hybridization with FC and SNP targets, injection of 5% v/v F in BB is sufficient to denature the SNP, with the signal from the SNP target being reduced to the background level within experimental precision.

Addition of 5% v/v formamide was sufficient to melt the SNP TGT to levels that were undetectable within experimental precision (a FRET Ratio of 0.003 ± 0.004 from 0.09 ± 0.06). In contrast, the response of the assay to the FC TGT was unchanged with addition of formamide, (a FRET ratio of 0.37 ± 0.08 from 0.35 ± 0.08). This was not observed when the same assay was assembled using 3 µM probe instead of 10 µM. Not until a concentration of 25 % v/v formamide was used was SNP resolution observed (see Appendix 4, Figure A4.1). Since every % v/v formamide lowers the duplex T_m by 0.6 ºC,[172, 204] the T_m of the duplex in the on-chip assay was destabilized by *ca.* 3 ºC due to the aforementioned electrokinetically driven stringency factors under an applied field strength of 167 V·cm^{-1}. This allowed selective resolution of a SNP with a contrast ratio of 108:1, which is the highest contrast ratio reported for the SMN1 sequences as compared to previous studies that also employed QD-FRET transduction of nucleic acid hybridization using the same sequences.[220]

5.3.3 Regeneration of the In-channel Assay

The high speed (within min) of the in-channel assay provides opportunity to consider the potential for assay reusability. Given that 5% v/v formamide was sufficient to denature the 1BPM TGT, it was anticipated that between 15-20% v/v formamide would enable melting of the FC duplex as displayed by the melt profile of the FC TGT shown in Chapter 4 (Figure 26(b)(ii)) This level of formamide in solution is important for assay fidelity, as formamide percentages of 50 and over were shown to have detrimental effects on QD PL in previous assays.[172] Injection of 20% v/v formamide in 50 mM BB for 10 min displayed complete duplex melting as indicated by FRET sensitized A647 PL displaying a response characteristic of NC TGT as shown by the first regeneration cycle (R1) in Figure 33. The need for a longer duration of dispensing is likely a result of the weak EOF under these regeneration conditions due to the low ionic strength of the BB used. The 20% v/v formamide did not negatively impact QD PL and allowed faster assay cycling.

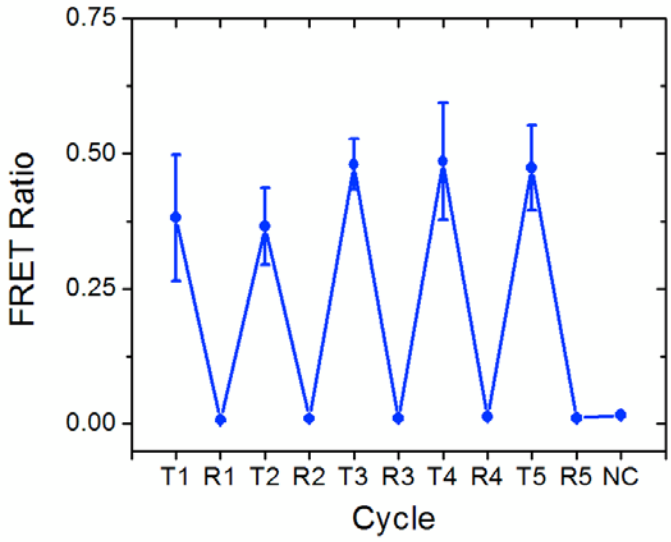

Figure 33. Regeneration of the in-channel assay after a first cycle of hybridization using 20 % v/v formamide in BB at an applied field of 167 $V \cdot cm^{-1}$. T denotes a target injection and R denotes a regeneration cycle. The final data point is the resulting FRET response after injection of NC TGT.

Repeated exposure to formamide ultimately denatures the SAv layer, exposing underlying carboxylic acid groups that facilitate oligonucleotide adsorption through a hydrogen bonding mechanism.[179] To test whether adsorption limited further cycles of assay regeneration, NC TGT was injected after R5. A response of 0.017 ± 0.03 was measured, which indicated some marginal oligonucleotide adsorption, consistent with some degradation of the SAv layer.[172]

5.3.4 Transduction of Unlabeled Target

A common challenge often faced with optical detection strategies, is the need to label the target biomolecule. Alternate transduction strategies can be used to introduce a label indirectly, avoiding the need for an intensive labeling step. A sandwich hybridization assay as shown in Figure 30 represents one such strategy. This strategy relies on hybridization of a longer target to the interfacial oligonucleotide probe, leaving a single stranded portion extending from the partially completed duplex. The remaining single stranded segment of nucleotides can hybridize to another nucleic acid sequence that is labeled with the appropriate dye to enable FRET. This hybridization format allows for detection of longer nucleic acid sequences as found in clinical samples and samples for pathogen determination. One concern is the potential loss of FRET as the distance of the fluorescent label from the QD can increase significantly for a sandwich assay

motif. To examine the application of the on-chip assay to longer targets, a 34mer target was prepared based on the initial labeled 19mer target used in the earlier optimization studies.

Quantitative on-chip hybridization still offers a spatial profile as seen in Chapters 2 and 3,[79, 209] and is characteristic of FRET sensitized A647 emission from the channel interior as shown in Figure 34(a)(i). The corresponding QD PL shown in Figure 34(a)(ii) is used as a reference, where the crossover between the two PL signals is used to determine the spatial length for a given amount of target. The three channel microfluidic chip displayed by Figure 34(a) shows the assay response to the injection of a different quantity of UNL TGT in each channel. FRET sensitized A647 PL is realized after subsequent injection of REP. In this unlabeled target transduction format, the A647 acceptor is theoretically *ca.* 20 nucleobases away from the rQD donor. Given the proximity driven dependence of FRET, an energy transfer efficiency decrease is confirmed by the spectra shown in Figure 33(b) where the blue and red spectra show the normalized PL response to FC and NC UNL TGTs, respectively.

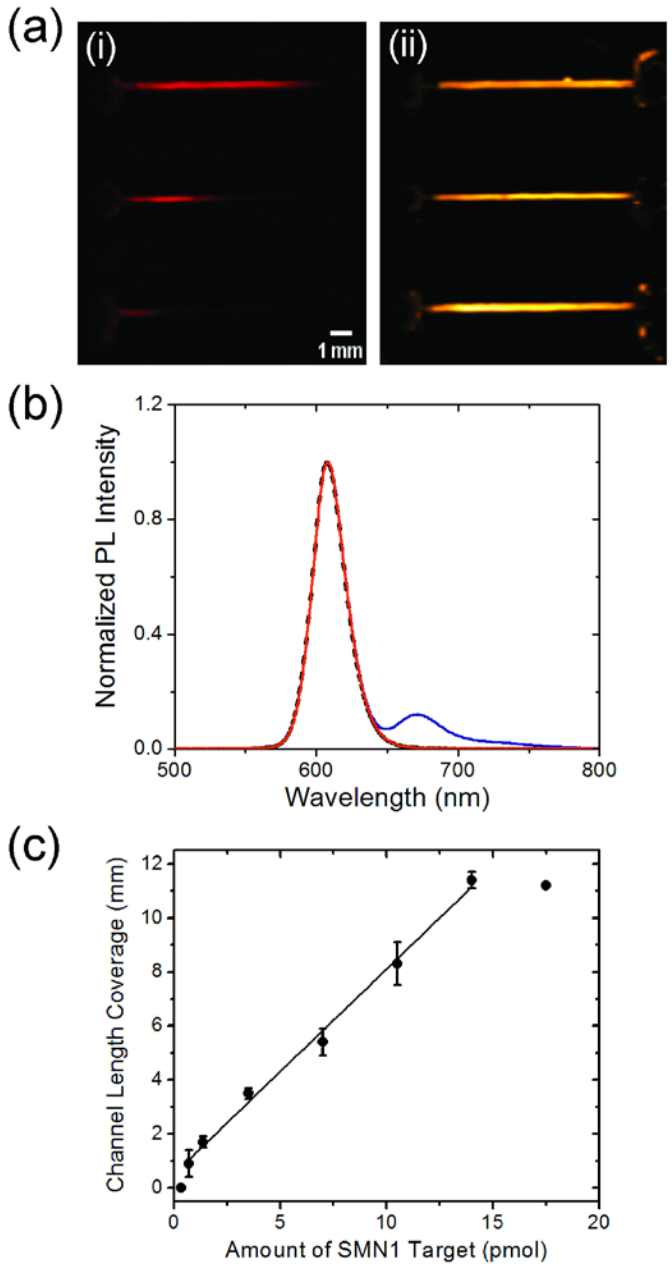

Figure 34. (a) False color epifluorescence images (i) A647 PL (ii) rQD PL after the in-channel injection of 10.5 pmol, 3.5 pmol, 1.4 pmol of UNL FC TGT and 21 pmol A647 REP. (b) Normalized average PL intensities of the assay response to FC (blue) and NC (red). PL from immobilized rQDs is shown by the dashed black line. (c) Quantitative assay response to 0.35-17.5 pmol of UNL-FC TGT as a function of the in-channel FRET profile.

Adsorption of NC oligonucleotides was not detected. The FRET ratio for the FC UNL TGT decreased as a result of a larger donor-acceptor separation distance. Higher ionic strength was required (100 mM NaCl) in sandwich assays to facilitate interfacial hybridization. To evaluate whether this was a result of kinetic or steric constraints, UNL TGT was injected and allowed to equilibrate for 30 min in pH 9.25 50 mM BB with 20 mM NaCl. After subsequent injection of

A647 REP, FRET sensitized emission was still not visible from the channel interior (data not shown). Increasing the concentration of NaCl to 100 mM offered hybridization within 10 min indicating that lower ionic strength conditions did not afford stable interfacial hybrids due to the polyanionic nature of the oligonucleotides. To accommodate analysis in higher ionic strength buffer, it was necessary to lower the applied electric field strength to 100 $V \cdot cm^{-1}$ from 200 $V \cdot cm^{-1}$ to minimize Joule heating. To introduce more target oligonucleotide at lower field strengths, all solutions contained 0.1 % PVP to suppress EOF and injection was allowed to proceed for 10 min instead of 5 min. Despite the reduction in FRET efficiency in the sandwich assay format, it was still possible to quantitatively transduce oligonucleotide hybridization via spatial length coverage with a dynamic range (R^2, 0.995) that spanned more than an order of magnitude as shown in Figure 34(c). The lower and upper boundary limits were determined to be 0.7 pmol and 14 pmol, respectively. The upper limit was bounded by the length of the microfluidic channel. At the lower end, injection of 0.35 pmol did not display any measureable FRET sensitized emission from the channel interior. The limit of detection corresponding to a FRET spatial profile length of 0.9 ± 0.5 mm was 0.7 pmol which resided on the bottom end of the dynamic range.

5.3.5 Unlabeled SNP Transduction and Analyses in Complex Matrices

Since hybridization of the UNL TGTs required higher ionic strength to facilitate interfacial hybridization, dispensing of higher stringency buffer would have to be done after initial target capture. Furthermore, given that the stringency conditions required to melt the SNP would also cause dissociation of the dsDNA segment of the bound REP, an indirect two-step wash-injection protocol was used.

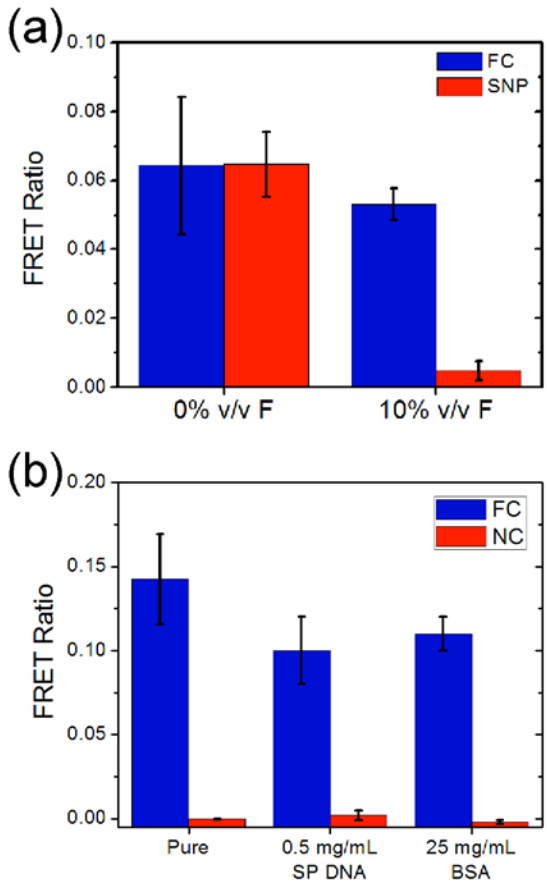

Figure 35. (a) Assay response to UNL FC (blue) and UNL SNP (red) TGTs in the absence and presence of 10% v/v formamide. In the presence of formamide, discrimination of a SNP was possible with a contrast ratio of 11:1. (b) Transduction of UNL FC (blue) and UNL NC (red) TGTs without background (left), in the presence of 0.5 $mg \cdot mL^{-1}$ SP DNA (middle) and in 25 $mg \cdot mL^{-1}$ BSA (right).

After FC/SNP TGT delivery (100 $V \cdot cm^{-1}$), BB and BB containing 10% v/v formamide was dispensed into the microchannel for 10 min (200 $V \cdot cm^{-1}$), followed by subsequent injection of REP in BB containing 100 mM NaCl. The response of the assay to FC and SNP-UNL TGTs is displayed by Figure 35(a), and indicated that no resolution was visible after washing with BB. Dispensing of 5% v/v formamide in BB also did not result in melting of the SNP (data not shown). The contrast between targets was observed to be FC:SNP, 11:1 when using 10% v/v F in BB.

To further evaluate the selectivity of the assay transduction of hybridization was done in more complex matrices. Two matrices were evaluated herein: 0.5 $mg \cdot mL^{-1}$ of salmon sperm (SP) DNA and 25 $mg \cdot mL^{-1}$ of bovine serum albumin (BSA). The response to FC and NC oligonucleotides in these more challenging environments is shown by Figure 34(b), and the assay response in BB

(pure) is shown for comparison purposes. Within experimental precision, the mean FRET ratios remained unchanged for analyses in SP DNA and BSA, respectively. Given that the SP DNA was in 250 fold and the BSA was in 12500 excess relative to the FC and NC TGTs, occlusion of target oligonucleotides from the selective interfacial chemistry was expected. Nonetheless, any physisorption of background material did not result in false positives from the two-step hybridization assay, and the response to the NC TGTs in all samples was undetectable within experimental precision.

5.4 Conclusions

In this chapter, the impact of designing QD-FRET assays on-chip using the SAv-rQD system was evaluated with an aim towards optimization of the selectivity and sensitivity of the nucleic acid hybridization assay. In earlier reports of chip-based single colour and multi-colour assays where gQDs were used, SNP selectivity and regeneration were not possible. Assembly of the solid-phase assay on-chip with SAv-rQDs provided detection of 1BPM targets with a contrast ratio of 108:1. In addition, up to three cycles of assay regeneration were possible. In moving toward analyses of real nucleic acid samples, a sandwich assay approach enabled unlabeled target transduction. No loss in sensitivity was observed despite the lower FRET efficiencies as a result of increased donor-acceptor distance. This highlights the advantage of the spatially based quantitative transduction of nucleic acids that requires only a signal above background to translate into the length measurement. SNP resolution was also possible in the sandwich assay format with a contrast ratio of 11:1, which was lower than the direct label assay due to reduced FRET efficiency. Furthermore, analyses in complex matrices containing a large excess of BSA and genomic nucleic acid did not influence the selectivity or performance of the on-chip assay.

6 Conclusions

In this work, the integration of a solid-phase nucleic acid hybridization assay within an electrokinetically microfluidic chip was explored. Hybridization was transduced by FRET from immobilized QDs to dye tagged oligonucleotide targets and reporters. The two FRET pairs used in PL transduction were a 525 nm emitting gQD-Cy3 and a 605 nm rQD-A647. The microfluidic chip was comprised of PDMS and glass slides that had been functionalized with biotin to afford immobilization of SAv-QDs. Assay assembly was done *in situ* through electrokinetic delivery where QDs were transported using EOF and nucleic acids moved by EPF. In-channel design enabled rapid reaction kinetics where both assay assembly and target transduction could be done within minutes. Tens of femtomole amounts of labeled and unlabeled oligonucleotide targets could be detected through direct and sandwich assay transduction designs. The novelty of the work is highlighted by the new detection strategy provided by the microfluidic assay format. As a result of immobilization of the selective interfacial chemistry throughout the entire microchannel in combination with very rapid hybridization, dispensing of target nucleic acid into the microchannel resulted in hybridization along the length of the glass surface of the channel. As probe sites adjacent to the inlet reservoir were saturated, subsequent target was delivered further along the channel length. For a defined set of injection parameters including the applied field strength and dispensing time, the length of the FRET spatial profile from the channel interior could be used to quantify the amount of DNA in the sample. The area of channel where probe sites were not hybridized displayed homogenous QD PL, where the crossover position of both FRET and QD PL was utilized a reference point to measure the length of the FRET spatial response. Through this quantitative analytical measurement, a dynamic range spanning more than an order of magnitude could be realized for a microchannel measuring 1.2 cm in length. Multiplexed concurrent detection of two targets by FRET was also possible as a result of the combination of two different QDs and probes. While earlier solid-phase QD-FRET assays displayed limited LODs when multiplexed analyses were implemented,[168] the opposite was seen in quantification via spatial length coverage. The presence of two probes diluted the interfacial chemistry such that the target response in each channel doubled (resolution based on length doubled) in comparison to single-color assay channels comprised of a single probe oligonucleotide sequence. Assay sensitivity improved in the multiplexed format and femtomole amounts of DNA could be detected.

As a gold-standard for nucleic acid hybridization selectivity the ultimate test is the ability to resolve SNPs. A non-traditional approach was taken in order to optimize the selectivity of the in-channel assay. The stringency of hybridization at both the SAv-gQD and SAv-rQD interface was investigated with the intention of finding suitable conditions for SNP resolution. At room temperature without any added formamide, SNP discrimination was possible at the SAv-rQD interface. Interestingly, a chemically identical SAv-gQD system did not offer SNP resolution. The higher effective charge of the larger SAv-rQDs that accommodated a greater number of immobilized probe oligonucleotides resulted in improved stringency conditions. Assembly of an on-chip assay using SAv-rQDs and A647 as the FRET reporter resulted in SNP resolution with a contrast ratio of 108:1 for short oligonucleotides. Assay regeneration was possible where three cycles of hybridization could proceed in a given channel prior to any noticeable degradation of the interfacial chemistry. Transduction of unlabled target was possible with femtomole detection limits by implementation of a sandwich assay. Despite the added donor-acceptor separation distance as a result of this format, the FRET sensitized emission was significant above background to translate detection through FRET spatial profiles. Through this method of quantification, no sensitivity was lost and similar LODs were observed. Moreover, SNP resolution was possible using unlabeled target in combination with a sandwich assay. The robustness of the assay was further demonstrated by loading the sample matrix with substantial quantities of of BSA and genomic nucleic acids. These potential interferents did not alter the assay response and did not generate false positive signals.

This thesis contributes to the field of bioanalytical chemistry, and more specifically to bioassay and biosensor design. The spatial detection platform is a novel approach to the limitations of signal-to-noise when relying on fluorescence intensity for quantification, and the work exemplifies the advantages offered by microfluidics as a format for bioassay design.

6.1 Future Work

The fundamental investigations explored herein have demonstrated the advantages of the electrokinetic microfluidic platform toward assembly of solid-phase QD-FRET nucleic acid hybridization assays. While the spatial length method of quantitative nucleic acid transduction is

advantageous in comparison to traditional analyses based solely on the intensity of FRET sensitized PL, further opportunities warrant investigation.

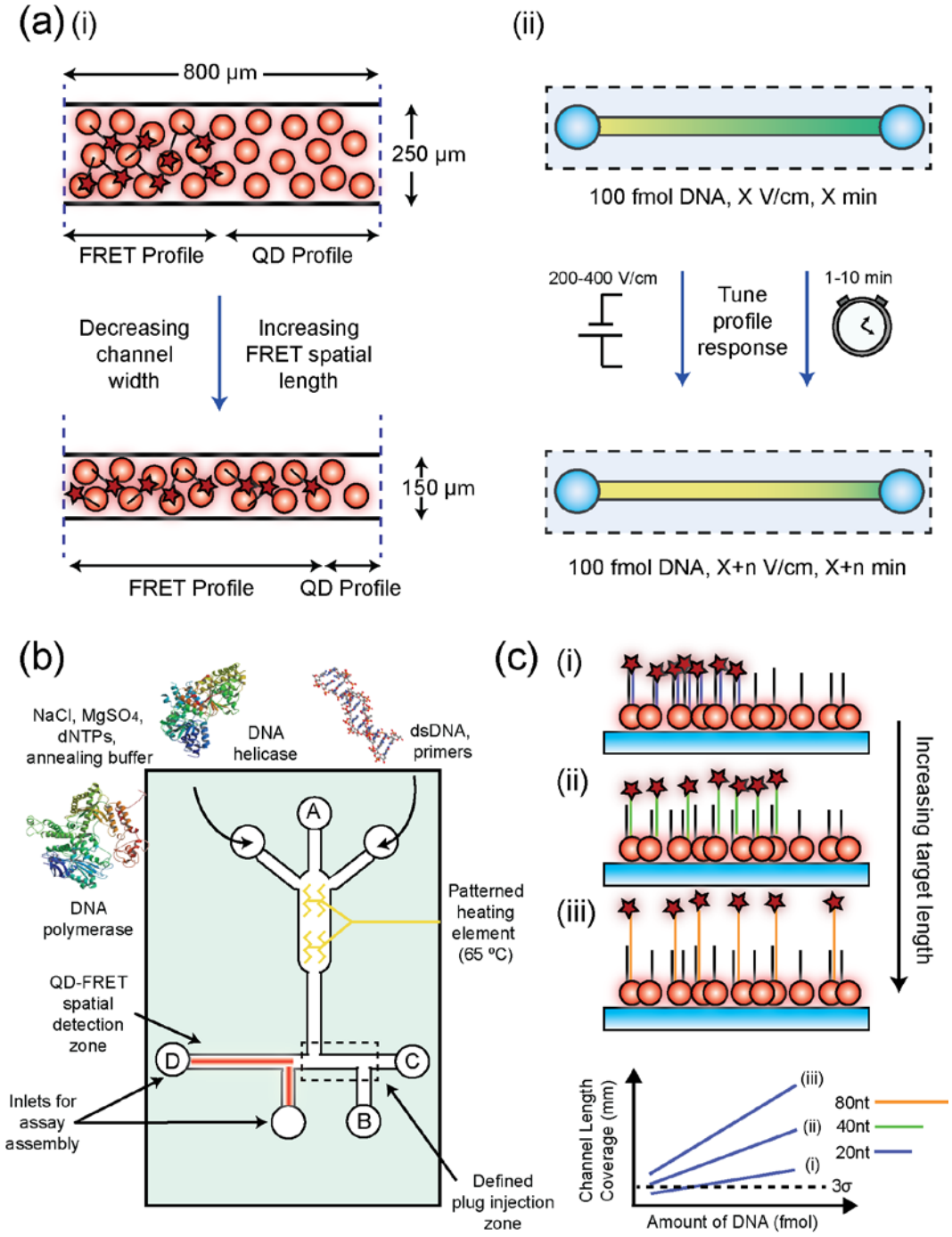

Figure 36. A collection of future directions for further investigation based on the work presented in this thesis. (a)(i) Control over channel dimensions should enable refinement and optimization of assay sensitivity and potentially improve LODs. Channel dimensions govern the spatial response of FRET sensitized emission from hybridized target. By reducing the channel width, saturation of recognition sites for a defined channel area should require less amount of target and ultimately this should increase the profile for a given target concentration. (ii) Control over flow injection parameters should enable an "on the fly" tunable dynamic response to ensure a given

target concentration falls within the dynamic range of the assay. Furthermore, control over injection parameters could be coupled with channel dimensions as smaller microchannels can afford higher electric field strengths and still maintain low current and Joule heating effects. Optimization of such control could offer lower LODs and a collective dynamic range spanning more than two-three orders of magnitude based. (b) A schematic design of a LOC system for amplification of nucleic acid targets followed by on-chip spatial transduction. The inlet ports and central channel at the top of the chip illustrate the zone of amplification, were enzymes and dNTP precursors can be added for nucleic acid amplification. Controlled micro heating elements can be patterned into the chip design to afford isothermal conditions for amplification to proceed. Assay assembly is localized at the end of the chip, where a plug injection of amplified material can proceed using the additional inlet ports toward the detection platform. (c) Improved spatial assay sensitivity and LODs toward longer nucleic acid targets as a result of reduced hybridization efficiency with immobilized probe. Such a phenomenon would further highlight the advantage of spatial transduction and may overcome limitations discussed in much of the literature about analyses by hybridization of nucleic acid targets associated with real samples.

Some of these concepts are displayed by Figure 36 schematically, where (a)(i) and (ii) illustrate the advantages of the fluidic platform and its control over analytical figures of merit; in particular sensitivity and LOD. The control over the length of a spatial FRET response is governed by the channel dimensions as shown in Figure 36(a)(i). By reducing the channel width, saturation of a given area of channel should occur for a reduced amount of hybridized target and it is likely that the FRET spatial response would increase. This should afford both increased sensitivity and LODs as less nucleic acid is required to saturate the response of the interfacial recognition chemistry. Manipulation of channel dimensions along with flow injection parameters (see Figure 36(a)(ii)), such as time and the applied field strength may enhance the sensitivity of the spatial response and offer lower LODs. Furthermore, this should enable a “tunable” dynamic range to ensure that a specific target concentration reside within the response bound by the LOD and the upper limit of quantification.

The microfluidic designs presented in the work of this thesis were utilized for assay development rather than the practical construction of a self-contained LOC system. A potential further direction may include development of LOC system that integrates both isothermal nucleic acid amplification and on-line transduction using the QD-FRET spatial detection method (Figure 36(b)). Isothermal amplification kits are commercially available; one example is helicase dependent amplification from BioHelix.[2] This method utilizes DNA polymerase and helicase along with the require deoxynucleotide triphosphates (dNTPs), enzyme cofactors, and suitable annealing conditions. Primer design characteristic of a specific gene can be integrated into a contained amplification zone on-chip as illustrated by the straight channel with three inlet ports

[2] http://www.biohelix.com/hda_technology.asp

at the top of the chip design. Heating elements can be patterned into the chip design to enable appropriate temperature conditions to offer efficient amplification of the nucleic acid targets. Application of a voltage from A to B will afford a defined plug of amplified material localized toward the detection platform. The extra reservoir to the left of B along with D can be utilized for routine QD-FRET assay assembly as previously described. Application of a voltage from C to D affords target dispensing to toward the QD-FRET detection zone. This self-contained system would only require DNA isolation from a patient or pathogenic species while amplification and detection could be done within 1-2 hours. Such a LOC would enable POC application for nucleic acid analysis.

Based on the work presented in Chapter 5 for longer nucleic acid targets, it was observed that the spatial profiles increased in comparison to those associated with short oligonucleotides. This result is consistent with lower hybridization efficiency toward longer targets by the interfacial oligonucleotide probes. While this is disadvantageous for traditional PL intensity based measurements, this concept should afford an extension of spatial response as shown by Figure 35(c), leading to improved LODs. Ultimately the compromise may come from such reduction in hybridization efficiency that the FRET PL may no longer be discernable above background levels and thus a spatial FRET profile would no longer be observed.

The ideas presented herein may provide direction and present a foundation from which future research work can be conducted.

Appendix 1 – Supporting Information for Chapter 2

A1.1 Detailed Experimental Methods

A1.1.1 Materials and Reagents

Ammonium hydroxide (30%), hydrochloric acid (16 M) and hydrogen peroxide (30%) were obtained from EMD Chemicals (San Diego, CA). Methanol, ethanol, isopropanol, dichloromethane, and diethylether were reagent grade or better and were acquired from Caledon Laboratories (Georgetown, ON, Canada). Anhydrous toluene (99.8%), 3-aminopropyltrimethoxysilane (APTMS, 97%), *N*,*N*-diisopropylethylamine (DIPEA, 99.5%), anhydrous *N*,*N*-dimethylformamide (DMF, 99.8%), biotin (99%), *N*,*N*-diisopropylcarbodiimide (DIC, 99%), *N*-hydroxysuccinimide (NHS, 99%), and formamide (99.5%) were from Sigma Aldrich (Oakville, ON, Canada). All buffers were prepared with deionized water from a Milli-Q cartridge purification system (Millipore Corporation, Mississauga, ON, Canada) and sterilized by autoclaving. Buffers used included borate buffer (BB; 50 mM, pH 9.25) and Tris-Borate (TB) buffer (100 mM, pH 7.44, 20 mM NaCl). For microfluidic experiments, buffers were filtered through a Acrodisc 0.2 µm syringe filter from Pall Corp. (Ann Arbor, MI) prior to use. Microscope glass slides (25 mm × 75 mm) and glass cover slips (22 × 22 mm) were from Fischer Scientific (Pittsburgh, PA). P-type boron doped <100> silicon wafers, 515 ± 30 µm thick and 100.0 ± 0.5 mm in diameter were obtained from Empak (Chanhassen, MN). Polydimethylsiloxane (PDMS) Sylgard 184 silicone elastomer kit was obtained from Dow Corning (Newton, MA). Su-8 5 photoresist was from MicroChem (Newton, MA). Oligonucleotides were purchased from Integrated DNA technologies (Coralville, IA) and were HPLC purified by the manufacturer. CdSe/ZnS Qdot® 525 ITK™ Streptavidin Conjugates were from Invitrogen by Life Technologies (Oakville, ON, Canada).

A1.1.2 Instrumentation

Solution phase PL measurements were made using a QuantaMaster PTI spectrofluorimeter (Photon Technology International, London, ON, Canada) equipped with a xenon arc lamp (Ushio, Cypress, CA) and a red-sensitive photomultiplier tube (R928P; Hamamtsu, Bridgewater,

NJ). Time-resolved fluorescence decay curves were obtained with a dye laser (GL-302, Photon Technology International) that was pumped using a pulsed nitrogen laser (GL-3300, Photon Technology International). The lasing dye used was 4,4´-(1,2-ethenediyl)bis-1, 1-biphenyl (DPS) in dioxane (Exciton, Dayton, OH) and the output of the dye laser was tuned to 402 nm. Time resolved PL measurements were made using the stroboscopic technique.[46] Absorption spectra were obtained using a HP8452A Diode-Array Spectrophotometer (Hewlett Packard Corporation, Palo Alto, CA).

In-channel PL measurements were made using an epifluorescence microscope custom built in house, and based on a Nikon Eclipse L150 model (Nikon, Mississauga, ON, Canada) that was equipped with a motorized xyz translational stage. A schematic of the instrument can be found elsewhere.[2] A diode laser with an output of 406 nm (Radius 405, 25 mW, Coherent Inc, Santa Clara, CA) was used as the excitation source. A filter cube containing a 405/20x nm excitation filter and a Z405 rdc dichroic mirror was used to direct the laser light through a 40x Nikon ELWD Plan Fluor Objective (NA = 0.60) to the sample stage. PL was collected in the backwards direction using the same lens and detected using a diode array spectrophotometer (QE6500, Ocean Optics Inc., Dunedin, FL) by means of a fiber optic waveguide. SpectraSuite software (Ocean Optics) was used for spectra acquisition, and PL spectra were averaged from measurements made at 3-5 points along the length of the microfluidic channel. A program written in LabVIEW (National Instruments, Austin, TX) was used to control the microscope for image collection. Channel images were obtained using a PMT and by raster scanning over the sample surface. Filter cubes containing bandpass filters: a D525/20 and HQ570/20 (Chroma Technologies Corp., Bellows Falls, VT) were used to isolate QD and Cy3 FRET sensitized PL, respectively. Images were obtained by point-by-point reconstructions of the raster scans and processed using ImageJ software (National Institutes of Health, Bethesda, MD).

The data for the electrophoretic mobility of the target nucleic acid sequence was acquired using a similar Nikon Eclipse epifluorescent microscope setup that was upgraded to a Nikon C2si confocal microscope. Excitation of the Cy3 labeled sequence was accomplished using a 543 nm, 1.5 mW HeNe laser (Electro-Optics Inc., Boulder, CO) and detection using a PMT. Time based signals were acquired using NIS-Elements imaging software (Nikon, Mississauga, ON, Canada).

Electrokinetic microfluidic experiments were conducted using a High Voltage Sequencer HVS448 3000V (Labsmith, Livermore, CA).

Monochromatic ellipsometry measurements were made using a Rudolph Auto EL III ellipsometer equipped with a HeNe laser source (632.8 nm emission) with an angle of incidence of 70º. Prior to measurements, the instrument function was checked against a reference silicon wafer of known film thickness (455 ± 3 Å) and refractive index (1.463).

A1.1.3 Glass Substrate Modification and Microfluidic Chip Fabrication

Microscope glass substrates (slides or coverslips) were first etched using a two-step RCA cleaning protocol to generate silanol groups. Substrates were placed inside a Teflon holder that prevented the glass slides from contacting one another, and were then treated with a 5:1:1 mixture of deionized water, ammonium hydroxide, and hydrogen peroxide. The solution was heated to 85 ºC and kept at this temperature for 5 min. The slides were then rinsed twice with deionized water. A 5:1:1 mixture of deionized water, hydrochloric acid, and hydrogen peroxide was added to the slides, heated to 85 ºC and kept at this temperature for 5 min. The slides were then rinsed twice with deionized water, twice with methanol, and then sonicated twice in methanol for 10 min. After sonication, the slides were rinsed twice with dichloromethane, twice with ether and then placed in a dessicator until further use.

The RCA cleaned slides were then aminated through silanization with APTMS. The substrates were immersed in *ca.* 300 mL of anhydrous toluene and 7.5 mL of APTMS (2.5% v/v) in the presence of 0.5 mL of DIPEA, and the mixture refluxed under argon for 6 h. After reaction, the substrates were rinsed twice with methanol and then sonicated twice in methanol for 10 min, followed by rinsing twice with dichloromethane and ether. APTMS slides were further derivatized with biotin by amide formation through carbodiimide activation. The APTMS slides were immersed in *ca.* 150 mL of DMF containing 250 mg (1 mmol) of biotin and 200 mg (1.7 mmol) of NHS. The mixture was stirred until dissolution of the reagents and then a solution of 200 µL (1.3 mmol) of DIC in 5 mL of DMF was added dropwise into the flask while stirring. The mixture was then placed on a shaker for 24-48 h. Once the reaction was complete, the substrates were rinsed twice with isopropanol and then sonicated twice in isopropanol for

10 min. Slides were then rinsed twice with dichloromethane and ether and stored in a dessicator until further use.

Silicon substrates used in ellipsometry measurements were cut to dimensions of 22 × 22 mm so that they fit within the Teflon holders used for glass cover slips. Silicon slides were aminosilanized in parallel with glass substrates for quality control purposes and measurement of film thickness (the silanol surfaces are analogous between the substrates, but only the silicon is suitably reflective for ellipsometry measurements). The refractive index (1.463) of the silicon wafer was used as an approximation when measuring derivatized substrates. Two samples from each modification step were measured four times and the change in thickness was calculated by subtracting the measured thickness from the RCA etched silicon wafer. For an in-depth characterization of silane modified surfaces, the reader is referred elsewhere.[47]

PDMS chips were made by mixing 10 g of the elastomer with 1 g of curing agent in a small beaker and stirring vigorously for 10 min. The mixture was then degassed for 30 min, poured (*ca.* 3 g) on the microfluidic template and baked at 120 ºC for 25 minutes. Microfluidic templates were fabricated as previously reported by using standard lithography methods.[17] PDMS chips were cut to dimensions of *ca.* 2 mm less than those of the substrates and the reagent and waste reservoirs were made manually using a metal bore. Reservoirs were inserted such that the length of the microchannels was *ca.* 1 cm. The channel width and height were 250 μm and 9 μm, respectively. The PDMS was sealed to the glass substrates by first rinsing the PDMS cover with 95% ethanol, drying with nitrogen, and then oxidizing the chip using air plasma at 10.5 W for 30 s. After annealing the PDMS to the glass substrate, the channels were immediately filled with 50 mM pH 9.25 BB. A schematic of the PDMS-glass chip is displayed by Figure A1.1.

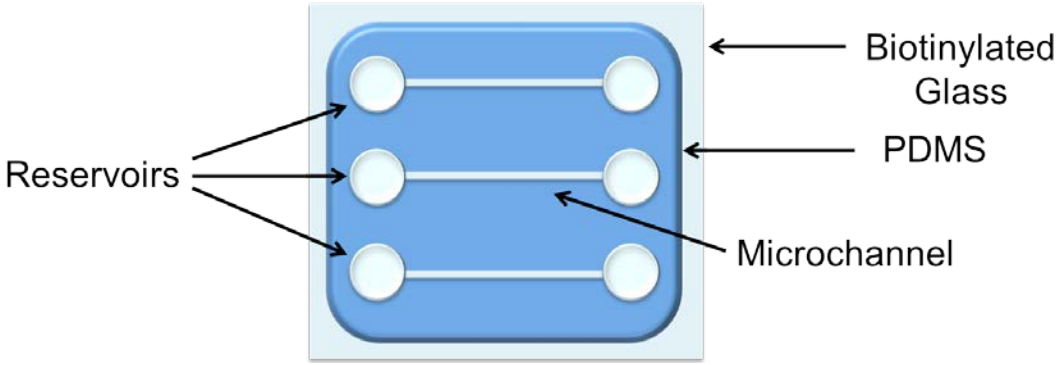

Figure A1.1. Schematic representation of the three channel PDMS/glass microfluidics chip used in the assay. Reservoirs were inserted such that the microchannel was 1 cm long.

A1.1.4 Gel Electrophoresis and Mobility Experiments

To prepare the on-chip assay, both electrophoretic force (EPF) and electroosmotic flow (EOF) were used to deliver reagents within the microfluidic channel. Since both forces acted in tandem on both QDs and oligonucleotides, it was the net mobility of a reagent that determined the mechanism of delivery in-channel. SAv-QDs were delivered into the channel using their cathodic EOF mobility, while nucleic acid sequences were injected using EPF and traveled in the direction of the anode. Although the SAv-QDs were delivered by EOF, their mobility under EPF was not assumed to be negligible. Given the alkaline pH of the injection buffer, both the conjugated SA (pKa ~ 6.8-7.5) and the underlying surface chemistry of SAv-QDs were expected to be negatively charged. Gel electrophoresis experiments were done to assess the electrophoretic mobility relative to QDs coated with a negatively charged ligand, mercaptopropionic acid (MPA), which were known to migrate with a net mobility dominated by the EPF.[48] The MPA-QD and SAv-QD samples were run on a 1% agarose gel, in 25 mM borate buffer at pH of 9.25. The concentration of the MPA-QDs and SAv-QDs were 2 µM and 0.1 µM, respectively, after 20% dilution with a 40% w/v sucrose solution. The gel was run at an applied field strength of 2.5 V cm^{-1} for 30 min. A PL image, displayed by Figure A1.2, was then obtained using a BioRad Molecular Imager® GelDoc™ XR.

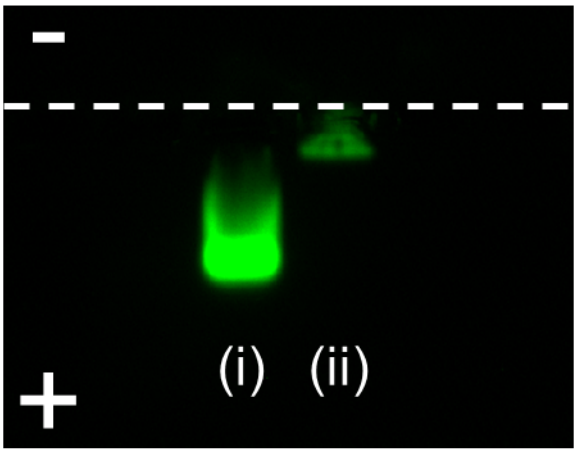

Figure A1.2. False color gel electrophoresis image of (i) MPA-QDs and (ii) SAv-QDs at pH 9.25 in 25 mM borate buffer. The negative and positive symbols indicate the polarity of the electric field, and the dashed line represents the position of the loading wells.

The gel PL image clearly shows that the SAv-QDs have a much lower electrophoretic mobility than MPA-QDs. While it was also necessary to consider the larger size of the SAv-QDs compared to the MPA-QDs, this result strongly suggested that EOF would dominate the delivery of SAv-QDs, despite their weakly opposing positive electrophoretic mobility. This was confirmed experimentally: the migration velocity of the SAv-QDs was determined to be 0.08×10^{-2} cm s^{-1} (cathodic), while the EOF velocity within the PDMS/derivatized glass chip was estimated to be 5×10^{-2} cm s^{-1}. EOF velocity was determined using the current monitoring method.[32, 33] The average velocities were determined for an applied field strength of 200 V cm^{-1} and using 50 mM, pH 9.25 borate buffer.

A1.2 Data Analysis

A1.2.1 Förster Formalism and Time-Resolved Fluorescence Measurements

The SAv-QD/Cy3 FRET pair was characterized using the Förster formalism, the Förster distance (R_o, in units of cm) was calculated from solution based measurements using Eqn. A1.1:

$$R_o^6 = 8.79 \times 10^{-28}\,\text{mol} \times (n^{-4}\kappa^2\Phi_D J) \qquad \text{[A1.1]}$$

where n is the refractive index of the surrounding medium and was approximated as 1.33, κ^2 is the orientation factor (a value of 2/3 is assumed)[49], Φ_D is the quantum yield of the donor (a value of 0.2 was used from a previously published study)[34] and J is the spectral overlap which was determined using Eqn. A1.2:

$$J = \frac{\int F_D(\lambda)\varepsilon_A(\lambda)\lambda^4 d\lambda}{\int F_D(\lambda) d\lambda} \qquad \text{[A1.2]}$$

where F_D is the fluorescence intensity of the donor and ε_A is the molar absorptivity coefficient of the acceptor as a function of wavelength, λ. The qualitative spectral overlap for the FRET pair is displayed by the shaded region in Figure A1.3. The spectral overlap was determined to be 3.03×10^{-10} $M^{-1}cm^6$ and the Förster distance was calculated to be 4.63 nm.

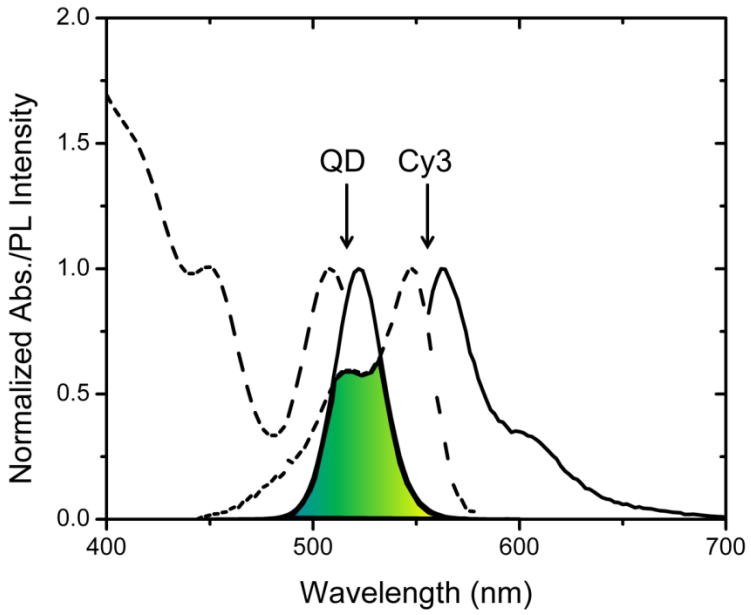

Figure A1.3. Normalized absorption (dashed lines) and emission spectra (solid lines) for the SAv-QD and Cy3 FRET pair, the spectral overlap is shaded.

PL decay curves of the hybrid solutions and QD-probe conjugates were also measured and the data was fit against the instrument response function while minimizing the χ^2. PL decay curves were fit using a two component lifetime and then averaged. The FRET efficiency was calculated from the time-resolved PL measurements using Eqn. A1.3:

$$E = 1 - \frac{\tau_{DA}}{\tau_A} \qquad \text{[A1.3]}$$

where τ_D and τ_{DA} correspond to the lifetime of the QD probe conjugates (D – Donor) before and after hybridization (DA – Donor in the presence of Acceptor) with labeled target, respectively. The average donor-acceptor separation distance from the FRET efficiencies calculated using the time resolved measurements was determined using Eqn. A1.4.

$$r = \left[\frac{nR_o^6 (1-E)}{E} \right]^{\frac{1}{6}} \qquad \text{[A1.4]}$$

where *r* is the donor-acceptor separation distance, *n* is the number of acceptors (a value of 10 was used). For quantitative comparison and analysis purposes, it was necessary to assign a FRET ratio *R* for each normalized, background subtracted PL spectrum. The FRET ratio is shown by Eqn. A1.5.

$$R = \left(\frac{\sum_{\lambda=560}^{590} PL(\lambda)}{\sum_{\lambda=510}^{540} PL(\lambda)} \right)_{DA} - \left(\frac{\sum_{\lambda=560}^{590} PL(\lambda)}{\sum_{\lambda=510}^{540} PL(\lambda)} \right)_{D} \qquad [A1.5]$$

where the wavelength range from 560 nm to 590 nm in the numerator of each term was chosen to correspond to a region of significant acceptor PL, while a wavelength range from 510 nm to 540 nm in the denominator of each term was chosen to correspond to a region of significant donor PL. The subscript DA indicates a measurement made in the presence of both the donor (QD) and the acceptor (Cy3), while the subscript D indicates a measurement made in the absence of acceptor.

For the images acquired using an epifluorescence microscope setup, two images were obtained for each sample scanned: one image corresponding to the wavelengths associated with significant QD PL (QD channel), and one image corresponding to the wavelengths associated with significant Cy3 PL (Cy3 channel). (See instrumentation section for the specification of emission filter used for each channel). The resulting images were opened and processed using Image J software, and the dimensions of the images were adjusted to match the size of the chip area scanned. Images were also contrast adjusted, background corrected for contributions from QD PL, the space between channels was cropped for clarity, and channels were realigned for comparison purposes. The length of the microfluidic channel in the image was determined by first calibrating the scale in Image J and then using the line tool to measure the distance.

The apparent FRET efficiencies from the steady state measurements for the experiments done in bulk and microfluidics were estimated using Eqn. A1.6. (based on the Cy3/QD PL ratio),

$$E = \frac{\left(\int_{542}^{700} A \Big/ \int_{450}^{580} D\right)}{\left(\int_{542}^{700} A \Big/ \int_{450}^{580} D\right) + \Phi_A} \qquad [A1.6]$$

where A represents the integrated area under the curve for the PL intensity of the Cy3 acceptor between a wavelength range of 542 nm to 700 nm, D represents the integrated area under the curve for the PL intensity of the gQD donor between a wavelength range of 450 nm to 580 nm, and Φ_A represents the quantum yield of the Cy3 acceptor. The PL intensity of Cy3 was determined by subtracting the PL spectrum of the QD from the composite PL spectrum of the QD in the presence of Cy3 acceptor. From the lifetime data in Fig. 2(b), the solution-phase FRET efficiencies were independently known from the PL ratios determined for Fig. 2(a). As such, it was possible to back-calculate the apparent quantum yield of the Cy3 bound to the solution-phase QDs as Φ_A = 0.33 and 0.23 for FC-D TGT and FC-P TGT, respectively. The Cy3/QD PL ratios for the data in Fig. 3 were then substituted into Eqn. S6 with the appropriate solution-phase Cy3 quantum yield values to calculate apparent solid-phase FRET efficiency.

A1.3 Additional Results and Discussion

A1.3.1 Silanization Quality Control

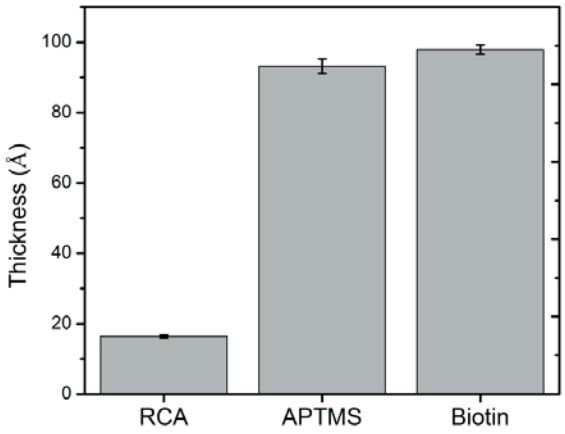

Figure A1.4. Film thickness as a function of various derivatization steps to impart biotin functionality to silicon wafers.

The chemical derivatization of glass substrates with biotin was characterized using ellipsometry by subjecting reflective silicon wafer to the same chemical modification steps. The results are shown in Figure A1.4. The film thickness increased from 16.4 ± 0.4 Å to 93.2 ± 2.1 Å after the immobilization of APTMS, which corresponded to an increase in thickness of 76.8 ± 2.1 Å, suggesting some multilayer formation. The film thickness for the immobilization of a monolayer of APTMS has been reported to be *ca.* 7Å.[50] Following the biotinylation step, the film thickness increased by 5 ± 2 Å, which was consistent with expectations.

A1.3.2 Conformation of Oligonucleotide Probes Conjugated to Solution-Phase QDs

The conformation of biotinylated oligonucleotide probes conjugated to solution-phase SAv-QD was estimated from the combined FRET efficiencies for FC-D TGT and FC-P TGT, and the well-known length scaling of Watson-Crick double-stranded DNA helices (0.34 nm per base pair). The efficiencies were converted into center-to-center QD-Cy3 separation distances using Eqn. A1.4, and the length of the 19-mer probe/target duplex was estimated as *ca.* 6.5 nm. A

simple trigonometric model as shown in Figure A1.5, allowed the time- and ensemble-averaged angle between the oligonucleotide duplex and SAv-QD surface normal to be estimated. Although the oligonucleotide duplex is within the persistence length of DNA, if the rigid-rod model were to fail, a more acute angle to the normal might be the case with some flexure in the duplex.

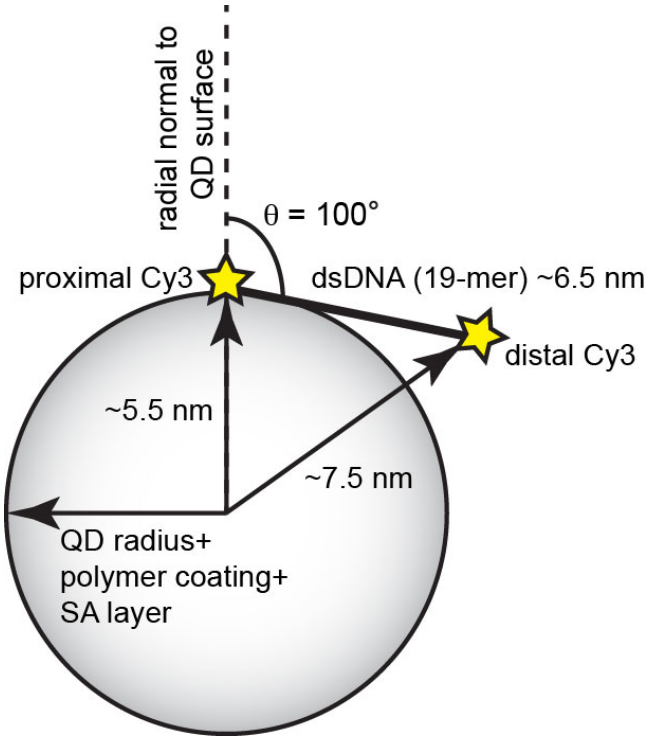

Figure A1.5. Trigonometric model, derived from solution-phase FRET efficiencies, for the average conformation of oligonucleotide duplexes bound to the SAv-QDs. The inorganic QD nanocrystal, polymer coating, and SA layer are treated as a single sphere.

As noted in the main text, the FC-D TGT was used in model assays since the distal Cy3 label mimics the position of Cy3 labeled to a reporter oligonucleotide for use in a sandwich assay. This is shown schematically in Figure A1.6. A sandwich assay format enables QD-FRET assays without directly labeling target nucleic acids.

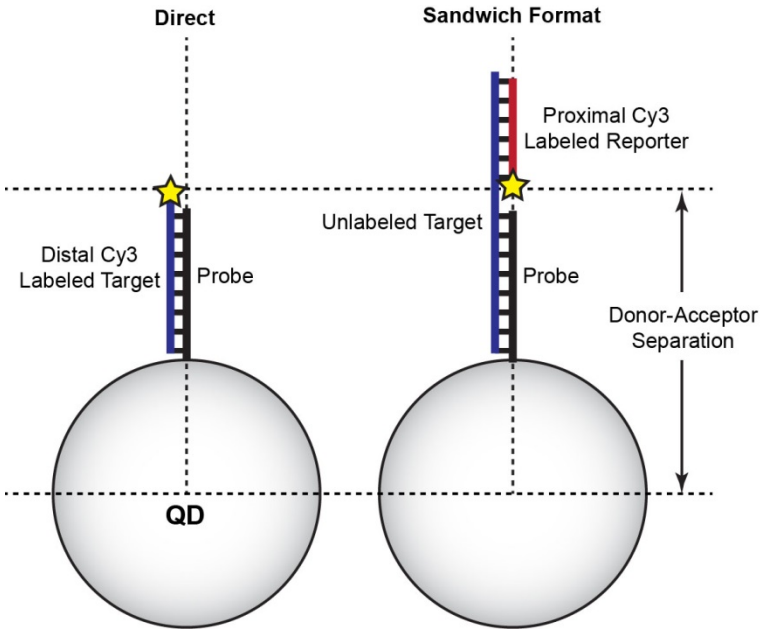

Figure A1.6. Similar donor (QD)-acceptor (Cy3) distances exist when comparing a direct assay format using distal Cy3 labeled target (FC-D TGT), and a sandwich assay format with unlabeled target nucleic acid and a proximal Cy3 labeled reporter oligonucleotide. The nucleic acids are shown extending normal to the QD surface for clarity; however, the same congruence would hold for a tangential conformation (see Fig. A1.5) with approximately rod-like dsDNA.

Appendix 2 – Supporting Information for Chapter 3

A2.1 Detailed Experimental Methods

A2.1.1 Instrumentation

Absorption spectra were acquired using a HP8452A Diode-Array Spectrophotometer (Hewlett Packard Corporation (Palo Alto, CA). Solution phase PL measurements were made using a QuantaMaster Photon Technology International spectrofluorimeter (London, ON, Canada). The excitation source was a xenon arc lamp (Ushio, Cypress, CA) and the detector was a red-sensitive R928P photomultiplier tube (PMT, Hamamatsu, Bridgewater, NJ).

PL measurements from the interior of the microfluidic channels were made using a Nikon Eclipse L150 epifluorescence microscope (Nikon, Mississauga, ON) that was custom modified with a motorized xyz translational stage. The excitation source included a 25 mW diode laser with an output of 402 nm (Radius 402, Coherent Inc, Santa Clara, CA). The light from the laser was directed through a filter cube (excitation filter: ZET405/20x, dichroic mirror: Z405rdc (Chroma Technologies Corp., Bellows Falls, VT)) to excite the chemistry on the glass wall of the microfluidic channels using a 40x Nikon ELWD Plan Fluor objective lens (NA = 0.60). The PL intensity was collected in the backward direction by the same objective lens and was coupled into a diode array spectrophotometer (QE65000, Ocean Optics Inc., Dunedin, FL) using an optical fiber waveguide. Data acquisition was done using a SpectraSuite software (Ocean Optics). On average, 3 to 5 PL spectra were collected at different positions along the length of a microfluidic channel. Epifluorescence images were collected using a custom written LabVIEW (National Instruments, Austin, TX) program to control the data acquisition and the operation of the xyz translational stage of the epifluorescence microscope described above. Images for the two QDs donor detection channels (gQDs and rQDs) and the two FRET sensitized acceptor detection channels (Cy3 and A647) were collected by raster scanning over the microfluidic chip using H5784-20 PMT (Hamamatsu, Bridgewater, NJ) as the detector. For each QD and FRET sensitized detection channel, a different emission filter was associated with the filter cube to isolate the PL intensities associated with each of the detection channels. D525/20x and D620/40x emission filters (Chroma Technologies Corp., Bellows Falls, VT) were used to image the PL

associated with gQDs and rQDs (donor detection channels), while HQ570/20x and HQ680/30x (Chroma Technologies Corp., Bellows Falls, VT) emission filters were used to image the PL associated with Cy3 and A647 (acceptor detection channels).

The data for the net mobility of A647 labeled DNA targets (SMN1 and uidA) was acquired using an epifluorescence microscope setup (described above) that was equipped with a 10 mW diode laser with an output of 635 nm. The laser light was passed through an excitation filter D640/20x (Chroma) and reflected off a ZT647rdc dichroic mirror to excite the sample through a ELWD 20x Nikon Plan Fluor objective lens (NA = 0.45). The PL intensity was collected in the backward direction by the same objective lens, passed through a HQ680/30x emission filter (Chroma) and finally detected by a H5784-20 PMT (Hamamatsu, Bridgewater, NJ). The program used for time based monitoring and data acquisition was written in-house using LabVIEW software.

Electrokinetic flow within the walls of microfluidic channels was controlled using a Labsmith High Voltage Sequencer (HVS448-3000, Livermore, CA).

Scanning electron microscope (SEM) images were acquired using a Hitachi s-5200 SEM (Hitachi High Technologies America, Pleasanton, CA).

A2.1.2 Chemical Modification of Glass Coverslips and Silicon Wafers

The chemical modification scheme described below was concurrently applied to 32 glass coverslips. The microscope glass coverslips were placed inside mini-racks made of Teflon (Invitrogen by Life Technologies) to prevent contact between the coverslips. The coverslips were then cleaned with the RCA1 and RCA2 methods (described below) to generate surface silanol groups.

The coverslips were initially subjected to a base wash treatment consisting of 1:1:5 (v/v) mixture of ammonium hydroxide, hydrogen peroxide and deionized water respectively at 85°C for 5 min. The slides were then rinsed twice with deionized water. This was followed by an acid wash treatment consisting of 1:1:5 (v/v) mixture of hydrochloric acid, hydrogen peroxide and deionized water respectively at 85°C for 5 min. The slides were then rinsed twice with deionized water, sonicated twice in methanol, and then rinsed with dichloromethane and diethylether in a

sequential manner. The slides were dried using a nitrogen spray and kept inside a desiccator until further use.

Cleaned coverslips were modified with APTMS to yield amine terminated coverslips via a silanization reaction. The cleaned coverslips were immersed in anhydrous toluene solution (*ca.* 300 ml) containing APTMS at 3-5% (v/v) and 1 ml of DIPEA. The dispensing of the reagents was carried out inside a glovebox filled with nitrogen. The reaction mixture was refluxed under argon for 6 hours at *ca.* 120°C. After the reaction, the slides were rinsed twice with methanol, sonicated twice in methanol for 10 min, and then rinsed with dichloromethane and diethylether in sequentially. APTMS modified glass coverslips were stored inside a desiccator until further use.

APTMS modified coverslips were further derivatized with a biotin functionality by an amide bond formation using carbodiimide chemistry. The slides were immersed in *ca*. 150 mL of anhydrous DMF containing 350 mg (1.4 mmol) of biotin, 400 mg (3.5 mmol) of NHS and 1 ml of DIPEA. The reaction mixture was then placed on an orbital shaker until complete dissolution of the reagents and then 350 µl of DIC (2.3 mmol) dissolved in 5 ml of DMF was added dropwise to the reaction mixture while stirring. The reaction was allowed to proceed for 24 hours, followed by rinsing of the glass coverslips once with DMF, twice with isopropanol. The glass coverslips were then sonicated twice in isopropanol for 10 min, rinsed once with dichloromethane and once with diethylether. The biotin modified coverslips were stored in a desiccator until further use.

The chemical modification of silicon wafers with a biotin functionality proceeded in the same manner as for the glass coverslips, except the silicon wafers were cut to dimensions of 22 mm × 22 mm to accommodate placement in mini-racks during the chemical modification steps.

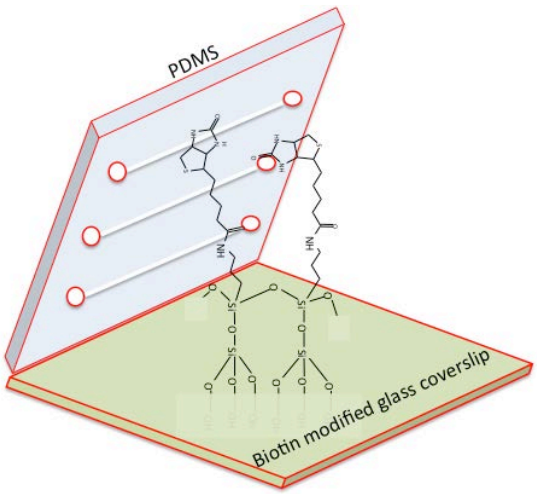

Figure A2.1. Schematic illustration of the three channel hybrid glass/PDMS based microfluidic chip. The surface of the glass coverslip was functionalized with biotin. The length, width and height of each microfluidic channel were 1.2 cm, 250 μm and 12 μm, respectively.

A2.1.3 Immobilization of QDs within hybrid silicon wafer/PDMS based microfluidic chips

For SEM imaging, the QDs were immobilized on the biotinylated silicon surface of a hybrid silicon wafer/PDMS based microfluidic channels. A 7 μL solution of QDs (gQDs to rQDs in 12 to 1 molar ratio) was dispensed in one reservoir and a negative pressure via vacuum was applied at the other reservoir to bring the solution of QDs inside the channels. The conductive nature of a doped silicon wafer renders this substrate suitable for SEM imaging but incompatible for electrokinetic delivery. As a result, vacuum-based injection was used to bring the solution of QDs into the microfluidic channel. The solution was allowed to sit inside the channels for 10 min. The residual solution of the QDs within the reservoirs was removed and replaced with BB buffer. The channels were then washed three times with BB buffer by an application of negative pressure for 3 min each for each wash. PL spectra along the channels were then measured. For SEM imaging, the PDMS cover was removed from the silicon wafer and the surface of the silicon wafer was then rinsed with deionized water to remove excess buffer salts. The area of the silicon wafer with QDs immobilized along the channel length was then trimmed using a diamond cutter.

It should be noted that the plasma oxidation of the PDMS cover was necessary to render channels hydrophilic for the injection of aqueous solution. However, due to the presence of biotin functionality on the glass coverslips, they could not be subjected to plasma oxidation. As a result, biotin-modified coverslips offer a weak seal of the PDMS cover, which rendered the bonding reversible. In other words, it was possible to remove PDMS cover from the glass coverslip. Due to the aforementioned weak seal, vacuum injection instead of pressure injection was applied to bring QDs inside the microfluidic channels.

A2.2 Data Analysis

A2.2.1 Quantum Yields

For gQDs dissolved in 50 mM BB (pH 9.25), the QY value was estimated using fluorescein dye as a standard that was dissolved in 0.1 M NaOH. The QY of fluorescein under these conditions is reported to be 0.92 [221]. In case of rQDs dissolved in 50 mM BB (pH 9.25), the QY standard used was sulforhodamine 101 dissolved in ethanol. The QY of sulforhodamine 101 under these conditions is reported to be 1.00 [222]. For Cy3 dissolved in 100 mM TB (pH 7.44, 20 mM NaCl), the QY standard used was 5-carboxytetramethylrhodamine (5-CTMR) that was dissolved in methanol. The QY of 5-CTMR under these conditions is reported to be 0.68 [223]. In case of A647 dissolved in 100 mM TB (pH 7.44, 20 mM NaCl), the QY standard used was Nile Blue perchlorate that was dissolved in acidic ethanol. The QY of Nile Blue perchlorate under these conditions is reported to be 0.27 [224]. The Cy3 and A647 dyes were conjugated with SMN1 and uidA targets, respectively. Using equation 1, the QY values were obtained from the relative slopes of the plots of integrated fluorescence intensity versus absorbance for the sample and the standard at different concentrations. The trapezoidal approximation was made in calculating the value of the integrated fluorescence intensity. The QY standards fluorescein, sulforhodamine 101, 5-CTMR and nile blue perchlorate were excited at 470 nm, 560 nm, 520 nm and 600 nm, respectively. Cy3, A647 and both colors of QDs were excited at 518 nm, 620 nm and 406 nm, respectively. The path length was kept constant for all the measurements and is assumed in Eqn. A2.1.

$$\frac{\int F d\lambda}{\int F_{ref} d\lambda} = \frac{\varepsilon}{\varepsilon_{ref}} \frac{\Phi}{\Phi_{ref}} \frac{c}{c_{ref}} \qquad [A2.1]$$

The QYs of gQDs and rQDs donors were determined to be 47.8% and 89.1%, respectively. The QYs of Cy3 and A647 acceptors were determined to be 19.7% and 51.6%, respectively.

The Förster distance, R_o, which is a characteristic of the donor-acceptor FRET pair, was determined using Eqn. A2.2. The Förster distance depends on the refractive index of the medium, n, the quantum yield of the donor, Φ_D, the relative orientation in space of the emission dipole of donor and absorption dipole of acceptor, κ^2, and spectral overlap between the emission of the donor and the absorption of the acceptor, J, a value described by Eqn. A2.3. The spectral overlap integral is a wavelength dependent function of the fluorescence intensity of the donor, F_D, and molar absorptivity coefficient of the acceptor, ε_A, normalized by the integrated fluorescence intensity of the donor. The trapezoidal approximation was made in calculating the various integrals. A qualitative representation of the spectral overlaps for the gQD/Cy3 and rQD/A647 FRET pairs is shown in the shaded area in Figure A2.2.

$$R_o^{\,6} = 8.79 \times 10^{-28}\, mol \times (n^{-4}\kappa^2 \Phi_D J) \qquad [A2.2]$$

$$J = \frac{\int F_D(\lambda)\varepsilon_A(\lambda)\lambda^4 d\lambda}{\int F_D(\lambda) d\lambda} \qquad [A2.3]$$

A2.2.2 FRET Ratios

For single-color hybridization experiments, the quantitative and comparative analysis was done by assigning a FRET ratio, R, for each normalized and background corrected PL spectrum. For the experiments done with gQD/Cy3 FRET pair, the $R_{gQD/Cy3}$ is given by Eqn. A2.4.

$$R_{gQD/Cy3} = \left(\frac{\sum_{\lambda=560}^{\lambda=590} PL(\lambda)}{\sum_{\lambda=510}^{\lambda=540} PL(\lambda)} \right)_{DA} - \left(\frac{\sum_{\lambda=560}^{\lambda=590} PL(\lambda)}{\sum_{\lambda=510}^{\lambda=540} PL(\lambda)} \right)_{D} \qquad [A2.4]$$

In Eqn. A2.4, a wavelength range from 560 nm to 590 nm in the numerator corresponds to a region of significant acceptor (Cy3) PL intensity, while a wavelength range from 510 nm to 540 nm in the denominator corresponds to a region of significant donor (gQDs) PL intensity. The subscript DA indicates the measurements made in the presence of both the donor (gQDs) and the

acceptor (Cy3), while the subscript D indicates the measurements made in the absence of acceptor.

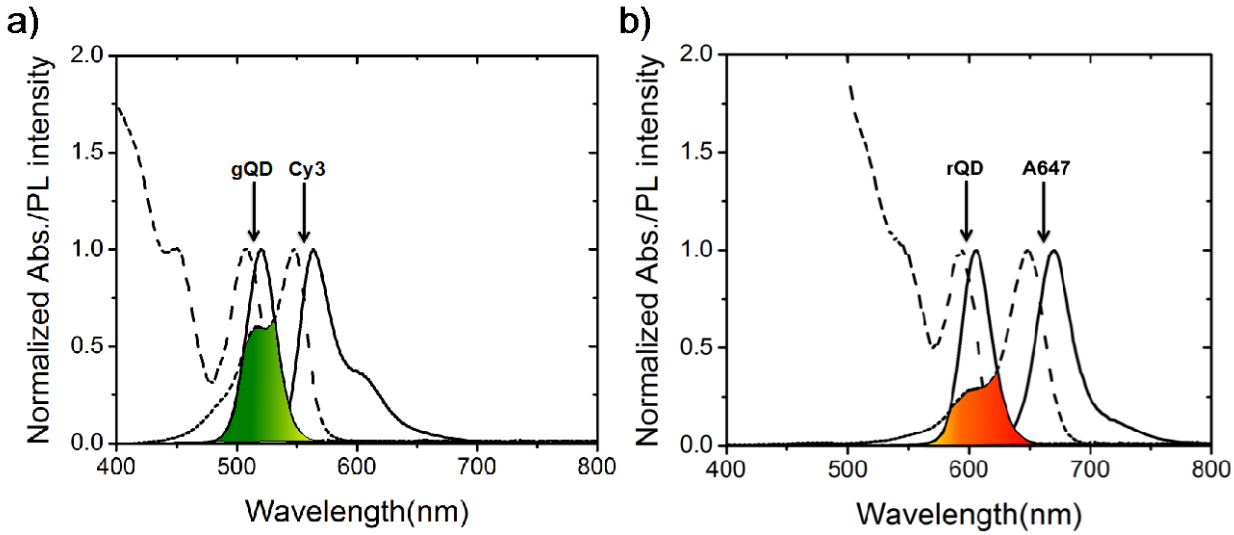

Figure A2.2. Normalized absorption (dashed lines) and emission spectra (solid lines) for the (a) gQD/Cy3 FRET pair and (b) rQD/A647 FRET pair. A qualitative representation of the spectral overlaps for each FRET pair is shown in the shaded area.

For the experiments done with rQD/A647 FRET pair, the $R_{rQD/A647}$ is given by Eqn. A2.5.

$$R_{rQD/A647} = \left(\frac{\sum_{\lambda=660}^{\lambda=690} PL(\lambda)}{\sum_{\lambda=590}^{\lambda=620} PL(\lambda)} \right)_{DA} - \left(\frac{\sum_{\lambda=660}^{\lambda=690} PL(\lambda)}{\sum_{\lambda=590}^{\lambda=620} PL(\lambda)} \right)_{D} \qquad [A2.5]$$

In Eqn. A2.5, a wavelength range from 660 nm to 690 nm in the numerator corresponds to a region of significant acceptor (A647) PL intensity, while a wavelength range from 590 nm to 620 nm in the denominator corresponds to a region of significant donor (rQDs) PL intensity. The subscript DA indicates the measurements made in the presence of both the donor (rQDs) and the acceptor (A647), while the subscript D indicates the measurements made in the absence of acceptor.

In terms of the fluorescence imaging of the microfluidic chips for single-color experiments, two images were obtained for each microfluidic chip scanned: one image corresponding to the wavelengths associated with significant donor PL (gQDs or rQDs), and one image corresponding to wavelengths associated with significant acceptor PL (Cy3 or A647). For two-color hybridization experiments, four images were obtained for each microfluidic chip scanned: two

images corresponding to the wavelengths associated with significant donors PL (gQDs and rQDr) and two images corresponding to the wavelengths associated with significant acceptors PL (Cy3 and A647). (See instrumentation section for the specification of emission filter used for imaging each detection channel).

A2.2.3 Determination of the Net Mobilities of SMN1 and uidA Targets

The net mobilities of the SMN1 and uidA targets were in the direction of the anode. Mobilities were experimentally determined using time-based measurements. The sequence for tracking of motion was Cy5 labeled, and an epifluorescence microscope equipped with the excitation and detection of Cy5 dye (see instrumentation section for details) was used for imaging. A 7 μL solution of an oligonucleotide sequence at 1 μM concentration dissolved in TB buffer was dispensed in a reservoir connected to the cathode. A voltage of 200 V was applied across the length of a microfluidic channel to introduce Cy5-labeled sequence into the channel. Time-based measurements associated with observation of the location of Cy5 fluorescence were done at the end of the channel close to a reservoir connected to the anode. Knowledge of the length of the microfluidic channel (ca. 1.2 cm) and the time required for the appearance of a fluorescence signal, was sufficient to determine the net mobilities of SMN1 and uidA target. The net mobilities of SMN1 and uidA targets were determined to be 1.1×10^{-4} $cm^2\ V^{-1}s^{-1}$ and 1.6×10^{-4} $cm^2\ V^{-1}s^{-1}$, respectively.

A2.2.4 Cross-over Point Calibration

An estimation of the length of a microfluidic channel exhibiting target hybridization as a function of the amount of target DNA delivered into a microfluidic channel was done using a cross-over point analysis. Cross-over point is a distance along a microfluidic channel where the normalized PL intensities of the donor and the acceptor meet. An example of a cross-over point for the gQD/Cy3 FRET pair for determination of the channel length coverage exhibiting target hybridization is shown in Figure. A2.3. The acquired epifluorescence images were opened and background corrected using ImageJ software, and the plot line profile feature was used to plot the donors and acceptors PL intensity profiles along the microfluidic channels. The PL profiles were then normalized to a maximum value.

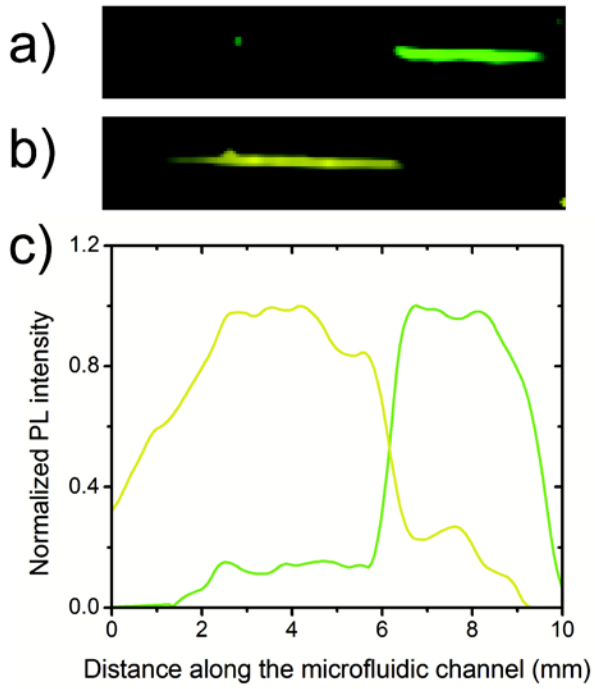

Figure A2.3. Cross-over point analysis for determining the length of a microfluidic channel exhibiting target hybridization as a function of the amount of target DNA injected into a microfluidic channel. Pseudocolor epifluorescence images of a microfluidic channel taken under (a) gQD detection channel and (b) Cy3 detection channel for the injection of 297 fmol of SMN1 FC TGT. (c) Corresponding normalized PL intensity profiles of gQDs (in green) and Cy3 (in yellow) along the microfluidic channel. The cross-over point is the point along a microfluidic channel where the donor (gQDs or rQDs) and the acceptor (Cy3 or A647) PL intensity profiles meet.

A2.3 Additional Results and Discussion

A2.3.1 Determination of oligonucleotide probe loading capacity on rQDs and gQDs

In case of rQDs, absorption spectroscopy was used for the determination of SMN1 probe loading capacity, while in case of gQDs, fluorescence spectroscopy was used for the determination of SMN1 probe loading capacity. The oligonucleotide sequence (SMN1 probe) was dual functionalized with a Cy5 dye and a biotin-TEG (triethylene glycol) modification at the 5' and 3' termini (Sequence 1), respectively. The Cy5 dye modification was used as an internal standard for the determination of SMN1 probe loading capacity on the two colors of QDs, while the biotin modification was used for the conjugation of SMN1 probe to the surface of rQDs and gQDs via the streptavidin-biotin interaction. The SMN1 probe sequence is given below and was obtained from Integrated DNA Technologies (Coralville, IA).

Cy5 – 5'– ATT TTG TCT GAA ACC CTG T – TEG biotin–3' [Sequence 1]

QDs with a molar concentration range of 80-100 nM were incubated with an 80 fold excess of Sequence 1 in TB buffer. The mixture was shaken overnight on a vortex mixer. The QD-probe conjugates were then purified from excess oligonucleotides by centrifugation three times using an Amicon Ultra-0.5, 50kDa centrifugal filter (Millipore Corporation, Billerica, MA) at 7500 rpm. The purified QD-probe conjugates were then suspended in TB buffer.

For determining the SMN1 probe loading density on rQDs, absorption spectra of the purified rQD-SMN1 probe conjugates and two additional reference samples were measured; one containing Sequence 1 at 2 μM concentration and the other containing just rQDs at 200 nM concentration. The results are shown in Figure. A2.4. The ratio of the absorbance value at 640 nm for a sample containing purified rQD-SMN1 probe conjugates and a reference sample containing just Sequence 1 allowed for the determination of SMN1 probe concentration in the sample containing rQD-SMN1 probe conjugates, while the ratio of the absorbance value at 450 nm for a sample containing purified rQD-SMN1 probe conjugates and a reference sample containing just rQDs allowed for the determination of rQDs concentration in the sample containing rQD-SMN1 probe conjugates . The path length of the cuvette was kept constant for all the absorbance measurements. The ratio of the SMN1 probe concentration to rQDs concentration in the sample containing rQD-SMN1 probe conjugates allowed for the determination of SMN1 probe loading capacity on rQDs. It is important to note that 640 nm wavelength for measuring the absorbance of Cy5 dye for the determination of SMN1 probe concentration was chosen because rQDs absorb to a negligible extent at this wavelength, while 450 nm wavelength for measuring the absorbance of rQDs for the determination of rQDs concentration was chosen because the Cy5 dye, DNA and proteins absorb to a negligible extent at this wavelength. Using the above analysis, the ensemble average loading capacity of SMN1 probes on rQDs was determined to be 68 SMN1 probe molecules per rQD.

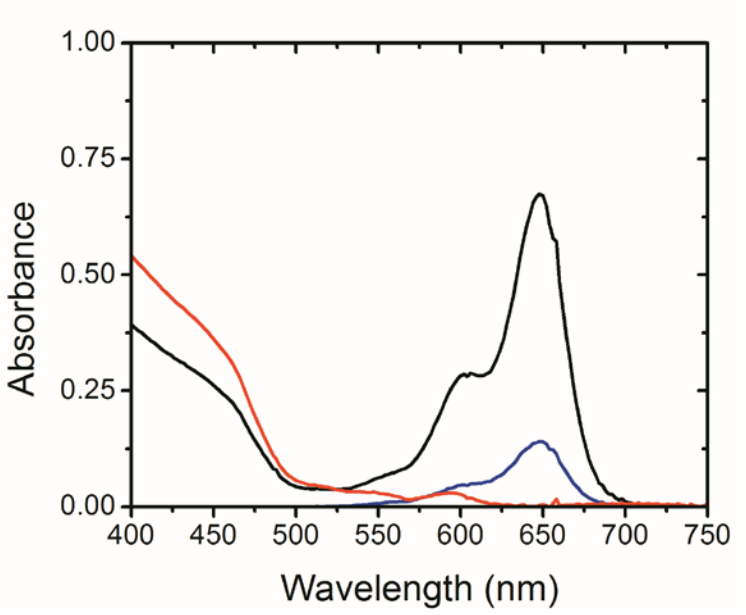

Figure A2.4. Determination of SMN1 probe loading capacity on rQDs using absorption spectroscopy. Absorption spectra of 2 μM solution of Sequence 1 (in blue), 200 nM solution of rQDs (in red) and rQD-SMN1 probe conjugates (in black).

In determining the SMN1 probe loading capacity on gQDs, PL spectra corresponding to the gQDs and the Cy5 dye of the purified gQD-SMN1 probe conjugates and two addition reference samples were measured; one containing Sequence 1 at 1 μM concentration and the other containing just gQDs at 62.5 nM concentration. The gQDs, were excitated at a wavelength of 405 nm and PL scans were done from a wavelength range of 450 nm to 600 nm. In case of the Cy5 dye, an excitation wavelength of 632 nm was used and PL scans were done from a wavelength range of 645 nm to 750 nm. The results are shown in Figure. A2.5.

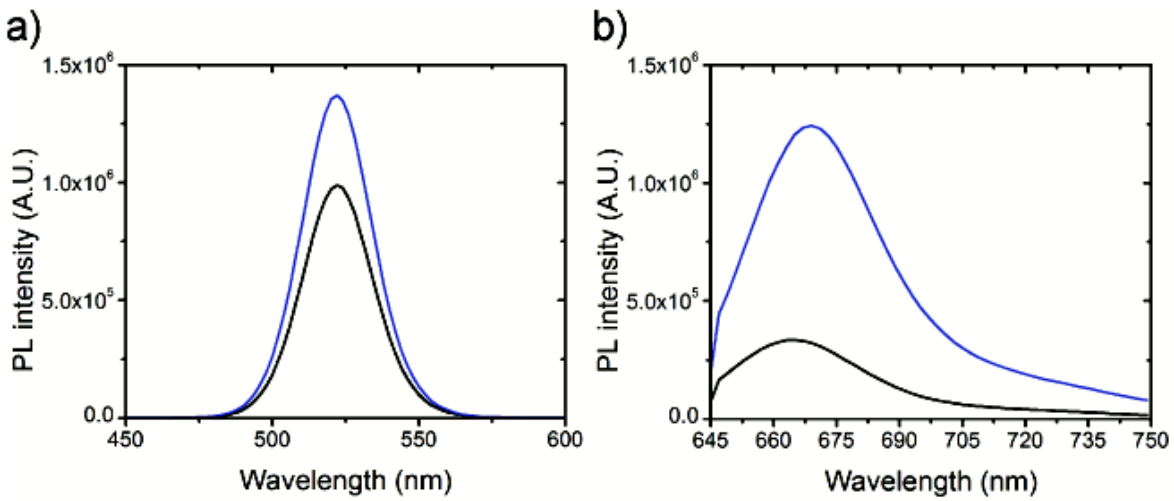

Figure A2.5. Determination of SMN1 probe loading capacity on gQDs using fluorescence spectroscopy. (a) gQD PL spectra corresponding to 62.5 nM of gQDs (in black) and gQD-SMN1 probe conjugates (in blue). (b) Cy5 PL spectra corresponding to 1 μM solution of Sequence 1 (in black) and gQD-SMN1 probe conjugates (in blue). An excitation wavelength of 405 nm was used to acquire PL spectra corresponding to gQDs emission, while 632 nm excitation wavelength was used to acquire PL spectra corresponding to Cy5 emission.

The ratio of the integrated PL intensity corresponding to the Cy5 emission for a sample containing purified gQD-SMN1 probe conjugates and a reference sample containing just Sequence 1 allowed for the determination of SMN1 probe concentration in the sample containing gQD-SMN1 probe conjugates, while the ratio of the integrated PL intensity corresponding to the gQD emission for a sample containing purified gQD-SMN1 probe conjugates and a reference sample containing just gQDs allowed for the determination of gQDs concentration in the sample containing gQD-SMN1 probe conjugates. The path length of the cuvette was kept constant for all the measurements. The ratio of the SMN1 probe concentration to gQD concentration in the sample containing gQD-SMN1 probe conjugates allowed for the determination of SMN1 probe loading capacity on gQDs. Using the above analysis, the ensemble average loading capacity of SMN1 probes on gQDs was determined to be 46 probe molecules per gQD.

It is important to note that while it was possible to use fluorescence spectroscopy for the determination of SMN1 probe loading capacity on gQDs, the same could not be done with rQDs due to a possibility of FRET based energy transfer between rQDs (donor) and Cy5 dye (acceptor) upon excitation of rQDs as reported elsewhere.[180] As a result, absorption spectroscopy was used for the determination of SMN1 probe loading capacity on rQDs. Additionally, absorption spectroscopy could not be applied to gQDs for the determination of oligonucleotide probe loading capacity on gQDs due to the issue associated with the experimental sensitivity.

The gQDs used in the work have a smaller molar extinction coefficient value as compared to the rQDs. The wavelength used to monitor the absorbance value of the QDs was 450 nm. At this wavelength, the molar extinction coefficient of rQDs and gQDs are 6.0 $\times 10^6$ $M^{-1}cm^{-1}$ and 2.0 $\times 10^5$ $M^{-1}cm^{-1}$ respectively. As an example, a 1 μM solution of gQDs will provide an absorbance value of 0.06, while in case of 1 μM solution of rQDs, the absorbance value will be 1.81. It should be noted that the stock concentration of QDs provided by the manufacturer was 2 μM. For an improved signal to noise consideration, fluorescence spectroscopy was used to determine probe loading capacity on gQDs.

A2.3.2 Solution-phase Hybridization Assays

Solution-phase hybridization experiments were done with both colors of QDs to investigate the effect of probe loading capacity on the hybridization efficiency, and also to cross-correlate the probe loading capacity results with the hybridization results. Moreover, for FRET applications it is not the presence of probes but rather those available for hybridization at the given temperature and ionic strength. The oligonucleotide probe and target sequences used for solution-phase hybridization assays are given in Table A2.1.

Table A2.1. Oligonucleotide sequences used for solution-phase hybridization assays

Name	Sequence
SMN1 probe	BiotinC6 - 5'- ATT TTG TCT GAA ACC CTG T - 3'
SMN1 Cy3 FC TGT	Cy3 - 3′-TAA AAC AGA CTT TGG GAC A-5′
SMN1 A647 FC TGT	A647 - 3′-TAA AAC AGA CTT TGG GAC A-5′

TGT = target, FC = fully-complementary, A647 = Alexa Fluor 647

Solution-phase preparation of QD-probe conjugates was done by incubating gQDs and rQDs with 80 times molar excess of SMN1 probe in TB buffer. The concentration of the QDs in the final solution was 200-250 nM. The mixture was placed on an orbital shaker for 2 hours followed by purification of QD-probe conjugates from excess probe by centrifugation three times using an Amicon Ultra-0.5, 50kDa centrifugal filter (Millipore Corporation, Billerica, MA) at

7500 rpm. The concentration of purified QD-probe conjugates was subsequently determined by absorption spectroscopy. Purified gQD-SMN1 probe conjugates and rQD-SMN1 probe conjugates were hybridized with 0, 20, 40, 60 and 80 times molar excess of SMN1 Cy3 FC TGT and SMN1 A647 FC TGT respectively in TB buffer by incubating overnight on an orbital shaker. The results for the solution-phase hybridization assays are shown in Figure A2.6.

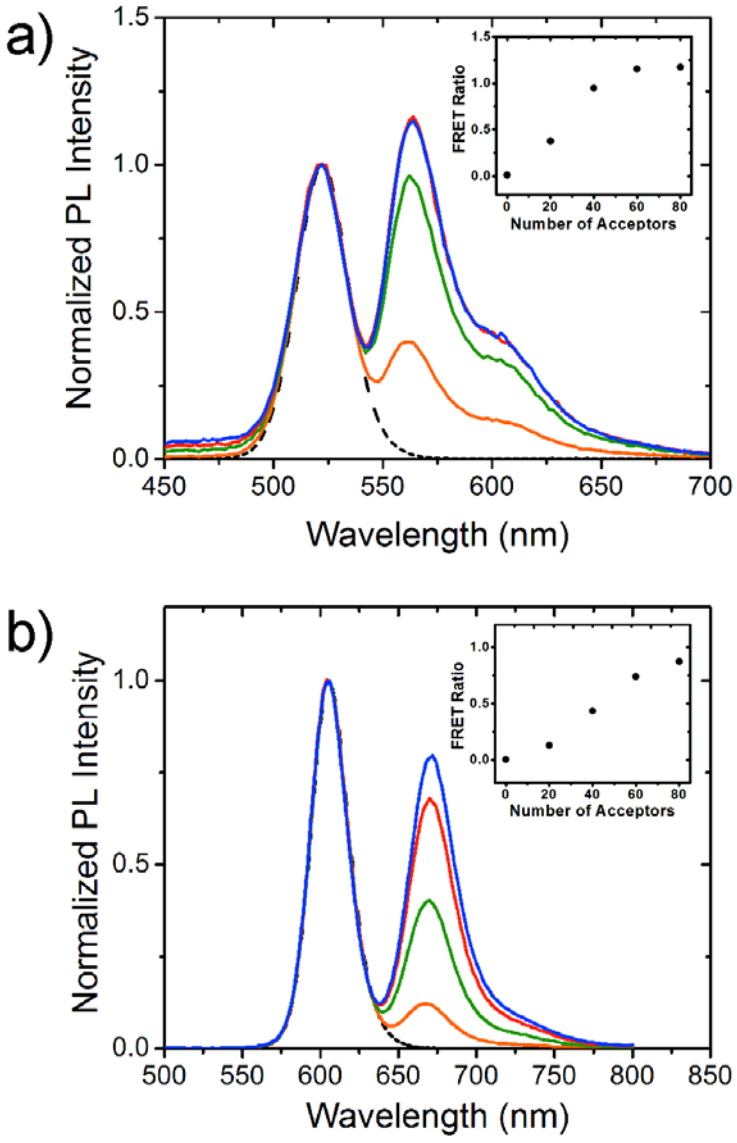

Figure A2.6. Solution-phase PL spectra of (a) gQD-SMN1 probe conjugates and (b) rQD-SMN1 probe conjugates after hybridization with a 20 (orange), 40 (green), 60 (red), and 80 (blue) fold excess of SMN1 Cy3 FC TGT and SMN1 A647 FC TGT, respectively. The dashed black line in each figure represents the PL spectrum of the corresponding QD-probe conjugates without exposure to target. The inset in each figure shows the FRET ratio corresponding with the amount of acceptor for each PL spectrum.

Based on the saturation of FRET ratio response, the response for the gQD/Cy3 FRET pair saturated at 48 acceptors (48 SMN1 Cy3 FC TGTs), while in case of the rQD/A647 FRET pair, the FRET ratio response saturated at 69 acceptors (69 SMN1 A647 TGTs). These numbers are in agreement with the SMN1 probe loading capacity of 46 and 68 on gQDs and rQDs, respectively. Overall, these results suggest that the hybridization efficiency of the assay was not compromised despite the presence of different probe loading capacity on the two colors of QDs.

Appendix 3 – Supporting Information for Chapter 4

A3.1 Experimental

A3.1.1 Reagents and Materials

Buffers used included 50 mM borate buffer (BB) pH 9.25 and 100 mM Tris-borate buffer with 20 mM NaCl (TB) pH 7.43. In experiments evaluating the effect of ionic strength on hybridization selectivity, additional NaCl was added to the BB in 25 mM increments from 25 to 100 mM. Buffer solutions were prepared using deionized water from a Millipore Synergy UV R system (Millipore Corp., Mississauga, ON, Canada) and autoclaved. Oligonucleotide probe and target sequences were purchased from Integrated DNA Technologies (Coralville, IA) and HPLC purified by the manufacturer. Additional reagents that included agarose, dioxane (anhydrous, 99.8%), formamide (99.5%), and goat serum were from Sigma Aldrich (Oakville, ON, Canada).

A3.1.2 Instrumentation

Steady-state and time-resolved photoluminescence (PL) measurements were made using a PTI QuantaMaster spectrofluorimeter (Photon Technology International, London, ON, Canada) through use of Felix GX software. The stroboscopic method was used in acquisition of PL lifetimes through use of a dye laser (GL-302, Photon Technology International) pumped by a pulsed nitrogen laser (GL-3300, Photon Technology International). The lasing dye was comprised of a saturated solution of 4,4’-(1,2-ethenediyl)bis-1,1-biphenyl (DPS) from Exciton (Dayton, OH) in dioxane, and the output of the dye laser was tuned to 402 nm.

A3.2. Data Analysis

A3.2.1 Steady State and Time-Resolved Fluorescence Measurements

For quantitative comparison, all acquired PL spectra were first background subtracted, normalized to the QD emission maximum and then a FRET ratio *R* was assigned as shown in Eqn. A3.1.

$$R = \left(\frac{\sum_{\lambda=560}^{590} PL(\lambda)}{\sum_{\lambda=510}^{540} PL(\lambda)}\right)_{DA} - \left(\frac{\sum_{\lambda=560}^{590} PL(\lambda)}{\sum_{\lambda=510}^{540} PL(\lambda)}\right)_{D} \qquad (A3.1)$$

The wavelength ranges 560 nm to 590 nm and 510 nm to 540 nm, were selected to represent significant regions of acceptor (Cy3) and donor (gQD) PL, respectively. For analyses using the rQD and A647 FRET pair, the wavelength range of significant PL for the rQD was set from 590 nm to 620 nm while for A647, 660 nm to 690 nm was chosen. The subscripts DA and D in Eqn. A3.1 denote measurements made in the presence and absence of acceptor, respectively.

Acquisition of PL lifetimes was conducted in triplicate and deconvolution of the decay curve was done against the instrument response function. The data were fit as a single exponential function by minimizing the χ^2 value and residuals.

A3.2.2 Gel Electrophoresis

Agarose gels were cast at 2% w/v in BB and run in BB at an applied field strength of 3.6 Vcm^{-1} for 90 min. Gels were imaged using a ChemiDoc™ XRS+ gel doc (Bio-Rad Laboratories, Mississauga, ON, Canada) and imaged under QDOT®525 and 605 bandpass filters. Composite images were created Image J and were stacks of the individual component acquisitions under each bandpass filter. In Ferguson analysis, agarose gels were cast at 0.5, 1, 1.5, and 2% w/v and run under the same aforementioned conditions. The resultant band migration was measured center-to-center from the lane reservoir using line plots from Image J. The migration distances were reported as absolute mobilities (in either $cm^2V^{-1}s^{-1}$ or $m^2V^{-1}s^{-1}$ for Ferguson analysis) by dividing the average velocity from three migrated bands by the applied field strength.[217]

A3.3 Additional Results and Discussion

A3.3.1 Steady State and Time-Resolved PL Measurements of QD-Hybrids

To determine the maximum attainable FRET efficiency of each of the gQD-Cy3 and rQD-A647 FRET pairs for the SMN1 hybridization assays, time-resolved PL measurements were made for an increasing number of Cy3 and A647 acceptor labeled oligonucleotide targets. These data are presented in Figure A3.1 where the QD PL lifetimes are normalized to the IRF seen as the purple curve. In (a) the response of the gQD-SMN1-PC to 0, 25, 50, and 75 equivalents of Cy3 labeled FC-TGT is shown by the green, black, blue, and red curves, respectively. The response of the rQD-SMN1-PC (b) to 0, 24, 48, 76, and 96 equivalents of A647 labeled FC-TGT correspond to the red, blue, black, yellow, and green curves, respectively.

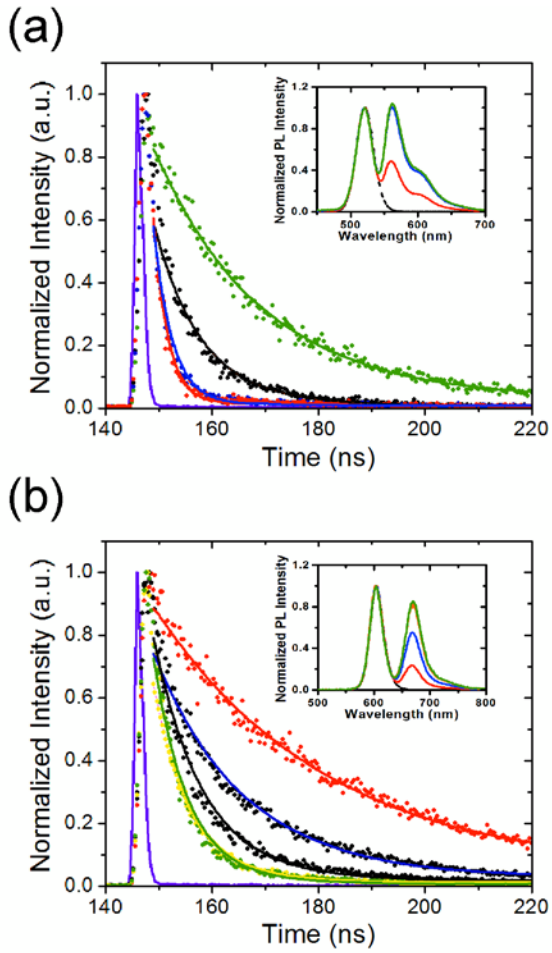

Figure A3.1. Time-resolved PL decay curves normalized to the IRF (purple curve) for the response of (a) the gQD-SMN1-PC to 0, 25, 50, and 75 equivalents of Cy3-FC TGT (green, black, blue, and red curves, respectively) and (b) the rQD-SMN1-PC to 0, 24, 48, 72, and 96 equivalents of A647-FC TGT (red, blue, black, yellow, and green curves, respectively.). The concentration of the gQD was 50 nM while that of the rQD was 20 nM, the insets in (a) and (b) are the corresponding steady state PL spectra.

The insets in both (a) and (b) are the respective steady state PL spectra which were used to identify the equivalents of target that signified acceptor saturation in each FRET pair prior to

time-resolved measurements. Maximum FRET efficiencies were obtained at *ca*. 46 and 67 acceptors for the gQD-Cy3 and rQD-A647 FRET pairs for the SMN1 hybridization assay, which is consistent with previously published studies suggesting minimal batch-to-batch variation in QD synthesis and functionalization.[209] In the gQD-Cy3 system, hybridization with this many equivalents of target resulted in a FRET efficiency of 0.86 ± 0.03 as the gQD lifetime decreased from 18.9 ± 0.2 ns to 2.6 ± 0.1 ns. For the rQD-A647 FRET pair, 0.78 ± 0.02 was the FRET efficiency at acceptor saturation, where the rQD lifetime decreased from an initial value of 29.5 ± 0.6 ns to 6.4 ± 0.1 ns.

A3.3.2 Gel Electrophoresis Mobility Shifts of SAv-QDs and QD-SMN1-PCs

SAv-QDs and the resultant SMN1 oligonucleotide conjugates were analyzed by gel electrophoresis to initially provide insight into differences in surface charge and to characterize oligonucleotide bioconjugation. Figure A3.2 displays a composite, pseudocolored image of a 2% agarose gel where lanes (i) and (ii) are SAv-rQDs and SAv-gQDs, respectively. The anodic migration is consistent with an anionic surface charge of the SAv at pH 9.25 BB along with the underlying carboxylic acid groups of the QD polymer coating. The slightly higher relative mobility of the SAv-rQD to that of the SAv-gQD is consistent with a higher net charge (*cf.* 4.77×10^{-5} $cm^2V^{-1}s^{-1}$ vs 3.64×10^{-5} $cm^2V^{-1}s^{-1}$) given the difference in the size of the two colors of QDs. Lane (iii) shows the migration of the gQD-SMN1-PC at a saturated valency of 46 oligonucleotides per QD, resulting in *ca.* an order of magnitude increase in mobility to 2.29×10^{-4} $cm^2V^{-1}s^{-1}$. Similar increases in mobility of the rQD-SMN1-PC at 10, 25, 50, and saturation (67) oligonucleotides per QD were also observed and are displayed qualitatively by lanes (v-viii), respectively. From left to right, the respective mobilities were determined to be 1.40, 1.76, 2.13, and 2.18 $cm^2V^{-1}s^{-1}$. Lane (iv) contains SAv-rQDs to serve as a reference point for comparison in the change in mobility after oligonucleotide conjugation that is anticipated due to the polyanionic nature of DNA.

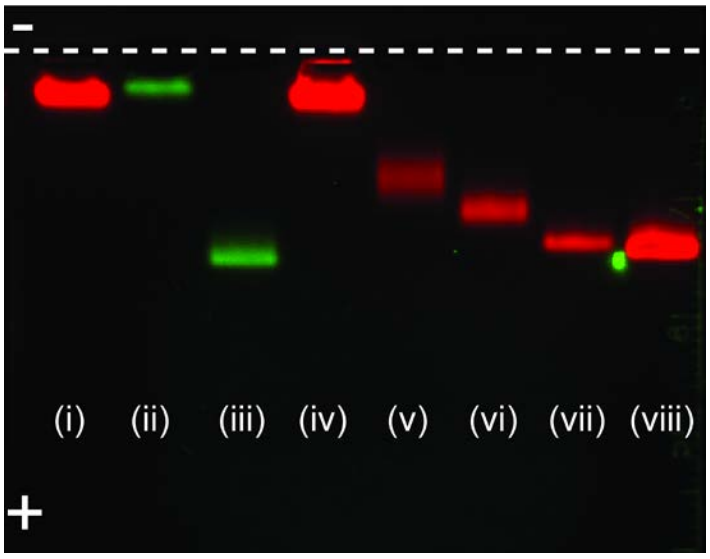

Figure A3.2. False colored composite image of a 2% agarose gel acquired under QDOT®525 (green bands) and 605 (red bands) bandpass filters. Lanes (i) and (ii) are SAv-rQDs and SAv-gQDs, respectively. SAv-gQDs at saturation of probe (46 probes per QD) are given by lane (iii), the increased migration toward the anode in comparison to lane (ii) is expected due to the polyanionic nature of the conjugated oligonucleotides. SAv-rQDs are shown again in lane (iv) to compare the shifts in band migration after conjugation of 10, 25, 50, and 67 SMN1 probes per QD, these are given by lanes (v-viii), respectively.

A3.3.3 Calculation of QD Zeta Potentials from Gel Mobility

In calculation of QD zeta potentials using Ferguson analysis, the migration distances (L) of SAv-gQDs and SAv-rQDs in gels of varying thickness (T) were measured in triplicate. The migration distance was converted to mobility (M) as shown by Eqn. A3.2:

$$M = \left(\frac{v}{E}\right) = \frac{L}{tE} \tag{A3.2}$$

where v is the particle average velocity, E is the applied electric field strength, and t is the length of time the gel was run in seconds. All gels were run for 90 min in 50 mM BB at pH 9.25 at an applied electric field strength of (3.6 Vcm^{-1}).

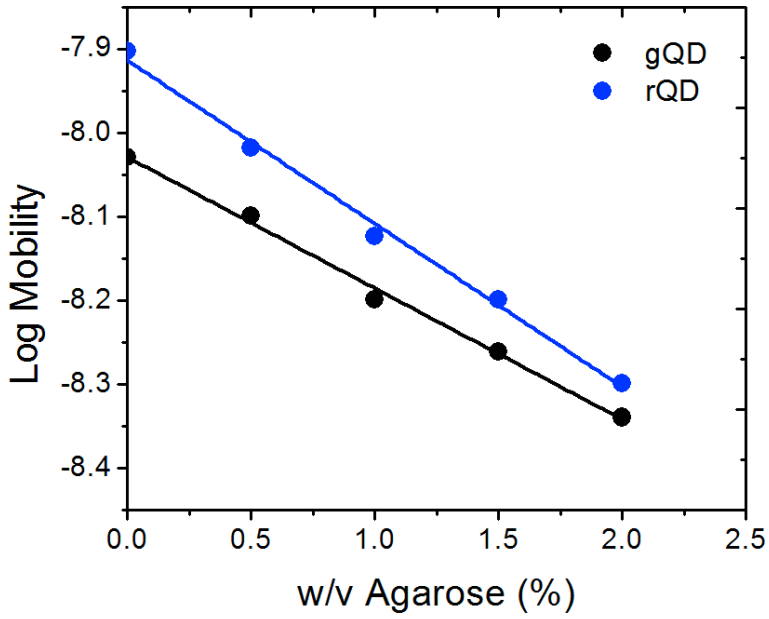

Figure A3.3. Ferguson plots of the SAv-gQD (black) and SAv-rQD (blue) from the respective particle mobilities in 0.5-2% agarose gels in pH 9.25 BB at an applied field strength of 3.6 Vcm^{-1} for 90 min. The free mobilities of SAv-gQD and SAv-rQD were estimated by extrapolation to the y-intercept as found to be 9.35×10^{-9} and 1.25×10^{-8} $m^2V^{-1}s^{-1}$.

The Ferguson plot shown by Figure A3.3 was created by plotting the $\log_{10}$ of the particle mobility as a function of the gel thickness (T, % w/v). The resultant linear plots are described by Eqn. A3.2 where the slope, K_R, is the retardation factor and the free mobility of the particle M_0 can be found through extrapolation of the plot to the y-intercept.

$$\log_{10} M = \log_{10} M_0 - K_R T \tag{A3.2}$$

From Eqn. A3.2 the free mobilities of the SAv-gQD and SAv-rQD were estimated to be 9.35×10^{-9} and 1.25×10^{-8} $m^2V^{-1}s^{-1}$, respectively. Using the free mobilities, the zeta potential (ζ) of the QDs were calculated using Eqn. A3.3 and A3.4.

$$M_0 = \frac{\varepsilon_0 \varepsilon_R \zeta}{\eta} f(\kappa R) \tag{A3.3}$$

$$f(\kappa R) \approx \frac{2}{3}\left(1 + \frac{1}{2}\left(1 + \frac{2.5}{\kappa R_H}\right)^{-1}\right), \frac{2}{3} < f(\kappa R) < 1 \tag{A3.4}$$

In Eqn. A3.3, ε_0 and ε_R are the permittivity of free space and the relative permittivity of the medium, respectively, the viscosity of the medium is given by η, which was approximated as water. The particle Debye length is given by (κ^{-1}) and can be calculated from the ionic strength of the buffer as described in the publication by Park et al.[217] The radius of hydration for each type of SAv-QD as determined from fluorescence correlation spectroscopy measurements was used in the calculation but can also be estimated from the gel data.[217] From Eqn. A3.3 the zeta potentials of the SAv-gQDs and SAv-rQDs were determined to be -20 and -25 mV, respectively.

Appendix 4 – Supporting Information for Chapter 5

A4.1 Detailed Experimental Methods

A4.1.1 Reagents and Materials

Hydrogen peroxide (30%), ammonium hydroxide (30%), hydrochloric acid (16 M), methanol, ethanol, isopropanol, dichloromethane and diethyl ether were obtained from Caledon Laboratories (Georgetown, ON, Canada) and were reagent grade or better. Toluene (anhydrous, 99.8%), *N*,*N*-dimethylformamide (DMF) (anhydrous, 99.8%) 3-aminopropyltrimethoxysilane (APTMS, 97%), *N*,*N*-diisopropylethylamine (DIPEA, 99.5%), *N*-hydroxysuccinimide (NHS, 99%), *N*,*N*-diisopropylcarbodiimide (DIC, 99%), biotin (99%), dioxane (anhydrous, 99.8%), and formamide (99.5%) were from Sigma Aldrich (Oakville, ON, Canada). Deuterated dimethylsulfoxide (DMSO-d_6) was from Cambridge Isotope Laboratories (Cambridge, MA). Buffers used were borate (BB; 50 mM, pH 9.25) and borate (BB + NaCl; 50 mM + 20 mM NaCl, pH 9.25), and tris-borate (TB; 100 mM tris, 100 mM borate and 20 mM NaCl, pH 7.4). All buffers were prepared using deionized water from a Millipore Synergy UV R purification system (Millipore Corp., Mississauga, ON, Canada) and autoclaved prior to use. Before use in microfluidic experiments, all buffers were filtered using an Acrodisc 0.2 μm syringe filter, Pall Corp. (Ann Arbor, MI). CdSe/ZnS Qdot® 525 ITK™ and 605 ITK™ Streptavidin Conjugates were from Life Technologies (Oakville, ON, Canada). Oligonucleotides were from Integrated DNA Technologies (Coralville, IA) and were HPLC purified by the manufacturer. Fisher's Finest glass microscope slides (25 mm × 75 mm) and coverslips (22 mm × 22 mm) were obtained from Fisher Scientific (Ottawa, ON, Canada). Su-8 5 photoresist was obtained from MicroChem (Newton, MA). A PDMS Sylgard 184 silicone elastomer kit was from Ellsworth Adhesives (Stoney Creek, ON, Canada).

A4.1.2 Instrumentation

On-chip PL measurements were acquired using an in house, custom-built epifluorescence microscope that was based on a Nikon Eclipse L150 platform (Nikon, Mississauga, ON,

Canada). The microscope contained a 406 nm diode laser (Radius 405, 25 mW, Coherent Inc., Santa Clara, CA) and a motorized xyz translation stage. The intensity of the laser light was modulated using optical density filters. A filter cube comprised of a 405/20 nm excitation filter and Z405 rdc dichroic mirror (Chroma Technology Corp., Bellows Falls, VT) was used to direct the light to a 40x Nikon ELWD Plan Fluor Objective lens (NA: 0.60). PL emission was collected through the same lens and measured using a diode array spectrophotometer and SpectraSuite software (QE6500, Ocean Optics Inc., Dunedin, FL) via a fiber optic waveguide. Images of microfluidic chips were acquired using a photomultiplier tube and by raster scanning over the sample. Point-by-point reconstruction enabled image processing using ImageJ software (National Institutes of Health, Bethesda, MD). PL intensities from the rQD and A647 were isolated using D620/20 and 680/30 bandpass filters (Chroma Technology Corp.), respectively.

Electrokinetic control in microfluidic chips was facilitated by use of a High Voltage Sequencer HVS448 3000V (Labsmith, Livermore, CA). Platinum wire electrodes were soldered onto high voltage silicone coated wire for delivery of the required voltages on-chip.

Scanning electron microscopy (SEM) images of in-channel immobilized QDs were obtained at the Centre for Nanostructure Imaging (Toronto, ON, Canada) using a FEI Quanta FEG 250 Environmental SEM/STEM.

A4.1.3 Microfluidic Chip Assembly

A4.1.3.1 Cleaning of Glass Coverslips using RCA Protocol

The microfluidic chips were hybrid PDMS-glass structures; glass coverslips were modified with interfacial chemistry in batches of 32 and fixed with PDMS prior to assay assembly. Coverslips were processed using the RCA protocol to expose surface silanol groups by means of sequential treatment with base and acid in oxidizing conditions. Substrates were immersed in a 5:1:1 v/v of deionized water, 30% ammonium hydroxide, and 30% hydrogen peroxide for 10 min at 85-90 °C. Glass coverslips were then washed twice thoroughly with deionized water before immersion in the acidic wash of 5:1:1 v/v deionized water, 16 M hydrochloric acid, and 30% hydrogen peroxide for 10 min at 85-90 °C. Coverslips were then washed again twice with deionized water,

and then were sonicated in methanol twice for 10 min each time. This was followed by rinsing two times with dichloromethane and diethyl ether. The processed coverslips were stored in a vacuum oven at 60 °C.

A4.1.3.2 Silanization of Cleaned Coverslips

Etched slides were immersed in *ca.* 300 mL of anhydrous toluene, 0.5 mL of DIPEA, and 7.5 mL of APTMS and then the mixture was refluxed for 6 hrs under argon on an orbital shaker. After the allotted time, the solution was decanted, rinsed twice with methanol and then sonicated in methanol two times for 10 min each time. Coverslips were then rinsed twice with dichloromethane and diethylether and stored in a dessicator.

A4.1.3.3 Biotinylation of APTMS Modified Coverslips

In earlier work, APTMS modified coverslips were amide coupled to biotin by *in situ* activation of the carboxylic acid group using carbodiimide/NHS activation. This procedure was modified due to the poor solubility of biotin in DMF and the reduced yield (*ca.* 50-60%) of the carbodiimide activation at room temperature. In this new protocol, biotin NHS ester was synthesized in a separate step,[218] purified and then reacted with the APTMS coated coverslips. The process began by combining 2.5 g (10 mmol) of biotin and 1.5 g (13 mmol) of NHS with 75 mL of anhydrous DMF in a 250 mL Schlenk flask. The mixture was stirred and heated to 70 °C under argon until complete dissolution was achieved. DIPEA (1 mL) was added to the solution followed by the dropwise addition of 1.9 mL (12 mmol) of DIC. An air condenser was installed and the temperature of the solution was maintained at 70 °C for *ca.* 2 hrs. The reaction mixture was removed from heat, allowed to cool to room temperature and the solvent was removed under reduced pressure. The crude off white precipitate was recrystallized from isopropanol and the resultant white powder was collected via vacuum filtration, washed with three successive portion of cold isopropanol and then stored in a dessicator. NMR ^{1}H (400 MHz, DMSO-d_6) δ: 1.37-1.64 (m; 6H), 2.54-2.57 (d; 1H), 2.63-2.67 (t; 2H), 2.79-2.87 (m; 5H), 3.07-3.10 (m; 1H), 4.11-4.14 (m; 1H), 4.27-4.30 (m; 1H), 6.34 (s; 1H), 6.39 (s; 1H) ppm.

APTMS modified coverslips were added to a 500 mL beaker along with ca. 250-300 mL of anhydrous DMF and 0.4 g (1.2 mmol) of Biotin-NHS. A watch glass was placed on top, sealed with Parafilm® and the mixture was placed on an orbital shaker for 24 hrs. The substrates were then washed twice with DMF, sonicated twice for 10 min each time in isopropanol, washed twice with dichloromethane and diethylether and then stored in a dessicator.

A4.1.3.4 Fabrication of PDMS Microfluidic Chips

PDMS elastomer and curing agent were mixed 10:1 w/w, respectively, by vigorous stirring. The mixture was then degassed for *ca.* 1 hr. PDMS chips were made by pouring *ca.* 3.2 g onto a positive relief template followed by curing in an oven at 110 °C for 30 min. Microfluidic master templates were manufactured in a clean room facility using Su-8 5 photoresist as previously reported.[146] The channel dimensions measured 12 mm in length, 250 μm in width and 12 μm in height. Cured PDMS chips were cut to 20 mm × 20 mm and reagent wells were manually bored. PDMS chips were sealed irreversibly to modified coverslips, with the glass first being treated by air plasma oxidation for 2 min at 10.5 W using a Harrick Plasma Cleaner (Harrick Plasma, Ithaca, NY).

A4.2. Data Analysis

A4.2.1 Steady State and Time-Resolved Fluorescence Measurements

For quantitative comparison, all acquired PL spectra were first background subtracted, normalized and then a FRET ratio *R* was assigned as shown in Eqn. A4.1.

$$R = \left(\frac{\sum_{\lambda=690}^{660} PL(\lambda)}{\sum_{\lambda=590}^{620} PL(\lambda)}\right)_{DA} - \left(\frac{\sum_{\lambda=690}^{660} PL(\lambda)}{\sum_{\lambda=590}^{620} PL(\lambda)}\right)_{D} \quad \text{(A4.1)}$$

The wavelength range of significant PL for the rQD was set from 590 nm to 620 nm while for A647, 660 nm to 690 nm was chosen. The subscripts DA and D in Eqn. A4.1 denote measurements made in the presence and absence of acceptor, respectively. Acquisition of PL spectra from the microchannels was conducted by interrogating three points along the length of a

channel, followed by averaging of all acquired spectra.Acquisition of PL lifetimes was conducted in triplicate and deconvolution of the decay curve was done against the instrument response function. The data were fit as a single exponential function by minimizing the χ^2 value and residuals.

A4.2.2 QD Immobilization Density

SEM images were contrast enhanced for clarity and the QD immobilization density was determined manually. The scale in the image was used to define a region of known area, the QDs residing in this boundary were sequentially counted and then the respective density was reported in units of QDs/cm^2 for comparison purposes.

A4.3. Additional Results and Discussion

3.2 On-Chip SNP Resolution with 3 μM SMN1 Probe

Prior to investigation of differences between SMN1 probe loading capacity of gQDs and rQDs, 3 μM SMN1 probe was used to assemble the interfacial chemistry in-channel.[79, 209] At this concentration of probe oligonucleotide, assays had only offered sufficient selectivity to discriminate target sequences containing at least three mismatches.

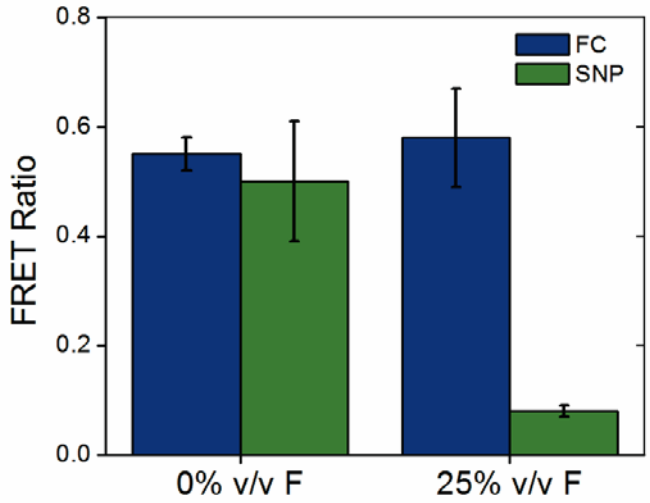

Figure A4.1. Response of the on-chip assay to FC (blue) and SNP (green) targets in BB with 0% and 25 % v/v formamide for a concentration of the SMN1 probe oligonucleotide delivered in channel of 3 μM. SNP resolution was not observed until the addition of 25% v/v formamide in BB, where a contrast ratio of 7:1 was achieved.

Moreover, previous in-channel assay selectivity has been investigated using only the gQD-Cy3 system and not the rQD-A647 FRET pair. To further illustrate the impact of QD size and the resulting oligonucleotide probe density on assay selectivity, resolution of a SNP was attempted with the rQD-A647 FRET pair using the aforementioned SMN1 probe concentration of 3 μM. The response of the on-chip assay to FC and 1BPM TGTs is shown in Figure A4.1. In the absence of formamide, resolution of a SNP is not possible where the FRET ratios for FC and the 1BPM TGTs were 0.55 ± 0.03 and 0.50 ± 0.11, respectively. To offer any selectivity against a SNP, 25% v/v formamide was required, which left the signal of the FC TGT unchanged at 0.58 ± 0.09 while the response to the 1BPM TGT decreased to 0.09 ± 0.01 and gave rise to a contrast ratio of 7 for FC:SNP targets. These results are in contrast to what was seen when 10 μM SMN1 was delivered in-channel, where discrimination against a SNP was possible without any added formamide. These data illustrate the impact of oligonucleotide probe density on the stringency of hybridization, which in turn is determined by the size of the nanocrystal for the QDs used herein.

Copyright Acknowledgements

Indications of Copyright permissions can be found in each figure caption for the specific illustration shown. Sections of this thesis in particular those of the body have been published prior to formatting of this thesis, the relevant Copyright acknowledgements are listed below.

References

(1) Kneipp, K.; Wang, Y.; Kneipp, H.; Perelman, L. T.; Itzkan, I.; Dasari, R.; Feld, M. S., *Phys. Rev. Lett.* **1997,** *78*, 1667-1670.

(2) Weiss, S., *Science* **1999,** *283*, 1676-1683.

(3) Anger, P.; Bharadwaj, P.; Novotny, L., *Phys. Rev. Lett.* **2006,** *96*.

(4) Willets, K. A.; Van Duyne, R. P., Localized surface plasmon resonance spectroscopy and sensing. In *Annu. Rev. Phys. Chem.*, 2007; Vol. 58, pp 267-297.

(5) Anker, J. N.; Hall, W. P.; Lyandres, O.; Shah, N. C.; Zhao, J.; Van Duyne, R. P., *Nat. Mater.* **2008,** *7*, 442-453.

(6) Elghanian, R.; Storhoff, J. J.; Mucic, R. C.; Letsinger, R. L.; Mirkin, C. A., *Science* **1997,** *277*, 1078-1081.

(7) Watson, J. D.; Crick, F. H. C., *Nature* **1953,** *171*, 737-738.

(8) Griffiths, A. J. F.; Wessler, S. R.; Lewontin, R. C.; Gelbart, W. M.; Suzuki, D. T.; Miller, J. H., *Introduction to Genetic Analysis*. 7th ed.; W. H. Freeman and Company: New York, 2005.

(9) Adams, R. L. P.; Knowler, J. T.; Leader, D. P., *The Biochemistry of the Nucleic Acids*. 11th ed.; Chapman & Hall Ltd: New York, 1992.

(10) Wilusz, C. J.; Wormington, M.; Peltz, S. W., *Nat. Rev. Mol. Cell Biol.* **2001,** *2*, 237-246.

(11) Gilli, G.; Bellucci, F.; Ferretti, V.; Bertolasi, V., *J. Am. Chem. Soc.* **1989,** *111*, 1023-1028.

(12) Coll, M.; Frederick, C. A.; Wang, A. H. J.; Rich, A., *Proc. Natl. Acad. Sci. U. S. A.* **1987,** *84*, 8385-8389.

(13) Wetmur, J. G., *Crit. Rev. Biochem. Mol. Biol.* **1991,** *26*, 227-259.

(14) SantaLucia, J., *Proc. Natl. Acad. Sci. U. S. A.* **1998,** *95*, 1460-1465.

(15) Tinoco, I., *J. Phys. Chem.* **1996,** *100*, 13311-13322.

(16) Zuker, M., *Nucleic Acids Res.* **2003,** *31*, 3406-3415.

(17) Allawi, H. T.; SantaLucia, J., *Biochemistry* **1997,** *36*, 10581-10594.

(18) Allawi, H. T.; SantaLucia, J., *Biochemistry* **1998,** *37*, 9435-9444.

(19) Allawi, H. T.; Santalucia, J., *Nucleic Acids Res.* **1998,** *26*, 2694-2701.

(20) Allawi, H. T.; SantaLucia, J., *Biochemistry* **1998,** *37*, 2170-2179.

(21) Peyret, N.; Seneviratne, P. A.; Allawi, H. T.; SantaLucia, J., *Biochemistry* **1999,** *38*, 3468-3477.

(22) Lefebvre, S.; Burglen, L.; Reboullet, S.; Clermont, O.; Burlet, P.; Viollet, L.; Benichou, B.; Cruaud, C.; Millasseau, P.; Zeviani, M.; Lepaslier, D.; Frezal, J.; Cohen, D.; Weissenbach, J.; Munnich, A.; Melki, J., *Cell* **1995,** *80*, 155-165.

(23) Lorson, C. L.; Hahnen, E.; Androphy, E. J.; Wirth, B., *Proc. Natl. Acad. Sci. U.S.A.* **1999,** *96*, 6307-6311.

(24) Kerem, E.; Corey, M.; Kerem, B. S.; Rommens, J.; Markiewicz, D.; Levison, H.; Tsui, L. C.; Durie, P., *N. Engl. J. Med.* **1990,** *323*, 1517-1522.

(25) Blake, R. D.; Delcourt, S. G., *Nucleic Acids Res.* **1996,** *24*, 2095-2103.

(26) Lackowicz, J. R., *Principles of Fluorescence Spectroscopy*. 3rd ed.; Springer Science+Business Media, LLC: New York, 2006.

(27) Skoog, D. A.; Holler, F. J.; Nieman, T. A., *Principles of Instrumental Analysis*. 5th ed.; Thomson Learning, Inc.: Toronto, 1998.

(28) Skoog, D. A.; West, D. M.; Holler, F. J.; Crouch, S. R., *Fundamentals of Analytical Chemistry*. 8th ed.; Brooks/Cole: Belmont, 2004.

(29) Engel, T., *Quantum Chemistry and Spectroscopy*. Pearson Education, Inc.: San Francisco, 2006.

(30) Jares-Erijman, E. A.; Jovin, T. M., *Nat. Biotechnol.* **2003,** *21*, 1387-1395.

(31) Algar, W. R.; Tavares, A. J.; Krull, U. J., *Anal. Chim. Acta* **2010,** *673*, 1-25.

(32) Alivisatos, A. P., *ACS Nano* **2008,** *2*, 1514-1516.

(33) Bruchez, M.; Moronne, M.; Gin, P.; Weiss, S.; Alivisatos, A. P., *Science* **1998,** *281*, 2013-2016.

(34) Klein, D. L.; Roth, R.; Lim, A. K. L.; Alivisatos, A. P.; McEuen, P. L., *Nature* **1997,** *389*, 699-701.

(35) Greenham, N. C.; Peng, X. G.; Alivisatos, A. P., *Phys. Rev. B* **1996,** *54*, 17628-17637.

(36) Alivisatos, A. P.; Gu, W. W.; Larabell, C., Quantum dots as cellular probes. In *Annu. Rev. Biomed. Eng.*, 2005; Vol. 7, pp 55-76.

(37) Dabbousi, B. O.; RodriguezViejo, J.; Mikulec, F. V.; Heine, J. R.; Mattoussi, H.; Ober, R.; Jensen, K. F.; Bawendi, M. G., *J. Phys. Chem. B* **1997,** *101*, 9463-9475.

(38) Murray, C. B.; Norris, D. J.; Bawendi, M. G., *J. Am. Chem. Soc.* **1993,** *115*, 8706-8715.

(39) Alivisatos, A. P., *J. Phys. Chem.* **1996,** *100*, 13226-13239.

(40) Manna, L.; Scher, E. C.; Alivisatos, A. P., *J. Am. Chem. Soc.* **2000,** *122*, 12700-12706.

(41) Peng, X. G.; Manna, L.; Yang, W. D.; Wickham, J.; Scher, E.; Kadavanich, A.; Alivisatos, A. P., *Nature* **2000,** *404*, 59-61.

(42) Hines, M. A.; Guyot-Sionnest, P., *J. Phys. Chem.* **1996,** *100*, 468-471.

(43) Peng, X. G.; Schlamp, M. C.; Kadavanich, A. V.; Alivisatos, A. P., *J. Am. Chem. Soc.* **1997,** *119*, 7019-7029.

(44) Bailey, R. E.; Nie, S. M., *J. Am. Chem. Soc.* **2003,** *125*, 7100-7106.

(45) Park, J. H.; Gu, L.; von Maltzahn, G.; Ruoslahti, E.; Bhatia, S. N.; Sailor, M. J., *Nat. Mater.* **2009,** *8*, 331-336.

(46) Sun, Y. P.; Zhou, B.; Lin, Y.; Wang, W.; Fernando, K. A. S.; Pathak, P.; Meziani, M. J.; Harruff, B. A.; Wang, X.; Wang, H. F.; Luo, P. J. G.; Yang, H.; Kose, M. E.; Chen, B. L.; Veca, L. M.; Xie, S. Y., *J. Am. Chem. Soc.* **2006,** *128*, 7756-7757.

(47) Alivisatos, A. P., *Science* **1996,** *271*, 933-937.

(48) Wilson, W. L.; Szajowski, P. F.; Brus, L. E., *Science* **1993,** *262*, 1242-1244.

(49) Peng, X. G.; Wickham, J.; Alivisatos, A. P., *J. Am. Chem. Soc.* **1998,** *120*, 5343-5344.

(50) Peng, Z. A.; Peng, X. G., *J. Am. Chem. Soc.* **2001,** *123*, 183-184.

(51) Qu, L. H.; Peng, Z. A.; Peng, X. G., *Nano Lett.* **2001,** *1*, 333-337.

(52) Kim, S. W.; Zimmer, J. P.; Ohnishi, S.; Tracy, J. B.; Frangioni, J. V.; Bawendi, M. G., *J. Am. Chem. Soc.* **2005,** *127*, 10526-10532.

(53) Yu, W. W.; Qu, L. H.; Guo, W. Z.; Peng, X. G., *Chem. Mater.* **2003,** *15*, 2854-2860.

(54) Atkins, P.; de Paula, J., *Atkins' Physical Chemistry*. 8th ed.; W. H. Freeman and Company: New York, 2006.

(55) Nirmal, M.; Brus, L., *Acc. Chem. Res.* **1999,** *32*, 407-414.

(56) Bawendi, M. G.; Steigerwald, M. L.; Brus, L. E., *Annu. Rev. Phys. Chem.* **1990,** *41*, 477-496.

(57) Efros, A. L.; Rosen, M.; Kuno, M.; Nirmal, M.; Norris, D. J.; Bawendi, M., *Phys. Rev. B* **1996,** *54*, 4843-4856.

(58) Norris, D. J.; Bawendi, M. G., *Phys. Rev. B* **1996,** *53*, 16338-16346.

(59) Chan, W. C. W.; Maxwell, D. J.; Gao, X. H.; Bailey, R. E.; Han, M. Y.; Nie, S. M., *Curr. Opin. Biotechnol.* **2002,** *13*, 40-46.

(60) Kuno, M.; Lee, J. K.; Dabbousi, B. O.; Mikulec, F. V.; Bawendi, M. G., *J. Chem. Phys.* **1997,** *106*, 9869-9882.

(61) Kim, S.; Fisher, B.; Eisler, H. J.; Bawendi, M., *J. Am. Chem. Soc.* **2003,** *125*, 11466-11467.

(62) Kim, S.; Lim, Y. T.; Soltesz, E. G.; De Grand, A. M.; Lee, J.; Nakayama, A.; Parker, J. A.; Mihaljevic, T.; Laurence, R. G.; Dor, D. M.; Cohn, L. H.; Bawendi, M. G.; Frangioni, J. V., *Nat. Biotechnol.* **2004,** *22*, 93-97.

(63) Chan, W. C. W.; Nie, S. M., *Science* **1998,** *281*, 2016-2018.

(64) Pellegrino, T.; Manna, L.; Kudera, S.; Liedl, T.; Koktysh, D.; Rogach, A. L.; Keller, S.; Radler, J.; Natile, G.; Parak, W. J., *Nano Lett.* **2004,** *4*, 703-707.

(65) Gao, X. H.; Cui, Y. Y.; Levenson, R. M.; Chung, L. W. K.; Nie, S. M., *Nat. Biotechnol.* **2004,** *22*, 969-976.

(66) Susumu, K.; Uyeda, H. T.; Medintz, I. L.; Pons, T.; Delehanty, J. B.; Mattoussi, H., *J. Am. Chem. Soc.* **2007,** *129*, 13987-13996.

(67) Uyeda, H. T.; Medintz, I. L.; Jaiswal, J. K.; Simon, S. M.; Mattoussi, H., *J. Am. Chem. Soc.* **2005,** *127*, 3870-3878.

(68) Medintz, I. L.; Uyeda, H. T.; Goldman, E. R.; Mattoussi, H., *Nat. Mater.* **2005,** *4*, 435-446.

(69) Susumu, K.; Oh, E.; Delehanty, J. B.; Blanco-Canosa, J. B.; Johnson, B. J.; Jain, V.; Hervey, W. J.; Algar, W. R.; Boeneman, K.; Dawson, P. E.; Medintz, I. L., *J. Am. Chem. Soc.* **2011,** *133*, 9480-9496.

(70) Zhan, N. Q.; Palui, G.; Safi, M.; Ji, X.; Mattoussi, H., *J. Am. Chem. Soc.* **2013,** *135*, 13786-13795.

(71) Johnson, I.; Spence, M. T. Z., *The Molecular Probes Handbook: A Guide to Fluorescent Probes and Labeling Technologies*. 11th ed.; Life Technologies Corporation: USA, 2010.

(72) Derfus, A. M.; Chan, W. C. W.; Bhatia, S. N., *Nano Lett.* **2004,** *4*, 11-18.

(73) Blanco-Canosa, J. B.; Wu, M.; Susumu, K.; Petryayeva, E.; Jennings, T. L.; Dawson, P. E.; Algar, W. R.; Medintz, I. L., *Coord. Chem. Rev.* **2014,** *263*, 101-137.

(74) Algar, W. R.; Prasuhn, D. E.; Stewart, M. H.; Jennings, T. L.; Blanco-Canosa, J. B.; Dawson, P. E.; Medintz, I. L., *Bioconjugate Chem.* **2011,** *22*, 825-858.

(75) Jennings, T. L.; Becker-Catania, S. G.; Triulzi, R. C.; Tao, G. L.; Scott, B.; Sapsford, K. E.; Spindel, S.; Oh, E.; Jain, V.; Delehanty, J. B.; Prasuhn, D. E.; Boeneman, K.; Algar, W. R.; Medintz, I. L., *ACS Nano* **2011,** *5*, 5579-5593.

(76) Medintz, I. L.; Mattoussi, H., *Phys. Chem. Chem. Phys.* **2009,** *11*, 17-45.

(77) Wagner, M. K.; Li, F.; Li, J. J.; Li, X. F.; Le, X. C., *Anal. Bioanal. Chem.* **2010,** *397*, 3213-3224.

(78) Algar, W. R.; Wegner, D.; Huston, A. L.; Blanco-Canosa, J. B.; Stewart, M. H.; Armstrong, A.; Dawson, P. E.; Hildebrandt, N.; Medintz, I. L., *J. Am. Chem. Soc.* **2012,** *134*, 1876-1891.

(79) Tavares, A. J.; Noor, M. O.; Vannoy, C. H.; Algar, W. R.; Krull, U. J., *Anal. Chem.* **2011,** *84*, 312-319.

(80) Algar, W. R. Toward Multiplexed Nucleic Acid Assays and Biosensors Using Immobilzed Quantum Dots as Donors in Fluorescence Resonance Energy Transfer. University of Toronto, Toronto, 2010.

(81) Petryayeva, E.; Algar, W. R.; Krull, U. J., *Langmuir* **2013,** *29*, 977-987.

(82) Freeman R.; Bahshi L.; Finder T.; Gill R.; Willner I., *Chem. Commun.* **2009**, 764-766.

(83) Chen, Z.; Li, G.; Zhang, L.; Jiang, J. F.; Li, Z.; Peng, Z. H.; Deng, L., *Anal. Bioanal. Chem.* **2008,** *392*, 1185-1188.

(84) Medintz, I. L.; Clapp, A. R.; Melinger, J. S.; Deschamps, J. R.; Mattoussi, H., *Adv. Mater. (Weinheim, Ger.)* **2005,** *17*, 2450-2455.

(85) Zhang, C. Y.; Johnson, L. W., *Anal. Chem.* **2009,** *81*, 3051-3055.

(86) Freeman, R.; Li, Y.; Tel-Vered, R.; Sharon, E.; Elbaz, J.; Willner, I., *Analyst* **2009,** *134*, 653-656.

(87) Boeneman, K.; Mei, B. C.; Dennis, A. M.; Bao, G.; Deschamps, J. R.; Mattoussi, H.; Medintz, I. L., *J. Am. Chem. Soc.* **2009,** *131*, 3828-3829.

(88) Lowe, S. B.; Dick, J. A. G.; Cohen, B. E.; Stevens, M. M., *ACS Nano* **2011,** *6*, 851-857.

(89) Algar, W. R.; Ancona, M. G.; Malanoski, A. P.; Susumu, K.; Medintz, I. L., *ACS Nano* **2012,** *6*, 11044-11058.

(90) Algar, W. R.; Malanoski, A. P.; Susumu, K.; Stewart, M. H.; Hildebrandt, N.; Medintz, I. L., *Anal. Chem.* **2012,** *84*, 10136-10146.

(91) Freeman, R.; Willner, I., *Chem. Soc. Rev.* **2012,** *41*, 4067-4085.

(92) Blanco-Canosa, J. B.; Wu, M.; Susumu, K.; Petryayeva, E.; Jennings, T. L.; Dawson, P. E.; Algar, W. R.; Medintz, I. L., *Coord. Chem. Rev. this issue*.

(93) Zhang, C. Y.; Yeh, H. C.; Kuroki, M. T.; Wang, T. H., *Nat. Mater.* **2005,** *4*, 826-831.

(94) Zhang, C. Y.; Johnson, L. W., *Angew. Chem.-Int. Edit.* **2007,** *46*, 3482-3485.

(95) Zhang, C.-y.; Johnson, L. W., *Anal. Chem.* **2006,** *78*, 5532-5537.

(96) Zhang, Y.; Zhang, C.-y., *Anal. Chem.* **2012,** *84*, 224-231.

(97) Zhang, C.-y.; Hu, J., *Anal. Chem.* **2010,** *82*, 1921-1927.

(98) Algar, W. R.; Krull, U. J., *Anal. Chim. Acta* **2007,** *581*, 193-201.

(99) Vannoy, C. H.; Chong, L.; Le, C.; Krull, U. J., *Anal. Chim. Acta* **2013,** *759*, 92-99.

(100) Medintz, I. L.; Berti, L.; Pons, T.; Grimes, A. F.; English, D. S.; Alessandrini, A.; Facci, P.; Mattoussi, H., *Nano Lett.* **2007,** *7*, 1741-1748.

(101) Bailey, V. J.; Easwaran, H.; Zhang, Y.; Griffiths, E.; Belinsky, S. A.; Herman, J. G.; Baylin, S. B.; Carraway, H. E.; Wang, T.-H., *Genome Res.* **2009,** *19*, 1455-1461.

(102) Zhou, D.; Ying, L.; Hong, X.; Hall, E. A.; Abell, C.; Klenerman, D., *Langmuir* **2008,** *24*, 1659-1664.

(103) Feng, C. L.; Zhong, X. H.; Steinhart, M.; Caminade, A.-M.; Majoral, J. P.; Knoll, W., *Small* **2008,** *4*, 566-571.

(104) Jiang, G.; Susha, A. S.; Lutich, A. A.; Stefani, F. D.; Feldmann, J.; Rogach, A. L., *ACS Nano* **2009,** *3*, 4127-4131.

(105) Zhou, D. J.; Ying, L. M.; Hong, X.; Hall, E. A.; Abell, C.; Klenerman, D., *Langmuir* **2008,** *24*, 1659-1664.

(106) Olmsted, J.; Kearns, D. R., *Biochemistry* **1977,** *16*, 3647-3654.

(107) Zhang, H. Y.; Zhou, D. J., *Chem. Commun. (Cambridge, U. K.)* **2012,** *48*, 5097-5099.

(108) Tyagi, S.; Kramer, F. R., *Nat. Biotechnol.* **1996,** *14*, 303-308.

(109) Kim, J. H.; Morikis, D.; Ozkan, M., *Sens. Actuator B-Chem.* **2004,** *102*, 315-319.

(110) Cady, N. C.; Strickland, A. D.; Batt, C. A., *Mol. Cell. Probes* **2007,** *21*, 116-124.

(111) Kim, J. H.; Chaudhary, S.; Ozkan, M., *Nanotechnology* **2007,** *18*.

(112) Li, Y. Q.; Guan, L. Y.; Wang, J. H.; Zhang, H. L.; Chen, J.; Lin, S.; Chen, W.; Zhao, Y. D., *Biosens. Bioelectron.* **2011,** *26*, 2317-2322.

(113) Freeman, R.; Liu, X. Q.; Willner, I., *J. Am. Chem. Soc.* **2011,** *133*, 11597-11604.

(114) Wu, C. S.; Oo, M. K. K.; Cupps, J. M.; Fan, X. D., *Biosens. Bioelectron.* **2011,** *26*, 3870-3875.

(115) Yeh, H. Y.; Yates, M. V.; Mulchandania, A.; Chen, W., *Chem. Commun. (Cambridge, U. K.)* **2010,** *46*, 3914-3916.

(116) Wu, S. M.; Tian, Z. Q.; Zhang, Z. L.; Huang, B. H.; Jiang, P.; Xie, Z. X.; Pang, D. W., *Biosens. Bioelectron.* **2010,** *26*, 491-496.

(117) Liu, L. Z.; Li, H.; Qiu, T.; Zhou, G. H.; Wong, K. Y.; He, Z. K.; Liu, Z. H., *Chem. Commun. (Cambridge, U. K.)* **2011,** *47*, 2622-2624.

(118) Charbonniere, L. J.; Hildebrandt, N., *Eur. J. Inorg. Chem.* **2008**, 3241-3251.

(119) Liu, X. Q.; Niazov-Elkan, A.; Wang, F. A.; Willner, I., *Nano Lett.* **2013,** *13*, 219-225.

(120) Golub, E.; Niazov, A.; Freeman, R.; Zatsepin, M.; Willner, I., *J. Phys. Chem. C* **2012,** *116*, 13827-13834.

(121) Cissell, K. A.; Campbell, S.; Deo, S. K., *Anal. Bioanal. Chem.* **2008,** *391*, 2577-2581.

(122) Kumar, M.; Zhang, D. H.; Broyles, D.; Deo, S. K., *Biosens. Bioelectron.* **2011,** *30*, 133-139.

(123) Whitesides, G. M., *Nature* **2006,** *442*, 368-373.

(124) Sanders, G. H. W.; Manz, A., *Trends Anal. Chem.* **2000,** *19*, 364-378.

(125) Teles, F. R. R.; Fonseca, L. R., *Talanta* **2008,** *77*, 606-623.

(126) Song, H.; Chen, D. L.; Ismagilov, R. F., *Angew. Chem.-Int. Edit.* **2006,** *45*, 7336-7356.

(127) Teh, S. Y.; Lin, R.; Hung, L. H.; Lee, A. P., *Lab Chip* **2008,** *8*, 198-220.

(128) Fair, R. B., *Microfluid. Nanofluid.* **2007,** *3*, 245-281.

(129) Abdelgawad, M.; Wheeler, A. R., *Adv. Mater. (Weinheim, Ger.)* **2009,** *21*, 920-925.

(130) Kurita, R.; Yokota, Y.; Sato, Y.; Mizutani, F.; Niwa, O., *Anal. Chem.* **2006,** *78*, 5525-5531.

(131) Springer, T.; Piliarik, M.; Homola, J., *Sensors and Actuators B-Chemical* **2010,** *145*, 588-591.

(132) Gao, Y. L.; Lam, A. W. Y.; Chan, W. C. W., *ACS Appl. Mater. Interfaces* **2013,** *5*, 2853-2860.

(133) Gao, Y.; Stanford, W. L.; Chan, W. C. W., *Small* **2011,** *7*, 137-146.

(134) Sun, S.; Ossandon, M.; Kostov, Y.; Rasooly, A., *Lab Chip* **2009,** *9*, 3275-3281.

(135) Islam, K.; Jha, S. K.; Chand, R.; Han, D.; Kim, Y. S., *Microelectron. Eng.* **2012,** *97*, 391-395.

(136) Lu, X. N.; Samuelson, D. R.; Xu, Y. H.; Zhang, H. W.; Wang, S.; Rasco, B. A.; Xu, J.; Konkel, M. E., *Anal. Chem.* **2013,** *85*, 2320-2327.

(137) Cao, L. L.; Cheng, L. W.; Zhang, Z. Y.; Wang, Y.; Zhang, X. X.; Chen, H.; Liu, B. H.; Zhang, S.; Kong, J. L., *Lab Chip* **2012,** *12*, 4864-4869.

(138) Triroj, N.; Jaroenapibal, P.; Shi, H.; Yeh, J. I.; Beresford, R., *Biosensors and Bioelectronics* **2011,** *26*, 2927-2933.

(139) Escobedo, C.; Chou, Y. W.; Rahman, M.; Duan, X. B.; Gordon, R.; Sinton, D.; Brolo, A. G.; Ferreira, J., *Analyst* **2013,** *138*, 1450-1458.

(140) Lam, B.; Fang, Z. C.; Sargent, E. H.; Kelley, S. O., *Anal. Chem.* **2012,** *84*, 21-25.

(141) Michalzik, M.; Wilke, R.; Büttgenbach, S., *Sens. Actuators, B* **2005,** *111–112*, 410-415.

(142) Ceyssens, F.; Witters, D.; Van Grimbergen, T.; Knez, K.; Lammertyn, J.; Puers, R., *Sens. Actuators, B* **2013,** *181*, 166-171.

(143) Hu, J.; Wang, S. Q.; Wang, L.; Li, F.; Pingguan-Murphy, B.; Lu, T. J.; Xu, F., *Biosens. Bioelectron.* **2014,** *54*, 585-597.

(144) Lei, K. F., *Jala* **2012,** *17*, 330-347.

(145) Kumar, S.; Ali, M. A.; Anand, P.; Agrawal, V. V.; John, R.; Maji, S.; Malhotra, B. D., *Biotechnol. J.* **2013,** *8*, 1267-1279.

(146) Whitesides, G. M., *Nature* **2006,** *442*, 368-373.

(147) McDonald, J. C.; Duffy, D. C.; Anderson, J. R.; Chiu, D. T.; Wu, H.; Schueller, O. J. A.; Whitesides, G. M., *Electrophoresis* **2000,** *21*, 27-40.

(148) Xia, Y.; Whitesides, G. M., *Annu. Rev. Mater. Sci.* **1998,** *28*, 153-184.

(149) McDonald, J. C.; Whitesides, G. M., *Acc. Chem. Res.* **2002,** *35*, 491-499.

(150) Lewis, L. N.; Lewis, N., *J. Am. Chem. Soc.* **1986,** *108*, 7228-7231.

(151) Marko, I. E.; Sterin, S.; Buisine, O.; Mignani, G.; Branlard, P.; Tinant, B.; Declercq, J.-P., *Science* **2002,** *298*, 204-206.

(152) Shallan, A. I.; Smejkal, P.; Corban, M.; Guijt, R. M.; Breadmore, M. C., *Anal. Chem.* **2014,** *86*, 3124-3130.

(153) Kitson, P. J.; Rosnes, M. H.; Sans, V.; Dragone, V.; Cronin, L., *Lab Chip* **2012,** *12*, 3267-3271.

(154) Dutta, D.; Ramachandran, A.; Leighton, D. T., *Microfluid. Nanofluid.* **2006,** *2*, 275-290.

(155) Squires, T. M.; Quake, S. R., *Rev. Mod. Phys.* **2005,** *77*, 977-1026.

(156) Di Carlo, D., *Lab Chip* **2009,** *9*, 3038-3046.

(157) Stone, H. A.; Stroock, A. D.; Ajdari, A., *Annual Review of Fluid Mechanics* **2004,** *36*, 381-411.

(158) Kirby, B. J.; Hasselbrink, E. F., *Electrophoresis* **2004,** *25*, 187-202.

(159) Sze, A.; Erickson, D.; Ren, L. Q.; Li, D. Q., *J. Colloid Interface Sci.* **2003,** *261*, 402-410.

(160) Cheng, Y. F.; Dovichi, N. J., *Science* **1988,** *242*, 562-564.

(161) Chien, R. L.; Burgi, D. S., *Anal. Chem.* **1992,** *64*, 1046-1050.

(162) Makamba, H.; Kim, J. H.; Lim, K.; Park, N.; Hahn, J. H., *Electrophoresis* **2003,** *24*, 3607-3619.

(163) Efimenko, K.; Wallace, W. E.; Genzer, J., *J. Colloid Interface Sci.* **2002,** *254*, 306-315.

(164) Liu, Y.; Fanguy, J. C.; Bledsoe, J. M.; Henry, C. S., *Anal. Chem.* **2000,** *72*, 5939-5944.

(165) Kaneta, T.; Ueda, T.; Hata, K.; Imasaka, T., *J. Chromatogr. A* **2006,** *1106*, 52-55.

(166) Erickson, D.; Liu, X. Z.; Krull, U.; Li, D. Q., *Anal. Chem.* **2004,** *76*, 7269-7277.

(167) Erickson, D.; Liu, X. Z.; Venditti, R.; Li, D. Q.; Krull, U. J., *Anal. Chem.* **2005,** *77*, 4000-4007.

(168) Algar, W. R.; Krull, U. J., *Anal. Chem.* **2009,** *81*, 4113-4120.

(169) Algar, W. R.; Krull, U. J., *Anal. Chim. Acta* **2007,** *581*, 193-201.

(170) Algar, W. R.; Krull, U. J., *Langmuir* **2009,** *25*, 633-638.

(171) Algar, W. R.; Krull, U. J., *Anal. Chem.* **2010,** *82*, 400-405.

(172) Algar, W. R.; Krull, U. J., *Sensors* **2011,** *11*, 6214-6236.

(173) Algar, W. R.; Krull, U. J., *Langmuir* **2010,** *26*, 6041-6047.

(174) Algar, W. R.; Krull, U. J., *Langmuir* **2008,** *24*, 5514-5520.

(175) Massey, M.; Krull, U. J., *Anal. Bioanal. Chem.* **2010,** *398*, 1605-1614.

(176) Wheeler, A. R.; Trapp, G.; Trapp, O.; Zare, R. N., *Electrophoresis* **2004,** *25*, 1120-1124.

(177) Wu, Y.; Lopez, G. P.; Sklar, L. A.; Buranda, T., *Anal. Biochem.* **2007,** *364*, 193-203.

(178) Algar, W. R.; Krull, U. J., *Langmuir* **2006,** *22*, 11346-11352.

(179) Algar, W. R.; Krull, U. J., *J. Colloid Interface Sci.* **2011,** *359*, 148-154.

(180) Boeneman, K.; Deschamps, J. R.; Buckhout-White, S.; Prasuhn, D. E.; Blanco-Canosa, J. B.; Dawson, P. E.; Stewart, M. H.; Susumu, K.; Goldman, E. R.; Ancona, M.; Medintz, I. L., *ACS Nano* **2010,** *4*, 7253-7266.

(181) Noor, M. O.; Krull, U. J., *Anal. Chim. Acta* **2011,** *708*, 1-10.

(182) Zhang, C. Y.; Johnson, L. W., *Angew. Chem. Int. Ed.* **2007,** *46*, 3482-3485.

(183) Suzuki, M.; Husimi, Y.; Komatsu, H.; Suzuki, K.; Douglas, K. T., *J. Am. Chem. Soc.* **2008,** *130*, 5720-5725.

(184) Goldman, E. R.; Medintz, I. L.; Whitley, J. L.; Hayhurst, A.; Clapp, A. R.; Uyeda, H. T.; Deschamps, J. R.; Lassman, M. E.; Mattoussi, H., *J. Am. Chem. Soc.* **2005,** *127*, 6744-6751.

(185) Shi, L. F.; De Paoli, V.; Rosenzweig, N.; Rosenzweig, Z., *J. Am. Chem. Soc.* **2006,** *128*, 10378-10379.

(186) Oh, E.; Hong, M. Y.; Lee, D.; Nam, S. H.; Yoon, H. C.; Kim, H. S., *J. Am. Chem. Soc.* **2005,** *127*, 3270-3271.

(187) Erickson, D.; Li, D. Q.; Krull, U. J., *Anal. Biochem.* **2003,** *317*, 186-200.

(188) Medintz, I. L.; Clapp, A. R.; Brunel, F. M.; Tiefenbrunn, T.; Uyeda, H. T.; Chang, E. L.; Deschamps, J. R.; Dawson, P. E.; Mattoussi, H., *Nat. Mater.* **2006,** *5*, 581-589.

(189) Hu, M.; Yan, J.; He, Y.; Lu, H. T.; Weng, L. X.; Song, S. P.; Fan, C. H.; Wang, L. H., *ACS Nano* **2010,** *4*, 488-494.

(190) Jokerst, J. V.; Raamanathan, A.; Christodoulides, N.; Floriano, P. N.; Pollard, A. A.; Simmons, G. W.; Wong, J.; Gage, C.; Furmaga, W. B.; Redding, S. W.; McDevitt, J. T., *Biosens. Bioelectron.* **2009,** *24*, 3622-3629.

(191) Klostranec, J. M.; Xiang, Q.; Farcas, G. A.; Lee, J. A.; Rhee, A.; Lafferty, E. I.; Perrault, S. D.; Kain, K. C.; Chan, W. C. W., *Nano Lett.* **2007,** *7*, 2812-2818.

(192) Tavares, A. J.; Noor, M. O.; Vannoy, C. H.; Algar, W. R.; Krull, U. J., *Anal. Chem.* **2012,** *84*, 312-319.

(193) Duffy, D. C.; McDonald, J. C.; Schueller, O. J. A.; Whitesides, G. M., *Anal. Chem.* **1998,** *70*, 4974-4984.

(194) Erickson, D.; Sinton, D.; Li, D., *Lab Chip* **2003,** *3*, 141-149.

(195) Erickson, D.; Liu, X.; Krull, U. J.; Li, D., *Anal. Chem.* **2004,** *76*, 7269-7277.

(196) Noor, M. O.; Krull, U. J., *Anal. Chim. Acta* **2011,** *708*, 1-10.

(197) Kim, J. H. S.; Marafie, A.; Jia, X. Y.; Zoval, J. V.; Madou, M. J., *Sensors and Actuators B-Chemical* **2006,** *113*, 281-289.

(198) Clapp, A. R.; Medintz, I. L.; Mauro, J. M.; Fisher, B. R.; Bawendi, M. G.; Mattoussi, H., *J. Am. Chem. Soc.* **2004,** *126*, 301-310.

(199) Clapp, A. R.; Medintz, I. L.; Uyeda, H. T.; Fisher, B. R.; Goldman, E. R.; Bawendi, M. G.; Mattoussi, H., *J. Am. Chem. Soc.* **2005,** *127*, 18212-18221.

(200) Cesaro-Tadic, S.; Dernick, G.; Juncker, D.; Buurman, G.; Kropshofer, H.; Michel, B.; Fattinger, C.; Delamarche, E., *Lab Chip* **2004,** *4*, 563-569.

(201) Noor, M. O.; Shahmuradyan, A.; Krull, U. J., *Anal. Chem.* **2013,** *85*, 1860-1867.

(202) Gong, P.; Levicky, R., *Proc. Natl. Acad. Sci. U. S. A.* **2008,** *105*, 5301-5306.

(203) Watterson, J. H.; Piunno, P. A. E.; Wust, C. C.; Krull, U. J., *Langmuir* **2000,** *16*, 4984-4992.

(204) Sadhu, C.; Dutta, S.; Gopinathan, K. P., *J. Biosci.* **1984,** *6*, 817-821.

(205) Piunno, P. A. E.; Watterson, J.; Wust, C. C.; Krull, U. J., *Anal. Chim. Acta* **1999,** *400*, 73-89.

(206) Watterson, J.; Piunno, P. A. E.; Krull, U. J., *Anal. Chim. Acta* **2002,** *469*, 115-127.

(207) Watterson, J. H.; Raha, S.; Kotoris, C. C.; Wust, C. C.; Gharabaghi, F.; Jantzi, S. C.; Haynes, N. K.; Gendron, N. H.; Krull, U. J.; Mackenzie, A. E.; Piunno, P. A. E., *Nucleic Acids Res.* **2004,** *32*.

(208) Peterson, A. W.; Heaton, R. J.; Georgiadis, R. M., *Nucleic Acids Res.* **2001,** *29*, 5163-5168.

(209) Noor, M. O.; Tavares, A. J.; Krull, U. J., *Anal. Chim. Acta* **2013,** *788*, 148-157.

(210) Medintz, I. L.; Clapp, A. R.; Mattoussi, H.; Goldman, E. R.; Fisher, B.; Mauro, J. M., *Nat. Mater.* **2003,** *2*, 630-638.

(211) Swift, J. L.; Heuff, R.; Cramb, D. T., *Biophys. J.* **2006,** *90*, 1396-1410.

(212) Arnspang, E. C.; Brewer, J. R.; Lagerholm, B. C., *PLoS One* **2012,** *7*, e48521.

(213) Mittal, R.; Bruchez, M. P., *Bioconjugate Chem.* **2011,** *22*, 362-368.

(214) Jennings, T. L.; Rahman, K. S.; Fournier-Bidoz, S.; Chan, W. C. W., *Anal. Chem.* **2008,** *90*, 2849-2856.

(215) Pons, T.; Medintz, I. L.; Wang, X.; English, D. S.; Mattoussi, H., *J. Am. Chem. Soc.* **2006,** *128*, 15324-15331.

(216) Sivasankar, S.; Subramaniam, S.; Leckband, D., *Proc. Natl. Acad. Sci. U. S. A.* **1998,** *95*, 12961-12966.

(217) Park, S.; Sinha, N.; Hamad-Schifferli, K., *Langmuir* **2010,** *26*, 13071-13075.

(218) Tavares, A. J.; Noor, M. O.; Uddayasankar, U.; Krull, U. J.; Vannoy, C. H., *Methods Mol. Bio.*, In press.

(219) Piruska, A.; Nikcevic, I.; Lee, S. H.; Ahn, C.; Heineman, W. R.; Limbach, P. A.; Seliskar, C. J., *Lab Chip* **2005,** *5*, 1348-1354.

(220) Noor, M. O.; Krull, U. J., *Anal. Chem.* **2013,** *85*, 7502-7511.

(221) Grabolle, M.; Spieles, M.; Lesnyak, V.; Gaponik, N.; Eychmuller, A.; Resch-Genger, U., *Anal. Chem.* **2009,** *81*, 6285-6294.

(222) Karstens, T.; Kobs, K., *J. Phys. Chem.* **1980,** *84*, 1871-1872.

(223) Magde, D.; Brannon, J. H.; Cremers, T. L.; Olmsted, J., *J. Phys. Chem.* **1979,** *83*, 696-699.

(224) Sens, R.; Drexhage, K. H., *J. Lumin.* **1981,** *24-25*, 709-712.